Fabrication and Characterisation of Microcavity Opto-electronic Devices via Heterogeneous Integration using Transfer Printing

The University Of Sheffield.

Philippe Rooswell Bantsi Mongapndam

Supervisor: Dr. Richard smith

A thesis submitted in partial fulfilment of the requirements for the degree of Doctor of Philosophy

The University of Sheffield

Faculty of Engineering

Department of Electronic and Electrical Engineering

March 2023

Acknowledgements

All praise to God for giving me the strength, knowledge, courage and patience for pursuing and successfully completing my PhD

I would like to thank my esteemed supervisor Dr. Richard Smith for his invaluable advice and continuous support throughout my PhD journey. His immense knowledge and plentiful experience have encouraged and inspired me throughout my research. I will like to extend my gratitude to him and our group head Prof. Tao Wang for affording me the incredible opportunity to become part of the centre for GaN materials and devices.

I would also like to extend my gratitude to some of my group members; Dr. Henry Worthy for training me on PDMS casting procedures and transfer printing operation. Si Chen for his help in the development of SU-8 master moulds. Dr Guillem Martinez for his help in DBR reflectivity measurements and Dr Suneal Gathora for his help in building the reflectivity measurement set up. I am grateful for all their contributions including advices and discussion. Thank you also to all technical staff for maintaining a safe working environment in all labs and ensuring the continuous good operation of the equipment

Finally, I will like to express my appreciation to my parents and family for their unconditional love, support, encouragements, for believing in me and always being there for me

Abstract

This research involved the use of a novel fabrication approach for the development of optical microcavity devices by heterogeneous integration of various material systems using transfer printing. Owing to their exceptional ability of light confinement, micro cavities have gathered a lot of scientific interest both at academic and industry level. The photonic confinement leads to the modification of the photonic density of states and allows cavity mode coupling with quasiparticle excitons within the emitter leading to exciting phenomena such as spontaneous emission rate enhancement, emission spectrum width reduction and radiation spatial directional re-distribution. Optical microcavities are appealing as they offer the possibility of controlling light emission and for such specific design conditions need to be followed. The development of microcavities is usually by monolithic integration of materials using epitaxy, despite being a relatively old process with numerous benefits, direct epitaxy also present some challenges and limitations. These include high cost and limitation of types of emitters that can be integrated into them due to their extreme deposition conditions, scarcity of compatible DBR material configuration particularly in the GaN material series, and small reflectivity bandwidth due to the small refractive index contrast for existing compatible DBR configurations. Our new optical microcavity fabrication approach has as aim of mitigating some of the existing issues while using standard, simple and less costly processing. Standard dielectric DBRs with large refractive index contrast (wide reflectivity band gap and low cost PECVD deposition) were used. The platform involves the anchor undercutting of the DBR into suspended array of DBRs which can then be transfer printed and integrated heterogeneously in any material system to fit the reflecting purpose, for optical microcavity applications.

Successful anchor undercutting of DBR coupon array with yield of almost 100% was achieved. The transfer printing of high quality DBRs was also demonstrated with reflectivity and bandwidth of 99% and 95nm respectively. Three types of cavity were fabricated (using our developed platform) and characterised; GaN based RCLED device, light emitting polymer microcavity and QD microcavity. We demonstrated multiple cavity modes emission for the incavity RCLED device with the peak mode showing an emission linewidth reduction from 21nm to 3nm from outcavity and incavity devices. The multiple modes are due to the wide cavity length as the full LED epilayer is transfer printed into the cavity together with adhesion layers. The device showed high series resistance due to the non-optimised fabrication processing with turn on voltage of approximately 2.7V. Smaller cavity length were realised for

the F8BT and QD microcavity. F8BT microcavity Purcell effect with a FWHM reduction from 80.6nm to 8.3nm due to the cavity effects was demonstrated. Carrier lifetime reduction of 68% from non-resonant cavity to resonant cavity was also demonstrated. The QD microcavity showed high quality factor of 1305 with FWHM reduction from 100nm to 0.4nm due to the microcavity effects. Power dependent non-linearity measurements were non-conclusive for lasing claims. Detailed process development including design, fabrication procedures and characterisation with relevant diagrammatic representations are provided. Discussion of the results obtained with routes for improvement are also provided.

List of publication

Journal publications

1. P. Bantsi, R. Smith “Development of heterogeneous fabrication approaches for the fabrication of microcavity devices by transfer printing showing Purcell effect” (in preparation)
2. P. Bantsi, R. Smith “Fabrication of GaN based RCLED via a Modified Transfer Printing Technique” (in preparation)

Conference Contributions

1. P. Bantsi, H. Worthy, S. Chen, R. Smith “Anchor undercutting towards high throughput transfer printing of device size high reflective SiN_x/SiO_2 DBR for microcavity applications”, Semiconductor and Integrated Optoelectronics (SOIE) conference April 2022
2. P. Bantsi, H. Worthy, S. Chen, R. Smith “Resonant cavity effects in transfer printed SiN_x/SiO_2 DBR microcavities”, UK semiconductors 2022

Table of content

1) Chapter 1 - Introduction

1.1 Introduction

In this chapter, a general introduction to the thesis context and subject is given. This research involved the fabrication and characterisation of novel hybrid micro-cavity optoelectronic light emitting devices using transfer-printing techniques. This include the use of various light emitting materials such as organic light emitting polymers, quantum dots and inorganic compound semiconductors. The aims and motivation for the research are discussed together with the major GaN research challenges. A brief history of light emitting devices with particular emphasis on GaN based LEDs is given. The chapter ends with a brief depiction of the new developed micro-assembly platform for simple micro-cavity devices fabrication.

1.2 Preface

1.2.1 Motivation

The importance of light to humankind and society is undeniable, from photosynthesis to illumination, light serves applications in different areas of communication, energy, education, health, design, agriculture, sports and more, this account for it having an annual market of a €350 billion [1]. Conventional lighting sources are the incandescent and florescent light sources. Incandescent lighting involves the use of filament wire, which glows when heated to produce light while florescent lighting uses electric field to excite mercury gas in tubes and emitting UV radiations, which lights phosphor coating in the tubes. These light sources serve their applications, but have drawback of low conversion efficiencies, 16 lm/W and 105 Lm/W for incandescent and fluorescent light respectively [2]. Considering that lighting accounts for about 29% of the global electricity usage [3], this implies a lot of energy is wasted. This together with other non-environmental friendly electricity manufacturing sources (coal, gas and oil) contributes to the growing world energy crisis and caused climate change hence, the need for research on new lighting solutions. The advent of solid-state lighting (SSL), which is a form of lighting by the use of Light Emitting Diodes (LEDs), Organic LEDs (OLEDs) or organic polymers, provides potential replacement candidates. LEDs are semiconductor based devices and offer advantages of improved luminous efficiency (three or four times more than conventional lighting), longer life time (lasting about fifty times more than conventional lighting), purer light quality, possibility to integrate in smart lighting system, low maintenance required and flexibility in deployment [4]. The LED's full potential as light sources could be

exploited thanks to 2014 Nobel Prize in Physics winners Shuji Nakamura, Hiroshi Amano and Isamu Akasaki for inventing efficient Gallium nitride based blue emitting LED which led to bright and effective white emitting LEDs [5].

1.2.2 Current state of art and applications of GaN based microcavities

GaN and other III nitrides (AlN, InN) are wide bandgap direct semiconductor which have revolutionised the solid-state optoelectronics industry as emission across the whole visible spectrum and beyond (that is wavelength between 200nm to 1771nm) is possible using this material series by alloying and composition changes in the material. Other exceptional GaN properties include high thermal stability, high chemical stability and high-energy efficiency therefore, good for the environment [6][7][8]. These account for the high interest in GaN material series and they already serve in applications such as LED for lighting, Visible Light Communication (VLC), next generation displays, photodetectors and solar cells, lasers, sensors [6] [9]. Despite their current exceptional properties, continuous research is still been carried out to further improve their performance in order to meet the demands. The current growing trend involves their incorporation into resonant optical microcavities[9] in order to exploit the novel phenomena arising from the quasiparticle-optical mode coupling enabled by such structures. Different types of microcavities exist such as DBR, photonic crystal, microdisk and surface plasmon [10] [11], [12] [13], [14]. Their optical performance improvement is possible by controlling their emission properties such as spontaneous emission rate, emission spectrum width and radiation spatial distribution [15] [16]. This have led to the development of novel important devices such as DBR based Resonant Light emitting Diode (RCLED), DBR based Vertical Cavity Surface Emitting Laser (VCSEL), surface plasmon enhanced photodetectors, surface plasmon enhanced LEDs, Whispering gallery microcavity lasers and more. Therefore, optical microcavities offer the possibility to exploit the full potential of III-Nitride (GaN in particular) based optoelectronics.

1.2.3 Current Challenge

The ultimate white light source is still a topic of research, current state of art involves the use of blue emitting InGaN/GaN LEDs to radiatively pump and down convert another fluorophore(s) [4]. Example of such fluorophores include organic light emitting polymers and quantum dots. These materials have the ability to emit photons of specific energy upon excitation (optical or electrical). They are characterised by their absorption and emission peak wavelengths, quantum yield and photo stability. Numerous development in material science has paved the way for various good performing organic polymers and quantum dots materials.

Optical micro-cavities are optical structures providing optical confinement and resonance, this allows the control of the emission [16] [17] [18]. This have been key in the understanding of fundamental physics of light matter interaction [16] [17] [18] and in the development of novel light emitting devices such as resonant cavity LEDs (RCLEDs) [19] [20] [21], Lasers [22] [23] and potentially threshold-less lasers [24] [25]. Planar optical micro-cavities are the most popular ones thanks to the ease of fabrication. They consist of two spaced high reflective mirrors (distributed Bragg Reflectors DBRs commonly used). DBRs are a type of reflectors consisting of alternating layers of high and low refractive index material leading to selective high reflectivity along the spectrum [22]. One of the critical conditions to be fulfilled is having cavity length comparable to the emission wavelength [17] [18] to ensure resonance. This means submicron dimensions are required for visible emission wavelengths. Current state of art optical micro-cavities are fabricated by epitaxy as developments in epitaxial processes such as Molecular Beam epitaxy (MBE) and Metal Organic Chemical Vapour Deposition (MOCVD) led to possibility of good quality thin film deposition. Despite offering advantage of in situ device growth with possibility of electrical injection, epitaxial grown GaN based optical micro cavities offer drawbacks of severe growth conditions of very high temperatures (up to 1000 °C) and low pressures hindering the incorporation of certain emitting materials (organics and certain QDs) who cannot survive such conditions. High cost processeing limiting their wide spread development. Also, DBRs (which are major components of optical micro-cavities) grown by epitaxy present some limits of lack of material configuration options for the DBRs, low refractive index contrast between existing DBR material configurations leading to small reflectivity bandwidth. Due to the nature of deposition, there also exist non-compatibility issues resulting from lattice mismatch between various DBR material configurations (AlN/GaN DBR for example) and between DBRs-active layers leading to defects (non-radiative recombination centres). This explain the need for a new platform which mitigate these issues

1.2.4 Developed technology

Photonic devices usually involve epilayers on top of a substrate solely serving a mechanical role, for this reason, the possibility of transferring optimised functional epilayer onto new layers presents an attractive way to integrate materials and devices into new configurations for improving their performances. Layers transfer have been realised over the years using methods such as wafer bonding followed by substrate removal and epitaxial lift off [1]. These are usually costly and challenging as different materials have different optimal device structure [26]. A new micro-assembly technique allowing manipulation and transfer of small dimension thin

layers materials in a parallel configuration with micron scale precision of placement was developed, this technique is called transfer printing [27] [1]. Using this technique, a material layer can be transferred from its original substrate to a new target substrate, this usually first involves the separation of the material from its original substrate. This is achieved using relevant selective etching methods [28]. Transfer printing offers the advantage of parallel stamp pick and printing leading to high yield and different sorts of materials (metals, colloids, organic materials, inorganic materials and more) with different geometries (quantum dots, nanowires, thin films, platelets and more) can be transferred onto a broad range of architectures as required by the application [27]. A new low cost platform using simple fabrication techniques was developed for the assembly of hybrid micro-cavity devices with the aim of mitigating challenges encountered by current used methods mentioned earlier. This platform involved anchor undercutting followed by transfer printing of the materials as stacks to form high quality factor optical micro-cavities. This has the potential of improving light emitting devices performance.

1.3 History of light sources for illumination – LEDs

Before the advent of electricity, fire was the main source of artificial light. It was made in different form for transportation purposes such as candles, torch, oil lamp and gas lamp. Since then, better quality and brighter light sources have been a major topic of interest. The first gas lighting device was developed in the 1800s, in 1809, Sir Humphry Davy developed the first carbon arc lamp which was powered by a basic battery which didn't lasted long [29] [30]. Many developments were done in the late 1800s including Thomas Edison buying the early incandescent lamp patent and developing the carbonized bamboo filament based incandescent lamp capable for lasting 1200 hours. The first tungsten filament lamp was developed by William Coolidge in 1911 but it wasn't until 1925 that the current design consisting of twisted filament and inert gas filled interior silica coated clear glass was developed [30]. Its working principle involves passing an electrical current through the filament, the filament then glow because of the resistive heating. Halogen lamps came into existence in the 1950s thanks to scientists working at GE, these are similar to incandescent lamps but with some halogen (iodine, bromine) added to it. The first fluorescent lamp was developed in 1976, it involved a glass coated with fluorescent material and filled with low pressure mercury gas which get ionised creating a plasma, the fluorescent material glow when struck by the plasma particle producing light [29] [30]. As lighting accounts for up to 29% of the global electricity consumption [3], it is very important to develop new lighting sources which are more energy efficient and green

in order to reduce energy wastage and carbon emission. Solid-state lighting appears to be the ideal replacement as shown in figure 1.1 showing the evolution and prediction of different light sources luminous efficacy over the years [31] . The figure shows a sharp rise in LEDs efficacies above all other sources with projections of continuous increase in the future. LEDs in general have greater efficiencies compared to traditional lighting sources (incandescent and fluorescent), that is more than 10 times and offer greater lifetime of about 50000 hours [31]. They produce purer emissions (smaller emission linewidth) and serve many applications in addition to illumination such as screen display technology, communication technology, traffic lights and more.

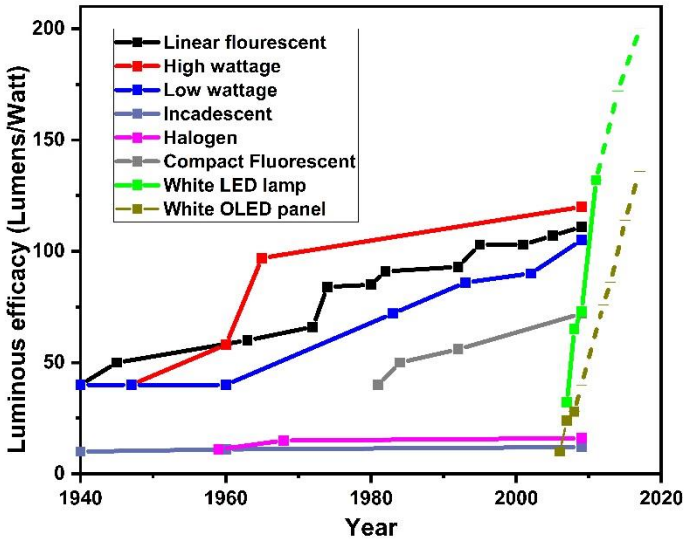

Figure 1.1 Plot of luminous efficacies evolution over the years for various light sources, adapted from [31]

The first discovery of emission from an inorganic material as a result of a potential applied across was shown in 1907 by English scientist Henry Joseph Round, since then multiple developments were made in the development of LEDs emitting in the yellow to red range of the spectrum [32]. This include development of the red emitting GaAsP LED in 1962 [33] and the AlInGaP Led system in the 1980s [32]. In the 1970s, LED found application in display lights and electrical indicators and at this period, they were mainly phosphide semiconductor based diodes. One particular colour was missing, that is the blue for white light generation. This was developed by 2014 Nobel prize in Physics winners Isamu Akasaki, Hiroshi Amano

and Shuji Nakamura “for the invention of efficient blue light-emitting diodes which has enabled bright and energy saving white light sources” [34], based on GaN.

1.3.1 Blue emitting LED historical developments

The development of blue emitting LED was a key breakthrough that permitted the full exploitation of solid-state lighting. These LEDs are made from the nitride system (GaN, AlN and InN) and expanded LED emission to the blue and green region of the spectrum. They are also essential in white emitting LEDs. As GaN is not a naturally occurring semiconductor, it needs to be synthesised. The first GaN crystal was grown in 1969 via chemical vapour deposition [32]. Finding the appropriate substrate for GaN growth has been a challenge due to lattice mismatch issues leading to cracks in the epilayer. It was not until 1986 that Amano et al [32] demonstrated a crack free GaN film on sapphire substrate using an AlN buffer layer. In addition, Nakamura et al [35] showed that growing first a 20nm GaN buffer layer at low temperature of 500°C before growing the main GaN could also have the same effect of reducing the cracks. Another challenge in GaN based LEDs is the conductivity of Mg doped P-type GaN. It was showed in 1989 again by Amano et al [36] that irradiating the layer with electron beams tends to activate the P-type layer conductivity. Heating the P-type GaN could also activate the layer making it more conductive, this was showed in 1992 by Nakamura et al [37]. This paved the way for GaN based PN- junction development. In 1993, the first blue emitting LED was presented by Nakamura et al [38], the LED active region was made of a double hetero-structure. White light generation using LEDs became a possibility and 2 years later in 1997 the first white light emitting LED was presented again by Nakamura et al [39]. Their structure involved the use of a blue LED exciting a yellow phosphor to emit apparent white light.

1.4 III nitrides emitters’ and resonant cavity devices challenges

Over the past decade, interest in GaN material series for opto-electronic devices has increased. This is thanks to numerous pioneering work in the field especially the development of the first blue emitting LED by professors Nakamura, Amano and Akasaki. This is shown by the high increase in publications in the subject over the years [40]. Despite all the innovations, there are still some challenges that need to be overcome. This section depicts some of these

1.4.1 Quantum Confined Stark Effect

III nitrides tend to crystallise naturally as Wurtzite crystals, this leads to spontaneous polarised crystals when grown along the C-plane of the lattice due to the lack of symmetry in the ions (see section 1.4.4). Extra strain on the lattice will cause further separation of the ions leading

to an increase in polarisation hence, piezoelectric effect [32]. The strain is usually because of difference in lattice mismatch and thermal expansion coefficient between the grown layers and the substrate. GaN/InGaN QW are widely used in optoelectronics applications especially as active regions in blue and violet emitters. InGaN having a larger lattice constant compared to GaN will strain GaN layer, the differences in polarity between the well (InGaN) and barrier (GaN) will create an electric field across the QW. This difference is further increased with more indium incorporation in the InGaN. This will have an effect of tilting the bands and separating the electron and hole wave functions as shown in figure 1.2 (b). This is called the Quantum Confined Stark Effect (QCSE) [41] [42] [43]. The band tilting reduces the overlap between electrons and holes in conduction and valence bands respectively, hence reducing radiative recombination. Also, the quantum well emitted photon energy will be reduced (red shifted) as the effective band is reduced as shown in figure 1.2 (c)

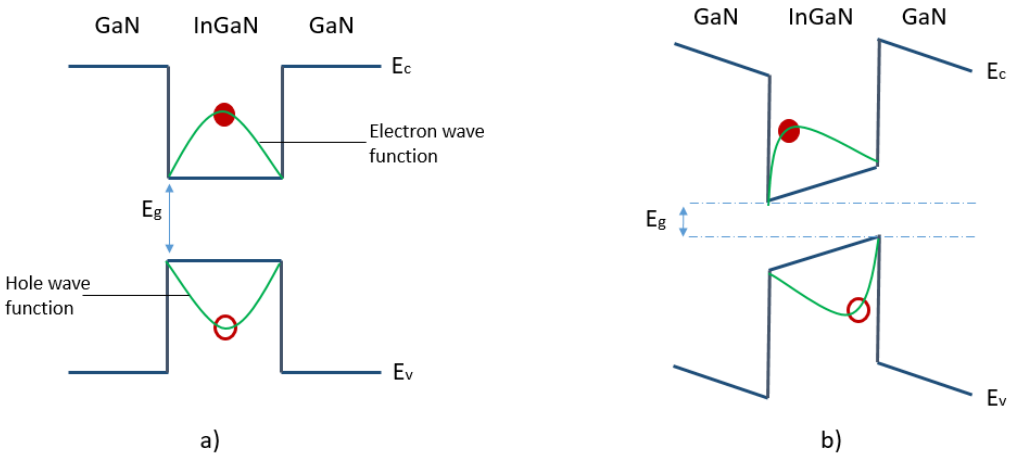

Figure 1.2 Quantum confined stark effect band structure illustration on GaN/InGaN quantum wells (a) with no electric field, (b) with electric field (from strained piezoelectric GaN)

The QCSE was studied by multiple groups [41] [43] it should also be noted that there are other phenomenon that can generate an electric field across the QW which might also cause QCSE for example increased carrier injection (optical, electrical, doping) [44], [45]. Despite the detrimental effects of QCSE, most GaN epitaxial growths still take place along the c-axis on sapphire and not along nonpolar axis (a-axis, m-axis) or semi-polar axis [46] [47] [48]. This is mainly due to three main reasons; poor indium incorporation for InGaN grown along non-polar and semi-polar axis compared to c-axis growth, incorporations 2 to 3 times lower were reported [49]. High defect density when grown along other axis compared to the c-axis [50] and for emission wavelengths greater than 400nm there is a dramatic decrease in emitted output power for devices employing nonpolar axis grown GaN [49]. Native GaN substrate can be used as

substrate to lower defect density along non-polar axis but they are scarce and expensive for common use. This is because they have high melting point and dissociation pressures of approximately 2800K and 40kbar respectively therefore, cannot be grown from stoichiometric melts via Czochralski methods [32]

1.4.2 The Green gap

Despite all advancement done involving LED research, there still exist a problem of differences in efficiencies for different types of LEDs, the so-called "green gap" [51]. This can be described as a decrease in LED efficiency as emission wavelength approaches the green region of the spectrum. This decrease is seen in nitrides and phosphide based LEDs. In the case of phosphides, for shorter emission wavelengths (less than 600nm), the semiconductor tend to transition from direct to indirect semiconductors hence, the drop in efficiency [32]. In the case of nitrides, the drop in efficiency is still a debate, but could be attributed to the existing miscibility gap between GaN and InN and increased strain effects due to increased indium incorporation. This leads to strain polarisation QCSE described above, this is amplified with more indium incorporation (shifting towards longer wavelengths) [52]. This problem is important as it affects the development of the ultimate white light source that is, white light generation by combination of Red, Green and Blue LEDs (RGB technology). Figure 1.3 depicts the efficiency decrease green gap phenomenon.

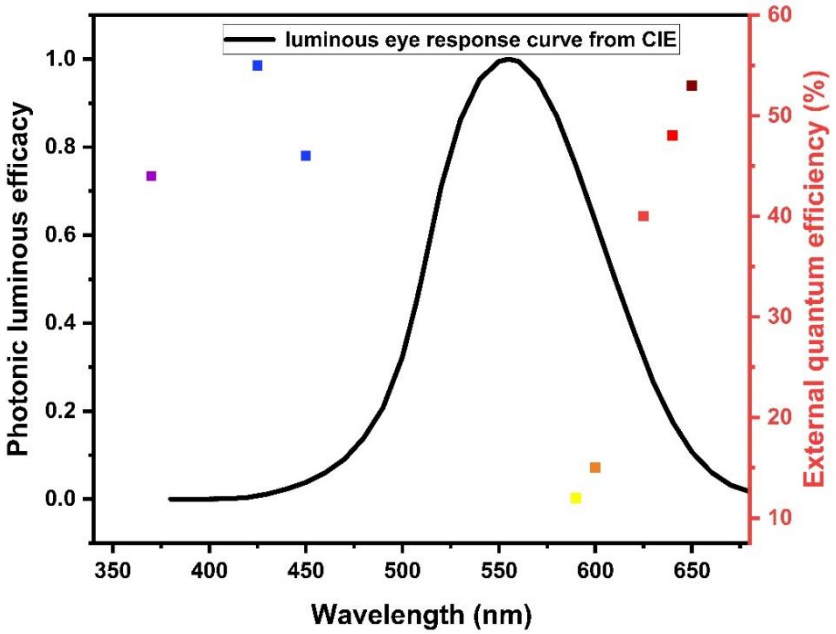

Figure 1.3 plot of external quantum efficiency against emission wavelength for various LEDs showing the green gap effect around the green region, luminous eye response also shown for comparison, adapted from [51]

1.4.3 Efficiency droop

During III nitride based LED operation, increase in drive current leads to decrease in the device efficiency. This is another puzzle associated with LED operation and is called the efficiency droop [53]. This is problematic as efficiency droops of up to 50% are possible. The source of the efficiency droop is still a scientific research mystery. Possible causes include Auger recombination [54] [55] that is, a non-radiative recombination were the excess energy from recombination leads to either excitation of electrons higher up the conduction band or holes further down the valence band. This type of recombination occurs more with higher carrier density and temperatures. Other possible causes of the efficiency droop are increase in other non-radiative recombination processes due to heating, carrier leakage [56] [57], built in electric field across the junction leading to more polarisation [58], carrier delocalisation as a result of high current density [59].

1.4.4 Problems associated with Light emitting devices epitaxy

In this section, the challenges associated to the epitaxial growth of GaN based light emitting devices layers in the making of the device will be discussed. This include lack of lattice match substrates for growth and challenge of achieving P-type doped GaN.

1.4.4.1 Challenge in GaN based light emitting devices growth

GaN is usually synthesised via epitaxial growth methods such MOCVD (Metalorganic Chemical Vapour Deposition), also commonly called MOVPE (Metalorganic Vapour Phase Epitaxy). Hence the need of a convenient (lattice matched) substrate for growth. Unfortunately, bulk GaN substrate are not easy to produce by stoichiometric melts (Czoxhralski method) due to their high dissociating pressure 40kbar and melting temperatures 2800K [47]. One way of making them is via Hydride Vapour Phase Epitaxy (HVPE) technique. This involves deposition of 300um GaN on sapphire substrate using GaCl and NH_3 [60] followed by laser lift up or any other technique to remove the sapphire substrate [61]. This process is expensive and has numerous problems associated with it such as bowing and cracking, so for this reason, free standing GaN substrate is not widely used.

The substrate used for GaN growth affects the film morphology, defect density, strain and crystallographic orientation [32]. Commonly used substrates are sapphire and silicon carbide (SiC). Sapphire and SiC offer lattice mismatch of 16% and 3.4% respectively [62], sapphire also has a thermal expansion difference of 25.5% compared to that of GaN but sapphire is more commonly used as it's less expensive than SiC. A 2-inch SiC wafer can cost around $1000 hence not popular [63]. Si wafers thanks to their low cost (8 inch wafer can cost about $40), large availability in large diameters and compatibility with current electronic processing have also been investigated as potential substrates [32]. Si has a lattice mismatch of 17% with GaN [60] and an even higher thermal expansion difference when compared to sapphire hence yielding a less good quality GaN epilayer but Si could provide other specific advantages abundance wafers at relatively low cost and compatibility with existing processing lines.

Sapphire usage as a substrate involves the growth of a buffer layer (AlN and GaN as examples) prior to the GaN epilayer growth. This is to minimise defects in the GaN epilayer. These defects acts as non-radiative recombination centres and tend to reduce the quantum efficiency of the end device. Due to the large lattice mismatch, GaN grown on sapphire offer threading dislocation density of about 10^8 cm^{-2}. Their device based on such configuration still shows good performance thanks to the localisation energy effect, which prevents carrier diffusion to the non-radiative recombination centres [64] [65] [66] [67]. It should also be noted that GaN is usually grown along its c-plane [0001] (polar plane) rather than other semi and non-polar planes [1-100], [11-20] and [11-22] respectively even though the polar planes provide more polarisation (higher QCSE). This is done because semi-polar and non-polar planes yield higher

defects densities [50] and lower indium incorporation for InGaN growth [49], hence not suitable for light emitting devices GaN growth

1.4.4.2 Challenge of achieving P-type doped GaN

P-type doping of GaN has always been a challenge for GaN based light emitting devices. Mg is commonly used as the P-type dopant and is usually made inactive due to two different processes. Both MOCVD and HVPE chambers are rich in hydrogen, this leads to the formation of Mg-H complexes, which are inactive complexes [32]. In addition, Mg have low acceptor states between 160 to 200 meV above the valence band [68] hence a large proportion are inactive at room temperature. These two processes leads to low conductivity of P typed GaN. Thanks to developments in epitaxial growth, the issues could be resolved. The Mg-H complex issue can be solved by annealing at temperatures of 700 °C in nitrogen rich atmosphere [69] [37] electron irradiation also helps in reactivating the Mg. This solution led to considerable increase in carrier distribution in p-type GaN though they are still orders of magnitude less than the n-type counterpart.

1.4.4.3 Challenge in assembling microcavity light emitting devices

Microcavity devices refer to optical structures used to confine light thanks to the multiple reflection happening within the structure [72]. They employ reflectors as major components to enable feedback within the structure. These structures are also sometimes called resonant cavities or quantum microcavities [18]. Example of such devices include lasers, RCLEDs, optical filters and anti-reflective coating. Good quality reflectors are required having properties of high peak reflectivity, broad reflectivity stop band, omni-directionality and low electrical resistance for electrically injected devices [73]. Many different reflectors exists such as metallic mirrors, Distributed Bragg Reflectors (DBRs), hybrid metallic DBRs and Total Internal Reflectors (TIR) [73]. Out of all, DBRs are usually preferred as they offer very high peak reflectivity (99.99% can be reached), selective reflectivity along the spectrum, easy controllability on the reflectivity peak value, stop bandwidth, and wide range of material configurations. Three major types of DBRs exist air gap based, epitaxial and dielectric DBRs. They all offer advantages and disadvantages as discussed below

Epitaxial grown DBR is a well-established process and usually involves the use of costly, high vacuum epitaxial process MOCVD (Metal Organic Chemical Vapour Deposition) and MBE (Molecular Beam Epitaxy) using costly precursor materials. DBRs grown this way offer advantages of ease of fabrication (as the full device stack including the active region can be

grown in situ) and good electrical and thermal conductivity [22] for electrical current injection and heat dissipation. However, there is a limit of the materials configuration available offering good lattice matching, a good example is the AlN/GaN epitaxy DBR forming cracks (non-radiative recombination centres) in the device. The concept of buffer layer is usually used to reduce the defects and allow some configurations to be used such as AlInN/GaN. In addition, the available material configurations usually have small refractive index contrast hence smaller stop bandwidth (fine-tuning is required) and more layer pairs are required to achieve high reflectivity [22]. An example is GaN/AlN with refractive index contrast of 0.08.

Dielectric DBRs are grown using less costly and conventional techniques such as sputtering and Plasma Enhanced Chemical Vapour Deposition (PECVD). Dielectric materials tend to have very low electrical and thermal conductivity. However, dielectric DBRs offer higher refractive index contrast compared to epitaxial ones, hence lower number of layer pairs required to achieve a high reflectivity peak wider stop bandwidth and wider emitting range. Dielectric DBRs also have much more material configurations, which are compatible [22].

Air gap DBR generally involved epitaxial grown DBR followed electrochemical etching of one of the layers leading to porous layer. The porous layer account for the air gap with very low refractive index of one. For this reason, the refractive index contrast of air gap DBRs is usually high. Hence, lower number of pairs are required and stop bandwidth is high but the compatibility issues and lack of available compatible material configuration exist still. In addition to that, their thermal and electrical conductivity is drastically reduced due to the air gap [22].

1.5 Optical micro-cavity assembly platform

Our platform involves the use of conventional dielectric SiN_x/SiO_2 DBRs. Compared to their epitaxial grown counterpart, dielectrics DBRs offer advantages of higher refractive index contrast of about 0.54 in the visible spectrum range. Hence, they have a wider stop band (meaning fine-tuning is less critical and wider range of emitters can be used as active layer in a set of cavity) and fewer pairs are required to achieve high reflectivity peak. In addition, they can be grown using less costly growth technique such as Plasma Enhanced Chemical Vapour Deposition (PECVD). Unfortunately, the growth conditions (temperatures of about 300°C) are still severe for some of the active layers such as organic polymers for example hence preventing the in situ incorporation of the active materials during growth. Our platform mitigate that by implementing the heterogeneous assembly of the individual elements forming the cavity by

transfer printing. The high reflectivity SiN_x/SiO_2 DBRs are first grown on Si (111) wafer substrate next, the DBRs are patterned via lithography, metallisation masking and Reactive Ion Etching (RIE, to expose the silicon substrate vertices) into arrays of coupons attached to anchors by tethers. The anchors are aligned to be parallel to the <110> orientation direction. Owing to the much larger Si KOH etch rate (100x) along the [110] plane compared to [111] plane, the DBR coupons only (not the anchors) could be undercut by KOH wet etch (anisotropic etch) [74] [75] . The result is freely suspended DBR coupons attached to anchors via tethers hence, anchor undercutting. These can then be transfer printed as stacks to sandwich a pre deposited emitting layer(s). The active layer deposited by simple spin coating, drop casting and even transfer printing depending on their morphology. This platform offer the possibility of high yield and throughput in micro-cavities fabrication as the transfer printing of multiple coupons can be done in parallel. In addition, lattice matching between grown layers, which is a key requirement (and the source of many defects) in epitaxial grown micro-cavities, is eliminated using this platform. Therefore, offering the potential for better quality micro-cavities.

1.6 Thesis outline

The report starts with a general abstract providing a general summary of the report, research undertaken, key findings with brief discussions. Then, the introduction chapter introduces the subject including motivation, current state of art, challenges and planned solutions related to the research. The background chapter follows the introduction, here, detailed relevant literature and theory is presented. All used laboratory equipment and techniques in the undertaking of the research are provided in the experimental techniques chapter. The first research result chapter is Chapter 4. In this chapter, the detailed processing description of the novel platform development for the heterogenous integration of GaN based emitters and other active emitters in optical microcavities by transfer printing is provided with results obtained and discussions. In Chapter 5, an actual functioning electrical injected optical microcavity device, the RCLED is fabricated using our developed platform via transfer printing. Detailed device fabrication and characterisation are also provided. Two different kinds of active material light emitting organic polymer F8BT and nanocrystal colloidal quantum dots (CQD) were also fabricated using our developed platform, their processing and characterisation are presented in Chapter 6. The report ends with the conclusion and future works chapter were a summary of the research is provided with key results and suggestions for future work improvements

1.7 References

[1] B. Corbett, R. Loi, W. Zhou, D. Liu, and Z. Ma, "Transfer print techniques for heterogeneous integration of photonic components," *Prog. Quantum Electron.*, vol. 52, pp. 1–17, Mar. 2017.

[2] M. G. Craford, "Current State of the Art in High Brightness LEDs," *Am. Phys. Soc. - SSL Sess.*, 2007.

[3] "Light goes out for incandescent bulbs | Energy efficiency | The Guardian." [Online]. Available https//www.theguardian.com/environment/2012/aug/31/lightbulbs-incandescent-europe. [Accessed 24-Oct-2022].

[4] J. Bruckbauer *et al.*, "Colour tuning in white hybrid inorganic/organic light-emitting diodes," *J. Phys. D. Appl. Phys.*, vol. 49, no. 40, p. 405103, Sep. 2016.

[5] M. Ilegems and R. Dingle, "Luminescence of Be- and Mg-doped GaN," *J. Appl. Phys.*, vol. 44, no. 9, p. 4234, Oct. 2003.

[6] L. X. Zhao *et al.*, "Progress and prospects of GaN-based LEDs using nanostructures," *Chinese Physics B*, vol. 24, no. 6. IOP Publishing, p. 068506, 20-May-2015.

[7] S. Nakamura, "Nobel Lecture Background story of the invention of efficient blue InGaN light emitting diodes," *Rev. Mod. Phys.*, vol. 87, no. 4, p. 1139, Oct. 2015.

[8] H. Amano, "Nobel Lecture Growth of GaN on sapphire via low-temperature deposited buffer layer and realization of p -type GaN by Mg doping followed by low-energy electron beam irradiation," *Rev. Mod. Phys.*, vol. 87, no. 4, p. 1133, Oct. 2015.

[9] L. X. Zhao *et al.*, "GaN-based LEDs for light communication," *Science China Physics, Mechanics and Astronomy*, vol. 59, no. 10. Science in China Press, pp. 1–10, 01-Oct-2016.

[10] I. Aharonovich *et al.*, "Low threshold, room-temperature microdisk lasers in the blue spectral range," *Appl. Phys. Lett.*, vol. 103, no. 2, p. 021112, Jul. 2013.

[11] Y. J. Lu *et al.*, "Plasmonic nanolaser using epitaxially grown silver film," *Science (80-.).*, vol. 337, no. 6093, pp. 450–453, Jul. 2012.

[12] Y. Hou, P. Renwick, B. Liu, J. Bai, and T. Wang, "Room temperature plasmonic lasing in a continuous wave operation mode from an InGaN/GaN single nanorod with a low threshold," *Sci. Rep.*, vol. 4, no. 1, pp. 1–6, May 2014.

[13] T. Tawara, H. Gotoh, T. Akasaka, N. Kobayashi, and T. Saitoh, "Low-threshold lasing of InGaN vertical-cavity surface-emitting lasers with dielectric distributed Bragg reflectors," *Appl. Phys. Lett.*, vol. 83, no. 5, pp. 830–832, Aug. 2003.

[14] B. Gayral and J.-M. Gerard, "Strong Purcell Effect for InAs Quantum Boxes in Three-Dimensional Solid-State Microcavities," *J. Light. Technol. Vol. 17, Issue 11, pp. 2089-*, vol. 17, no. 11, pp. 2089-, Nov. 1999.

[15] L. Zhao, C. Liu, K. Wang, L. Zhao, C. Liu, and K. Wang, "Progress of GaN-Based Optoelectronic Devices Integrated with Optical Resonances," *Small*, vol. 18, no. 14, p. 2106757, Apr. 2022.

[16] H. Yokoyama, "Physics and device applications of optical microcavities," *Science (80-.).*, vol. 256, no. 5053, pp. 66–70, 1992.

[17] X. Yu, Y. Yuan, J. Xu, K. T. Yong, J. Qu, and J. Song, "Strong Coupling in Microcavity Structures Principle, Design, and Practical Application," *Laser Photon. Rev.*, vol. 13, no. 1, p. 1800219, Jan. 2019.

[18] C. Schneider *et al.*, "Strong coupling phenomena in quantum microcavity structures," *Semicond.*

Sci. Technol., vol. 13, no. 7, p. 645, Jul. 1998.

[19] E. F. Schubert, N. E. J. Hunt, R. J. Malik, M. Micovic, and D. L. Miller, "Temperature and modulation characteristics of resonant-cavity light-emitting diodes," *J. Light. Technol.*, vol. 14, no. 7, pp. 1721–1728, 1996.

[20] F. Sarcan, Y. Wang, T. F. Krauss, T. Erucar, and A. Erol, "Dilute nitride resonant-cavity light emitting diode," *Opt. Laser Technol.*, vol. 122, 2020.

[21] S. Yang *et al.*, "GaN-based green resonant-cavity light-emitting diodes with Al mirror and copper plate," *Opt. Lett.*, vol. 47, no. 11, p. 2858, Jun. 2022.

[22] R. Kumar, K. Thakor, S. Gupta, R. Maripeddi, and D. Nag, "Design and Optimization of Dielectric DBR for VCSEL , Targeting Emission Range of 520-550 nm," Bombay, 2019.

[23] J. Hecht, "Short history of laser development," *SPIE Reviews*, vol. 1, no. 1. SPIE, 01-Sep-2010.

[24] F. De Martini and G. R. Jacobovitz, "Anomalous spontaneous–stimulated-decay phase transition and zero-threshold laser action in a microscopic cavity," *Phys. Rev. Lett.*, vol. 60, no. 17, p. 1711, Apr. 1988.

[25] H. Yokoyama, M. Suzuki, and Y. Nambu, "Spontaneous emission and laser oscillation properties of microcavities containing a dye solution," *Appl. Phys. Lett.*, vol. 58, no. 23, p. 2598, Jun. 1998.

[26] R. Nagarajan *et al.*, "InP photonic integrated circuits," *IEEE J. Sel. Top. Quantum Electron.*, vol. 16, no. 5, pp. 1113–1125, Sep. 2010.

[27] A. Carlson *et al.*, "Transfer Printing Techniques for Materials Assembly and Micro/Nanodevice Fabrication," *Adv. Mater.*, vol. 24, no. 39, pp. 5284–5318, Oct. 2012.

[28] K. Hjort, "Sacrificial etching of III-V compounds for micromechanical devices," *J. Micromechanics Microengineering*, vol. 6, no. 4, pp. 370–375, 1996.

[29] "The Historical Evolution of Lighting." [Online]. Available https//www.stouchlighting.com/blog/the-historical-evolution-of-lighting. [Accessed 24-Oct-2022].

[30] M. S. Zubairy, "A very brief history of light," *Opt. Our Time*, pp. 3–24, Jan. 2016.

[31] R. Van Buskirk, "Doubling the Global Pace of Progress for Energy Efficiency (EE) Applying a'Moore's Law' of EEto technology innovation for off-grid applications," Mar. 2015.

[32] D. Zhu and C. J. Humphreys, "Solid-state lighting based on light emitting diode technology," *Opt. Our Time*, pp. 87–118, Jan. 2016.

[33] N. Holonyak and S. F. Bevacqua, "Coherent (visible) light emission from Ga(As1-xPx) junctions," *Appl. Phys. Lett.*, vol. 1, no. 4, pp. 82–83, Dec. 1962.

[34] "The Nobel Prize in Physics 2014 - NobelPrize.org." [Online]. Available https//www.nobelprize.org/prizes/physics/2014/summary/. [Accessed 24-Oct-2022].

[35] S. Nakamura, M. Senoh, and T. Mukai, "Highly p-typed Mg-doped GaN films grown with GaN buffer layers," *Jpn. J. Appl. Phys.*, vol. 30, no. 10A, pp. L1708–L1711, Oct. 1991.

[36] H. Amano, M. Kito, K. Hiramatsu, and I. Akasaki, "P-type conduction in Mg-doped GaN treated with low-energy electron beam irradiation (LEEBI)," *Jpn. J. Appl. Phys.*, vol. 28, no. 12 A, pp. L2112–L2114, Dec. 1989.

[37] S. Nakamura, T. Mukai, M. Senoh, and N. Iwasa, "Thermal annealing effects on P-type Mg-doped GaN films," *Jpn. J. Appl. Phys.*, vol. 31, no. 2, pp. 139–142, Feb. 1992.

[38] S. Nakamura, M. Senoh, and T. Mukai, “High-power InGaN/GaN double-heterostructure violet light emitting diodes,” *Appl. Phys. Lett.*, vol. 62, no. 19, p. 2390, Jun. 1998.

[39] S. Nakamura and G. Fasol, “The Blue Laser Diode,” *Blue Laser Diode*, 1997.

[40] K. Takahashi, A. Yoshikawa, A. Sandhu, Y. Ishitani, and Y. Kawakami, *Wide bandgap semiconductors Fundamental properties and modern photonic and electronic devices*, 1st ed. Springer Berlin, Heidelberg, 2007.

[41] M. E. Aumer, S. F. LeBoeuf, S. M. Bedair, M. Smith, J. Y. Lin, and H. X. Jiang, “Effects of tensile and compressive strain on the luminescence properties of AllnGaN/lnGaN quantum well structures,” *Appl. Phys. Lett.*, vol. 77, no. 6, pp. 821–823, Aug. 2000.

[42] M. E. Aumer, S. F. LeBoeuf, B. F. Moody, and S. M. Bedair, “Strain-induced piezoelectric field effects on light emission energy and intensity from AlInGaN/InGaN quantum wells,” *Appl. Phys. Lett.*, vol. 79, no. 23, p. 3803, Nov. 2001.

[43] C. McAleese *et al.*, “Electric fields in AlGaN/GaN quantum well structures,” *Phys. status solidi*, vol. 243, no. 7, pp. 1551–1559, Jun. 2006.

[44] P. Riblet, H. Hirayama, A. Kinoshita, A. Hirata, T. Sugano, and Y. Aoyagi, “Determination of photoluminescence mechanism in InGaN quantum wells,” *Appl. Phys. Lett.*, vol. 75, no. 15, pp. 2241–2243, Oct. 1999.

[45] T. Kuroda and A. Tackeuchi, “Influence of free carrier screening on the luminescence energy shift and carrier lifetime of InGaN quantum wells,” *J. Appl. Phys.*, vol. 92, no. 6, pp. 3071–3074, Sep. 2002.

[46] “Popovici Deposition and properties of group III... - Google Scholar.” [Online]. Available https//scholar.google.com/scholar_lookup?&title=Deposition and properties of group III nitrides by molecular beam epitaxy&publication_year=1998&author=Popovici%2CG&author=Morkoç%2CH&author=Noor Mohammed%2CS. [Accessed 24-Oct-2022].

[47] M. J. Kappers, R. Datta, R. A. Oliver, F. D. G. Rayment, M. E. Vickers, and C. J. Humphreys, “Threading dislocation reduction in (0001) GaN thin films using SiNx interlayers,” *J. Cryst. Growth*, vol. 300, no. 1, pp. 70–74, Mar. 2007.

[48] D. D. Koleske, M. E. Coltrin, K. C. Cross, C. C. Mitchell, and A. A. Allerman, “Understanding GaN nucleation layer evolution on sapphire,” *J. Cryst. Growth*, vol. 273, no. 1–2, pp. 86–99, Dec. 2004.

[49] H. Yamada *et al.*, “Compositional dependence of nonpolar m-plane inxGa 1-xN/GaN light emitting diodes,” *Appl. Phys. Express*, vol. 1, no. 4, pp. 0411011–0411013, Apr. 2008.

[50] C. F. Johnston, M. J. Kappers, and C. J. Humphreys, “Microstructural evolution of nonpolar (11-20) GaN grown on (1-102) sapphire using a 3D-2D method,” *J. Appl. Phys.*, vol. 105, no. 7, p. 073102, Apr. 2009.

[51] M. R. Krames *et al.*, “Status and future of high-power light-emitting diodes for solid-state lighting,” *IEEE/OSA J. Disp. Technol.*, vol. 3, no. 2, pp. 160–175, Jun. 2007.

[52] N. A. El-Masry, E. L. Piner, S. X. Liu, and S. M. Bedair, “Phase separation in InGaN grown by metalorganic chemical vapor deposition,” *Appl. Phys. Lett.*, vol. 72, no. 1, p. 40, Jun. 1998.

[53] J. Cho, E. F. Schubert, and J. K. Kim, “Efficiency droop in light-emitting diodes Challenges and countermeasures,” *Laser Photon. Rev.*, vol. 7, no. 3, pp. 408–421, May 2013.

[54] Y. C. Shen, G. O. Mueller, S. Watanabe, N. F. Gardner, A. Munkholm, and M. R. Krames, “Auger recombination in InGaN measured by photoluminescence,” *Appl. Phys. Lett.*, vol. 91, no. 14, p. 141101, Oct. 2007.

[55] E. Kioupakis, P. Rinke, K. T. Delaney, and C. G. Van De Walle, "Indirect Auger recombination as a cause of efficiency droop in nitride light-emitting diodes," *Appl. Phys. Lett.*, vol. 98, no. 16, p. 161107, Apr. 2011.

[56] J. Xie, X. Ni, Q. Fan, R. Shimada, Ü. Özgür, and H. Morkoç, "On the efficiency droop in InGaN multiple quantum well blue light emitting diodes and its reduction with p -doped quantum well barriers," *Appl. Phys. Lett.*, vol. 93, no. 12, p. 121107, Sep. 2008.

[57] M. H. Kim *et al.*, "Origin of efficiency droop in GaN-based light-emitting diodes," *Appl. Phys. Lett.*, vol. 91, no. 18, p. 183507, Oct. 2007.

[58] J. Xu *et al.*, "Reduction in efficiency droop, forward voltage, ideality factor, and wavelength shift in polarization-matched GaInN/GaInN multi-quantum-well light-emitting diodes," *Appl. Phys. Lett.*, vol. 94, no. 1, p. 011113, Jan. 2009.

[59] A. Laubsch, M. Sabathil, J. Baur, M. Peter, and B. Hahn, "High-power and high-efficiency InGaN-based light emitters," *IEEE Trans. Electron Devices*, vol. 57, no. 1, pp. 79–87, Jan. 2010.

[60] M. Athanasiou, "Fabrication and Characterisation of III-Nitride based Nanostructure Devices using Nanosphere Lithography Techniques."

[61] S. S. Park, I. W. Park, and S. H. Choh, "Free-standing GaN substrates by hydride vapor phase epitaxy," *Jpn. J. Appl. Phys.*, vol. 39, no. 11 B, p. L1141, Nov. 2000.

[62] "Emerging markets to save sapphire substrates? - News." [Online]. Available https//compoundsemiconductor.net/article/90333/Emerging_markets_to_save_sapphire_substratestechnical. [Accessed 24-Oct-2022].

[63] "MTI Corp - Leading provider of lab equipments and advanced crystal substrates - SiC (6H)." [Online]. Available https//www.mtixtl.com/sic6h_1.aspx. [Accessed 24-Oct-2022].

[64] S. F. Chichibu *et al.*, "Origin of defect-insensitive emission probability in In-containing (Al,In,Ga)N alloy semiconductors," *Nat. Mater. 2006 510*, vol. 5, no. 10, pp. 810–816, Sep. 2006.

[65] D. M. Graham *et al.*, "Optical and microstructural studies of InGaN/GaN single-quantum-well structures," *J. Appl. Phys.*, vol. 97, no. 10, p. 103508, Apr. 2005.

[66] S. Hammersley *et al.*, "Study of efficiency droop and carrier localisation in an InGaN/GaN quantum well structure," *Phys. status solidi c*, vol. 8, no. 7–8, pp. 2194–2196, Jul. 2011.

[67] R. A. Oliver *et al.*, "Microstructural origins of localization in InGaN quantum wells," *J. Phys. D. Appl. Phys.*, vol. 43, no. 35, p. 354003, Aug. 2010.

[68] K. Doverspike and J. I. Pankove, "Chapter 9 Doping in the III-Nitrides," *Semicond. Semimetals*, vol. 50, no. C, pp. 259–277, Jan. 1997.

[69] S. Nakamura, N. Iwasa, M. Senoh, and T. Mukai, "Hole Compensation Mechanism of P-Type GaN Films," *Jpn. J. Appl. Phys.*, vol. 31, no. 5 R, pp. 1258–1266, May 1992.

[70] E. F. Schubert, W. Grieshaber, and I. D. Goepfert, "Enhancement of deep acceptor activation in semiconductors by superlattice doping," *Appl. Phys. Lett.*, vol. 69, no. 24, p. 3737, Jun. 1998.

[71] P. Kozodoy, M. Hansen, S. P. DenBaars, and U. K. Mishra, "Enhanced Mg doping efficiency in Al0.2Ga0.8N/GaN superlattices," *Appl. Phys. Lett.*, vol. 74, no. 24, p. 3681, Jun. 1999.

[72] E. F. Schubert, "Resonant-cavity light-emitting diodes," in *Light-emitting Diodes, Second Edition*, 2nd ed., Cambridge University Press, 2012, pp. 255–275.

[73] E. F. Schubert, "Reflectors," in *Light-Emitting Diodes*, 2nd ed., Cambridge University Press, 2006, pp. 163–190.

[74] H. S. Kim *et al.*, “Unusual strategies for using Indium Gallium Nitride grown on Silicon (111) for solid-state lighting,” *Proc. Natl. Acad. Sci. U. S. A.*, vol. 108, no. 25, pp. 10072–10077, Jun. 2011.

[75] K. E. Bean, “Anisotropic etching of silicon,” *IEEE Trans. Electron Devices*, vol. 25, no. 10, pp. 1185–1193, 1978.

2) Chapter 2 - Background

2.1 Bulk semiconductor

Three major materials types can be identified based on their electronic properties, which are determined by the materials electronic band structures and carrier's distribution. These types include conductors, insulators and semiconductors. Conductors have highest conductivity followed by semiconductors and insulators. In conductors, the valence band and conduction band overlap, making conduction band partially filled with electrons, which can be displaced to new free states by an applied external bias. This accounts for conductor's good electrical conductivity. Insulators on the other hand have a large energy barrier (band gap) separating the conduction band from the valence band therefore, limiting the opportunity for the electron to occupy new states required for conduction. Finally, a semiconductor band structure consists of a band gap also separating the conduction from the valence band but in this case, the gap is much narrower compared to that in insulators. This makes it possible for electrons in the valence band to be excited to the conduction band when the required amount of energy is supplied to the system (minimum the band gap energy). In addition, the conductivity of semiconductors can be varied upon doping the materials. Leading to n-type semiconductors (extra electrons) and p-type semiconductors (extra holes) when doped with donor and acceptor materials respectively. This accounts for the attractiveness of semiconductors in electronics applications. Many different semiconductor materials exist with individual benefits, below is a discussion on GaN, which offers amazing properties for optical applications and the main semiconductor material in this research.

2.1.1 Gallium Nitride (GaN)

GaN belongs to a group of compound semiconductor materials known as III-nitrides; they have been attractive in the past decade due to their exceptional electrical and optical properties, direct wide band gap, good thermal and electrical conductivity, and large breakdown voltage. Other III-nitrides include binary (AlN), ternary alloys (AlGaN, InGaN) and quaternary alloy (AlGaInN). They are all direct wide bandgap semiconductors and one of their key strengths is the possibility for their alloys energy bandgaps to be tuned continuously to cover the whole visible spectrum and beyond, from infrared up to the UV [1]. This can be seen in figure 2.1 showing bandgap energy against chemical bond length plot for GaN semiconductor systems

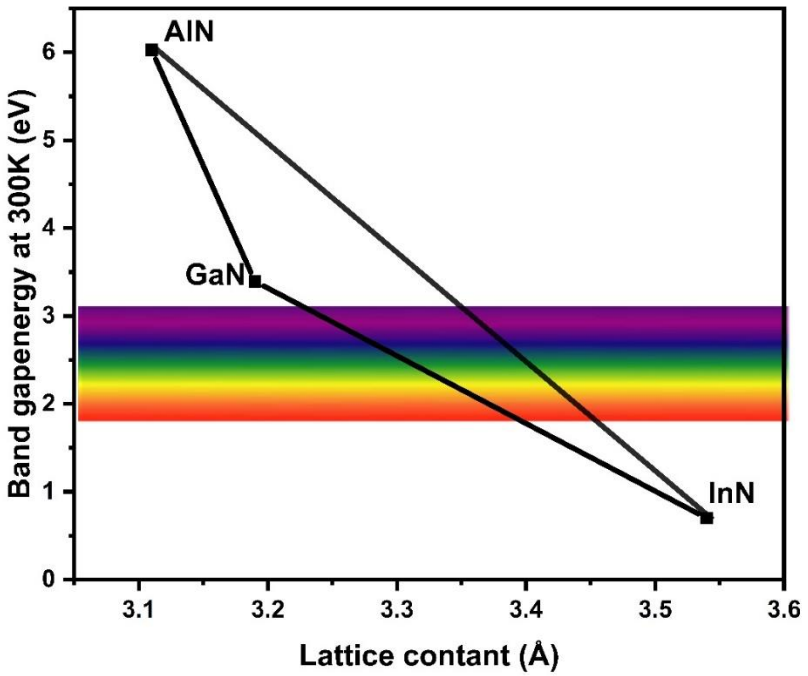

Figure 2.1 Bandgap energy against lattice constant (a) for various III-V compound semiconductors, adapted from [1]

Properties	GaN	AlN	InN
Bandgap (eV)	3.39	6.2	0.7
Density (g/cm^3)	6.10	3.26	6.99
Bond length (Å)	1.94	1.89	2.15
Melting point (°C)	>2500	>3000	>1100
lattice parameter a (Å)	3.189	3.112	3.545
lattice parameter c (Å)	5.185	4.982	5.703

Table 2.1 Physical properties of III nitrides, data obtained from [1] [2]

GaN has properties of thermal and chemical stability hence their use also in applications requiring harsh condition resistance. Table 2.1 summarises the physical properties of all binary III nitrides.

2.1.1.1 Crystal lattice

GaN just like other III nitrides can exist as in three different structures Wurtzite (hexagonal), zincblende (cubic) and rocksalt [3]. Wurtzite is the most thermodynamically stable of all under standard conditions hence, the most favoured structure. Wurtzite is composed of unit cell hexagonal in shape [5] [6] hence, has two lattice parameter a and c as shown in figure 2.2. Its unit cell is made up of Ga atom tetrahedrally bonded to four N atoms. As the two elements has different electronegativity, their bonding will be partially ionic bond. The ionic bonding together with the non-centro symmetry of the lattice along the c axis accounts for the spontaneous polarisation properties of GaN [4]. This spontaneous polarisation represents the base of the GaN piezoelectric properties.

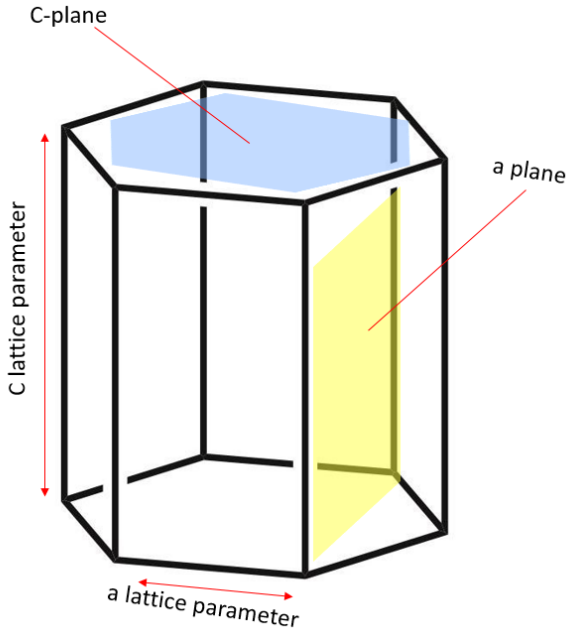

Figure 2.2 Schematic representation of C and a planes on III-nitride wurtzite crystal structure, adapted from [5]

2.1.1.2 Crystal growth

GaN is not a natural occurring semiconductor; it is usually obtained through chemical reaction. Two major processes are industry standards Metal-Organic Chemical Vapour Deposition (MOCVD) and Molecular Beam Epitaxy (MBE). The principal objective of these processes is to allow thin and very high purity layer growth. The growth process is critical as it determines the layer defect density, crystal orientation, intrinsic strain and surface morphology [4]. GaN growth in early days presented two major challenges lack of adequate substrate [6] and poor p-type GaN growth [7].

The lack of substrates with good lattice matching for GaN hetero-epitaxy and high cost of bulk GaN substrates has hindered high quality GaN layer growth. This lattice mismatch leads to threading dislocation development in the layer which act as non-radiative recombination centres [7]. Sapphire is the most widely used GaN epitaxy substrate, despite having a lattice mismatch of about 16%, useful GaN layer can be grown thanks to notable developments in growth techniques over the years. One method involves nucleation layer deposition [7], island formation and coalescence [7]. Threading dislocations can be reduced from $5x10^9$ cm^{-2} to $5x10^8$ cm^{-2} and even $1x10^8$ cm^{-2} by using multiple SiNx interlayer between GaN grown layers[4].

P-type GaN growth has always presented challenges compared to the n-type counterpart. Si is usually used as donor for n-type GaN and Mg as acceptors for p-type GaN [8]. The low concentration of holes is mainly due to two reasons formation of inactive Mg-Hydrogen during growth and deep acceptor states at about 200 meV hence, little to no room temperature activation [9]. The first issue is addressed by heating the layer in nitrogen rich atmosphere at temperatures greater than 700 °C to break the Mg-H complex bond [9]. Irradiating the layer with a beam of electrons can also be used [10].

2.1.1.3 Electrical and optical properties

Optical absorption occurs when an incident photon with energy hf $\geq Eg$ (semiconductor bandgap). This will have the effect of exciting an electron and promoting it from the valence band to the conduction band leaving a hole in the valence band. The coulombic interactions between the carriers leads to the formation of a quasi-particle electron-hole pair known as an exciton [11]. An exciton can be compared to a hydrogen atom and is usually described using the Bohr model with characteristic Bohr radius and binding energy. Two major types of exciton exist Wannier-Mott excitons and Frenkel excitons also referred to as free and bound excitons respectively. Wannier-Mott excitons tend to occur mostly in semiconductor crystals, the Bohr radius is greater than the lattice constant and the binding energy (E_b) of the electron hole pair is given by equation 2.1

$$E_b = -\frac{\mu}{m_0}\frac{1}{\varepsilon_r^2}\frac{R_H}{n^2} \qquad (2.1)$$

Where, $\frac{\mu}{m_0}\frac{1}{\varepsilon_r^2}$ = exciton Rydberg constant, R_H = Rydberg constant (13.61 eV) and n = quantum number.

The exciton stability is determined by its binding energy compared to ambient energy. A higher ambient energy compared to the exciton binding energy will cause the exciton to dissociate

into electron and holes and prevent exciton abilities to be exploited; this is the case in GaAs requiring cryogenic temperatures to witness excitonic properties as it has binding energy of only 8meV. GaN exciton has binding energy of around 26 meV hence, stable at room temperature [12]. The exciton dipole separation (r_n) can be calculated using equation 2.2

$$r_n = \frac{m_0}{\mu} \varepsilon_r \, n^2 a_H \qquad (2.2)$$

Where, $\frac{m_0}{\mu} \varepsilon_r a_H$ = exciton Bohr radius and a_H = hydrogen atom Bohr radius

2.2 Recombination processes

The recombination of electron and holes carriers can yield two different outcomes, radiative emission of photons or non-radiative recombination (phonon emission and hence temperature increase). The two outcomes are competitive with the radiative option preferred. At equilibrium, the law of mass action determines the relation between the carriers shown in equation 2.3 below. Upon excitation (optical or electrical), excess carriers are generated yielding equations 2.4 and 2.5 [13]

$$n_0 . p_0 = n_i^2 \qquad (2.3)$$

$$n = n_0 + \Delta n \qquad (2.4)$$

$$p = p_0 + \Delta p \qquad (2.5)$$

Where, n_0 = equilibrium electron concentration, p_0 = equilibrium holes concentration, n_i = intrinsic carrier concentration, Δn = excess electrons concentration, Δp = excess holes concentration

The excess electron are promoted to the conduction band of the energy band. The recombination process probability is proportional to both excess carrier concentration. Hence, the recombination rate is given by bimolecular rate equation 2.6 [13]

$$R = Bnp \qquad (2.6)$$

Where *B*, *n* and *p* are the bimolecular recombination coefficient, electron concentration, holes concentration respectively.

Under low-level pulse excitation, the generated excess carrier population decays exponentially and are given by equations 2.7 and 2.8

$$\Delta p(t) = \Delta p e^{\frac{-t}{\tau}} \qquad (2.7)$$

$$\Delta n(t) = \Delta n e^{\frac{-t}{\tau}} \qquad (2.8)$$

$$\tau = \frac{1}{B(n_0+p_0)} \qquad (2.9)$$

Where τ is the time constant

2.2.1 Radiative recombination

Recombination is governed by optical transitions within the material energy bands. Albert Einstein was the first to propose such theory in his Einstein model. Three main processes involved Stimulated absorption, spontaneous emission and stimulated emission [14] as illustrated in figure 2.3. In stimulated absorption, a photon is absorbed by the material causing an electron transition from the valence band to the conduction band leaving a hole behind. The photon energy must match or be larger than the material's energy band gap in order to cause the transition. This is illustrated in figure 2.3 (b) . In the case of spontaneous emission, the unstable promoted electron in the conduction band randomly transitions back to the valence band where it recombines with the hole, the transition causes release of the lost energy in the form of a photon. The emitted photon energy corresponds to the electron transition energy (material's band gap energy). This is illustrated in figure 2.3 (a). In stimulated emission, the transition of the excited electron from the conduction band to valence band is induced or provoked by an external stimulus, a photon. Therefore, the stimulated emission transition rate is directly proportional to the triggering photon density. Stimulated emission photons share multiple properties such as wavelength, phase, direction and intensity amplification, which serve in lasing [15]. Stimulated emission is illustrated in figure 2.3 (c)

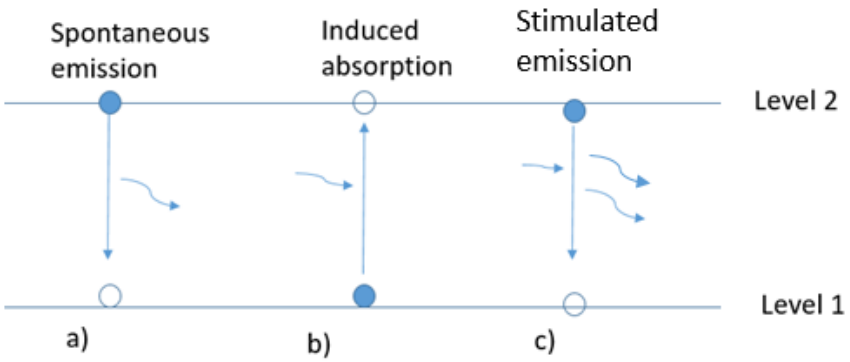

Figure 2.3 radiative processes a) spontaneous emission b) induced absorption c) stimulated emission

2.2.2 Non-radiative recombination

Here, the excess energy obtained from the carrier recombination is released as lattice vibrational energy, common referred to as a phonon. Various mechanisms can account for this non-radiative recombination effect such as;

Deep levels refers to energy levels, which occur near the material's band gap centre. They originate from impurities or defects present in the lattice and are effective non-radiative recombination centres. This illustrated in figure 2.4 (a). It should be noted that according to the Shockley-Read model, deep level recombination increases with increasing temperature [13]. Some deep level transition leads to radiative recombination, a good example is the point defect n-GaN broad deep level emission at 550nm wavelength [16].

Auger recombination is another non-radiative recombination mechanism where by the excess energy from the recombination causes an excitation of an electron further up in the conduction band or holes further down in the valence band, this is shown in figure 2.4 (b). The further excited carrier will eventually lose its excess energy to multiple phonon excitations and reach the band edge [13]. During high excitation, the Auger recombination rate (R_{Auger}) can be calculated using equation 2.10

$$R_{Auger} = Cn^3 \qquad (2.10)$$

Where C is the Auger coefficient (between 10^{-28} – 10^{-29} cm^6/s for III-V semiconductors) [17].

Because of the high dependent of R_{Auger} on the carrier concentration as shown in equation 2.10, it is negligible for low-level excitation where carrier concentration is low.

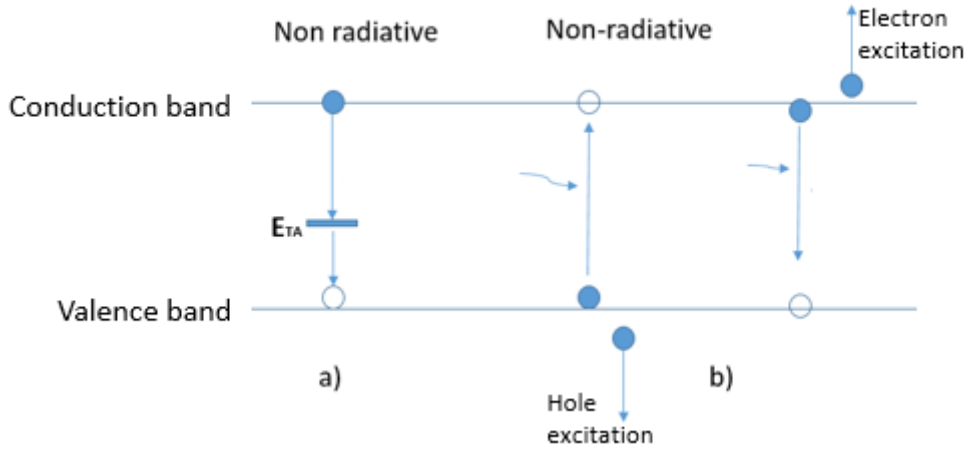

Figure 2.4 illustration of non-radiative processes a) due to deep levels b) due to Auger recombination, adapted from [13]

Surface state recombination is another non-radiative mechanism. Abrupt halt in the crystal periodicity of the material at the surface leads to unfilled orbitals and dangling bonds at this surface. This causes band gap modifications as unpredictable surface reconstruction may occur leading to multiple electronic states within the band gap at the surface. These surface states are effective non-radiative recombination states. As discussed, non-radiative recombination processes are not desirable for high efficiencies but cannot fully be eliminated. However, they can be minimised using some design strategies as discussed in section 2.8.3

2.3 Reflectors and microcavities

Reflectors are major components in optoelectronics microcavity devices as they help in optical confinement required for the optimal operation of such devices. Important resonant cavity effects can be observed and studied with such microcavities depending on the microcavity's quality factor that is how good the cavity is at preventing the dissipation of light. Some of these phenomena are enhanced and amplified spontaneous emission [18] [19], lasing [15], energy transfer beyond Förster limit [20] and more. Microcavity devices need reflectors satisfying a specific set of criteria such as high reflectivity, low electrical resistivity (for those that require charge transfer across), broad reflectivity linewidth and omni-directionality. For this purpose, different types of reflectors exists such as metallic reflectors, Distributed Bragg reflectors (DBRs), hybrid reflectors and Total Internal Reflector (TIR). They all have their advantages and disadvantages and the choice depends on the selected application. Below is an overview of the most commonly used reflectors for microcavity devices.

2.3.1 Metallic reflectors

These are the oldest type of reflectors, as the name implies they employ the metal-air/ metal-semiconductor interface to perform reflection. Metallic reflectors are characterised by their high and broad reflectivity spectrum with little incidence angular dependence. Metallic reflectors reflectance can be calculated using equation 2.11 [21]. As it can be seen, it is highly dependent on the refractive index contrast of the media, for this reason, metal-air mirrors have higher reflectance than metal-semiconductor ones (approximately 98.5% for Ag-air and 95% for Ag/GaAs mirror).

$$r = \frac{E_r}{E_i} = \left(\frac{N_1 - N_2}{N_1 + N_2}\right)^2 \qquad (2.11)$$

Where, N_1 and N_2 are complex refractive index of the materials used (metal and other media)

Another advantage of metallic reflectors is that they are simple to fabricate compared to other mirror types but they are also very lossy. Losses of 5% can be approximated from a single reflection event. In addition, metallic mirrors with thickness greater than 50nm provide nearly zero transmission hence cannot be used as exit mirrors, thinner metallic mirrors suffer from island deposition and potential high electrical resistance [21]. The reflectance band of a silver mirror is shown in figure 2.5, showing lower reflectance for Ag-GaAs compared to the Ag-air

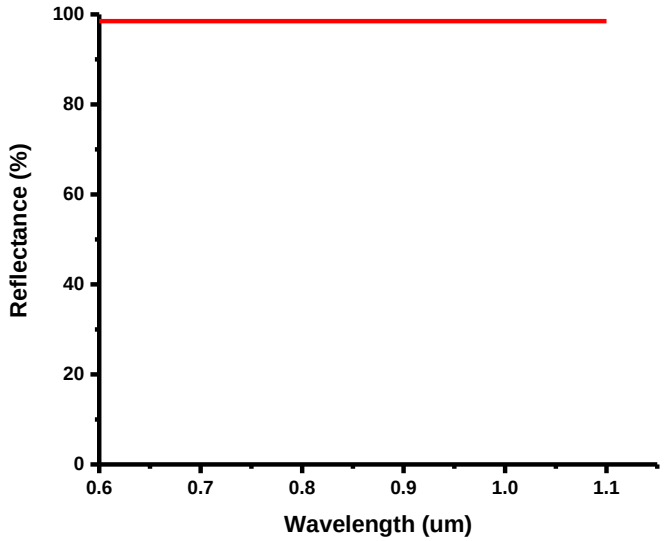

Figure 2.5 Reflectance spectrum (normal incidence) of metallic mirrors Ag/Air showing a high reflectance of 98.5% , adapted from [21]

2.3.2 Distributed Bragg Reflectors (DBRs)

DBRs are types of reflectors consisting of many layers of alternating refractive index materials. In contrast to metallic reflectors discussed above, DBRs reflectivity stop band (that is region of high reflectivity along the spectrum) is narrow and the peak reflectivity and stop band are controllable with reflectivity up to 99.99% achievable [21]. The working mechanism involves multiple Fresnel reflections at the material interface which constructively interfere and for this, specific conditions are required as depicted below [22]

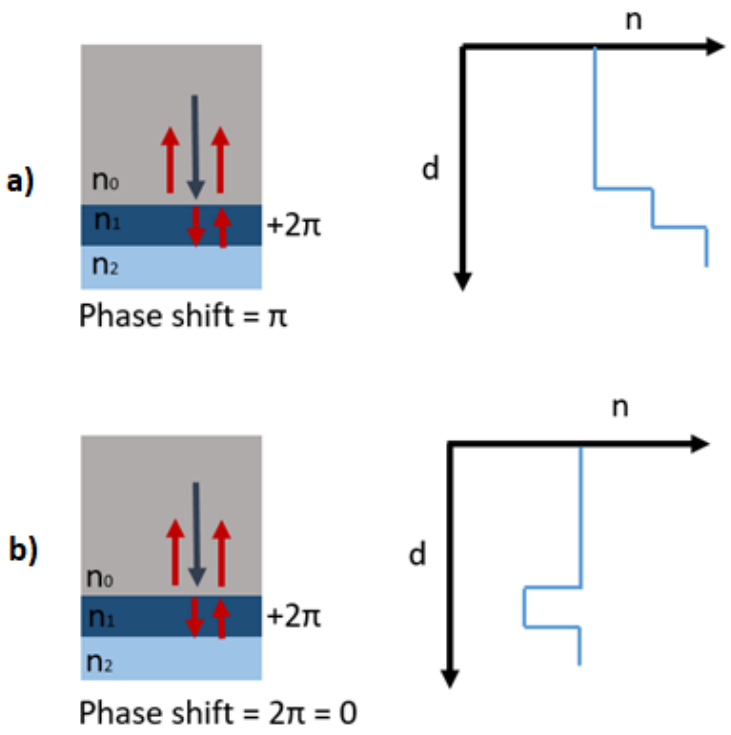

Figure 2.6 DBR reflection illustration a) constant increasing index $n_0<n_1<n_2$ b) Alternating index $n_0 = n_2 < n_1$

Light reflected from DBR's material interface can interfere either constructively or destructively. The phase change plays an important role. Consider light transitioning though a three layered DBR section, with refractive indices n_0, n_1, n_2 as shown in figure 2.6 (a). If $n_0<n_1<n_2$ that is, no alternation in refractive indices, two phase changes of π occurs at the n_0-n_1 and n_1-n_2 interfaces as the ray move from low refractive index material to a one with a higher value [23]. Another phase change occurs due to the optical length covered, for single layer optical length of $\lambda_0/4$ or pair with total optical thickness of $\lambda_0/2$ (λ_0 is centre wavelength of reflectivity stop band) optical length phase change is π [23]. This leads to a total phase change of $2\pi - \pi$ hence destructive interference (figure 2.6 (a)). However, if $n_0 = n_2 < n_1$ (alternating

refractive index, figure 2.6 (b)), the total material change phase will be only π as light moves from n_1 to n_2 (phase change from low index material to high index material is 0). There also exist an optical length phase change of π hence; the total phase change is zero, constructive interference. Therefore, DBR single layer or pair optical thickness of $\lambda_0/4$ and $\lambda_0/2$ respectively are needed for constructive interference.

$$nd = \frac{\lambda_0}{4} \qquad (2.12)$$

Where *n, d* and λ_0 are the refractive index, geometrical thickness and Bragg wavelength respectively.

In addition, it should be noted that, DBR layer optical thicknesses odd multiples of $\lambda_0/4$ will achieve the same results. Another requirement is that the materials are transparent or non-absorbing in order to maximise the reflectivity. The reflectivity R and stop band $\Delta\lambda_0$ can be calculated using equations 2.13 and 2.14 respectively

$$R = \left(\frac{1-\left(\frac{n_H^2}{n_a n_b}\right)\left(\frac{n_H}{n_L}\right)^{2N}}{1+\left(\frac{n_H^2}{n_a n_b}\right)\left(\frac{n_H}{n_L}\right)^{2N}}\right)^2 \qquad (2.13)$$

$$\Delta\lambda = \frac{4\lambda_0}{\pi}\arcsin\left(\frac{n_H - n_L}{n_H + n_L}\right) \qquad (2.14)$$

Where, n_L = low refractive index, n_H = high refractive index, n_a = initial medium refractive index, n_b = final medium refractive index, N = number of layer pairs

As seen in equation, 2.13 and 2.14, reflectivity is proportional to N, $\Delta\lambda_0$ is proportional to refractive index contrast and λ_0 can be chosen by varying layer optical thickness. It should also be noted that, the higher the refractive index contrast, the lower N are required to achieve higher reflectivity.

Angular incidence of light on a DBR can be resolved into vertical and horizontal components. Following equation 2.12, the vertical component is considered and can be re-written as equation 2.15 where θ is the oblique incidence angle to the normal. For this reason, increasing the oblique angle of incidence leads to blue shift in λ_0 and $\Delta\lambda_0$.

$$nd = \frac{\lambda_0}{4\cos\theta} \qquad (2.15)$$

One of the drawbacks of DBRs is their considerable penetration depth; therefore, in case of cavities, the effective cavity length is greater than the distance between the two mirrors. Also,

the low conductivity of some materials used for DBRs make them unreliable for electrically injected resonant cavity devices, an example include dielectric DBRs (Ta_2O_5/SiO_2) with low conductivity. Semiconductor based DBRs are more conductive and provide an alternative, an example is AlN/GaN.

Hybrid reflectors consisting of both DBRs and metals also exist; this also offers high reflectivity and almost zero transmission especially if the metal is thick (>50nm) [21].

2.3.3 Total Internal Reflectors (TIR)

Total Internal Reflection refers to a phenomenon where by a light ray is completely reflected back into its original medium as it travels across the boundary between two materials with different refractive index [21]. This phenomenon was first discovered by Kepler and then defined by Snell's in his equation the Snell's law given in equation 2.16

$$n_1 Sin\,\theta_1 = n_2 sin\,\theta_2 \qquad (2.16)$$

Where n_1, n_2, θ_1, θ_2 are refractive indices of medium 1 and 2, angle of incidence and angle of refraction respectively

Beyond a critical angle of incidence, the refracted angle can exceed 90° that is, total internal reflection. This critical angle can be calculated from Snell's law and is given by equation 2.17

$$\theta_c = Sin^{-1}(\frac{n_2}{n_1}) \qquad (2.17)$$

Therefore, n_1 has to be greater than n_2. Therefore, for TIR to occur, the original medium need to be optically denser than the second medium. TIR has the advantage of offering 100% reflectivity with almost zero transmission. This has been employed in lasers and optic fibres for communication applications as signal wave can be guided through an optical fibre via TIR with minimal loss as long as the incident angle is greater than or equal to the critical angle

2.4 DBR Fabry-Perot microcavities

Also called quantum microcavities (QMC), these are optical structures used to confined light thanks to the multiple reflection happening within the structure. The structure's optical length is comparable to the wavelength of the light to be confined; this allows the control of the emission. It is highly important for the exciton emission from the emitter to resonate with the cavity mode. Many different types of cavities have been reported such as micro-disk cavity [24], hybrid plasmonic laser microcavity [25], [26], photonic crystal nanocavity [26] and planar Fabry-Perot cavities [27] as shown in figure 2.7

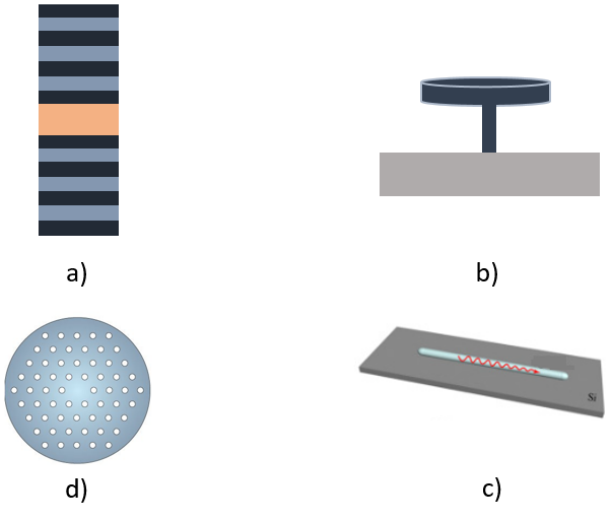

Figure 2.7 Illustrations of various optical microcavities a) Fabry-Perot microcavity b) microdisk microcavity c) plasmonic nanolaser d) photonic crystal

Microdisk, also called whispering gallery due to their mode of operation confine light via total internal reflection (TIR). The light circulating within the disk periphery reflects on the wall due to the surrounding air medium leading to TIR [29] [30]. This mode of confinement yields very high cavity Q factor.

Surface plasmon coupling is used in plasmonic lasers to ensure light confinement. This type of cavity is generally called a hybrid cavity. It consists of a thin layer (around 5nm) dielectric SiO2 deposited on silver metal, reflection occurs at the dielectric-metal interface [31].

2D Photonic crystals show in figure 2.7 (d), uses typically nanohole arrays to ensure reflection. A hole defect is intentionally produced at the centre of the structure, this causes light localisation as the density of states are higher for a specific wavelength [32]. The nanoholes are usually produced using Electron Beam Lithography (EBL) to achieve the small dimensions.

Fabry-Perot cavities are formed by stacking together two Bragg reflectors (Distributed Bragg Reflectors, DBR 1D photonic crystals) separated by the cavity layer. To ensure photon quantization in the cavity, some design considerations need to be taken. Figure 2.8 shows the schematic of a common QMC made of a cavity layer sandwiched by two DBRs.

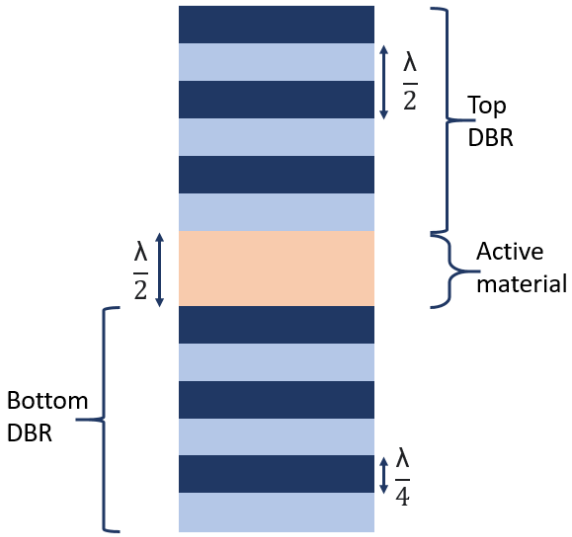

Figure 2.8 Planar Fabry-Perot optical microcavity, $\lambda/2$ cavity length

Having two high reflective DBRs forming a cavity will lead to the trapping of light plane waves in the cavity. The plane waves can interfere either constructively or destructively. Designing the cavity optical length to match a specific length criterion can allow certain optical modes to be sustained (constructive interference) and others attenuated (destructive interference). This criterion is given in equation 2.18. The sustained optical modes cause standing waves inside the cavity.

$$nL_c = \frac{m\lambda_c}{2} \qquad (2.18)$$

Where m, n, L_c, λ_c are an integer, cavity material refractive index, cavity length and centre wavelength (cavity mode) respectively

This standing wave leads to optical field nodes and antinodes in the cavity. Field distribution for m = 1 ($L_c = \frac{\lambda_c}{2}$) is shown in figure 2.9, it has a centred antinode with enhanced field strength compared to outside the cavity. As the photonic field can penetrate the DBRs up to a penetration depth L_{DBR} , the effective cavity length L_{eff} is larger than L_c and is given by equation 2.19 [33]

$$L_{eff} = L_c + L_{DBR} \qquad (2.19)$$

$$\text{Where, } L_{DBR} = \frac{\lambda}{2n_c}\frac{n_L n_H}{n_H - n_L} \qquad (2.20)$$

Where n_c = cavity material refractive index

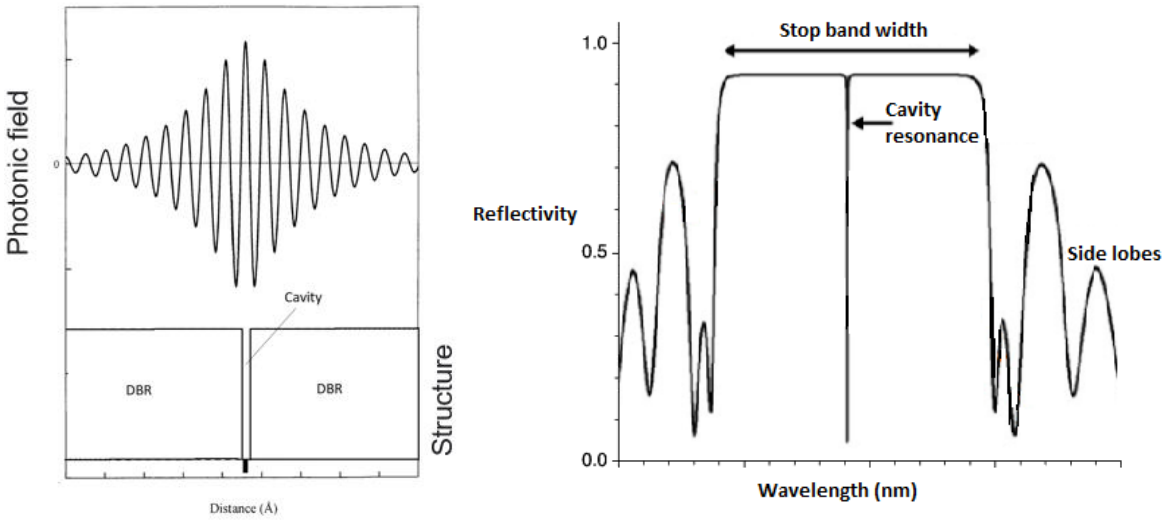

a) b)

Figure 2.9 a) Transfer matrix calculated plot of photonic field across cavity, photonic field enhancement by factor of 20 inside cavity, b) Obtained reflectivity spectrum of microcavity showing cavity mode dip, adapted from [34]

The standing wave leads to the formation of photonic modes which can be seen on the reflectivity spectrum stopband as dip(s) (low reflectivity areas) as shown in figure 2.9 (b) were one dip corresponds to λ cavity length. As the DBRs are not 100% reflective, there is decay in the cavity mode (mode lifetime) related to the width of the cavity mode [35]. The cavity mode width is given by equation 2.21

$$\hbar\Delta_c = \frac{\hbar c(1-R)}{n_c L_{eff}} \qquad (2.21)$$

The number of cavity modes formed in the cavity is directly proportional to the cavity length. This is related to one of the cavity parameters called the free spectral range (FSR). The free spectral range refers to the separation between successive cavity modes and is given by equation 2.22

$$FSR = \frac{(\lambda_c)^2}{2n_c L_c} \qquad (2.22)$$

As can be seen from equation 2.22, the FSR is inversely proportional to cavity optical length. Another very important cavity parameter is its quality factor (Q). This quality factor measures the ability of the QMC to confine photonic modes and prevent their escape from the cavity. The greater the photonic mode lifetime the better their confinement in the cavity leading to higher Q factor. This can be realised by minimising the losses. Numerous losses limit the cavity

Q factor; first, the fact that there will always be some leakage of the photon out as reflectance is always less than 100% reflectivity. In addition, the photons might be absorbed by the materials within the cavity or DBR. The material absorption coefficient at propagating wavelength determines the absorption loss. Scattering loss might also occur due to surface roughness and dislocations who originated from fabrication imperfections [36]. The cavity Q factor is given by equations 2.23 and 2.24

$$Q = \frac{4R}{(1-R)^2} \qquad (2.23)$$

$$Q = \frac{\lambda_c}{\Delta\lambda_m} \qquad (2.24)$$

Where $\Delta\lambda_m$ = cavity mode full width at half maximum (FWHM)

The cavity finesse (F) is also another measure of photonic mode leakage and is given by equation 2.25

$$F = \frac{\Delta\lambda_m}{FSR} \qquad (2.25)$$

2.5 Low dimensional structures

In bulk semiconductor materials (no carrier confinement region), carriers have a range of energy levels that are close to each other hence, considered continuous. Figure 2.10 (a) shows a representation of the parabolic energy band distribution in bulk material. There exists a forbidden band known as the band gap. Under steady state, majority carriers occupy the band lower to the band gap (valence band) and there might exist some excited carriers in the band above the band gap (conduction band). Transition of carriers from valence to conduction band require jumping of the band gap after excitation, forming an exciton (electron-hole pair).

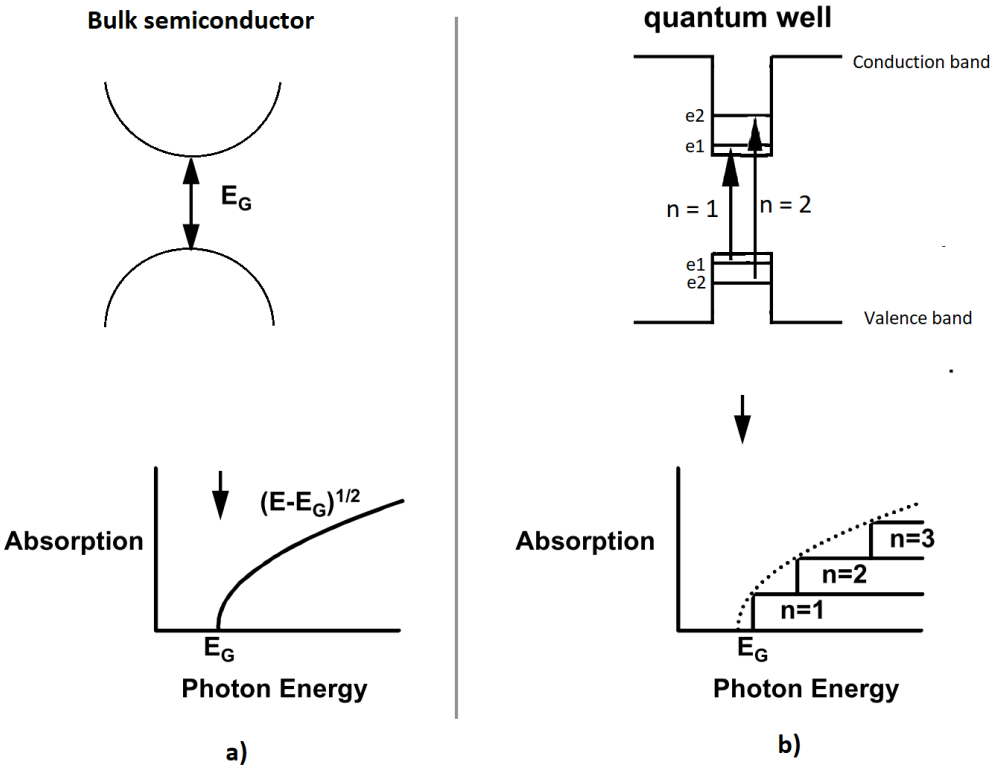

Figure 2.10 Optical absorption spectrum in bulk semiconductor and quantum wells, (a) bulk semiconductor (band to band transition), (b) quantum well semiconductor (sub-band to sub-band transitions)

Low dimensional semiconductors refer to those whose carriers' movements are restricted in at least one dimension. The carriers are said to be confined in the said direction if the confinement thickness (layer thickness) is comparable to the de Broglie wavelength (λ_{deB}) of the carriers given by equation 2.26

$$\lambda_{deB} = \frac{h}{\sqrt{2mk_BT}} \qquad (2.26)$$

Where, m = particle mass, T = temperature, k_B = Boltzmann's constant.

Table 2.2 and Figure 2.11 illustrates the different quantum confined structures quantum well, quantum wire and quantum dots offering 1, 2 and 3-dimensional confinement respectively. Quantum wells are widely used in optoelectronic applications as active layers due to the advantages they offer of improved radiative recombination in the active region and ability to tune the bandgap (emitted photon energy) by varying confinement energy [11]. Quantum well and quantum dots properties are reviewed in the next sections 2.5.1 and 2.5.2.

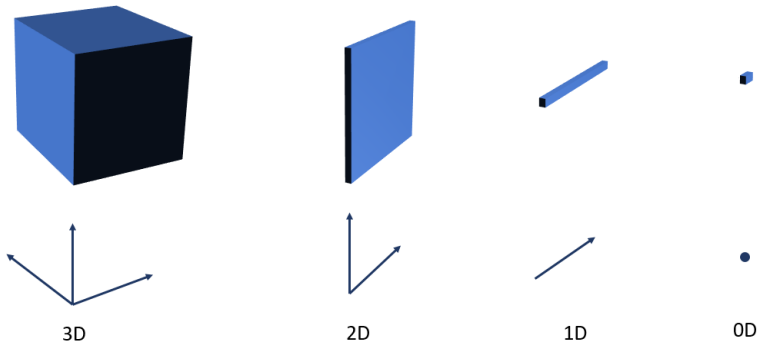

Figure 2.11 Different levels of quantum confinement bulk (3D), Quantum wells (2D), nanorod (1D) and Quantum dots (0D)

Structure	Dimensional confinement	Free carrier movement dimensions
Quantum well	1	2
Quantum wire	2	1
Quantum dot	3	0

Table 2.2 different quantum confined structures

2.5.1 Quantum wells

Quantum wells refer to quantum confined structures where the carriers are confined in one direction due to bandgap discontinuity existing as a lower bandgap thin layer, the well (around 100Å) is surrounded by two barrier layers of higher bandgap [11] [37]. Quantum confinement can only be achieved if the confinement width (well width) is comparable to the de Broglie wavelength of the carriers as explained in section 2.5. Notable advancements in epitaxial techniques for thin and pure layers growth has paved the way in the development of quantum wells. Quantum well is an example of a hetero-structure and serve many applications in electronic devices (modulation doped FET, bipolar transistors) and optoelectronic device (photodetectors, lasers) [37]. The confinement of carriers in a direction leads to discrete energy levels formation along the band perpendicular to the layers hence the system is said to be in a quantized state. This is illustrated in figure 2.12

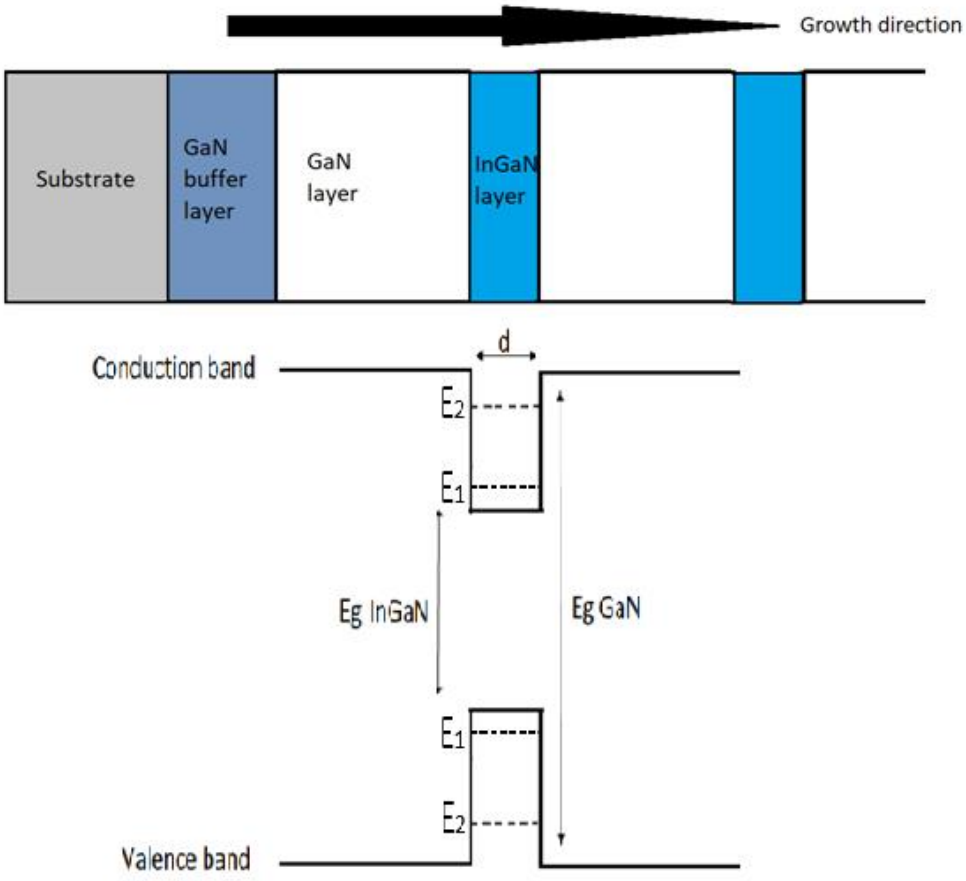

Figure 2.12 Grown GaN/InGaN quantum well layer diagram with corresponding band diagram, energy quantization due to confinement shown, adapted from [11]

The energy (E_n) at specific quantum number (n) in an ideal quantum well (infinite well) was derived from the infinite barrier model (particle in the box model) to yield the Schrödinger equation [38] [11] given in equation 2.27

$$E_n = \frac{\hbar^2 k_n^2}{2m_w^*} = \frac{\hbar}{2m_w^*}\left(\frac{n\pi}{d}\right)^2 \qquad (2.27)$$

Where, m_w^* = effective mass in well, d = well width

As seen from equation 2.27, E_n is inversely proportional to m_w^* and d^2 meaning heavier particles have smaller confinement energies compared to lighter particles (heavy holes compared to light holes) and narrower well width leads to higher confinement energy. This provides one of the benefits of quantum wells as the band edge energy can be shifted to higher energies by varying the confinement energy (or well width). This provide an alternative method to alloying (which is not preferred due to the inevitable impurities and defects addition) for

tuning the emitted photon energy (bandgap) of the semiconductor [37] [11]. Also, the confinement brought by the barrier brings the electron and hole wavefunctions closer. This greatly increases the probability of radiative recombination to occur which is beneficial for optoelectronic devices.

2.5.1.1 Optical absorption in QW

One other effect of quantum confinement is the modification of the semiconductor density of states (DOS). The DOS is the amount of available states that can be occupied by free electrons at each energy level [39]. In bulk semiconductor, DOS is continuous and follows the parabolic energy bands. Absorption follows this DOS and results in a spectrum as shown in figure 2.10 (a). In QW, absorption transition may occur between states of same quantum number in conduction and valence band [11]. n = 1 and n = 2 transitions are shown in figure 2.10 (b). n = 1 is the lowest transition and has energy slightly greater than the band edge and is known as the threshold energy given by equation 2.28

$$\hbar\omega = E_g + E_{h1} + E_{e1} \qquad (2.28)$$

Where E_{h1} and E_{e1} are holes and electron confinement energies respectively

As the carriers are free to move in two directions, the quantized energy levels are not discrete but can be regarded as sub-bands having minimum energy given by the confined states. As such the electrons can have extra energy contributing to its kinetic energy motion in free dimensions, this allows a constant DOS in the QW plane as energy varies hence, step increases in DOS which translates to the absorption spectrum [37] as shown in figure 2.10 b.

The creation of excitons needs to be considered. This greatly alters the observations made above giving rise to peaks in the absorption spectrum corresponding to the inter-band absorption (steps in figure 2.10 (b)). The main difference between bulk excitons and QW excitons is the “squeezing” of the exciton at least in the direction perpendicular to the well (and other directions too [37]), due to the narrow well width which has effects of reducing the Bohr radius and increasing the exciton binding energy. For this reason, excitonic effects are observable at room temperature in QW compared to bulk.

2.5.2 Quantum dots (QD)

Also referred to as semiconductor nanocrystals (NC), QD are semiconductor nano structures offering quantum confinement effect (QCE) in three dimensions therefore, 0 degree of motion for the carriers. This leads to the breaking of the continuous band structure of bulk

semiconductors to form quantized states [40] [41]. QDs are nanocrystals with width less than 10 – 20nm, at these dimensions (comparable to the de Broglie wavelength of the carriers), the band gap energy is dependent on the dot dimensions thanks to the quantum confinement effect [41] [42]. They exist in different shapes such as spheres, rods, cubes and tetrapods. The particularity of QD is that they allow tune-ability of the semiconductor's carrier transition energy based on dot dimension radius. This is thanks to the quantum confinement energy [43]. This allows optical absorption, emission and electrical properties engineering via sizing [42]. It should also be noted that confinement could also be caused by strain effects, impurities within the material and external potential [44]. One of the main limitations of QD is their degradation when subjected to photo-oxidation [45][46]. Therefore, the need for surface passivation to ensure better chemical, thermal and photo-stability. Different strategies have been reported such as capping the core with an extra layer of organic molecules. This layer of organic molecules provide electronic passivation of the nanocrystals and prevention of agglomeration of the nanocrystals as they can be manipulated as larger molecules with reactivity determined by the capping layer [41]. Some have a completely new semiconductor of larger bandgap encapsulating them as shells, this helps in surface passivation hence preventing carriers from migrating to non-radiative recombination centres and reduction of Auger recombination [41]. An illustration of a core/shell QD is shown in figure 2.13 with the CdSe QD size-emission colour variations. Some have surfaces laminated with affinity ligands for cells targeting and binding as required and act as protection layer also.

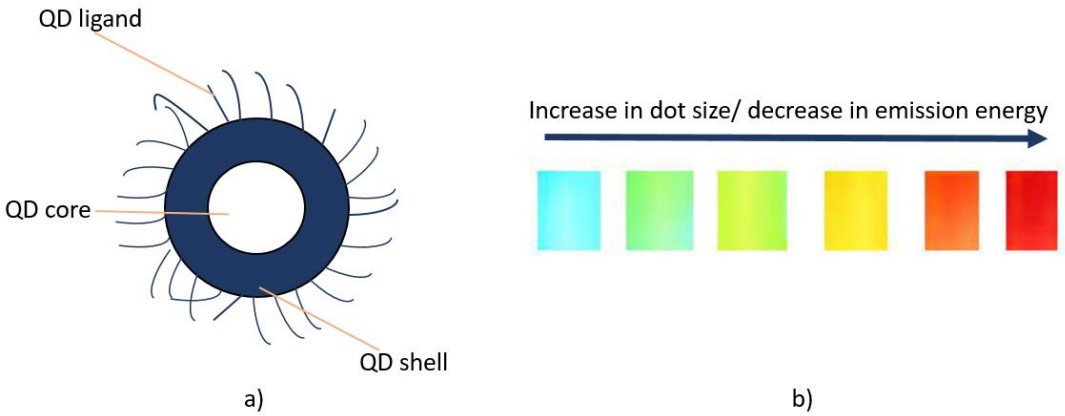

Figure 2.13 Quantum dots nanocrystal images a) illustration of single quantum dot structure b) quantum dot emission variation with size of the dots

Three dimensional quantum confinement of carriers in QD leads to the modification of the electronic states in QDs. New independent quantized states are produced which are different

from the continuous parabolic distribution from the bulk. This means optical absorption and emission can only happen at specific transitions. Just as quantum wells described above, QD have a modified DOS. Here, the DOS are discrete translating to sharp peaks on the absorption spectrum as shown in figure 2.14

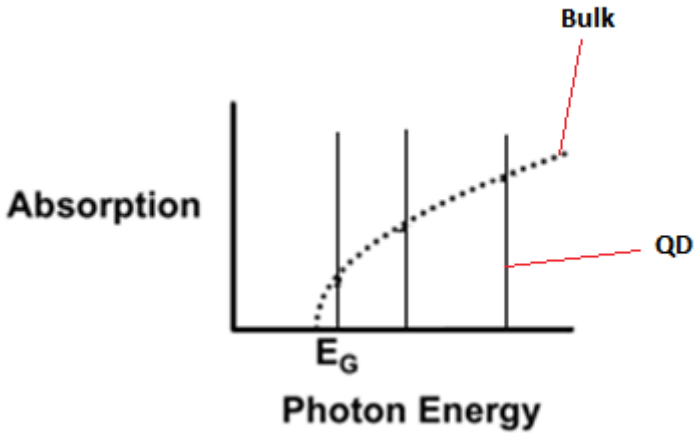

Figure 2.14 plot of absorption against photon energy of quantum dots showing the modification of the density of states

QDs can be synthesise in different ways with the main methods being epitaxy and colloidal synthesis.

By epitaxy, QDs are grown by the MBE (Molecular Beam Epitaxy), Laser ablation, Vapour Phase epitaxy (VPE) and Liquid Phase Epitaxy (LPE). By MBE process using the Stranski-Krastanow regime [11]. An example is the growth of InAs on GaAs substrate, due to the large lattice mismatch between the two layers, the strain effect favours formation of nanometre scale clusters islands of InAs. Epitaxial growth of the QD provides the advantage of in situ incorporation within the device but tend to be more costly than colloidal synthesis

Colloidal synthesis involves chemical reaction processing resulting in QD suspended in solution hence Colloidal Quantum Dots (CQD). The commonly used process involves hot solvent pyrolysis of metal-organic precursors; this is termed hot injection method [47] [48]. Here, the QD size can be controlled to a better precision compared to epitaxy [48] [49]. Some precursor chemicals are used which are heated at high enough temperature to breakdown into monomers which then nucleate to form the dots. The monomer concentration and temperature

are the two critical parameters for the process. Colloidal QDs offer larger batch synthesis of QD suspended in solutions such as toluene for example.

The QD bandgap energy $E_{g(QD)}$ can be approximated using Brus equation; this is shown in equation 2.29. The equation is based on excitons confined to a spherical space volume [50]. The equation consists of three different terms; the first term represents the bulk band-gap energy. The second summing term represents the quantum confinement energy of the carriers, as it can be seen this term is proportional to $1/R^2$ where R is the QD radius hence, this allow energy tuning of the dot using dot dimensions. The third term represents the electron hole coulombic interactions within the QD; this term is negligible for high dielectric constant semiconductors

$$E_{g(QD)} = E_{bulk} + \frac{h^2}{8R^2}\left(\frac{1}{m_e^*} + \frac{1}{m_h^*}\right) - \frac{1.786e^2}{4\pi\varepsilon_0\varepsilon_r R} \qquad (2.29)$$

Where, h,E_{bulk} , m_e^*, m_h^*, R, e and ε_0, ε_r are the Plank constant, bulk band gap, effective mass of electron, effective mass of hole, dot radius, electronic charge, permittivity of vacuum and relative permittivity

In addition to material electrical and optical properties tune-ability by sizing, QD are also characterised by their high quantum yield, this is because they have higher DOS near the bandgap edge hence, brighter emissions [51]. QD are also more resistant to photo bleaching compared to organic fluorophores and have broad absorption spectrum with narrow emission spectrum [43][51]. QD are attractive and already used in many applications thanks to their interesting properties mentioned above. Some of these applications include drug delivery [52], bio imaging [53], sensors [54] and active region material for optoelectronic devices such as LEDs [55][56], lasers [57] [58], light harvesting in solar cells [59] [60] and photodetectors [61].

2.5.2.1 Performance degradation due to photo-oxidation and thermal effects in CdSe QDs

Optical performance degradation of QDs has been reported due to photo-oxidation and thermal effects [62][63]. Specific studies on their degradation mechanisms have been made for Cd based colloidal QDs. CdSe QDs were reported to show improvements in photoluminescence emission when excited under minimal oxygen or water vapour exposure, this is known as photo-activation [62][63] [64][65][66][63]. The water and oxygen molecules gets adsorbed onto the CdSe core surface, this leads to their surface passivation and hence reduction in their trap states as the electrons are redistributed to the QD conduction band [64][65][66][63][67].

The adsorbed water and oxygen molecules can be detached from the QD via vacuum degassing or inert gas purging hence reversing the photo-activation effect [68]. However, under prolonged photoexcitation, the optical performance of the QD were seen to degrade permanently [66]. Prolonged exposure to oxygen and water molecules leads to the formation of photo-corrosive ions SeO^{3-} and Cd^{2+} (as the Cd and Se dissociate from the QD's core hence a reduction in QD core size), this causes surface trap states on the surface and therefore quantum yield quenching, emission blue shifting and emission band spreading [62][65][66][63][67][69]. Shell encapsulation is the common method used to reduce the instability of Cd based QDs [62][63][64] [69].

Heating the CdSe QD passed 200°C leads to the formation of thermally generated surface trap states due to the ion exchange happening between the dots [70][71]. This thermal degradation is however usually reversible when cooling. In addition to their instability and efficiency issues, Cd based QDs also suffer from toxicity issues as they are made of heavy metal Cadmium which is restricted within the European Union [45].

2.5.2.2 Colloidal lead-halide perovskite quantum dots

These are specific novel class of quantum dots generally consisting of monovalent cation (A), divalent cation (B) and a monovalent halide anion (X) with chemical formula ABX_3 [72]. As their name implies, they have a perovskite crystal structure. The cation B bonds with six X anions in an octahedral format, the A cation is shared between neighbouring octahedra. The A cation can be organic (MA or $CH_3NH_3^+$) or inorganic (Cs are usually used), Pb (sometimes Sn) serves as the B cation and the halide anions X commonly used are Cl, Br, I.

These perovskite structures optical and electronic properties can be varied by halide and cations composition changes [73][74] and via dimensionality and sizing changes [75][76], emission across the visible spectrum (400nm to 700nm). When reduced to 0D (quantum dots), they show strong quantum confinement effects and compared to other traditional QDs they offer advantages of higher resistance to structural defects, more affordable synthesis methods and narrower emission spectrum (as small as 10nm) [77][78]. One of the main limitations of halide perovskite QD is their high instability, their photo-oxidation induced degradation cannot be avoided. When photo-excited under prolonged oxygen or water vapour rich environment, free radicals are formed from the reaction between the electrons generated and oxygen and CO_2, these radicals then react with the amine salts leading the QD structure destruction [45]. In addition, the generated photo ions can migrate to neighbouring dots. This results in photoluminescence quenching [79] [80]. Optical performance degradation even in inert N_2 gas

rich atmosphere were reported for excitation at 466nm wavelength [81]. Nonetheless, they show more resistance to degradation compared to other traditional QDs (CdSe) as the generated trap sites are outside the bandgap hence, they can retain their high quantum yield without the need for surface passivation [82]. Quantum yields up to 95-100% were reported [75][83]. When subjected to high temperatures, the perovskite structures was also seen to show photoluminescence quenching due to increased surface trap states generation [45]. In addition, CsPbBr3 perovskite QDs were reported to show an emission redshift when heated due to the increase in their crystal size [84]. CsPbBr3 perovskite QDs structure is covered with functional ligands. These ligands have functions of improving the QD photo and thermal stability as dangling bonds on the surface for potential reactions are minimised [85] [86]. They could also be useful in functional application such as cell targeting for example.

Another common colloidal QD issue less severe in halide perovskite is the blinking of the nanocrystals upon photoexcitation. Blinking is caused by light excitation charging and discharging of neutral nanocrystals [82]. This tends to favour trap states and Auger recombination hence the blinking [87] [88]. Halide perovskites such as $CsPbBr_3$ have been reported to show more stable emission at room temperature [89]. As discussed above, QDs in general and halide perovskite QDs is a new field showing great potential in being the next generation optoelectronic device functional material.

2.6 Organic Light Emitting Polymers (LEP)

A different class of light emitting materials are light emitting polymers. Polymers are commonly known to be insulators but it was not until 1950s that Bernanose et al discovered electroluminescence from the organic materials acridine orange and quinacrine [90]. This was followed by 1990, Cambridge University's Opto-Electronics group reported on light emitting polymers. They managed to see emission from polymer poly(1,4-phenylenevinylene) (PPV) upon application of a bias across [91]. Even though the efficiency (0.005%) and lifetime (few minutes) were low, this was still a major discovery. Research developments throughout the years has enabled their performance to considerably improve with efficiencies approaching few whole percentages, lifetimes reaching 10000 hours and multiple different colour emitting polymers [92]. Certain polymers have semiconducting properties thanks to their chain conjugation nature. This was first demonstrated by the year 2000 Nobel laureates in chemistry A. Heeger, G. Mc Diarmid and H. Shirakawa during their work on polymer polyacetylene in the 1970s [93]. Organic polymers usually consists of carbon-carbon atomic bonding. Atomic electron orbitals interactions within the carbon atom ($s^2 2s^2 2p^2$) usually leads to the formation

of hybrid orbitals via the process of hybridisation [94]. Three different hybrid states exist sp, sp^2 and sp^3 hybridization depending on the amount of 2s and 2p orbitals involved. Consider a carbon=carbon double bonding in an ethylene molecule $H_2C = CH_2$ shown in figure 2.15 (a). As the carbon atoms have three bonding areas, the hybridisation is sp^2. This leads to the formation of 3 equivalent co-planar sigma bonds (σ-bonds) due to the sp^2 hybridization of the carbon orbitals and a remaining non-hybridized P_z electron orbital which forms a pie bond (π-bond) [94] between the adjacent atoms. A π-conjugated polymer is one having a backbone chain consisting of either alternating single-double or single-triple bonds. This leads to delocalised π-orbitals carriers across the complete molecular chain and accounts for the conduction[95]

The band properties of organic semiconductor polymers are analogous to their inorganic counterparts. In polymers, the band structure is defined as molecular orbitals of which two exist; the Highest Occupied Molecular Orbital (HOMO) and the Least Unoccupied Molecular Orbital (LUMO) analogous to the valence and conduction band in inorganic semiconductors. The HOMO is the highest molecular orbitals with quantum states filled meanwhile the LUMO is the next with unfilled quantum states. Upon excitation, the HOMO π electron will transition to the LUMO, this is known as π- π transition and the energy required describes the bandgap energy (this is shown in figure 2.15 (b)) [95]. Electrons can be move along the chain backbone via the π-bond while maintaining the structural stability of the molecule. The transition can be achieved by both electrical and optical excitation condition that the excitation energy is greater than the bandgap energy. This leads to the formation of excitons, which can dissociate, diffuse or recombine (radiative or non-radiative).

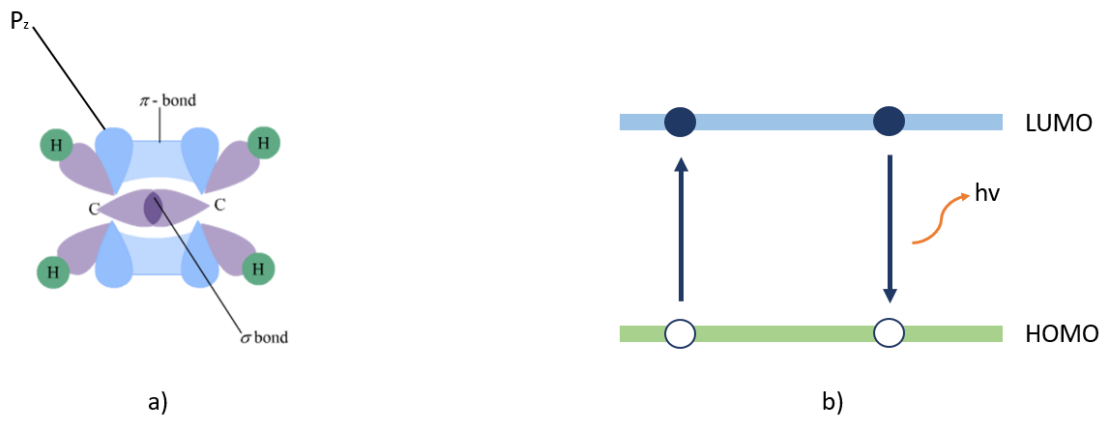

Figure 2.15 organic light emitting polymer conducting and emitting mechanism a) ethylene bonding structure showing P_z electron orbitals forming pie bonds which become delocalised as a result of conjugation b) π- π transition between HOMO and LUMO band structure as a result of optical excitation

LEP can be characterised by their quantum yield, Stokes shift, emission and absorption peaks and offer advantages of emitting colour tune-ability by chemical structure modifications [96]. They can also be processed in solutions; this allows low cost deposition such as ink jet printing and spin coating [94]. In addition, substrate compatibility is not an issue and flexible substrates can be used [94] leading to new devices.

One of the main problems of LEP is their poor carrier transport and injection (mobility less than 10 $cm^2V^{-1}s^{-1}$). In contrast to inorganic semiconductors, organic polymers have hole mobilities exceeding that of their electrons. This differences leads to reduction in electron-hole recombination, as most holes will not meet an electron before reaching the cathode. In the case of Organic LEDs (OLEDs), the recombination will occur near the electrode interface hence quenching luminescence. One of the method used to mitigate this is by using metal with work function close to the HOMO and LUMO energy levels [97]. Another very common method involves using extra layers between the metal contacts and the active region, electron transport layers and hole transport layers to promote carrier injection. Organic polymers also suffer from photo bleaching, that is degradation of the polymer due to successive excitations. Water and air are usually harmful to the polymer as it cause acceleration of degradation.

LEP serve in numerous applications such as OLEDs for display technology thanks to their small sizes and lighting [98]. They also serve in biology for cell tagging and sensing [99] [100], light trapping material in organic solar panels and optically pumped organic polymer lasers has also been reported [92].

2.7 Light-matter interaction

Light matter interaction is a phenomenon that has been of great importance and highly studied due to phenomena such as lasing [92], [101], emission intensity enhancement [102], spontaneous emission enhancement (Purcell effect) [103], [104], lasing threshold reduction [105], strong coupling [106] and more. The development of optical microcavity structures has facilitated the control over light matter interaction. In this section, a review on optical microcavities and important light-matter interaction phenomena are given

2.7.1 Coupling in microcavity

Placing an emitter inside the cavity can lead to light matter interaction, light corresponding to the photonic modes and matter corresponding to excitons in the emitter. During coupling, the exciton and cavity mode exchange energy at a rate depending on the coupling strength. Depending on how this coupling strength compares to cavity mode decay (k) and non-resonant emitter decay (γ) (shown in figure 2.16), two regimes exists weak coupling and strong coupling regimes. Below is an overview of both

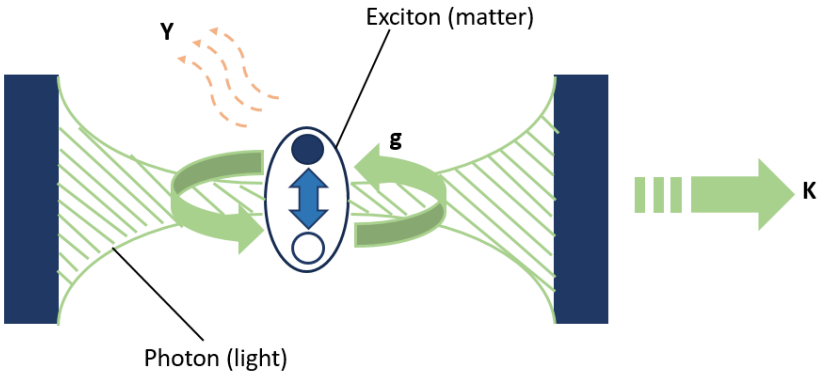

Figure 2.16 Main cavity mechanisms determining coupling strength, coupling strength (g), cavity mode decay (k) and non-resonant emitter decay (γ)

2.7.1.1 Weak coupling regime and Purcell effect

In this regime, the losses strength exceeds the exciton-photon coupling strength. This can occur when the emitter is not embedded inside a QMC or the QMC used is of low Q. The generated photons are rapidly lost in free space leading to rapid irreversible decay in the excitons (short exciton lifetime) [35]. Vacuum field interactions with an emitter affects its spontaneous emission, depending on whether the exciton transition within the emitter is in resonance with the cavity mode or not, the spontaneous emission rate can be greatly increased or reduced respectively compared to vacuum spontaneous emission [33]. When they are in resonance the

photonic density of states seen by the emitter exciton are increased hence, increase in their decay rate. The reverse occurs when they are out of resonance. The factor by which the spontaneous emission is improved or diminished is known as the Purcell factor [28] (F_p) published by Purcell in 1946 and is given by equation 2.30

$$F_p = \frac{3Q(\frac{\lambda_c}{n})^3}{4\pi^2 V_{eff}} \qquad (2.30)$$

Where, n = emitter refractive index, V_{eff} = effective mode volume

From equation 2.30, two main important points can be noted to achieve high Purcell factor. First, it can be seen that $F_p \propto Q$, this means that the higher the cavity quality factor the higher the spontaneous emission enhancement. Secondly, $F_p \propto 1/V_{eff}$ meaning the amount of cavity mode in resonance with the exciton transition must be less to achieve greater spontaneous emission enhancement. This is the reason why smaller cavity lengths are preferred. In addition to the Purcell factor, the exciton positioning affects the excitonic-optical mode coupling strength. This is related to the standing wave factor, which states that the maximum coupling occurs for thin emitter sources positioned at the cavity standing wave antinode [107], but rather supressed when positioned at the standing wave node. Therefore, the emitter should be positioned close enough to the field antinode [108]. Finally, the exciton transition needs to be at resonance with the cavity mode. Purcell effect is usually measured by time resolve spectroscopy where the decays of various profiles are compared.

All discussed criterions above for establishing weak coupling are also valid for strong coupling.

2.7.1.2 Strong coupling regime

In this regime, instead of the generated photons to be lost in free space as in the case of weak coupling regime, the photons are reflected back into the cavity and reabsorbed by the cavity medium. This makes the exciton decay reversible as they can be reformed by the reabsorbed photon. When the energy exchanged between the exciton transition and the cavity mode (coupling strength) is stronger than the loss, the system is said to be in strong coupling [35]. For this to be achieved the same conditions described in weak coupling above (emitter and cavity mode at resonance, emitter positioning at antinode, low mode volume) and an even higher quality factor to limit cavity mode leakage outside the cavity. The light matter coupling leads to the formation of a new eigen state known as the exciton-polariton. The characteristic

energy splitting at resonance between the emitter and cavity mode defines strong coupling, this splitting is known as the vacuum Rabi splitting ($\hbar\Omega_i$) [34] given by equation 2.31

$$\hbar\Omega_i \simeq 2\hbar\left(\frac{2\Gamma_0 c N_{qw}}{n_c L_{eff}}\right)^{1/2} \qquad (2.31)$$

Where, $\hbar\Gamma_0$ = radiative width of exciton, $N_{qw} =$ number of quantum wells in active region

The vacuum Rabi splitting energy is greater than the exciton and cavity mode linewidths in strong coupling. The aim is to have narrow exciton and cavity modes linewidths. The exciton linewidth mainly depends on the alloy fluctuations in the well lattice after epitaxy and well width meanwhile the cavity mode linewidth mainly depends on losses within the cavity (cavity finesse). Hence, the importance of QW epitaxial growth techniques and high finesse cavity (minimal loss). vacuum Rabi splitting of >5meV and >8meV [109] were reported for 1 λ and 3 λ /2 GaAs based cavities respectively. As the photonic component of the polariton has a finite lifetime inside the cavity, the polariton is converted into external photons. Therefore, the polariton dispersions can be measured from luminescence experiments (reflectivity, transmissivity measurements) [34]. This splitting is translated on a reflectivity spectrum at the resonance wavelength as two coupled mode dips on the high reflectivity stop band, having equal intensity and separated by corresponding vacuum Rabi splitting energy. A typical reflectivity spectrum under such phenomenon is shown in figure 2.17

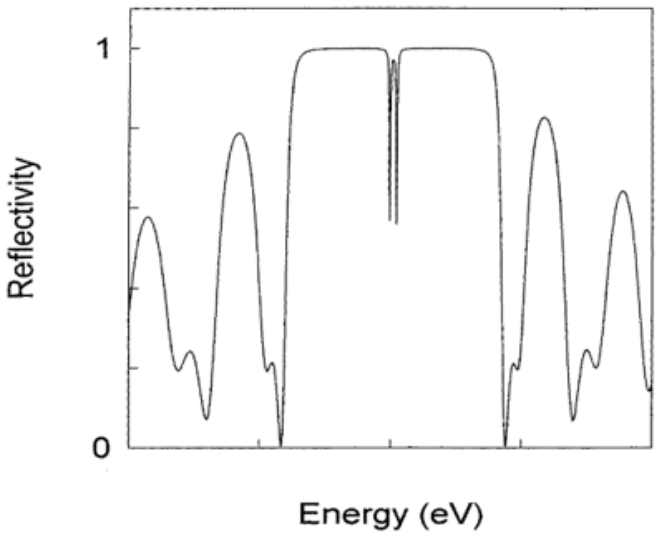

Figure 2.17 Calculated reflectivity spectrum for microcavity under strong coupling, two superimposed dips on the spectrum stop band shown, adapted from [34]

The high cavity quality factor causes the light to pass multiple times within the cavity, this leads to most of the non-reflected light to be absorbed rather than transmitted [34]. The two dips can also be regarded as the two polaritonic branches formed by the splitting, the lower (LPB) and upper (UPB) polaritonic branches.

Experimentally, in order to measure strong coupling, the polariton dispersion curve showing anti-crossing of the excitonic and cavity modes need to be plotted. The plotting of this dispersion curve requires the tuning of either the excitonic mode or cavity mode. Many different techniques have been reported such as

- cavity tuning by intentionally performing a wedge growth by stopping sample rotation during MOCVD or MBE growth of the cavity structure [110]. This has the effect of varying the cavity length. Therefore, the cavity mode is directly related to the cavity length.
- Material refractive index variation with temperature utilised to tune the cavity mode [110] and bandgap variation with temperature utilised to tune excitonic mode [110].
- Electric field tuning of the excitonic mode [110].
- Angle measurements to tune the cavity mode

They all offer their advantages and disadvantages and the choice is made depending on the specific experimental requirements. Angular measurements technique is highly effective with advantages ease in operation, as complicated wedge growth is not required, no possible detrimental effect on device as external parameters such as electric field and temperature are not used. Angular measurements also can be measured directly from luminous measurements such as reflectivity and photoluminescence measurements. Finally, incidence angle variations greatly affect the cavity mode with little to no effect on the excitonic mode hence, a good tuning technique. The cavity mode energy variation with incident angle is given by the equation 2.32 [34].

$$E(\theta) = E_0 \left(1 - \frac{sin^2\theta}{n_{eff}^2}\right)^{-1/2} \qquad (2.32)$$

A typical reflectivity spectrum at different tuning is shown in figure 2.18. Reflectivity plots at different cavity mode tuning of the same structure are presented. The top left curve shows one dip corresponding to the cavity mode out of resonance with the excitonic mode. As the cavity mode is tuned to get closer to the excitonic mode, a small second dip appears and at resonance,

two split dips of equal intensity can be seen (fourth plot from the top) and the last plot shows the cavity mode again away from resonance.

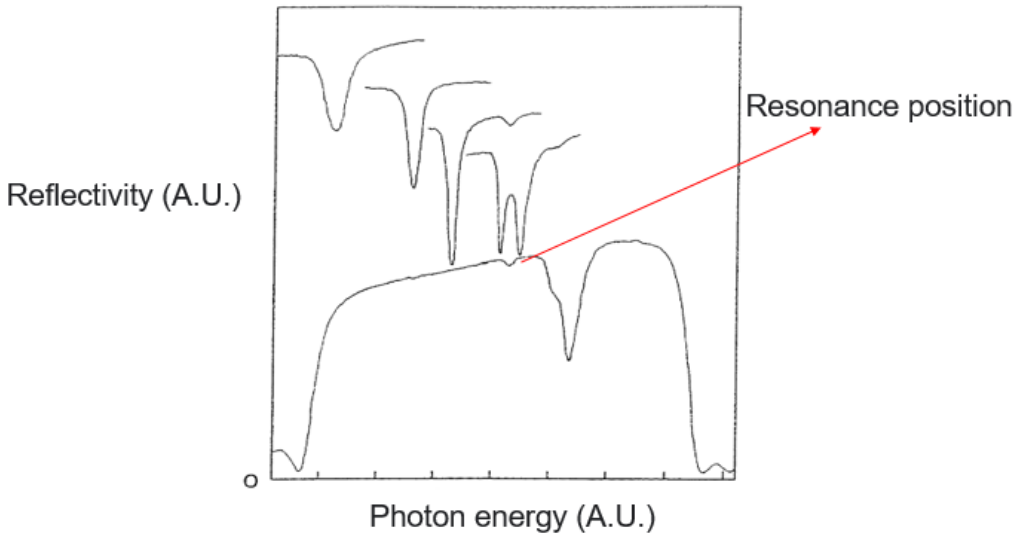

Figure 2.18 Effect of detuning on reflectivity spectrum, cavity mode increased from left to right and on resonance splitting effect shown on second plot from the bottom, adapted from [34]

The polariton dispersion curve can then be obtained by extrapolating the two polariton energies (two dips energies) at each angle of incidence. Figure 2.19 shows a typical polariton dispersion curve deduced from reflectivity energy dips position [111]. The two polaritons, upper and lower polaritons corresponding to the two branches. It should also be noted that angle resolved photoluminescence can also be done and polariton dispersion curve deduced from it.

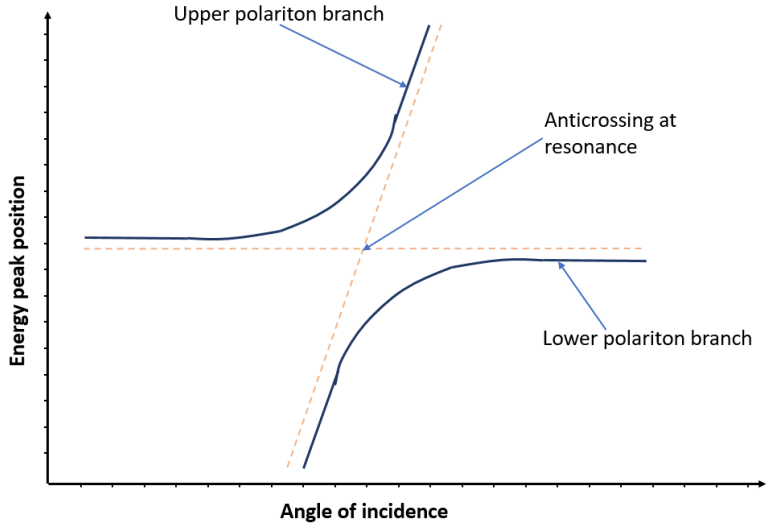

Figure 2.19 Polariton dispersion plot derived from reflectivity plots at different angles of incidence, upper and lower polariton corresponding to the two branches, adapted from [111]

2.8 Light Emitting Diodes (LEDs)

Light Emitting Diodes are one of the solid-state lighting sources with prominent importance in light generation, manipulation and applications. Compared to other light sources, LEDs offer advantages of environmental friendliness, higher energy efficiency, longer lifetime and emission spectrum controllability (narrower emission, emission direction, colour temperature, polarisation and modulation) [4]. They are generally composed of inorganic/organic materials capable of emitting light upon passing of an electric current across. In this section, the functioning of a typical LED, its electrical and optical properties, fabrication and design parameters, resonant cavity LEDs (RCLEDs), white light source LEDs and their applications will be discussed.

2.8.1 LED functioning

In its simplest form, an LED is a PN junction that is a p-type doped (holes majority carriers) semiconductor attached to an n-type doped (electrons majority carriers) semiconductor, separated by a depletion (active) region as illustrated in figure 2.20. Without external bias, the depletion region is depleted of free carriers (resistive in nature), the ionised donors and acceptors on the N and P sides respectively, leads to the formation of a built in potential called the diffusion potential (V_D). This is the potential barrier free carriers from either sides need to overcome in order to reach the active region and this can be calculated using equation 2.33 [112]. The depletion region width (W_D) can also be calculated by equation 2.34 [112].

$$V_D = \frac{KT}{e}\ln\left(\frac{N_A.N_D}{n_i^2}\right) \qquad (2.33)$$

$$W_D = \sqrt{\frac{2\varepsilon}{e}\,(V_D - V)\left(\frac{1}{N_A} + \frac{1}{N_D}\right)} \qquad (2.34)$$

Where, N_A, N_D, n_i, K, T, ε, V are the acceptor concentration, donor concentration, intrinsic carrier concentration, Boltzmann's constant, temperature, dielectric permittivity, applied bias voltage respectively.

Upon application of an external bias across the active region, the diffusion potential can either be increased or decreased for a reversed and forward bias respectively. Forward bias causes a reduction the diffusion potential barrier, beyond a bias threshold (V_{th}), carriers start flowing across. Further increase in the forward bias leads to increase in current flow as carriers are rapidly injected into the opposing region. The carriers then recombine and emit photons via the process of spontaneous emission. The emitted photon energy is close to the active region

semiconductor's bandgap energy (E_g). This is shown in equation 2.35. The mean distance the free carrier travels, before recombining with the opposite charge carrier is known as the diffusion length, and is given by equations 2.36 and 2.37 for holes and electrons respectively.

$$hf \approx E_g \qquad (2.35)$$

$$L_n = \sqrt{D_n \tau_n} \qquad (2.36)$$

$$L_p = \sqrt{D_p \tau_p} \qquad (2.37)$$

Where, h = Plank constant, f = photon frequency, L_p = hole diffusion length, L_n = electron diffusion length, τ_p = holes carrier lifetimes, τ_n = electron carriers lifetime, D_p = hole diffusion constant and D_n = electron diffusion constant respectively.

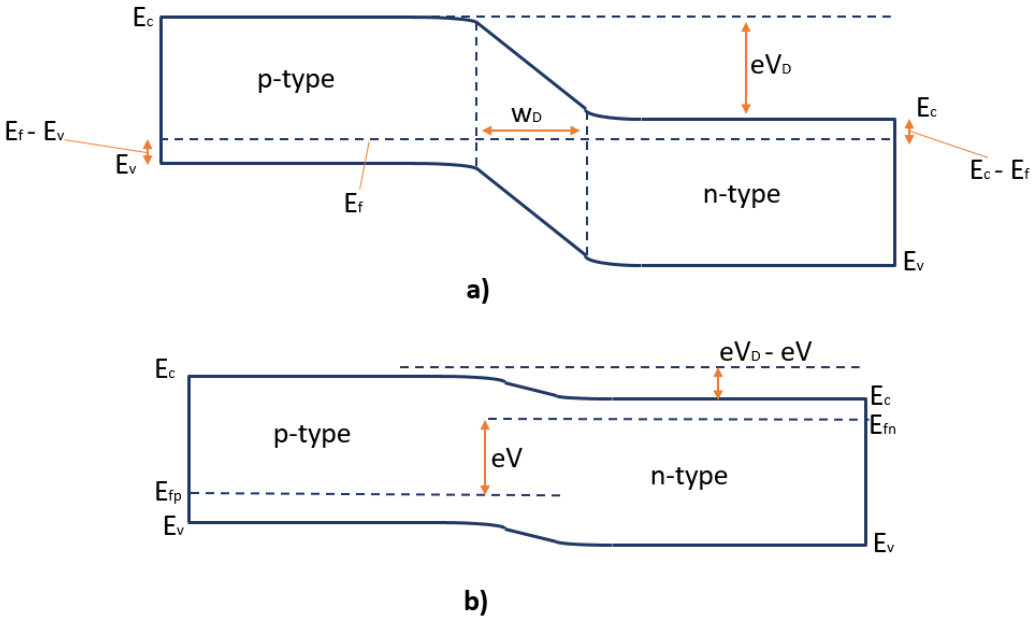

Figure 2.20 energy band illustration of PN junction under a) equilibrium (zero external bias) b) forward external bias

The PN junction described above with energy diagram shown in figure 2.20 is that of a homo-junction that is, one made from the same material. Under forward bias, the minority carriers are distributed over a wide region on the opposing side as common semiconductor diffusion lengths are in the micron range, an example is 15um for GaAs [112] [113], leading to a low concentration in the active region. As the recombination rate is directly proportional to the carrier concentration in the active region from equation 2.6, homo-junction LED devices are less effective. Double hetero-junction structures are more commonly used. They involve the use of active regions consisting of two different bandgap semiconductor materials. That is, a

low bandgap active region sandwiched by two wider bandgap barriers materials. This limits the recombination region of the LED to the active region as injected carriers are confined in this region thanks to the barriers. This is illustrated in figure 2.21 (b). These heterojunctions are also referred to as quantum wells

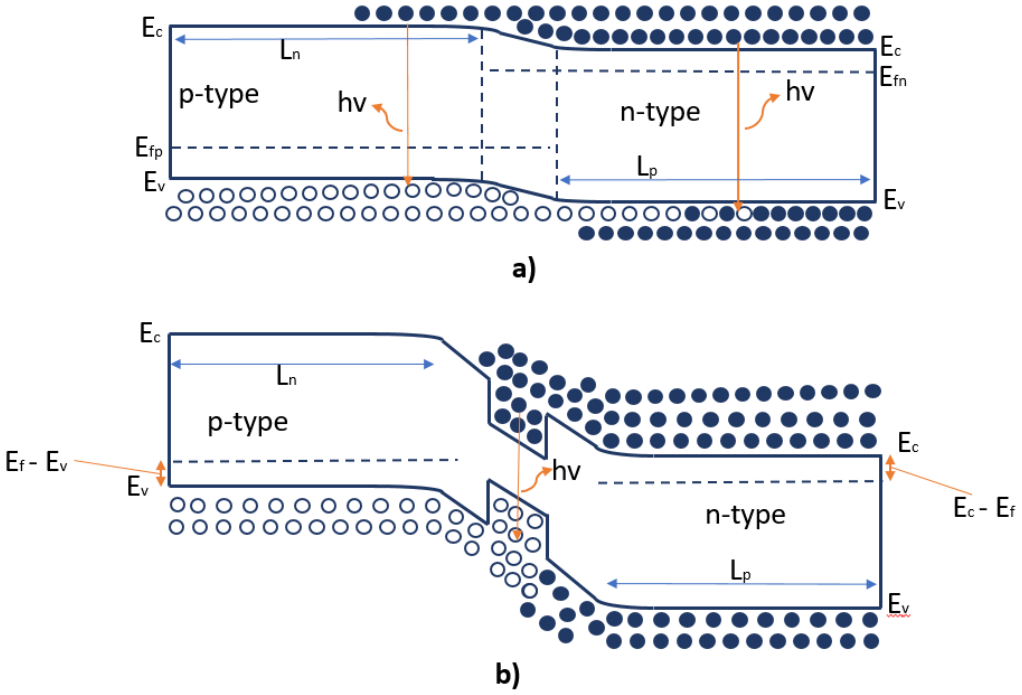

Figure 2.21 comparison of (a) homojunction and (b) heterojunction in their carrier confinement abilities when a forward bias is applied

2.8.2 Electrical and optical properties

The relationship between the current and voltage of an ideal PN junction is given by the Shockley Diode equation 2.38

$$I = I_s(e^{(\frac{eV}{KT})} - 1) \qquad (2.38)$$

$$\text{Where, } I_s = eA(\sqrt{\frac{D_p}{\tau_p}}\ \frac{n_i^2}{N_D} + \sqrt{\frac{D_n}{\tau_n}}\ \frac{n_i^2}{N_A}) \qquad (2.39)$$

Where, A, I_s are the cross sectional area and saturation current respectively

Generally, for forward bias V >> kT. Therefore, the I-V equation can be re-written as

$$I_s = eA\left(\sqrt{\frac{D_p}{\tau_p}}\ N_A + \sqrt{\frac{D_n}{\tau_n}}\ N_D\right)e^{\frac{e(V-V_D)}{kT}} \qquad (2.40)$$

Therefore, the diffusion voltage is the threshold voltage. This threshold voltage can be approximated as shown in equation 2.41

$$V_{th} \approx V_D \approx \frac{E_g}{e} \qquad (2.41)$$

Therefore, the threshold voltage is directly proportional to the bandgap energy of the semiconductor. Arsenide and phosphide based LED devices agree very closely with this approximation but not Nitrides. This is because of the additional potential drop in their structure from the bandgap discontinuities, ohmic contacts and p-type buffer layer, making the threshold voltage greater than E_g/e. Figure 2.22 shows the typical I-V curve of an LED. The threshold voltage is not a fixed value but rather occurs over a range of voltages. This is because of the presence of some parallel resistance to the device, leading to the device bypass [112]. This explains the sub-threshold turn-on. There also exist series resistance within the LED device, this accounts for the ohmic behaviour past the threshold voltage. Parallel resistances sources include carrier transport via surface states or deep levels and series resistance sources include ohmic contact resistance and band bending because of carrier diffusion [112].

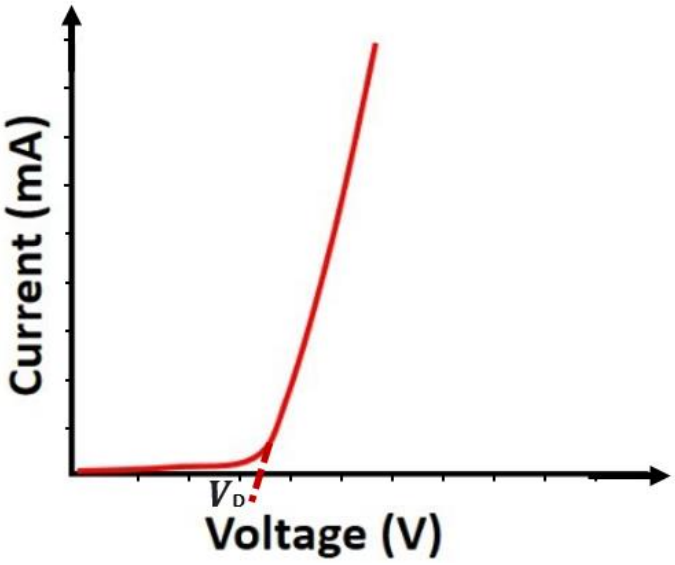

Figure 2.22 Typical current-voltage characteristic of an LED diode

The electron and holes distribution in semiconductors typically have a parabolic dispersion. Carrier recombination involves free electrons in the conduction band and holes in the valence band. Momentum conservation requirements ensure that the carrier transitions are only vertical and therefore electrons can only recombine with holes having the same momentum

(Boltzmann's distribution) value [114]. Energy conservation requirements shows that the transition energy (band gap energy) must be equal to the emitted photon energy hence, the emission can be tuned by selecting the appropriate semiconductor material. Figure 2.23 shows an example of the emission spectrum of an LED with important parameters emission peak wavelength, Full Width at Half Maximum (FWHM). They are characterised by narrow band, high intensity emission peak

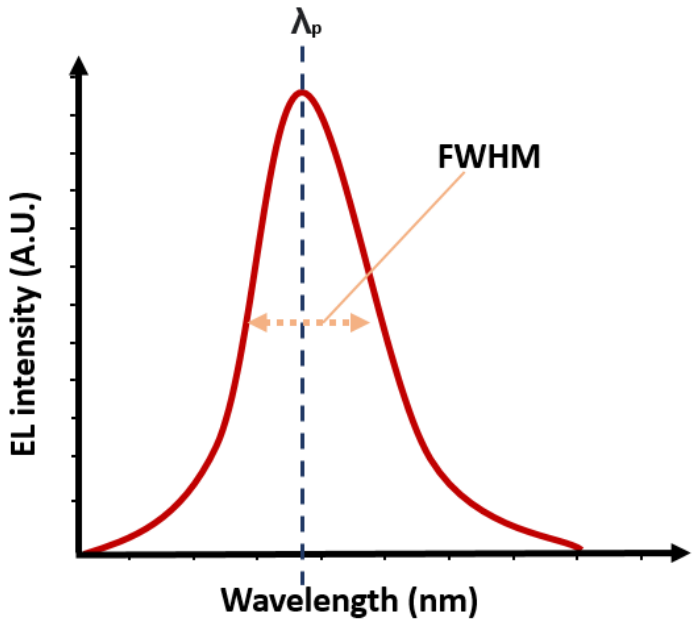

Figure 2.23 typical emission spectra of direct bandgap semiconductor showing characteristic Full Width at Half Maximum (FWHM) and wavelength at peak intensity

Ideally, for every single electron recombination with a hole, a photon would be emitted. This defines the efficiency of the LED. Various measures of efficiency exist such as Internal Quantum Efficiency (IQE), External Quantum Efficiency (EQE), and Power Efficiency (PE) [114]

IQE can be defined as the ratio of the emitted photons from the active region to the injected electrons into the active region. This can be calculated as shown in equation 2.42

$$IQE = \frac{\frac{P_{int}}{hf}}{\frac{I}{e}} = \frac{number\ of\ photons\ emitted\ from\ active\ region\ per\ second}{number\ of\ electrons\ injected\ into\ LED's active\ region\ per\ second} \quad (2.42)$$

Where P_{int} and I are the emitted optical power out of the active region and injected current into the active region respectively.

Ideally, all the emitted photons from the active region should be emitted into free space. This is not the case, some photons are reabsorbed by the substrate, Ohmic contacts and other defects within the semiconductor, and others might be total internally reflected back into the device vicinity, non-radiative emission processes (Auger recombination, deep level and surface states emissions). These are example of the loss mechanisms and can be depicted as the extraction efficiency $n_{extraction}$ given by equation 2.43

$$n_{extraction} = \frac{\frac{P_{out}}{hf}}{\frac{P_{int}}{hf}} = \frac{number\ of\ photons\ emitted\ into\ free\ space}{number\ of\ photons\ emitted\ from\ the\ active\ region} \qquad (2.43)$$

Where P_{out} is optical power emitted from device

The extraction efficiency determines the EQE; the EQE refers to the ratio of the photon emitted in free space to the electrical injected electrons in the LED, therefore the useful efficiency. The EQE can be calculated using equation 2.44

$$EQE = \frac{\frac{P_{out}}{hf}}{\frac{I}{e}} = \frac{number\ of\ photons\ emitted\ into\ free\ space}{number\ of\ electrons\ injected\ into\ LED\ per\ second} \qquad (2.44)$$

The power efficiency n_{power} also known as wall plug efficiency is involved mainly with the input and output power and is given by equation 2.45

$$n_{power} = \frac{P}{IV} \qquad (2.45)$$

Where P and IV are output optical power from the LED device and electrical injected power to the LED

2.8.3 LED fabrication and design considerations

The LED fabrication involves many steps and various consideration need to be taken to maximise the device performance. These are discussed in this section.

2.8.3.1 LED fabrication

The main component of an LED is its light emitting component. This component consists of semiconductor layers grown on a substrate. Example of substrates commonly used in nitride LEDs are sapphire, GaN and Si. A typical structure of InGaN/GaN quantum well blue emitting LED structure is shown in figure 2.24.

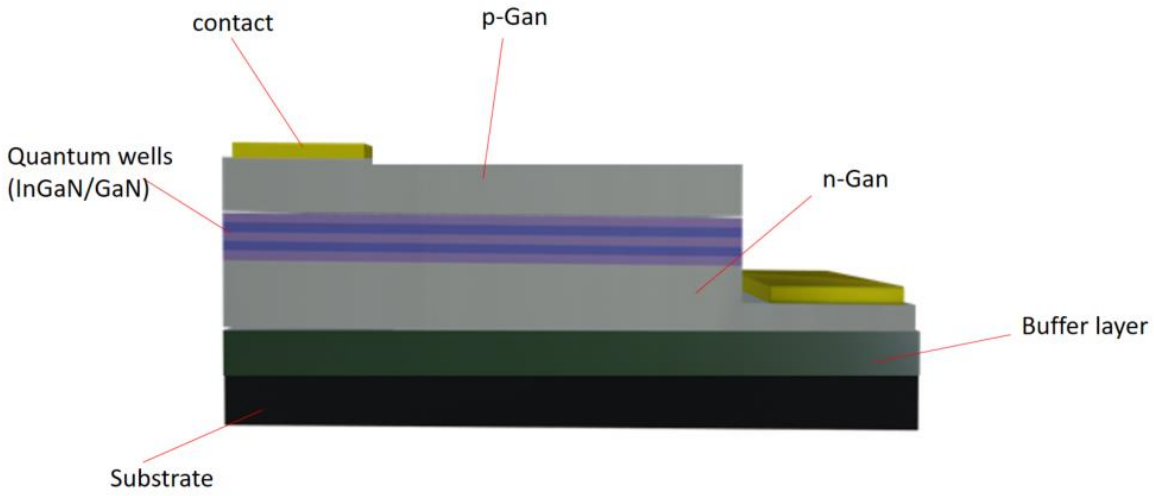

Figure 2.24 Schematic of typical InGaN/GaN blue emitting LED

The growth of semiconductor materials including GaN is usually done in a chemical reactor at high temperatures by the process of MOCVD (Metal Organic Chemical Vapour Deposition). The substrate used determines the grown GaN properties of crystal orientation, strain, morphology and defect density [4]. The lack of suitable substrate with lattice constant close to that of GaN has been a challenge in the development of GaN based LEDs. Sapphire with lattice mismatch of about 16% is the most commonly used substrate. Direct GaN growth on the sapphire substrate will lead to cracks and defects on the GaN. These defects are non-radiative recombination sites and therefore should be avoided. Many methods to avoid or limit the generation of these defects were developed and include deposition and low temperature annealing of a nucleation layer on substrate before the main GaN deposition [115], island formation followed by coalescence [116] [117]. These methods can lead to dislocation density reduction from $5x10^{-9}$ cm^{-2} to $1x10^{8}$ cm^{-2} [4]. These are still high values for threading dislocation but InGaN tends to perform relatively well thanks to the localisation effects. This prevents the carriers from migrating to defect (non-radiative recombination) sites [118] [119]. The use of lattice-matched substrates has also being proposed, lattice matched GaN substrates were used for second generation LEDs. This tends to reduce/eliminate dislocation density due to lattice mismatch and potential reflection at sapphire-GaN interface, which improves LED performance as demonstrated by Lee et al [120]. The cost associated with freestanding GaN substrate production hinders the commercialisation of this type. After growth of the full stack, photolithography processing including lithography patterning, dry etching, metallisation, surface roughening and cleaving or sawing are required to achieve the LED die. The die is then

encapsulated and packaged (depending on the chosen chip design) to form compact electrical components that can be powered externally.

2.8.3.2 LED design considerations

One of the major parameters to be considered for the effective performance of the LED is the device junction temperature. This refers to the temperature of the active region and can have detrimental effects on the device if not well controlled. These include semiconductor material degradation (hence device lifetime reduction), carrier overflow across the active region (current leakage), increase in non-radiative recombination processes (deep level, surface state and Auger recombination), damage of the encapsulant (reducing the extraction efficiency), and red shifting of the emission peak due to the quantum confined Stark effect [13] [121] on the effective bandgap energy. Hence, reducing the LED performance and lifetime. Heat generated within the LED can be controlled by reducing parasitic electrical resistance within the bands. A good example is the additional barrier creation due to band bending in hetero-structure active region because of charge transfer. This band bending can be reduced by grading composition of the hetero-structure rather than step composition, lattice matching of the layers is necessary to avoid misfit dislocations. Another design feature used to limit the device temperature is the heat sink.

The LED decay dynamic is one of the main factors determining the LED switching times, this is particularly important in communication applications where LED modulation speeds play key roles. As seen above, recombination rate is proportional to carrier concentration, so increasing the injected carriers or highly doping the active region are some ways of improving the recombination rate [13].

Carrier leakage and overflow is another consideration associated with hetero-structure designs. Despite the hetero-structure barriers energy being up to the 100s meV, some carriers still are able to overcome and escape the barrier. Carrier's energy distribution is given by the Fermi-Dirac distribution [112] where some carrier's energy is higher than the barrier allowing them to escape. This leads to recombination at the barrier layer. The parameters influencing this carrier loss are the carrier concentration at the band edge and barrier height. Therefore, high barrier height is required to avoid the carrier overflow. Barrier height energy much greater than kT (thermal energy). Increase of the injection current will lead to increase in population of the hetero-structure well's carriers, if the injection current keeps increasing, at a certain point the well becomes completely full and any further current increase will have no effect on the

recombination rate no matter the barrier height. Hence, the emission intensity will saturate. Increasing the active region volume provides a solution to this. That is, using multiple quantum wells which increases the current at which saturation might occur.

Well width in hetero-structures also affect LED IQE. Well width less than 10s of nm are commonly used for QW [113]. Wells too thin or too large will make the hetero-structure advantage to be lost due to carrier overflow and loss of carrier confinement respectively. Few nanometres well width were reported for InGaN/GaN [122]

Even with all measures above, certain carriers might still have enough energy to escape the active region into the confinement region. Electrons, owing to their higher mobility compared to holes will have higher leakage hence, the use of electron blocking layers. These are layers with very high bandgap energy grown on the p-type confinement layer-active region interface. For the GaInN/GaN LED system, AlGaN is commonly used as electron blocking layer. The free holes from the P-region screens the electron-blocking region so that no barrier exists in the valence band. This configuration reduces further carrier leakage and increases recombination [4] [13]

Semiconductor materials commonly used in LED structures are of high refractive index (GaAs and GaN having 3.4 and 2.4 respectively). This makes their semiconductor-air interface highly reflective for certain angles of incidence due to Total Internal Reflection (TIR) governed by Snell's law. The critical angle (θ_c) for TIR is given by equation 2.46. As refractive index of the semiconductor (n_s) is greater than that of air (n_{air}), θ_c will be small and all rays with incidence angle greater than θ_c will get total internally reflected. This is usually illustrated in terms of emission intensity percentage to emission angle to the normal, the LED Lambertian emission pattern [114]. TIR reduces the extraction of light from the LED and hence the EQE of the device. Dome shaped epoxy encapsulation of the LED die can help reduce this TIR effect. Refraction from the semiconductor epoxy interface causes the incidence angle to be normal at the epoxy-air interface hence no TIR.

$$sin\theta_c = \frac{n_{air}}{n_s} \qquad (2.46)$$

2.8.4 Resonant Cavity LEDs (RCLEDs)

As discussed in section 2.2, radiative recombination leading to photon emission usually can occur in two different ways within semiconductors, stimulated emission or spontaneous emission. The latter occurs randomly with little to no control over the process. However, the

use of resonators with optical dimensions within the order of the light's wavelength can be used to control the emission properties (spontaneous emission rate, emission pattern and purity) of a light emitting element [123] [19]. This was first developed by Purcell in 1946 with the simplest being the Fabry-Perot resonator.

RCLEDs is an example of a device making use of the spontaneous emission enhancement using micro-cavities. RCLEDs consist of an LED where the light emitting medium is placed inside a resonant cavity. This consists of two resonators sandwiching the emitting material with cavity optical thickness L_{cav} is comparable to the light wavelength λ. Small cavity optical thicknesses of λ/2 or λ are usually used (small cavity thickness for better overlap between the emission spectrum and cavity mode), a representation diagram is shown in figure 2.25.

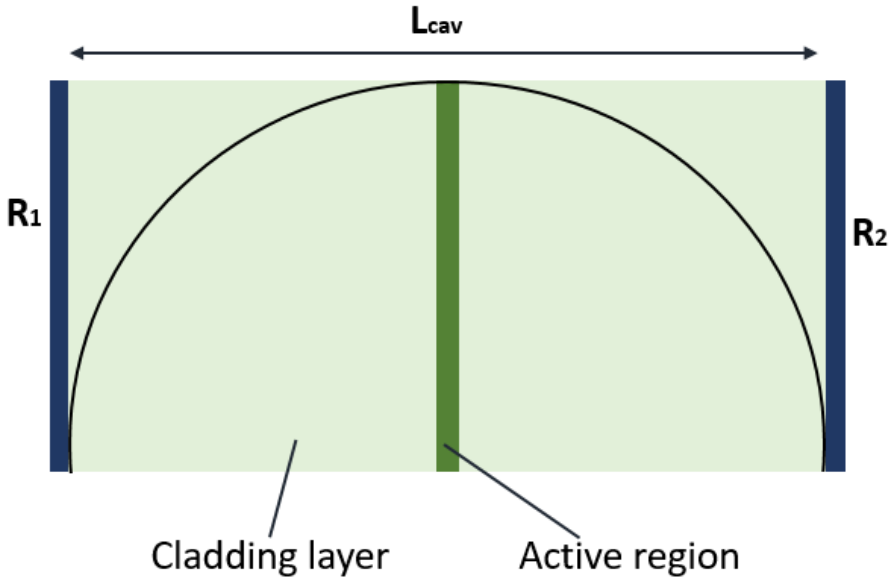

Figure 2.25 diagrammatic illustration of planar cavity showing active layer sandwiched by two reflective mirror and cladding layers

Various design criteria need to be obeyed for the effective operation of the RCLED.

First, the optical cavity length should be kept to the minimum that is $\frac{\lambda_c}{2}$ (m = 1). This helps in maximising the overlap between the cavity mode and emission wavelength and therefore maximising the integrated intensity. It should also be noted that the penetration depth within the reflectors adds to the cavity length, so using reflectors with minimum penetration depth is also required for instance DBRs with high refractive index contrast materials.

Secondly, the bottom DBR reflectivity need to be much greater than that of the top DBR reflectivity ($R_2 >> R_1$). This criterion ensures light exits via the exit mirror as it provides less optical resistance, this is essential in improving the LED emission directionality

Also, the emission rate enhancement factor G_e is given by equation 2.47

$$G_e = \frac{\xi}{2} \frac{\left(1+\sqrt{R_2}\right)^2 (1-R_1)}{(1-\sqrt{R_1 R_2})^2} \frac{\tau_c}{\tau} \qquad (2.47)$$

Where ξ, τ_c and τ are the antinode enhancement factor (determined by the active region positioning in the microcavity), carrier lifetimes in and out of the cavity respectively

As it can be seen from equation 2.47, the positioning of the active region within the cavity affects the emission rate enhancement. The ξ can take three different values depending on the active region position in the cavity 2, 1 and 0 when the active medium is at exactly the standing wave antinode, smeared over multiple period of the standing wave and is at exactly the standing wave node respectively [19]. Therefore, the emitting material should be placed preferably at the standing wave antinode's position for better performance.

Finally, the probability of the emitted photons to be released from the cavity should be much greater than that of the photons being reabsorbed by the active medium [124]. This is to minimise self-absorption within the cavity, which might lead to non-radiative recombination and/or reemission but along the waveguide modes (that is laterally and not vertically along the cavity modes) hence, decrease in cavity mode emission. This can be expressed mathematically in terms of the exit mirror reflectivity R_1 (assuming $R_2 \approx 1$) as shown in equation 2.48

$$2\xi\alpha L_{active} < (1 - R_1) \qquad (2.48)$$

This relation can be used to determine the adequate reflectivity for the exit mirror. Theoretical calculations yielded optimal exit mirror reflectivity in the range 50-60% [125]. However, RCLEDs with 99.9% reflectivity were also reported [126]. This affects the optical mode density and causes the spontaneous emission enhancement by the Purcell effect (resonant cavity effects). This leads to numerous interesting effects such as increase in the device emission intensity thanks to enhanced spontaneous emission due to the Purcell effect. Enhancement factors in the range of 2 – 20 were reported [127]. Secondly, reduction in the emission line width of the device, this makes the emission purer compared to the conventional LEDs. This can be explained by the fact that, in the resonant cavity, the emission spectrum line width is solely dependent on the cavity mode and not the thermal energy. Line width narrowing

factors of 2-5 were reported. Thirdly, the emission is more along an axis normal to the cavity that is, more directional emission. This is contrary to the isotropic emission pattern from conventional LEDs which suffer from Total Internal reflection (TIR) due to Snell's law [107], this is one of the major factors limiting LED's extraction efficiency and hence external quantum efficiency. Therefore, RCLEDs offer better external quantum efficiency compared to conventional LEDs. This can be applied to both inorganic and organic light emitting materials based LEDs [124].

2.9 Lasers

The development of lasers since 1960 has enabled the discovery and development of many other photonic technologies. LASER is acronym Light Amplification by Stimulated Emission of Radiations. Laser light compared to other light sources has properties of very narrow emission width, highly directional beams that can be focused on a small spot area with high peak powers and highly coherent beams [128]. At the core of laser technology, is the optical oscillator, this requires the presence of amplification and positive feedback [129] [130]. Below is a brief explanation of the laser's mode of functioning

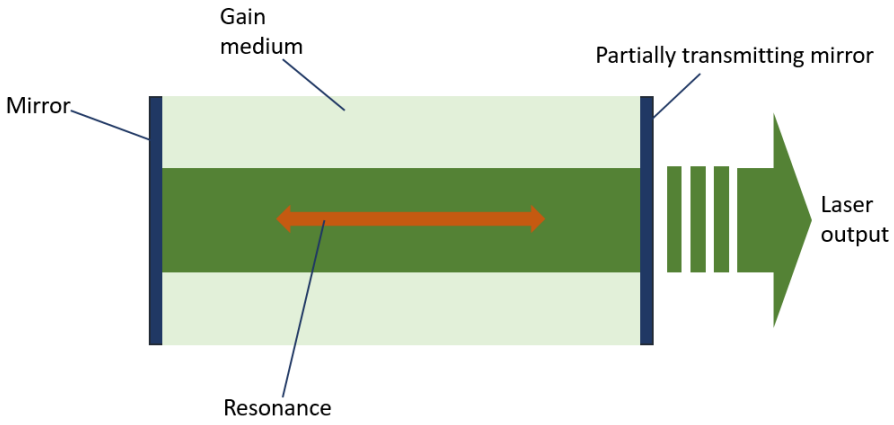

Figure 2.26 illustration of a Fabry-Perot structure laser

Carrier transition within the atom of a light emitting material leading to light emission can be regarded as an optical oscillator where the emitted photon frequency f, which can be considered as the oscillator resonance frequency, is given by equation 2.49

$$f = \frac{\Delta E}{h} \qquad (2.49)$$

Where h and ΔE are the Plank constant and transition energy respectively

Unfortunately, these transitions occur randomly (spontaneous emission) and independently across the emitting material leading to emission of photons with the same resonance frequency (as the transition energy is the same) but with different phases and in different directions. The result is light lacking collimation, coherence and hence cannot be focused to achieve high intensities. Hence, the need of a single general optical oscillator which will allow synchronisation of all photon emissions. Figure 2.26 shows a schematic of a Fabry-Perot structure laser [128]. It consists of a gain medium (optical amplifier) that is, a medium which emits more photons upon excitation. In addition, to ensure a single common optical oscillator, feedback is required and this is done thanks to the mirrors [129] [130]. The mirrors allow multiple passage of the light across the gain medium hence allowing amplification. Stimulated emission is required in order to ensure that the emitted photons have the same direction, phase and polarisation as the photon causing stimulation [129] [130]. During thermal equilibrium, the carriers within the gain medium will be unexcited and therefore, absorption will dominate. In order for stimulated emission to dominate, a thermal non-equilibrium state need to be achieved known as population inversion [130]. During this state, the medium's carrier are mostly excited and the medium can provide gain by stimulated emission. The lasing light is then emitted via the partially transmitting mirror. Population inversion is achieved via pumping that is, supplying energy to the system. A threshold pumping power is required for lasing to occur that is, when the gain exceeds the loss. Therefore, beyond the threshold, the laser optical power exponentially increases until gain equals loss (as population inversion is reduced by the de-excitation of carriers) and steady state is reached [130]. Pumping can be done optically using another light source at frequency within the absorption band of the material excluding the resonant frequency or electrically by passing current across the material [128].

Various types of reflectors have been used such as micro disks, Distributed Bragg Reflectors (DBRs), photonic crystal resonators. The resonator configuration commonly used is the two planar mirrors sandwiching the gain medium. The determining resonator property is its Q factor, the higher the Q factor, the lower the resonator losses.

2.9.1 QD lasers

Typically, lasers are made using Quantum Well (QW) optical gain material in diode-like structures, the 1 dimension quantum confinement of the QW allow for lower lasing threshold compared to bulk [131]. Semiconductors nanocrystals (quantum dots) are new promising materials for optical gain media of lasers. First stimulated emission observations in colloidal quantum dots (CQD) were made in 2000 [132] and since then, they attracted interest as laser

optical gain materials thanks to their numerous advantages such as; low cost, simple and scalable techniques for deposition such as spin coating and inkjet printing. As they are solution based, they do not have compatibility issues when deposited in micro-cavities (lattice matching is not a requirement unlike epitaxial grown QDs) [133]. They also have high temperature stability thanks to their high energy levels spacing energy (greater than thermal energy) [134] and even lower optical threshold gain compared to QW thanks to increased band edge energy states due to the QCSE [135], which are advantageous for lasing.

Just like other lasing gain materials, optical transition between the bands edges are required for light emission where stimulated emission must exceed absorption and spontaneous emission as explained above. In QDs, the situation is more complex as carrier degeneracy is involved with multi-exciton states recombination possible [136] [137]. These are influenced by the QDs shape, structure, crystal orientation and other parameters. Considering a level system shown in figure 2.27 with two electrons. The condition of optical transparency (shown in figure 2.27 (b)) needs to be avoided in order to sustain lasing. During this condition, the stimulated emitted photon is reabsorbed by the ground state electron hence, no gain. A bi or more order exciton state is required to achieve gain as shown in figure 2.27 (c)

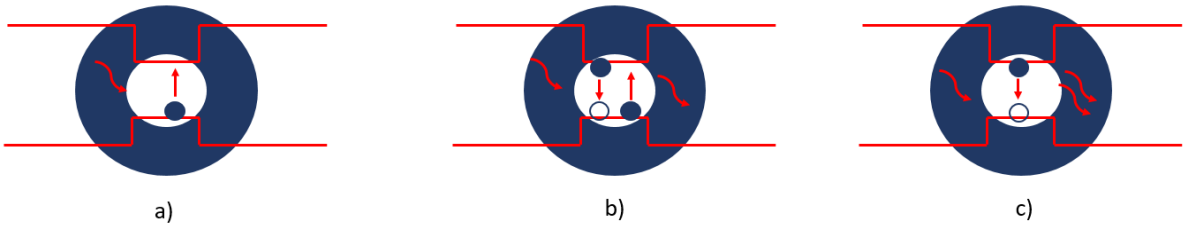

Figure 2.27 Illustration of carrier transitions in quantum dots leading to a) absorption b) optical transparency and c) gain

There exist multiple challenges limiting radiative recombination within QDs hence, inhibiting their use as optical gain media. Some of these include photo-induced absorption [138], surface trapping [139] and Auger recombination [140].

Auger recombination is a form of non-radiative recombination where the excess energy stimulate electron or holes to higher energy levels (phonon). Auger recombination has been presented as the main challenge to QD stimulated emission [141]. Auger recombination becomes very important in QDs due to the increased carrier interactions and loss in momentum conservation because of QCE [142]. Several factors influence Auger recombination rate in

QDs. Auger recombination tend to increase with increasing exciton concentration and decreasing in dot size [141] [143].

Different mechanisms have been used for supressing Auger recombination. One involves reducing the exciton-exciton interactions within the QD; this can be done by spatially separating electron and hole wave functions using QD heterostructures. An example from the CdSe QD are the type-I CdSe/ZnS, quasi-type-II CdSe/CdS CQDs and type-II CdSe/ZnTe or ZnTe/CdSe. Suppressing exciton interaction also leads to reduction in energy oscillation hence reduction in stimulated emission in the case of type II [144] for this reason, quasi type-II alignment is the most promising in mitigating Auger recombination while still allowing low optical gain threshold. Here, holes are confined in the valence band meanwhile electrons are free to move in the conduction band. This causes reduction in electrons and holes wave functions therefore reduction in exciton interactions [145] [146]. This configuration is possible with QDs having thick shells, often called giant QD. Suppression of Auger recombination (considerable increase in its lifetime) and reduction of optical gain has been reported on these types of QDs [147].

Another way of reducing Auger recombination involves engineering the core shell interface. Instead of an abrupt potential change potential change, a graded parabolic potential change can be implemented by alloying the interface. This leads to decrease in initial and final state Auger recombination overlap [148]. The alloyed interface QD configuration has also been found to reduce the optical gain threshold [149].

2.10 Transfer printing technique for micro/nano device assembly and fabrication

Transfer printing refers to a novel technique for the deterministic assembly and organisation of materials in micro/nano scale with high degree of precision, which can serve in functional device fabrication [150]. The versatility, scalability and relatively low cost associated offered by the technique makes it attractive for heterogeneous integration of electronic and optical systems [151] [152]. This involves the use of an elastomeric moulded stamp with pedestals for selective transfer of the ink (common term used to describe materials to be transfer printed including solid materials [150]) onto receiving substrate [153]. The basis of transfer printing is the fact that the stamp-ink adhesion can be kinetically controlled hence allowing picking of an ink from its original substrate and printing on a new substrate. This technique offer advantages of parallel stamp pick and printing leading to high through put and different sort of materials

(metals, colloids, organic materials, inorganic materials and more) with different geometries (quantum dots, nanowires, thin films, platelets and more) can be transferred onto a broad range of architectures as required by the application [150]. Three different categories of transfer printing exist Additive transfer, subtractive transfer and deterministic assembly as shown in figure 2.28. In the case of additive and subtractive transfer, the stamp is used in shaping the ink geometry before transfer. In additive, the ink is deposited all over the stamp using various techniques such as physical vapour deposition, spin coating or casting. The material is then printed on receiving substrate [154]. In subtractive transfer, the ink is deposited all over the receiving substrate and then a stamp with selectively positioned pedestals is used to remove specific regions of the film from the substrate, this is useful in material patterning. The last category, deterministic assembly is particularly useful as it allow wide variety of materials to be transferred as here, the ink processing on donor substrate is separated from the stamp transfer printing on receiving substrate. This category will be discussed in more detail below for device level transfer printing.

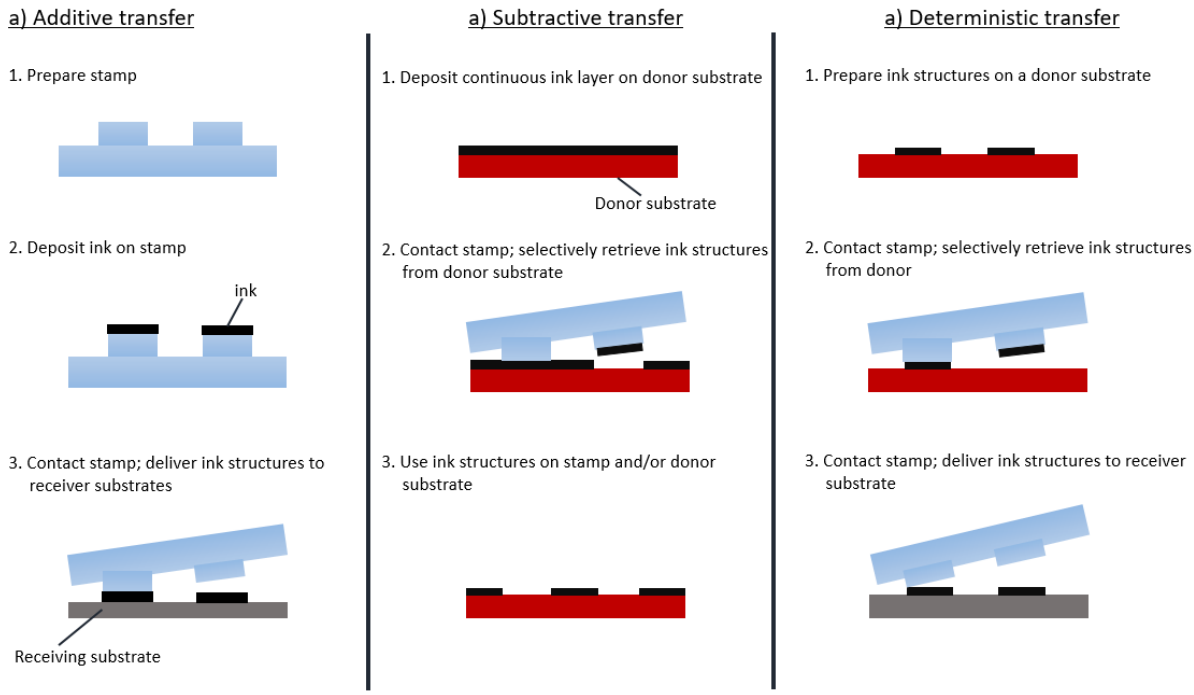

Figure 2.28 Schematic illustration of different transfer printing types a) additive transfer b) subtractive transfer and c) deterministic assembly, adapted from [150]

2.10.1.1 Anchored Transfer printing

Transfer printing of individual devices from original substrate to a different one for integration on other platforms has been a topic of research with main challenges being yield and precision on positioning [155]. Anchored transfer printing is a specific type introduced by the University

of Illinois's Rogers group [150] [155] [156]. This involves processing of the material (devices) to be transferred, to form suspended coupons held by an anchoring system. In order to ensure suspension of the coupon, its underlining layer (release layer) should have the ability to be etched selectively. Figure 2.29 shows an example of an anchoring system using a polymer

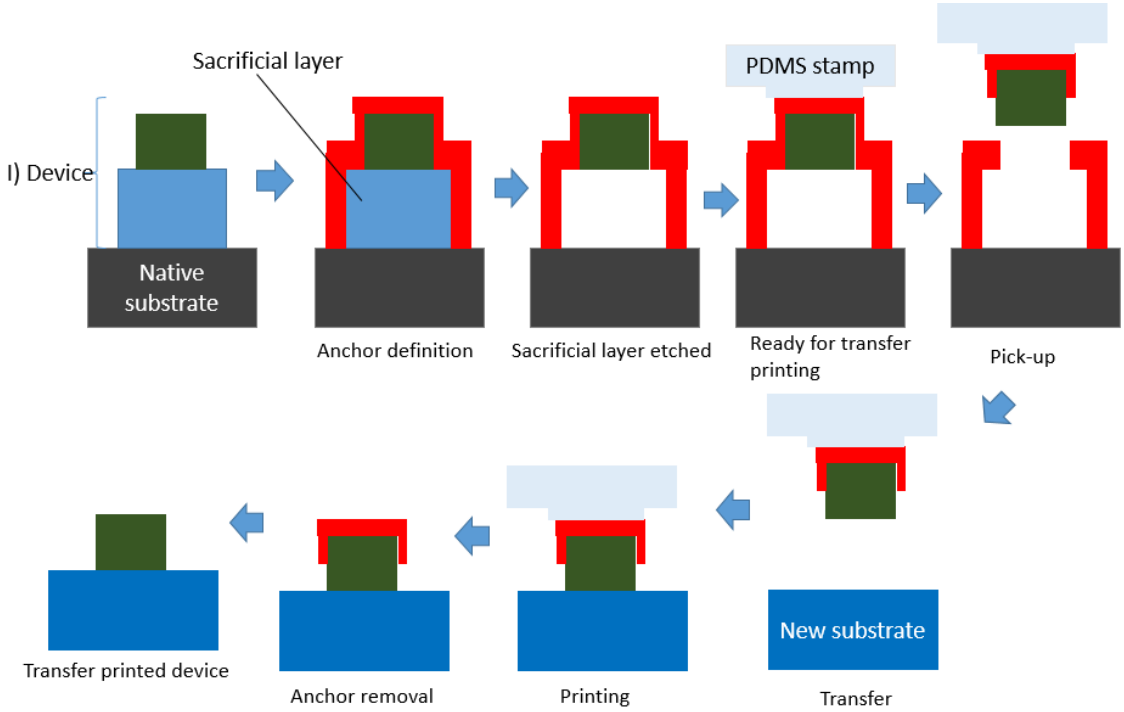

Figure 2.29 schematic illustration of an example of anchor transfer printing, adapted from [155]

The epilayer is patterned and anchored to the native substrate using a polymer; this is then followed by removal of the release layer resulting to suspended coupon attached to the native substrate by polymer tethers. A soft elastomeric stamp usually made of polydimethylsiloxane (PDMS) is used to pick and transfer print the suspended coupon from native substrate to target substrate. The PDMS stamp is usually made from a mould with dimensions corresponding to the coupon to be transferred. The governing parameter determining the transfer print is the stamp-ink and ink-target substrate adhesions, Van der Waals forces of attraction between the ink and target substrate can be enough for printing but if that is not the case, an additional adhesion promotion layer can be deposited on the targeted substrate.

2.10.1.2 Transfer printing mechanics

As mentioned above, the key parameters control of the transfer printing are the adhesion and fracture mechanics between the coupon-tether, ink-stamp and ink-target substrate [150]. For deterministic assembly transfer, the viscoelasticity property of the PDMS stamp is used to control the stamp-ink adhesion profile using rate of transfer (velocity of separation) [157]

[158]. Where, high velocities yield higher adhesions and lower velocities yield lower adhesions, velocities of 10cm/s and <1mm/s were reported [155] respectively. The stamp-ink interfacial adhesive strength G can be calculated using equation 2.50

$$G = \frac{F}{w} \qquad (2.50)$$

Where F, w are the force and stamp width respectively

Delamination at point of contact is achieved via initiation and propagation of cracks at the interface. Therefore, for retrieving (picking of coupon from original substrate), the interfacial release energy of stamp-ink must be greater than that of the ink-substrate and for printing the interfacial release energy of the stamp-ink must be lower than that of the ink-substrate [150]. Usually the ink and target substrate are rigid and hence, have constant interfacial release energies. On the other hand, the viscoelastic nature of the stamp makes its interfacial release energy velocity dependent. Figure 2.30 presents the interfacial release energy-velocity relation with the retrieval point shown to occur at critical velocity v_c. The critical velocity refers to the threshold velocity where the dominant interfacial release energy switches interfaces. This is dependent on the materials involved and the temperature.

vc can be calculated using equation 2.51

$$v_c = v_0 \left(\frac{G_c^{\frac{stamp}{ink}} - G_0}{G_0} \right)^{\frac{1}{n}} \qquad (2.51)$$

Where G_0, n, v, v_0, $G_c^{stamp/ink}$ are the zero-velocity energy release rate, scaling parameter, separation velocity, reference velocity, Stamp/ink interfacial release energy, reference velocity.

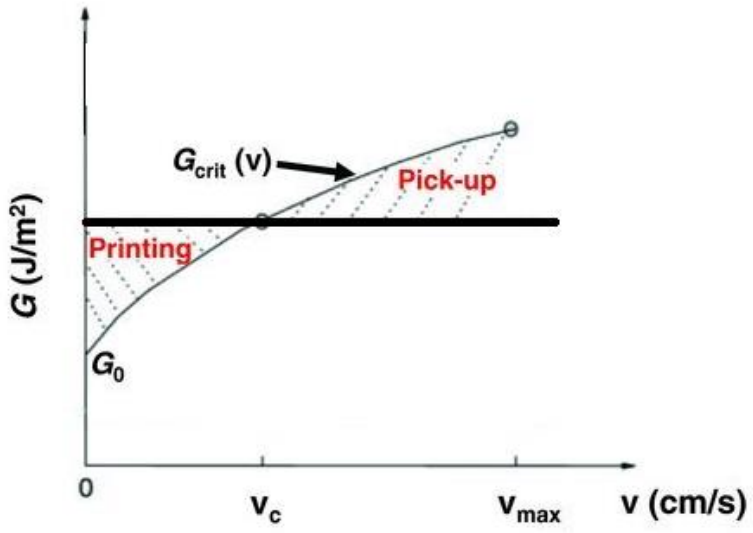

Figure 2.30 Interfacial release energy-velocity plot with the retrieval point shown to occur at critical velocity V_c.

Several novel strategies are also been employed to further influence the transfer printing such as laser thermal treatment of stamp/ink to cause separation [159], addition of surface relief features to improve stamp-ink contact hence increase adhesive strength of the interface [160] shear assisted printing [161].

2.11 References

[1] A. Teke and H. Morkoç, "Group III Nitrides," *Springer Handbooks*, pp. 753–804, 2007.

[2] B. Foutz, S. O'Leary, M. Shur, and L. Eastman, "Electron Transport Within the III–V Nitride Semiconductors, GaN, AIN, and InA A Monte Carlo Analysis," *Springer Handbooks*, pp. 805–828, 2007.

[3] S. L. Rumyantsev, M. S. Shur, and M. E. Levinshtein, "Materials properties of nitrides. Summary," *Int. J. High Speed Electron. Syst.*, vol. 14, no. 1, pp. 1–19, 2004.

[4] D. Zhu and C. J. Humphreys, "Solid-state lighting based on light emitting diode technology," *Opt. Our Time*, pp. 87–118, Jan. 2016.

[5] E. P. O'Reilly, "Valence band engineering in strained-layer structures," *Semicond. Sci. Technol.*, vol. 4, no. 3, pp. 121–137, Mar. 1989.

[6] D. Zhu, D. J. Wallis, and C. J. Humphreys, "Prospects of III-nitride optoelectronics grown on Si," *Reports Prog. Phys.*, vol. 76, no. 10, p. 106501, Oct. 2013.

[7] I. Vurgaftman and J. R. Meyer, "Band parameters for nitrogen-containing semiconductors," *J. Appl. Phys.*, vol. 94, no. 6, pp. 3675–3696, Sep. 2003.

[8] S. Nakamura, T. Mukai, and M. Senoh, "Si-doped InGaN films grown on GaN films," *Jpn. J. Appl. Phys.*, vol. 32, no. 1 A, pp. L16–L19, 1993.

[9] K. Doverspike and J. I. Pankove, "Chapter 9 Doping in the III-Nitrides," *Semicond. Semimetals*, vol. 50, no. C, pp. 259–277, Jan. 1997.

[10] H. Amano, M. Kito, K. Hiramatsu, and I. Akasaki, "P-type conduction in Mg-doped GaN treated

with low-energy electron beam irradiation (LEEBI)," *Jpn. J. Appl. Phys.*, vol. 28, no. 12 A, pp. L2112–L2114, Dec. 1989.

[11] M. Fox and R. Ispasoiu, "Quantum Wells, Superlattices, and Band-Gap Engineering," in *Springer Handbook of Electronic and Photonic Materials*, Cham Springer International Publishing, 2017, pp. 1–1.

[12] S. J. Pearton, *GaN and Related Materials*, 1st editio. CRC press, 2021.

[13] E. F. Schubert, "Radiative and non-radiative recombination," in *Light-Emitting Diodes*, 2nd ed., Cambridge University Press, 2006, pp. 27–47.

[14] E. F. Schubert, "Theory of radiative recombination," in *Light-Emitting Diodes*, 2nd ed., Cambridge University Press, 2006, pp. 48–58.

[15] J. Hecht, "Short history of laser development," *SPIE Reviews*, vol. 1, no. 1. SPIE, 01-Sep-2010.

[16] J. Neugebauer and C. G. Van de Walle, "Gallium vacancies and the yellow luminescence in GaN," *Appl. Phys. Lett.*, vol. 69, no. 4, pp. 503–505, 1996.

[17] R. Olshansky, C. B. Su, J. Manning, and W. Powazinik, "Measurement of Radiative and Nonradiative Recombination Rates in InGaAsP and AIGaAs Light Sources," *IEEE J. Quantum Electron.*, vol. 20, no. 8, pp. 838–854, 1984.

[18] M. Athanasiou *et al.*, "Efficient Amplified Spontaneous Emission from Solution-Processed CsPbBr3Nanocrystal Microcavities under Continuous Wave Excitation," *ACS Photonics*, vol. 8, no. 7, pp. 2120–2129, Jul. 2021.

[19] E. F. Schubert, N. E. J. Hunt, R. J. Malik, M. Micovic, and D. L. Miller, "Temperature and modulation characteristics of resonant-cavity light-emitting diodes," *J. Light. Technol.*, vol. 14, no. 7, pp. 1721–1728, 1996.

[20] X. Zhong *et al.*, "Energy Transfer between Spatially Separated Entangled Molecules," *Angew. Chemie*, vol. 129, no. 31, pp. 9162–9166, Jul. 2017.

[21] E. F. Schubert, "Reflectors," in *Light-Emitting Diodes*, Cambridge University Press, 2006, pp. 163–190.

[22] C. Zhang, R. Afandy, and J. Han, "Distributed Bragg reflectors for GaN-based vertical-cavity surface-emitting lasers," *Applied Sciences (Switzerland)*, vol. 9, no. 8. Multidisciplinary Digital Publishing Institute, p. 1593, 17-Apr-2019.

[23] R. Kumar, K. Thakor, S. Gupta, R. Maripeddi, and D. Nag, "Design and Optimization of Dielectric DBR for VCSEL , Targeting Emission Range of 520-550 nm," Bombay, 2019.

[24] I. Aharonovich *et al.*, "Low threshold, room-temperature microdisk lasers in the blue spectral range," *Appl. Phys. Lett.*, vol. 103, no. 2, p. 021112, Jul. 2013.

[25] Y. J. Lu *et al.*, "Plasmonic nanolaser using epitaxially grown silver film," *Science (80-.).*, vol. 337, no. 6093, pp. 450–453, Jul. 2012.

[26] Y. Hou, P. Renwick, B. Liu, J. Bai, and T. Wang, "Room temperature plasmonic lasing in a continuous wave operation mode from an InGaN/GaN single nanorod with a low threshold," *Sci. Rep.*, vol. 4, no. 1, pp. 1–6, May 2014.

[27] T. Tawara, H. Gotoh, T. Akasaka, N. Kobayashi, and T. Saitoh, "Low-threshold lasing of InGaN vertical-cavity surface-emitting lasers with dielectric distributed Bragg reflectors," *Appl. Phys. Lett.*, vol. 83, no. 5, pp. 830–832, Aug. 2003.

[28] B. Gayral and J.-M. Gerard, "Strong Purcell Effect for InAs Quantum Boxes in Three-Dimensional Solid-State Microcavities," *J. Light. Technol. Vol. 17, Issue 11, pp. 2089-*, vol. 17,

no. 11, pp. 2089-, Nov. 1999.

[29] G. Zhu *et al.*, "Research Progress of Gallium Nitride Microdisk Cavity Laser," *Front. Mater.*, vol. 9, p. 175, Apr. 2022.

[30] S. L. McCall, A. F. J. Levi, R. E. Slusher, S. J. Pearton, and R. A. Logan, "Whispering-gallery mode microdisk lasers," *Appl. Phys. Lett.*, vol. 60, no. 3, pp. 289–291, 1992.

[31] Y. Hou, P. Renwick, B. Liu, J. Bai, and T. Wang, "Room temperature plasmonic lasing in a continuous wave operation mode from an InGaN/GaN single nanorod with a low threshold," *Sci. Rep.*, vol. 4, no. 1, pp. 1–6, May 2014.

[32] S. Nakamura *et al.*, "Optical gain and carrier lifetime of InGaN multi-quantum well structure laser diodes," *Appl. Phys. Lett.*, vol. 69, no. 11, p. 1568, Jun. 1998.

[33] V. Savona, L. C. Andreani, P. Schwendimann, and A. Quattropani, "Quantum well excitons in semiconductor microcavities Unified treatment of weak and strong coupling regimes," *Solid State Commun.*, vol. 93, no. 9, pp. 733–739, Mar. 1995.

[34] M. S. Skolnick, T. A. Fisher, and D. M. Whittaker, "Strong coupling phenomena in quantum microcavity structures," *Semiconductor Science and Technology*, vol. 13, no. 7. pp. 645–669, 1998.

[35] R. P. Stanley, R. Houdré, U. Oesterle, M. Gailhanou, and M. Ilegems, "Ultrahigh finesse microcavity with distributed Bragg reflectors," *Appl. Phys. Lett.*, vol. 65, no. 15, pp. 1883–1885, Oct. 1994.

[36] A. H. W. Choi, *Handbook of optical microcavities*, 1st ed. Jenny Stanford Publishing, 2014.

[37] A. David and B. Miller, "Optical physics of quantum wells," in *Quantum Dynamics of Simple Systems*, CRC Press, 2020, pp. 239–266.

[38] N. P. Dasgupta *et al.*, "25th Anniversary Article Semiconductor Nanowires - Synthesis, Characterization, and Applications," *Adv. Mater.*, vol. 26, no. 14, pp. 2137–2184, Apr. 2014.

[39] C. Hamaguchi, *Basic semiconductor physics*, 2nd ed. Springer science and business media, 2010.

[40] R. D. Schaller and V. I. Klimov, "High efficiency carrier multiplication in PbSe nanocrystals Implications for solar energy conversion," *Phys. Rev. Lett.*, vol. 92, no. 18, p. 186601, May 2004.

[41] M. A. Reed, "Quantum Dots," *Sci. Am.*, vol. 268, no. 1, pp. 118–123, Jan. 1993.

[42] C. Wang, M. Shim, and P. Guyot-Sionnest, "Electrochromic nanocrystal quantum dots," *Science (80-.).*, vol. 291, no. 5512, pp. 2390–2392, Mar. 2001.

[43] H. Huang, L. Polavarapu, J. A. Sichert, A. S. Susha, A. S. Urban, and A. L. Rogach, "Colloidal lead halide perovskite nanocrystals synthesis, optical properties and applications," *NPG Asia Mater. 2016 811*, vol. 8, no. 11, pp. e328–e328, Nov. 2016.

[44] P. Michler, *Single Quantum Dots*, vol. 90. Berlin, Heidelberg Springer Berlin Heidelberg, 2003.

[45] H. Moon *et al.*, "Stability of Quantum Dots, Quantum Dot Films, and Quantum Dot Light-Emitting Diodes for Display Applications," *Adv. Mater.*, vol. 31, no. 34, p. 1804294, Aug. 2019.

[46] J. A. Christians, P. A. Miranda Herrera, and P. V. Kamat, "Transformation of the excited state and photovoltaic efficiency of CH3NH3PbI3 perovskite upon controlled exposure to humidified air," *J. Am. Chem. Soc.*, vol. 137, no. 4, pp. 1530–1538, Feb. 2015.

[47] A. K. Soni, R. Joshi, and R. S. Ningthoujam, "Hot Injection Method for Nanoparticle Synthesis Basic Concepts, Examples and Applications," pp. 383–434, 2021.

[48] L. Sinatra, J. Pan, and O. Bakr, "Methods of Synthesizing Monodisperse Colloidal Quantum

Dots," *Material Matters*, Thuwal, Saudi Arabia, 2017.

[49] S. Mahajan, M. Rani, R. B. Dubey, and J. Mahajan, "Synthesis of CdSe Crystal Using Hot Injection Method," *Int. J. Latest Res. Sci. Technol.*, vol. 2, no. 1, pp. 518–521, 2013.

[50] L. E. Brus, "Electron–electron and electron-hole interactions in small semiconductor crystallites The size dependence of the lowest excited electronic state," *J. Chem. Phys.*, vol. 80, no. 9, p. 4403, Aug. 1998.

[51] Y. Wang, G. Ding, J. Y. Mao, Y. Zhou, and S. T. Han, "Recent advances in synthesis and application of perovskite quantum dot based composites for photonics, electronics and sensors," *Sci. Technol. Adv. Mater.*, vol. 21, no. 1, p. 278, Jan. 2020.

[52] S. Ghaderi, B. Ramesh, and A. M. Seifalian, "Fluorescence nanoparticles 'quantum dots' as drug delivery system and their toxicity A review," *J. Drug Target.*, vol. 19, no. 7, pp. 475–486, Aug. 2011.

[53] D. Bera, L. Qian, T. K. Tseng, and P. H. Holloway, "Quantum dots and their multimodal applications A review," *Materials*, vol. 3, no. 4. pp. 2260–2345, 2010.

[54] W. R. Algar, A. J. Tavares, and U. J. Krull, "Beyond labels A review of the application of quantum dots as integrated components of assays, bioprobes, and biosensors utilizing optical transduction," *Analytica Chimica Acta*, vol. 673, no. 1. pp. 1–25, 2010.

[55] L. Qian, Y. Zheng, J. Xue, and P. H. Holloway, "Stable and efficient quantum-dot light-emitting diodes based on solution-processed multilayer structures," *Nat. Photonics*, vol. 5, no. 9, pp. 543–548, 2011.

[56] V. L. Colvin, M. C. Schlamp, and A. P. Alivisatos, "Light-emitting diodes made from cadmium selenide nanocrystals and a semiconducting polymer," *Nature*, vol. 370, no. 6488, pp. 354–357, 1994.

[57] C. Dang, J. Lee, C. Breen, J. S. Steckel, S. Coe-Sullivan, and A. Nurmikko, "Red, green and blue lasing enabled by single-exciton gain in colloidal quantum dot films," *Nat. Nanotechnol.*, vol. 7, no. 5, pp. 335–339, 2012.

[58] N. J. L. K. Davis *et al.*, "Photon Reabsorption in Mixed CsPbCl3CsPbI3 Perovskite Nanocrystal Films for Light-Emitting Diodes," *J. Phys. Chem. C*, vol. 121, no. 7, pp. 3790–3796, Feb. 2017.

[59] A. J. Nozik, "Quantum dot solar cells," *Phys. E Low-dimensional Syst. Nanostructures*, vol. 14, no. 1–2, pp. 115–120, Apr. 2002.

[60] F. Li *et al.*, "Perovskite Quantum Dot Solar Cells with 15.6% Efficiency and Improved Stability Enabled by an α-CsPbI3/FAPbI3 Bilayer Structure," *ACS Energy Lett.*, vol. 4, no. 11, pp. 2571–2578, Nov. 2019.

[61] Y. Wang *et al.*, "CsPbBr3 Perovskite Quantum Dots-Based Monolithic Electrospun Fiber Membrane as an Ultrastable and Ultrasensitive Fluorescent Sensor in Aqueous Medium," *J. Phys. Chem. Lett.*, vol. 7, no. 21, pp. 4253–4258, Nov. 2016.

[62] S. R. Cordero, P. J. Carson, R. A. Estabrook, G. F. Strouse, and S. K. Buratto, "Photo-activated luminescence of CdSe quantum dot monolayers," *J. Phys. Chem. B*, vol. 104, no. 51, pp. 12137–12142, Dec. 2000.

[63] K. Pechstedt, T. Whittle, J. Baumberg, and T. Melvin, "Photoluminescence of colloidal CdSe/ZnS quantum dots The critical effect of water molecules," *J. Phys. Chem. C*, vol. 114, no. 28, pp. 12069–12077, Jul. 2010.

[64] J. Müller, J. M. Lupton, A. L. Rogach, J. Feldmann, D. V. Talapin, and H. Weller, "Air-induced fluorescence bursts from single semiconductor nanocrystals," *Appl. Phys. Lett.*, vol. 85, no. 3, p. 381, Jul. 2004.

[65] S. Dembski *et al.*, “Photoactivation of CdSe/ZnS quantum dots embedded in silica colloids,” *Wiley Online Libr.*, vol. 4, no. 9, pp. 1516–1526, 2008.

[66] C. Carrillo-Carrión, B. M. Simonet, and M. Valcárcel, “Colistin-functionalised CdSe/ZnS quantum dots as fluorescent probe for the rapid detection of Escherichia coli,” *Biosens. Bioelectron.*, vol. 26, no. 11, pp. 4368–4374, Jul. 2011.

[67] M. Bawendi, P. Carroll, … W. W.-T. J. of C., and undefined 1992, “Luminescence properties of CdSe quantum crystallites Resonance between interior and surface localized states,” *aip.scitation.org*, vol. 96, no. 2, p. 946, 1992.

[68] J. Müller, J. M. Lupton, A. L. Rogach, J. Feldmann, D. V. Talapin, and H. Weller, “Monitoring surface charge movement in single elongated semiconductor nanocrystals,” *Phys. Rev. Lett.*, vol. 93, no. 16, p. 167402, Oct. 2004.

[69] W. G. J H M van Sark *et al.*, “Blueing, bleaching, and blinking of single CdSe/ZnS quantum dots,” *Wiley Online Libr.*, vol. 3, pp. 871–879, 2002.

[70] P. H. C. Camargo, Y. H. Lee, U. Jeong, Z. Zou, and Y. Xia, “Cation exchange A simple and versatile route to inorganic colloidal spheres with the same size but different compositions and properties,” *Langmuir*, vol. 23, no. 6, pp. 2985–2992, Mar. 2007.

[71] K. Miszta, D. Dorfs, A. Genovese, M. R. Kim, and L. Manna, “Cation exchange reactions in colloidal branched nanocrystals,” *ACS Nano*, vol. 5, no. 9, pp. 7176–7183, Sep. 2011.

[72] J. A. Christians, P. A. Miranda Herrera, and P. V. Kamat, “Transformation of the excited state and photovoltaic efficiency of CH3NH3PbI3 perovskite upon controlled exposure to humidified air,” *J. Am. Chem. Soc.*, vol. 137, no. 4, pp. 1530–1538, Feb. 2015.

[73] G. E. Eperon, S. D. Stranks, C. Menelaou, M. B. Johnston, L. M. Herz, and H. J. Snaith, “Formamidinium lead trihalide A broadly tunable perovskite for efficient planar heterojunction solar cells,” *Energy Environ. Sci.*, vol. 7, no. 3, pp. 982–988, 2014.

[74] F. Zhang *et al.*, “Brightly luminescent and color-tunable colloidal CH3NH3PbX3 (X = Br, I, Cl) quantum dots Potential alternatives for display technology,” *ACS Nano*, vol. 9, no. 4, pp. 4533–4542, Apr. 2015.

[75] L. Protesescu *et al.*, “Nanocrystals of Cesium Lead Halide Perovskites (CsPbX3, X = Cl, Br, and I) Novel Optoelectronic Materials Showing Bright Emission with Wide Color Gamut,” *Nano Lett.*, vol. 15, no. 6, pp. 3692–3696, Jun. 2015.

[76] J. A. Sichert *et al.*, “Quantum Size Effect in Organometal Halide Perovskite Nanoplatelets,” *Nano Lett.*, vol. 15, no. 10, pp. 6521–6527, Oct. 2015.

[77] Q. Van Le, K. Hong, H. W. Jang, and S. Y. Kim, “Halide Perovskite Quantum Dots for Light-Emitting Diodes Properties, Synthesis, Applications, and Outlooks,” *Adv. Electron. Mater.*, vol. 4, no. 12, p. 1800335, Dec. 2018.

[78] H. Huang, M. I. Bodnarchuk, S. V. Kershaw, M. V. Kovalenko, and A. L. Rogach, “Lead Halide Perovskite Nanocrystals in the Research Spotlight Stability and Defect Tolerance,” *ACS Energy Lett.*, vol. 2, no. 9, pp. 2071–2083, Sep. 2017.

[79] S. Huang *et al.*, “Morphology Evolution and Degradation of CsPbBr3 Nanocrystals under Blue Light-Emitting Diode Illumination,” *ACS Appl. Mater. Interfaces*, vol. 9, no. 8, pp. 7249–7258, Mar. 2017.

[80] J. You *et al.*, “Moisture assisted perovskite film growth for high performance solar cells,” *Appl. Phys. Lett.*, vol. 105, no. 18, p. 183902, Nov. 2014.

[81] G. Yuan, C. Ritchie, M. Ritter, S. Murphy, D. E. Gómez, and P. Mulvaney, “The Degradation and Blinking of Single CsPbI3 Perovskite Quantum Dots,” *J. Phys. Chem. C*, vol. 122, no. 25,

pp. 13407–13415, Jun. 2018.

[82] H. Huang, M. I. Bodnarchuk, S. V. Kershaw, M. V. Kovalenko, and A. L. Rogach, "Lead Halide Perovskite Nanocrystals in the Research Spotlight Stability and Defect Tolerance," *ACS Energy Lett.*, vol. 2, no. 9, pp. 2071–2083, Sep. 2017.

[83] L. Protesescu *et al.*, "Dismantling the 'red Wall' of Colloidal Perovskites Highly Luminescent Formamidinium and Formamidinium-Cesium Lead Iodide Nanocrystals," *ACS Nano*, vol. 11, no. 3, pp. 3119–3134, Mar. 2017.

[84] F. Palazon, F. Di Stasio, S. Lauciello, R. Krahne, M. Prato, and L. Manna, "Evolution of CsPbBr3 nanocrystals upon post-synthesis annealing under an inert atmosphere," *J. Mater. Chem. C*, vol. 4, no. 39, pp. 9179–9182, 2016.

[85] J. Pan *et al.*, "Highly Efficient Perovskite-Quantum-Dot Light-Emitting Diodes by Surface Engineering," *Adv. Mater.*, vol. 28, no. 39, pp. 8718–8725, Oct. 2016.

[86] H. Y. Yang *et al.*, "Multifunctional polymer ligand interface CdZnSeS/ZnS quantum dot/Cy3-labeled protein pairs as sensitive FRET sensors," *ACS Publ.*, vol. 8, no. 51, p. 10, Dec. 2016.

[87] S. Huang, Z. Li, L. Kong, N. Zhu, A. Shan, and L. Li, "Enhancing the Stability of CH3NH3PbBr3 Quantum Dots by Embedding in Silica Spheres Derived from Tetramethyl Orthosilicate in 'waterless' Toluene," *J. Am. Chem. Soc.*, vol. 138, no. 18, pp. 5749–5752, May 2016.

[88] H. C. Wang *et al.*, "Mesoporous Silica Particles Integrated with All-Inorganic CsPbBr3Perovskite Quantum-Dot Nanocomposites (MP-PQDs) with High Stability and Wide Color Gamut Used for Backlight Display," *Angew. Chemie - Int. Ed.*, vol. 55, no. 28, pp. 7924–7929, Jul. 2016.

[89] J. Hai, H. Li, Y. Zhao, F. Chen, Y. Peng, and B. Wang, "Designing of blue, green, and red CsPbX3 perovskite-codoped flexible films with water resistant property and elimination of anion-exchange for tunable white light emission," *Chem. Commun.*, vol. 53, no. 39, pp. 5400–5403, 2017.

[90] C. Xinbo, L. Yanjia, X. Naiwen, and al -, "Electroluminescence of organic compounds," *Br. J. Appl. Phys.*, vol. 6, no. S4, p. S54, Jan. 1955.

[91] J. H. Burroughes *et al.*, "Light-emitting diodes based on conjugated polymers," *Nat. 1990 3476293*, vol. 347, no. 6293, pp. 539–541, Oct. 1990.

[92] N. Tessler, G. J. Denton, and R. H. Friend, "Lasing from conjugated-polymer microcavities," *Nature*, vol. 382, no. 6593, pp. 695–696, 1996.

[93] "The Nobel Prize in Chemistry 2000. NobelPrize.org.," *Nobel Prize Outreach*, 2022.

[94] L. F. Santos, G. Gozzi, L. F. Santos, and G. Gozzi, "Electrical Properties of Polymer Light-Emitting Devices," *Conduct. Polym.*, Oct. 2016.

[95] Martin Pope and C. E. Swenberg, "Electronic Processes in Organic Crystals and Polymers - 2nd edition, ISBN 9780195129632," *Oxford Univ. Press USA 2nd Ed.*, p. 1360, 1999.

[96] P. L. Burn and I. D. W. Samuel, "Light-emitting polymers - The shape of things to come?," *Mater. Today*, vol. 1, no. 4, pp. 3–5, Jan. 1998.

[97] W. P. Su, J. R. Schrieffer, and A. J. Heeger, "Soliton excitations in polyacetylene," *Phys. Rev. B*, vol. 22, no. 4, p. 2099, Aug. 1980.

[98] A. C. Grimsdale, K. L. Chan, R. E. Martin, P. G. Jokisz, and A. B. Holmes, "Synthesis of light-emitting conjugated polymers for applications in electroluminescent devices," *Chem. Rev.*, vol. 109, no. 3, pp. 897–1091, Mar. 2009.

[99] D. Tyler McQuade, A. E. Pullen, and T. M. Swager, “Conjugated polymer-based chemical sensors,” *Chem. Rev.*, vol. 100, no. 7, pp. 2537–2574, Jul. 2000.

[100] H. Li *et al.*, “Chemical and Biomolecule Sensing with Organic Field-Effect Transistors,” *Chem. Rev.*, vol. 119, no. 1, pp. 3–35, Jan. 2019.

[101] H. Sakata, H. Takeuchi, K. Natsume, and S. Suzuki, “Vertical-cavity organic lasers with distributed-feedback structures based on active Bragg reflectors,” *Opt. Express*, vol. 14, no. 24, p. 11681, Nov. 2006.

[102] L. Frezza, M. Patrini, M. Liscidini, and D. Comoretto, “Directional enhancement of spontaneous emission in polymer flexible microcavities,” *J. Phys. Chem. C*, vol. 115, no. 40, pp. 19939–19946, Oct. 2011.

[103] S. Noda, M. Fujita, and T. Asano, “Spontaneous-emission control by photonic crystals and nanocavities,” *Nature Photonics*, vol. 1, no. 8. Nature Publishing Group, pp. 449–458, Aug-2007.

[104] M. Höijer and G. Björk, “Modification of spontaneous emission rate in planar dielectric microcavities - Seen as superradiance and subradiance,” *Opt. Commun.*, vol. 150, no. 1–6, pp. 319–330, May 1998.

[105] P. Lova, G. Manfredi, and D. Comoretto, “Advances in Functional Solution Processed Planar 1D Photonic Crystals,” *Advanced Optical Materials*, vol. 6, no. 24. Wiley-VCH Verlag, Dec-2018.

[106] H. J. Kimble, “Strong interactions of single atoms and photons in cavity QED,” *Phys. Scr. T*, vol. 76, no. T76, pp. 127–137, 1998.

[107] D. Delbeke, R. Bockstaele, P. Bienstman, R. Baets, and H. Benisty, “High-efficiency semiconductor resonant-cavity light-emitting diodes A review,” *IEEE J. Sel. Top. Quantum Electron.*, vol. 8, no. 2, pp. 189–206, Mar. 2002.

[108] S. Dufferwiel, “Strongly Confined Exciton-Polaritons in a Tunable Microcavity,” University of Sheffield, 2014.

[109] R. Houdre, R. P. Stanley, U. Oesterle, M. Ilegems, and C. Weisbuch, “Room temperature exciton-photon Rabi splitting in a semiconductor microcavity,” *J. Phys. IV JP*, vol. 3, no. 5, pp. 51–58, 1993.

[110] C. Weisbuch, M. Nishioka, A. Ishikawa, and Y. Arakawa, “Observation of the coupled exciton-photon mode splitting in a semiconductor quantum microcavity,” *Phys. Rev. Lett.*, vol. 69, no. 23, pp. 3314–3317, Dec. 1992.

[111] M. Alavi and S. Shojaei, “Large Vacuum Rabi Splitting in a Single Nitride-Based Quantum WellMicrocavity,” *Int. J. Nanosci. Nanotechnol.*, vol. 13, no. 4, pp. 289–298, 2017.

[112] E. F. Schubert, “LED basics Electrical properties,” in *Light-Emitting Diodes*, Cambridge University Press, 2010, pp. 59–85.

[113] E. F. Schubert, “High internal efficiency designs,” in *Light-Emitting Diodes*, Cambridge University Press, 2010, pp. 113–126.

[114] E. F. Schubert, “LED basics Optical properties,” in *Light-Emitting Diodes*, Cambridge University Press, 2010, pp. 86–100.

[115] D. D. Koleske, M. E. Coltrin, K. C. Cross, C. C. Mitchell, and A. A. Allerman, “Understanding GaN nucleation layer evolution on sapphire,” *J. Cryst. Growth*, vol. 273, no. 1–2, pp. 86–99, Dec. 2004.

[116] S. Figge, T. Böttcher, S. Einfeldt, and D. Hommel, “In situ and ex situ evaluation of the film

coalescence for GaN growth on GaN nucleation layers," *J. Cryst. Growth*, vol. 221, no. 1–4, pp. 262–266, Dec. 2000.

[117] M. J. Kappers, M. A. Moram, Y. Zhang, M. E. Vickers, Z. H. Barber, and C. J. Humphreys, "Interlayer methods for reducing the dislocation density in gallium nitride," *Phys. B Condens. Matter*, vol. 401–402, pp. 296–301, Dec. 2007.

[118] S. F. Chichibu *et al.*, "Origin of defect-insensitive emission probability in In-containing (Al,In,Ga)N alloy semiconductors," *Nat. Mater. 2006 510*, vol. 5, no. 10, pp. 810–816, Sep. 2006.

[119] D. Watson-Parris *et al.*, "Energy landscape and carrier wave-functions in InGaN/GaN quantum wells," *Phys. status solidi c*, vol. 7, no. 7–8, pp. 2255–2258, Jul. 2010.

[120] M. Lee, M. Yang, K. M. Song, and S. Park, "InGaN/GaN Blue Light Emitting Diodes Using Freestanding GaN Extracted from a Si Substrate," *ACS Photonics*, vol. 5, no. 4, pp. 1453–1459, Apr. 2018.

[121] E. F. Schubert, "Junction and carrier temperatures," in *Light-Emitting Diodes*, Cambridge University Press, 2010, pp. 101–112.

[122] C. Li, Z. Ji, J. Li, M. Xu, H. Xiao, and X. Xu, "Electroluminescence properties of InGaN/GaN multiple quantum well-based LEDs with different indium contents and different well widths," *Sci. Reports 2017 71*, vol. 7, no. 1, pp. 1–8, Nov. 2017.

[123] E. F. Schubert, "Spontaneous emission from resonant cavities," in *Light-Emitting Diodes*, Cambridge University Press, 2010, pp. 239–254.

[124] E. F. Schubert, "Resonant-cavity light-emitting diodes," in *Light-emitting Diodes, Second Edition*, 2nd ed., Cambridge University Press, 2012, pp. 255–275.

[125] H. De Neve, J. Blondelle, R. Baets, P. Demeester, P. Van Daele, and G. Borghs, "Resonant Cavity LED's," *Microcavities Photonic Bandgaps Phys. Appl.*, pp. 333–342, 1996.

[126] F. Sarcan, M. S. Nordin, F. Kuruoğlu, A. Erol, and A. J. Vickers, "Characterization of temperature dependent operation of a GaInNAs-based RCEPD designed for 1.3 μm," *Superlattices Microstruct.*, vol. 102, pp. 27–34, Feb. 2017.

[127] S. Yang *et al.*, "GaN-based green resonant-cavity light-emitting diodes with Al mirror and copper plate," *Opt. Lett. Vol. 47, Issue 11, pp. 2858-2861*, vol. 47, no. 11, pp. 2858–2861, Jun. 2022.

[128] B. Saleh, "The laser," *Opt. Our Time*, pp. 71–85, Jan. 2016.

[129] I. D. W. Samuel, E. B. Namdas, and G. A. Turnbull, "How to recognize lasing," *Nat. Photonics 2009 310*, vol. 3, no. 10, pp. 546–549, 2009.

[130] A. E. Siegman and D. J. Kuizenga, "Active mode-coupling phenomena in pulsed and continuous lasers," *Opto-electronics 1974 61*, vol. 6, no. 1, pp. 43–66, Jan. 1974.

[131] Y. Arakawa and H. Sakaki, "Multidimensional quantum well laser and temperature dependence of its threshold current," *Appl. Phys. Lett.*, vol. 40, no. 11, pp. 939–941, 1982.

[132] V. I. Klimov *et al.*, "Optical gain and stimulated emission in nanocrystal quantum dots," *Science (80-.).*, vol. 290, no. 5490, pp. 314–317, Oct. 2000.

[133] Y. Chen *et al.*, "Colloidal quantum dot random laser," *Opt. Express*, vol. 19, no. 4, p. 2996, 2011.

[134] H. Liu *et al.*, "Long-wavelength InAs/GaAs quantum-dot laser diode monolithically grown on Ge substrate," *Nat. Photonics*, vol. 5, no. 7, pp. 416–419, 2011.

[135] M. Asada, Y. Miyamoto, and Y. Suematsu, "Gain and the Threshold of Three-Dimensional

Quantum-Box Lasers," *IEEE J. Quantum Electron.*, vol. 22, no. 9, pp. 1915–1921, 1986.

[136] C. J. Tsai *et al.*, "Semiconductor clusters, nanocrystals, and quantum dots," *Science (80-.).*, vol. 271, no. 5251, pp. 933–937, Feb. 1996.

[137] D. Norris, A. L. Efros, and M. Rosen, "Size dependence of exciton fine structure in CdSe quantum dots," *Phys. Rev. B - Condens. Matter Mater. Phys.*, vol. 53, no. 24, pp. 16347–16354, 1996.

[138] A. Cretí, M. Zavelani-Rossi, G. Lanzani, M. Anni, L. Manna, and M. Lomascolo, "Role of the shell thickness in stimulated emission and photoinduced absorption in CdSe core/shell nanorods," *Phys. Rev. B - Condens. Matter Mater. Phys.*, vol. 73, no. 16, 2006.

[139] C. B. Murray, C. R. Kagan, and M. G. Bawendi, "Self-organization of CdSe nanocrystallites into three-dimensional quantum dot superlattices," *Science (80-.).*, vol. 270, no. 5240, pp. 1335–1338, 1995.

[140] A. Haug, "Auger recombination in direct-gap semiconductors band-structure effects," *J. Phys. C Solid State Phys.*, vol. 16, pp. 4159–4172, 1983.

[141] V. I. Klimov, A. A. Mikhailovsky, D. W. McBranch, C. A. Leatherdale, and M. G. Bawendi, "Quantization of multiparticle Auger rates in semiconductor quantum dots," *Science (80-.).*, vol. 287, no. 5455, pp. 1011–1014, Feb. 2000.

[142] Y. Wang and H. Sun, "Advances and prospects of lasers developed from colloidal semiconductor nanostructures," *Prog. Quantum Electron.*, vol. 60, pp. 1–29, Aug. 2018.

[143] V. I. Klimov, J. A. McGuire, R. D. Schaller, and V. I. Rupasov, "Scaling of multiexciton lifetimes in semiconductor nanocrystals," *Phys. Rev. B - Condens. Matter Mater. Phys.*, vol. 77, no. 19, May 2008.

[144] D. Oron, M. Kazes, and U. Banin, "Multiexcitons in type-II colloidal semiconductor quantum dots," *Phys. Rev. B - Condens. Matter Mater. Phys.*, vol. 75, no. 3, 2007.

[145] J. Kundu, Y. Ghosh, A. M. Dennis, H. Htoon, and J. A. Hollingsworth, "Giant nanocrystal quantum dots stable down-conversion phosphors that exploit a large stokes shift and efficient shell-to-core energy relaxation," *ACS Publ.*, vol. 12, no. 6, pp. 3031–3037, Jun. 2012.

[146] L. Zhang *et al.*, "Single-Mode Lasing from 'Giant' CdSe/CdS Core–Shell Quantum Dots in Distributed Feedback Structures," *ACS Publ.*, vol. 9, no. 15, pp. 13293–13303, Apr. 2017.

[147] F. García-Santamaría, Y. Chen, J. Vela, R. D. Schaller, J. A. Hollingsworth, and V. I. Klimov, "Suppressed auger recombination in 'Giant' nanocrystals boosts optical gain performance," *Nano Lett.*, vol. 9, no. 10, pp. 3482–3488, Oct. 2009.

[148] G. E. Cragg and A. L. Efros, "Suppression of auger processes in confined structures," *Nano Lett.*, vol. 10, no. 1, pp. 313–317, Jan. 2010.

[149] Y. Wang *et al.*, "Unraveling the ultralow threshold stimulated emission from CdZnS/ZnS quantum dot and enabling high-Q microlasers," *Laser Photonics Rev.*, vol. 9, no. 5, pp. 507–516, Sep. 2015.

[150] A. Carlson *et al.*, "Transfer Printing Techniques for Materials Assembly and Micro/Nanodevice Fabrication," *Adv. Mater.*, vol. 24, no. 39, pp. 5284–5318, Oct. 2012.

[151] H. Ahn, K. J. Lee, A. Shim, J. A. Rogers, and R. G. Nuzzo, "Additive soft-lithographic patterning of submicrometer- and nanometer-scale large-area resists on electronic materials," *Nano Lett.*, vol. 5, no. 12, pp. 2533–2537, Dec. 2005.

[152] E. Menard *et al.*, "Micro- and nanopatterning techniques for organic electronic and optoelectronic systems," *Chem. Rev.*, vol. 107, no. 4, pp. 1117–1160, Apr. 2007.

[153] S. Il Park *et al.*, "Printed assemblies of inorganic light-emitting diodes for deformable and semitransparent displays," *Science (80-.).*, vol. 325, no. 5943, pp. 977–981, 2009.

[154] J. Yeom and M. A. Shannon, "Detachment lithography of photosensitive polymers A route to fabricating three-Dimensional structures," *Adv. Funct. Mater.*, vol. 20, no. 2, pp. 289–295, Jan. 2010.

[155] B. Corbett, R. Loi, W. Zhou, D. Liu, and Z. Ma, "Transfer print techniques for heterogeneous integration of photonic components," *Prog. Quantum Electron.*, vol. 52, pp. 1–17, Mar. 2017.

[156] J. Yoon, S. M. Lee, D. Kang, M. A. Meitl, C. A. Bower, and J. A. Rogers, "Heterogeneously Integrated Optoelectronic Devices Enabled by Micro-Transfer Printing," *Adv. Opt. Mater.*, vol. 3, no. 10, pp. 1313–1335, Oct. 2015.

[157] X. Feng, M. A. Meitl, A. M. Bowen, Y. Huang, R. G. Nuzzo, and J. A. Rogers, "Competing fracture in kinetically controlled transfer printing," *Langmuir*, vol. 23, no. 25, pp. 12555–12560, Dec. 2007.

[158] Y. Sun, J. R.-A. materials, and undefined 2007, "Inorganic semiconductors for flexible electronics," *Wiley Online Libr.*, vol. 19, no. 15, pp. 1897–1916, Aug. 2007.

[159] S. Kim *et al.*, "Enhanced adhesion with pedestal-shaped elastomeric stamps for transfer printing," *Appl. Phys. Lett.*, vol. 100, no. 17, Apr. 2012.

[160] S. Kim *et al.*, "Microstructured elastomeric surfaces with reversible adhesion and examples of their use in deterministic assembly by transfer printing," *Proc. Natl. Acad. Sci. U. S. A.*, vol. 107, no. 40, pp. 17095–17100, Oct. 2010.

[161] A. Carlson *et al.*, "Shear-enhanced adhesiveless transfer printing for use in deterministic materials assembly," *Appl. Phys. Lett.*, vol. 98, no. 26, Jun. 2011.

3) Chapter 3 - Experimental techniques

3.1 Introduction

This chapter describes the experimental techniques employed for the fabrication and characterisation of the hybrid optical microcavity devices. Fabrication techniques used include photolithography, thermal evaporation, annealing, dry etching techniques (Reactive Ion Etching and Inductively Coupled Plasma Reactive Ion Etching), profilometry, spin coating, Plasma Enhanced Chemical Vapour Deposition (PECVD), wet etching techniques (KOH solution etching of Si and HCL solution etching of Ti/Ni), transfer printing. The characterisation techniques include confocal photoluminescence (PL), micro photoluminescence, Scanning Electron Microscopy (SEM), time resolved photoluminescence and electroluminescence.

3.2 Fabrication techniques

3.2.1 Photolithography

Photolithography is a core process used for the fabrication of micro/nano electronics devices and integrated circuits. Photolithography generally involves the patterning of a thin film sacrificial layer deposited on a substrate using light (UV light mostly) shone through a photomask. This patterned sacrificial layer protects specific areas of the underlying material for subsequent processes such as further depositions, etching or implantations. The sacrificial layer is photoresist, which is a photosensitive material. Photoresists exist in two polarity tones, positive and negative photoresist [1]. Positive photoresist has the characteristic of having their exposed areas to UV light removed (non-exposed areas are kept) upon development. Negative photoresist has the characteristic of having their non-exposed areas to UV light removed (exposed areas are kept) upon development. The photolithography process can be separated in different steps, which are sample cleaning, dehydration bake, photoresist deposition, soft bake, exposure, development and photoresist removal

a)

b) c)

Figure 3.1 Pictures of photolithography equipment a) The Karl Suss MJB3 mask aligner b) Electronic Micro System Photoresist Spin Coater 4000 c) Hot plate

A three solvent cleaning step is usually performed at the beginning. This is to ensure that the sample surface to be processed is clean from dirt and any contaminants. This involves cleaning the sample in a fume cupboard using three different solvents n-butyl acetate (using cotton buds), acetone and isopropyl alcohol. The sample is then blow-dried using a nitrogen gun. Photoresist deposition on the sample is done by spin coating using an Electronic Micro System Photoresist Spin Coater 4000 (image shown in Figure 3.1 (b)), this process is described in section 3.2.2. The Karl Suss MJB3 mask aligner (shown in Figure 3.1 (a)) is used to perform UV light exposure to the sample through a photomask, designed and fabricated for the required patterning. Before exposure, the sample on the stage needs to be aligned to the desired matching photomask patterns. This is done by moving the sample in the x, y and rotation (θ) directions until aligned, Vernier screws can be rotated for this. After alignment, the sample need to be

brought in contact with the mask (this is to prevent/reduce light diffraction during the exposure). An important parameter for efficient exposure is the supplied light power density [1]. For proximity lithography (no contact), the minimum achievable linewidth (W_{min}) without taking into consideration the photoresist performance, can be calculated using equation 3.1 below [2]

$$W_{min} = \sqrt{\lambda d} \qquad (3.1)$$

Where, λ = radiation wavelength, d = exposure gap

Development involves dipping the sample in a developer solution for a specific time; the developer solution is specific to the photoresist. Positive resist exposed areas are degraded by exposure to UV light hence those areas become soluble in the developer solution. Meanwhile, negative resist is naturally soluble in the developer solution and areas exposed to UV are strengthened and become insoluble. The development process results in the patterning of the resist and hence the subsequent process can be performed as required such as etching, metallisation and other. Removal of the remaining photoresist is done using resist remover solutions and oxygen plasma ashing.

3.2.2 Spin coating

Spin coating refers to a simple thin film deposition technique for liquid-based substances on a surface. The sample to be coated is mounted on the spinner head. Then few drops of the coating liquid are dispersed on top of the sample. This is then followed by spinning of the sample. The centripetal force generated due to the spinning causes spreading of the liquid over the whole sample surface and even coating of the surface. The spin speed and spin time are inversely proportional to the deposited thickness. Another parameter affecting the yield layer thickness is the coating solution viscosity [3]. Spin coating offers advantage of fast deposition at low cost hence its attractiveness. Figure 3.2 below shows a representation of the process

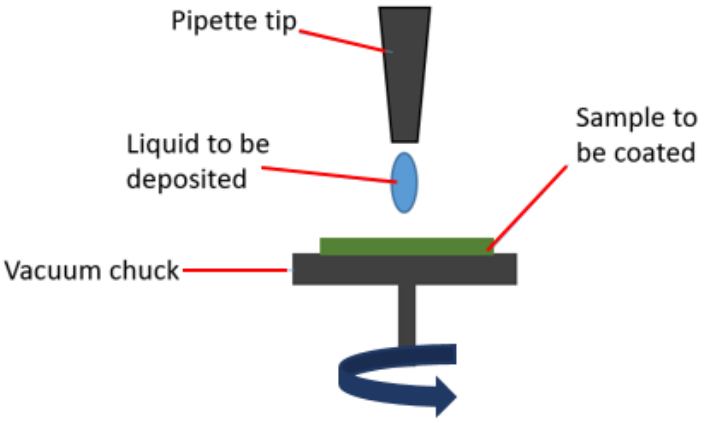

Figure 3.2 diagrammatic illustration of spin coating technique

3.2.3 Thermal evaporation

This refers to a physical vapour deposition process involving resistive heating of a metal in a vacuum for its evaporation and subsequent deposition on a sample surface. The Edwards thermal evaporators are used within the department (shown in Figure 3.3 (a) below). They consist of a bell jar protected chamber held at a high vacuum of about 10^{-6} mTorr. This is thanks to the combination of the rotary and diffusion pumps. Diffusion pump oil vapours are by-products from the diffusion pump operation, they are prevented from reaching the deposition chamber by liquid nitrogen inserted into the cold trap, and this causes their condensation and extraction.

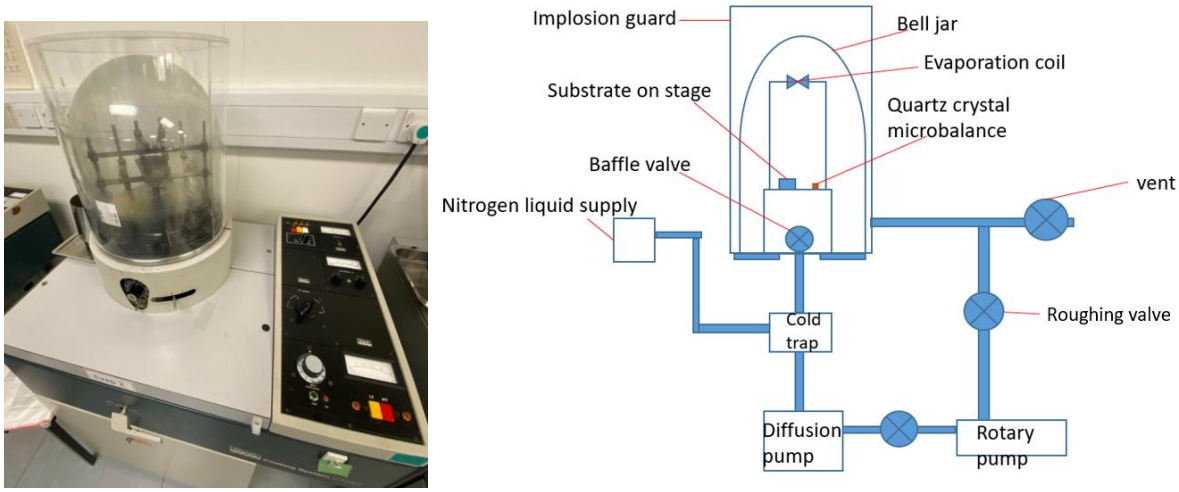

a) b)

Figure 3.3 Thermal evaporation images a) Edwards thermal evaporator b) schematic illustration of thermal evaporator

The high vacuum helps in increasing the evaporated metal particle mean free path and limiting number of contaminants in the chamber. The metal to be evaporated is loaded into a tungsten coil. The tungsten coil has a high melting point of about 5930^{o}C which allow evaporation of loaded metal without coil melting, this also limits the outgassing [4]. The coil is positioned at a long distance of about 120mm away from the sample; this is to prevent high temperatures from the heated coil to bake the photoresist mask. By flowing a high current (20 to 40 A) through the coil, the metal is melted and then evaporated by the process of resistive heating. The deposited thickness can be monitored in real time using the internal IL150 quartz crystal monitor. The crystal monitor is made of a crystal oscillating material whose resonant frequency can be accurately measured and is calibrated to output thickness based on mass deposited.

3.2.4 Dry etching techniques (Reactive Ion Etching and Inductively Coupled Plasma Reactive Ion Etching)

Dry etching generally involves the use ion (from reactive plasma) bombardments on the material to cause etching on the surface exposed. The reaction takes place in a vacuum. They are very useful in device fabrication especially for materials who are highly resistant to wet etching techniques such as GaN for instance. They also offer anisotropic etching which is sometimes desirable [5]. The two used dry etching techniques within the scope of the research are Reactive Ion Etch (RIE) and Inductively Coupled Plasma Reactive Ion Etching (ICPRIE). These are discussed below

3.2.5 Reactive Ion Etch (RIE)

As the name implies, RIE uses the reaction of various gases together with the electromagnetic field to produce a plasma. The plasma is generated by an RF generator across two parallel electrodes. Reactive gases are input via the gas inlet and when the RF power exceeds the gas breakdown potential, the gas particles are stripped of their electrons forming ions (hence plasma). The electrons landing on the substrate plate create a negative bias, as the plate is electrically isolated. Meanwhile the chamber walls are grounded. This leads to a bias between the relatively positive plasma and negatively charged plate. The positively charged plasma ions are accelerated downward vertically by the created electric potential, onto the sample holder stage [6]. These reactive ions attack the surface of the sample to be etched by adsorbing and bombarding the surface, hence etching. Different materials have different resistance to these ions therefore different selectivity (generally metals such as Ni have lower etch rates than dielectrics and polymers). Hence, certain materials can be used as patterned masks. An example

of RIE etching process is the etching of dielectrics SiO_2/SiN_x, gases used are CHF_3 and O_2 at flow rates 35 and 5 sccm respectively, RF power of 50W etch rates are about 45nm/min. The RF power is directly proportional to the etch rate. Figure 3.4 below shows the schematic representation of the process together with the JLS Design Plasma Technology RIE system used

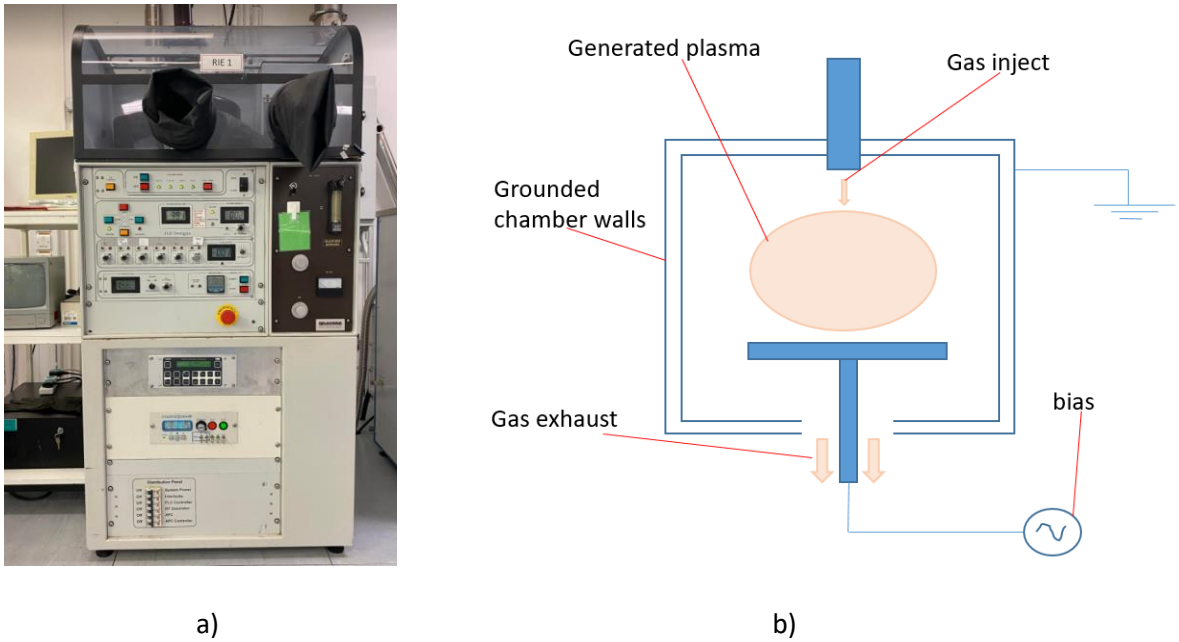

Figure 3.4 Reactive ion etch a) JLS Design Plasma Technology RIE system b) RIE process illustration

3.2.6 Inductively Coupled Plasma Reactive Ion Etching (ICPRIE)

The ICPRIE is an improved technique to the RIE described above. Here, a separate RF connected coil is wrapped around the process chamber for plasma generation. By the process of electromagnetic induction, a strong varying magnetic field is produced within the chamber by varying the electric current flowing through the coil. This leads RF power plasma generation controllability hence, high density plasma can be achieved [1]. A separate RF power is connected to the sample plate, which controls the ions energy and directionality. Therefore, high plasma density at lower operating pressure can be achieved leading higher etch rates and less isotropy (more directionality) compared to RIE. ICP was used to mainly dry etch GaN. The gases used where Cl_2 and Ar at gas flow rates of 45 and 12 sccm respectively, RF power of 50W yield etch rate of about 140nm/min. Figure 3.5 shows a schematic the Oxford Instruments Plasmalab System 100 ICPRIE system used together with an illustration of the process.

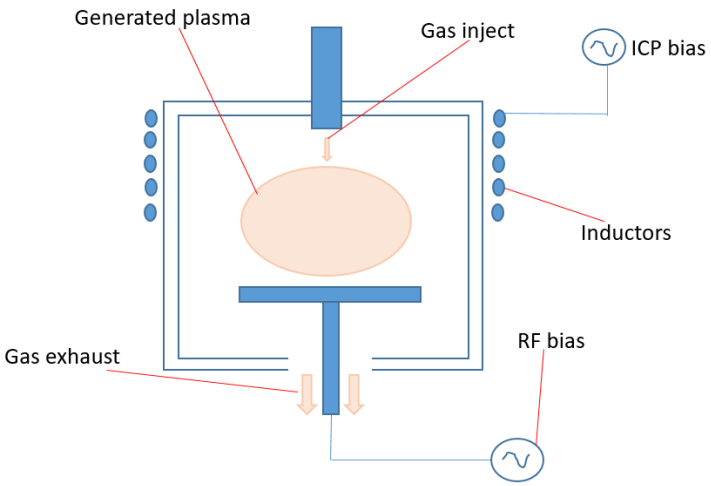

a) b)

Figure 3.5 Inductively coupled plasma reactive ion etch a) Oxford Instruments Plasmalab System 100 ICPRIE system b) ICPRIE process illustration

3.2.7 Plasma Enhanced Vapour Deposition (PECVD)

PECVD refers to a chemical vapour deposition technique used for the deposition of various materials including dielectrics under vacuum. These dielectrics served as hard masking materials and as Distributed Bragg Reflector (DBR) layers within the research. Precursor gases are input into the chamber via the gas inlet and set between the RF generator electrodes and the sample plate. They are injected at specific flow rates for a given time. RF power is used to generate plasma which then encourages the chemical reaction [1]. The reaction takes place in a vacuum, and the sample stage is set to high temperatures of 300^{o}C relative to the chamber walls 60^{o}C. The high sample plate temperatures serve as catalyst to ions decomposition and reaction on the plate, the low walls temperature has an opposing effect on the wall, hence, maximising deposition on the plate. Contrary to RIE, the sample plate is grounded hence limiting ion bombardment. The result is the deposition of homogenous solid coating on the sample from gas reactants. Table 3.1 below shows the parameters for SiN_x and SiO_2 PECVD deposition

Deposited layer	Gas reactants	Deposition rates
SiO_2	SiH_4, N_2O, N_2	40nm/min
SiN_x	SiH_4, NH_3, N_2	10nm/min

Table 3.1 SiN_x and SiO_2 PECVD deposition parameters

The deposited layers optical thicknesses can be measured using ellipsometry. Figure 3.6 below shows the Plasma-Therm 790 series PECVD setup used

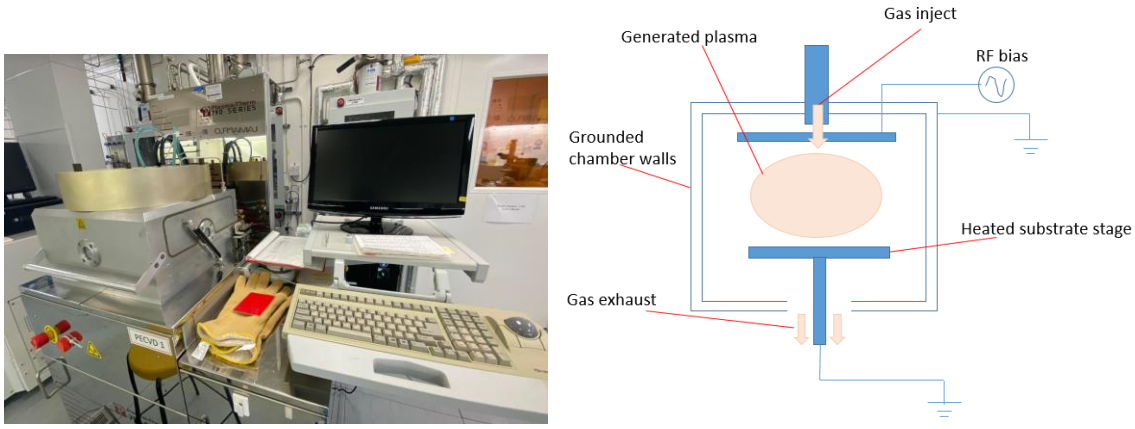

a) b)

Figure 3.6 Plasma enhanced chemical vapour deposition a) Plasma-Therm 790 series PECVD setup b) PECVD process illustration

3.2.8 Anaerobic glove box

Organic polymers and quantum dots are subject to degradation when exposed to moisture and oxygen atmospheric levels. This causes permanent quenching of their emissions, this phenomenon is known as photo-bleaching [7]. For this reason, their processing needs to be done inside a moisture and oxygen free environment therefore, the need of an anaerobic glove box. In the anaerobic glove box, oxygen and moisture levels can be kept below 0.5ppm concentrations. A KOREA KIYON glovebox system shown in Figure 3.7 below was used. The system is equipped with a blower, which ensures gas circulation through the solvent trap and purifier trap connected in series. The solvent trap is filled with material, which allows efficient removal of solvents from the glovebox, and the purifier trap ensures removal of the oxygen and moisture from the gas [8]. So the glovebox gas is permanently circulating through the solvent trap and purifier trap before been fed back into the chamber, this ensure stable values of relatively pure inert gas nitrogen. Regular nitrogen purging is also required to ensure effective pure inert glovebox condition.

Figure 3.7 KOREA KIYON glovebox system

3.2.9 Transfer printing

Transfer printing allows deterministic assembly of material layers by collection from their original substrates, transfer and printing on new substrates [9] [10] [11]. An illustration of the process is shown in Figure 3.8 below.

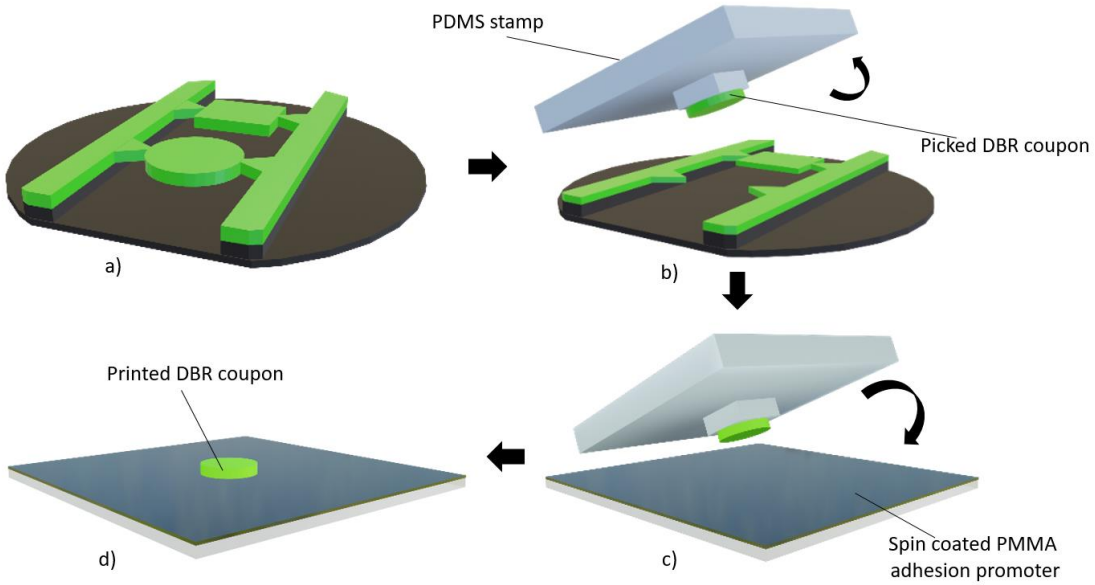

Figure 3.8 Transfer printing procedure of DBR coupon on glass substrate a) undercut DBR coupon sample b) DBR coupon picked by PDMS stamp c) DBR coupon printing d) DBR coupon transfer printed on new glass substrate

Therefore, at least a two stage setup was required, one stage to hold the sample (sample to be transferred and/or the receiving substrate) and on top of it, the stage to hold the PDMS stamp. Figure 3.9 below shows an annotated image of the transfer printing system used. As detailed in chapter 2, the viscoelastic properties of the PDMS stamps allow their adhesion to be velocity controllable. Characteristic high and low speeds in the z direction (normal to the sample surface) are required to perform the transfer printing. The systems vertical stage is responsible for this. The vertical stage consists of a direct drive linear motor with a nitrogen gas piston. The purpose of the gas piston is to reduce the load (from the heavy stage components) on the motor, this can be important in maintaining the vertical stage suspended at a particular vertical position and in providing a higher retraction force (speed). The vertical motor is connected to the ensemble motion controller from Aerotech via an encoder. This motion controller has characteristics resolution 2nm, repeatability +-75nm, accuracy of +-300nm, maximum speed of 200mm/s and maximum acceleration of 1g. The motion controller can be controlled manually via the software; ensemble motion composer and by programming using Aerobasic code. High accuracy, precision and high resolutions are needed especially for micro devices transfer printing. The PDMS stamp can be mounted on the vertical stage by sticking the stamp to a 2x3 inches glass slide. The glass slide is then held in upside down position by a vacuum chuck connected to a vacuum line.

The system also consists of an XY sample stage and a tilt stage. A vacuum chuck is mounted on top of the stages and is connected to a vacuum line; this provides the opposing force to the transfer printing retraction force therefore, holding the substrate to which the sample to be transfer printed is attached fixed while the sample is pulled upwards.

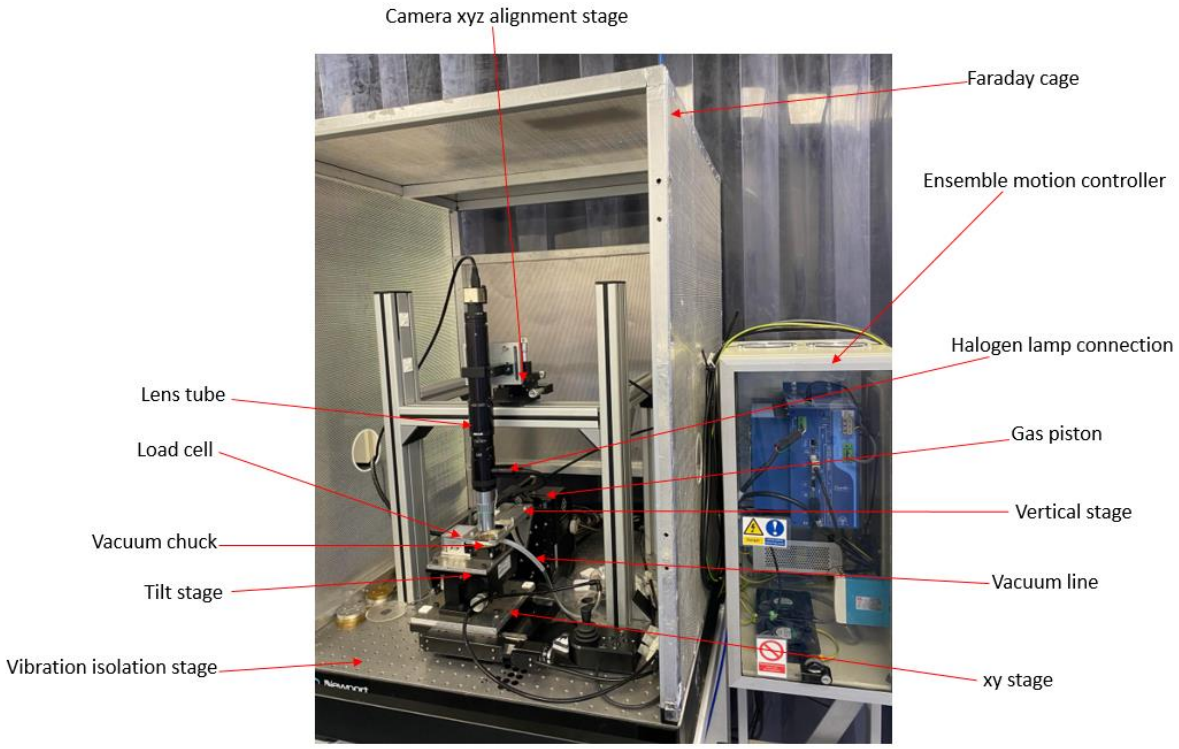

Figure 3.9 Transfer printing setup system

Visualisation of the process was also necessary to ensure good pedestal to coupon alignment, pedestal-coupon contact for successful pick up and good picked coupon to receiving substrate to ensure successful printing. Therefore, the need of a microscope setup. The set up consisted of a halogen lamp source for illumination connected to the lens tube through a 50x50-beam splitter for splitting and channelling light on both the sample and the camera. The lens tube consisted of a 12x zoom magnification, navitar tube together with a 20x magnification objective lens. The total tube magnification is dependent on the objective magnification, the zoom magnification, the lens tube magnification and the camera sensor. The magnification allowed visualisation in the micron scale as required for our device sizes. The lens tube could also be displaced in the xyz directions for alignment and focusing thanks to the camera xyz-alignment stage.

The system also consists of a load cell, which can be used to measure specific transfer print parameters such as adhesion force. The load cell has characteristics hysteresis 0.05%, accuracy +-0.005g, capacity 10g and safe overload of 150%. The whole setup was held on a vibration isolation table and enclosed in a Faraday cage for vibration isolation and electromagnetic filter respectively. The system was also powered through a UPS to filter any noise from the mains.

3.3 Characterisation techniques

3.3.1 Confocal photoluminescence

Photoluminescence (PL) is one of the most commonly used characterisation techniques for optical devices. It involves the use of an external light source (typically a laser) with appropriate emission energy (greater than or equal to the material's band gap) to excite and promote electrons in an optical material to the conduction band. Subsequent carriers' recombination leads to luminescence at energy equal to the carrier transition. This way, selective excitation is possible, as only the material with smaller band gap energy will absorb the excitation source. A good example is the InGaN/GaN QW system, a 375nm laser source will be absorbed by the InGaN well (460nm emission wavelength) but not the GaN barrier (365nm emission wavelength) as it has higher band gap energy hence transparent to the laser. This is illustrated in Figure 3.10. The technique is powerful as it helps obtain information about the material's band gap energy, alloy composition, and stress [12]. In addition, PL characterisation is relatively quicker compared to the electrical counterpart as PN junction and additional fabrication steps can be avoided.

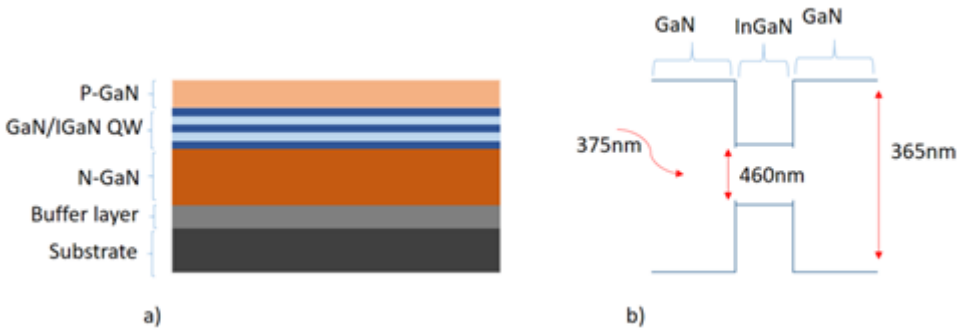

Figure 3.10 InGaN/GaN multi quantum well (MQW) a) structure of the MQW device b) energy level diagram of the MQW showing selective excitation using 375nm laser

Confocal PL is a type of PL where only part of the emission, that is the one focus on a pinhole is collected and measured [13]. This allows single point excitation (360nm) and spatial resolution collection thanks to the 10um pinhole. Therefore, a rejection of out of plane signals leading to better image contrast. A schematic representation and actual image of the confocal PL system used in this study is shown in Figure 3.11 below. The system consists of a XYZ piezoelectric scan stage having sub-nanometre precision with ranges 100x100um laterally and 20um axially. Beneath the scan-stage is a coarse alignment stage with XY range of 20mm. A

375nm stradus laser diode (from Vortran Laser Technologies) excitation source whose emission is coupled to a single optical fibre and channelled to the optics. The laser is then passed through a shutter, onto a 100x magnification 0.95 numerical aperture (NA) objective which focuses the source on the sample. The emitted light from the sample is collected by the same 100x objective, filtered (to remove any laser light trace), and channelled to the monochromator via a 10um diameter multi-mode PhC optical fibre. The optical fibre here acts as collection pinhole as any light not focused to it will be ignored. Therefore, good alignment for maximising collection is important. The 300mm Princeton Instruments SpectraPro 300i Czerny-Turner spectrometer serves in dispersing the collected light, which is then detected by the DU9770N-UVB-353 CCD array (from Andor Newton) cooled at -60°C to keep dark current generation at minimum

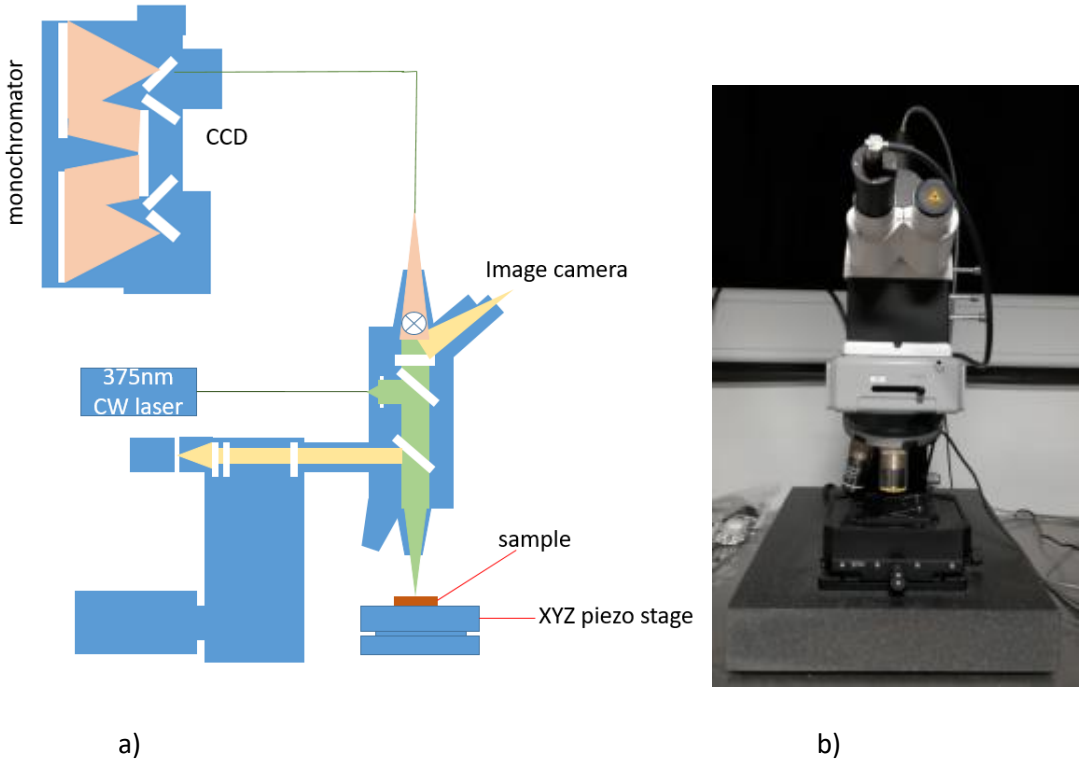

Figure 3.11 confocal photoluminescence a) schematic illustration of the system b) diagram of actual set up

The system spatial resolution that is, the Full Width at Half Maximum (FWHM) and mean wavelength (λ') can be calculated using equations 3.2 and 3.3 below. It can clearly be seen that the system's spatial resolution depends a lot on the excitation and emission wavelengths. The available Witec software allow mapping of the PL spectrum over the calculated resolution.

$$FWHM_{spatial} = 0.37 . \frac{\lambda'}{NA} \qquad (3.2)$$

$$\lambda' = \sqrt{2} . \frac{\lambda_{excit} \cdot \lambda_{emiss}}{\sqrt{\lambda_{excit}^2 + \lambda_{emiss}^2}} \qquad (3.3)$$

For a GaN based LED emitting at 450nm, λ' can be calculated to be approximately 407.41nm and $FWHM_{spatial}$ 158.68nm

3.3.2 Micro photoluminescence (uPL)

A schematic of the uPL system is shown in Figure 3.12 below. The system offers both continuous wave (CW) laser and pulsed waved laser excitation hence, an extra feature compared to the confocal PL above. This is thanks to the 375 nm laser diodes (CW and pulsed laser diodes) connected to the system, selection of the laser to be used is done using the flip mirror positioning.

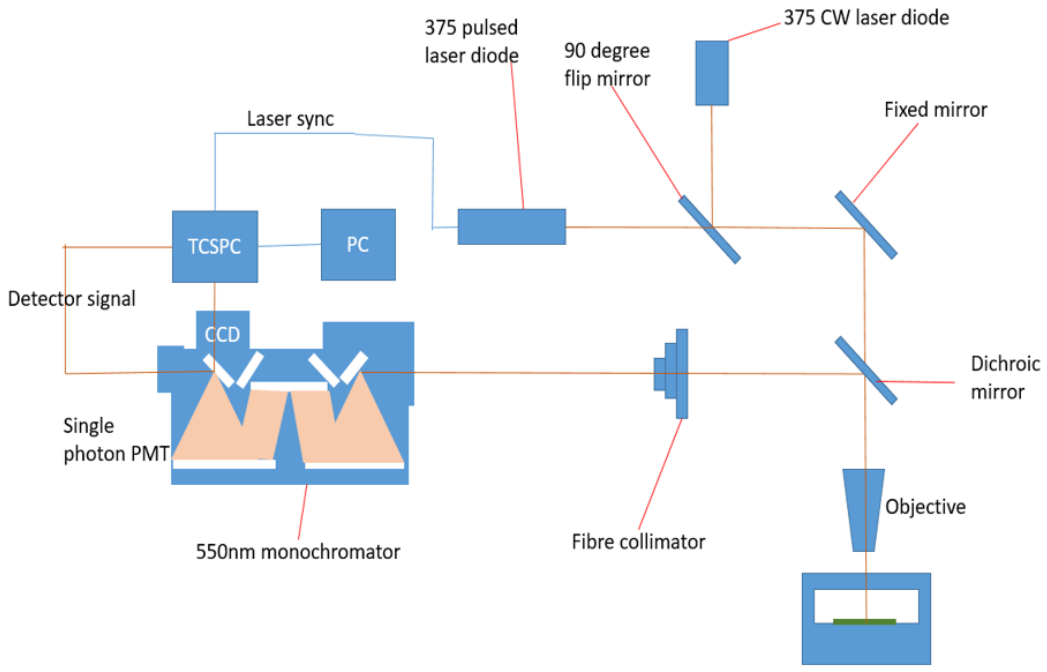

Figure 3.12 Schematic illustration of micro photoluminescence system and Time Resolved PL

The laser beam is then passed through an absorptive filter. This allows attenuation of the laser power hence allowing power dependent measurements. The CW laser power can also be varied directly from the laser itself up to powers of 60mW. The pulsed laser has properties; pulse width 50ps and average power 1mW. Upon reaching beam splitter 1, the laser beam is reflected on to the sample through the objective lens. The beam splitter has up to 99% reflectivity for

wavelengths less than 412nm. The objective lens has properties magnification 50x and numerical aperture (NA) 0.42, this is high magnification leading to a small spot size on the sample. The spot size can be calculated using equation 3.4 below, this gives a spot size diameter of 1um.

$$d_{spot} = 1.22 \ . \ \left(\frac{\lambda_{excit}}{NA}\right) \qquad (3.4)$$

Measurements can be done at varying sample temperatures thanks to the cryostat ST500 from Janis microscopy serving as stage on which the sample is mounted. Here liquid nitrogen can be used to vary temperatures from 77K to 300K. The cryostat also isolates the sample from unwanted vibrations, which can be detrimental especially at such nm scale distances. The sample can be moved by micron distances using the X-Y-Z positioner. The sample emission is collected by the 50X magnification lens and reach the beam splitter 2 (50 by 50 beam splitter) where half of the beam goes to the CCD for imaging and the other half to the 0.55m IHR 550mm spectrometer. The CCD for imaging allows real time visualisation of the sample on its stage, this is important in localising the laser spot. The spectrometer disperses the light, which is then detected by another CCD TE cooled at -70^{o}C.

3.3.3 Time Resolved Photoluminescence (TRPL)

Time resolved PL refers to a characterisation type where the excitonic decay dynamics of an emitter can be measured. This consists of the spontaneous recombination emission decay times and depends on the radiative recombination, non-radiative recombination process and the environment [14]. The non-radiative component can be considered negligible when the measured samples are frozen to temperatures of about 6.5K as the non-radiative recombination mechanisms drastically reduces [15]. The decay is usually measured after a short pulse excitation.

The system within the department is a time correlated single photon counting system (TCSPC). The system involves periodic excitation of the sample using a pulsed 375nm laser diode with properties pulse width 83ps, average power of 0.1W and repetition rate of 10MHz. This is followed by measurement of the sample emission; this is done using a hybrid photomultiplier (PMT) detector from Becker & Hickl. The Hybrid PMT has a response of about 120 ps. Ideally, the detector will measure 0 or 1 photons per excitation therefore, for full decay measurement with low signal to noise ratio, millions to billions of excitations are done. The pulsed laser diode is synchronised to the PMT detector via a TCSPC card having FWHM 6.5ps. The

Instrument Response Function (IRF) whose width gives an indication of the timing resolution is given by equation 3.5 below. As it can be seen from equation 3.5 below, the IRF is dependent on the laser, detector and TCSPC FWHM. This gives an IRF of about 150ps.

$$IRF = \sqrt{FWHM_{Laser}^2 + FWHM_{Detector}^2 + FWHM_{TCSPC}^2} \qquad (3.5)$$

The measured decay plot consists of both the emitter decay and the IRF therefore, the IRF need to be considered. Deconvolution of the plot is needed to obtain the real decay curve and this is done using FluoFit software from PicoQuant. Within the software, the decay can be fitted with a sum of exponential decay plots; commonly a bi-exponential is used as shown in equation 3.6 below

$$I(t) = A_1 e^{-\frac{t}{\tau_1}} + A_2 e^{-\frac{t}{\tau_2}} \qquad (3.6)$$

Where A_1 and A_2 are the fast and slow decays respectively, τ_1 and τ_2 are the fast and slow time constants respectively

3.3.4 Electroluminescence (EL) and reflectivity measurement

EL refers to an optical characterisation technique, which involves measurement of optical radiation from a sample upon electrical excitation. During EL, electric charges are injected into the material via electrodes. A good example is the EL of LED (P-N junction). Connecting the LED in a forward bias (that is P connected to the anode and N connected to the cathode) allow electrons and holes to be injected from the cathode and anode respectively. When the applied electric potential is greater than the threshold voltage, carriers are allowed to move across. Recombination of the carriers in the active region leads to radiation hence, electroluminescence. Figure 3.13 below shows a schematic representation of the EL setup.

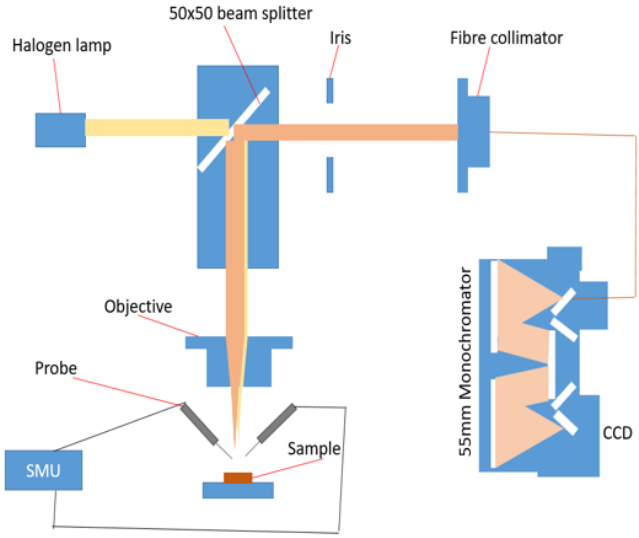

Figure 3.13 Illustration of the electroluminescence setup

The setup consists of a motorised XY stage on which the sample can be mounted and aligned to the optical axis. A probe station is also available for probing. This consists of two tungsten probe tips (600nm tip dimensions) to serve as anode and cathode. They can be moved at micron scale, a Keithley 2400 source meter unit for setting and measuring current and voltages and a digital camera (XIMEA xiQ global shutter CMOS colour video camera, having a 12x UltraZoom Navitar lens tube) mounted on top of the sample for visuals of the probing. Emitted light from the sample is collected by an objective lens with properties NA 0.42 and magnification 50x. The working distance of the objective to the sample is about 20.5mm. The collected light is passed through a 5050 beam splitter and then focussed onto the fibre collimator. The light is then channelled via a multimode optic fibre with diameter 400um and NA 0.22 to the shamrock 500i Czerny-Turner monochromator and CCD from Andor Newton for dispersing the light and measurement of the spectrum.

The same system set up is used to perform reflectivity measurements. This is done using a halogen broadband lamp source focused on the sample using the same optics as described above (beam splitter and objective). The reflected light is also channelled to the monochromator and CCD using the same path as during the electroluminescence. Figure 3.13 above shows a schematic representation of the system.

3.3.5 Scanning Electron Microscopy (SEM)

SEM refers to a very powerful microscopy technique offering high resolution and magnification visualisation of materials. Here, electrons are used for the imaging of the small features. Figure 3.14 below shows a schematic representation of the system. Electrons fired from an electron gun are accelerated and focused on the sample thanks to the action of condenser lenses, the deflection coils and final lens. This leads to a small electron beam spot (between 0.4nm to 5nm) which scans across the sample in a raster way [16]. Upon incidence with the material to be imaged atoms, various events can occur [17]; electrons getting reflected back, electromagnetic radiation emission, scattering which can be inelastic or elastic resulting to secondary electrons and backscattered electrons emission respectively. Secondary electrons are ejected from the conduction or valence band of the sample's atoms and have relatively low energies of <50eV (few nm from the sample surface) [18] detected by the secondary electron detector. Detection is done by accelerating the secondary electrons onto a scintillator to emit flashes. These flashes are converted to amplified electrical signals thanks to the photomultiplier, allowing the production of a 2D intensity distribution digital image (upon analog-digital conversion). The intensity of secondary electrons reaching the detector is dependent on the incidence beam angle on the sample surface where the steeper the surface the brighter the image hence, providing 3D imaging. Backscattered electrons are instead higher energy electrons and are detected by a special backscattered electron detector. Backscattered electrons can be used to provide compositional contrast of the imaged sample thanks to the difference in backscattered electrons atomic number detected at the detector (higher atomic number ones appear brighter than low atomic number one) [16] [18]. SEM of non-conducting samples will lead to accumulation of the charges on the sample's surface leading to poor imaging. For this reason, conducting samples yield better images. The SEM is a critical tool in the monitoring of nano and micro scale devices and features.

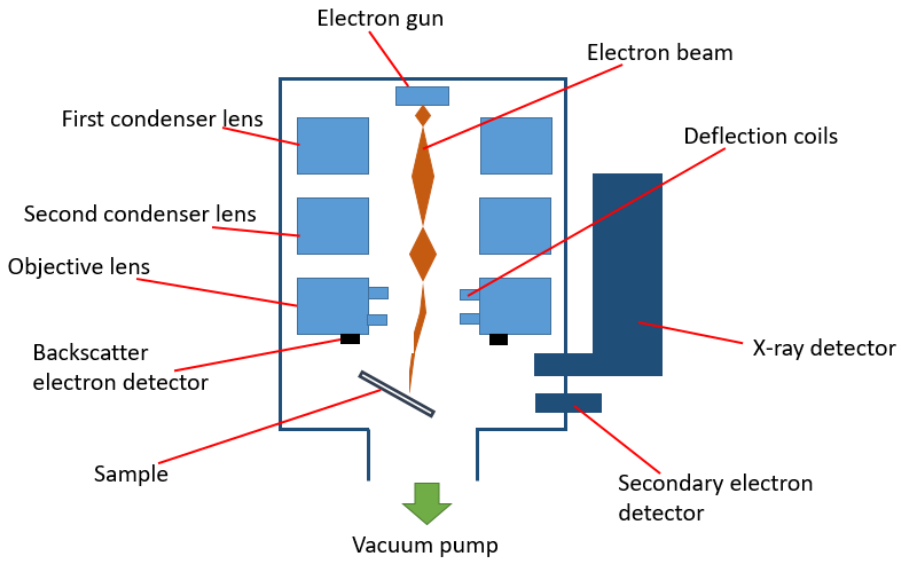

Figure 3.14 schematic illustration of the scanning electron microscope

3.3.6 Profilometry

Profilometry refers to a characterisation technique used for the measurement of a surface profile, this include information about surface roughness, step height and surface flatness [19]. Two main types exist contact and non-contact profilometry. Non-contact methods are usually optical by nature. Contact profilometry involves the use of a diamond stylus in contact with the surface to carry out measurements. The stylus is lowered vertically on the surface to be measured and then moved horizontally with a specific force, velocity and distance. As the stylus moves across the surface, it is caused to move in vertical directions due to the sample roughness. The vibration movements are then converted to an analog then digital electrical signal, which can then be displayed as height-position plot on the computer. The measurement resolution is dependent on the set scan speed and sampling rate of the data during analog to digital conversion. Typical diamond stylus has a tip radius of ranging from 10nm to 1mm [19]. The Veeco Dektak 150 profiler shown in Figure 3.15 below was used during this research for average step height (ASH) measurements.

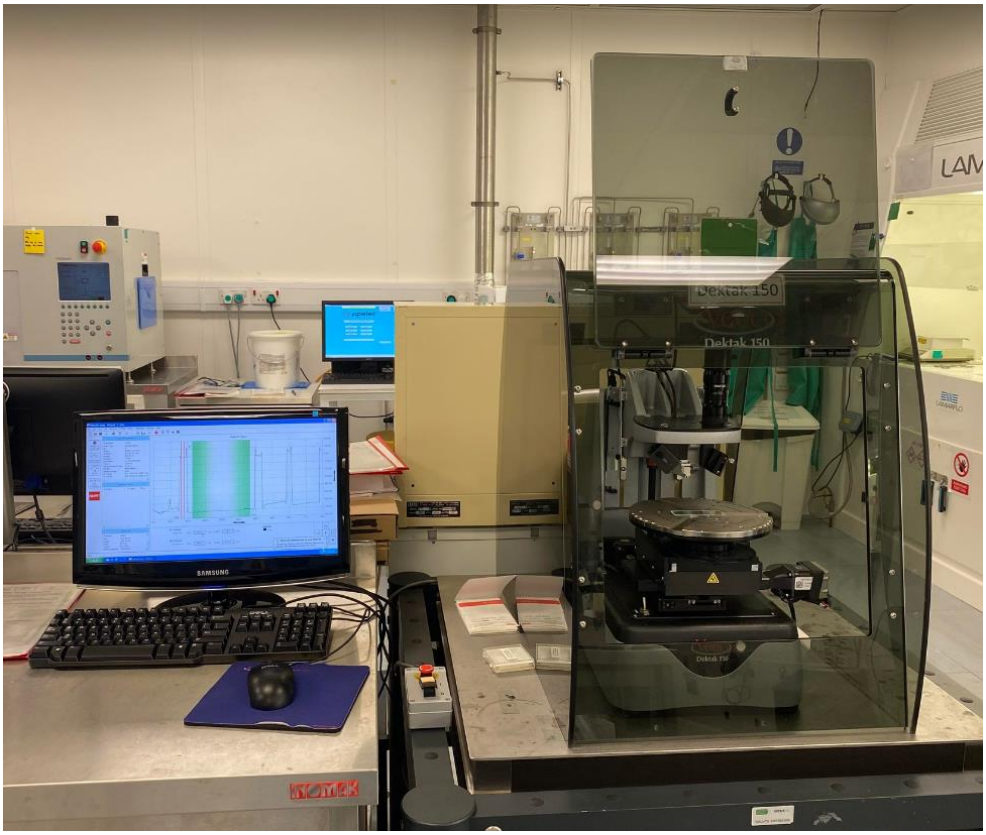

Figure 3.15 Veeco Dektak 150 profiler

3.3.7 Ellipsometry

Ellipsometry refers to a technique that measures the change in polarisation of light as it is reflected or transmitted through a thin film for determination of the thin film properties [20]. Ellipsometry is commonly used for determining thin films optical constant (refractive index and extinction coefficient) and thickness. Other properties that can be measured using ellipsometry include; material composition, roughness, crystallinity and more. Figure 3.16 present an illustration of the ellipsometer configuration.

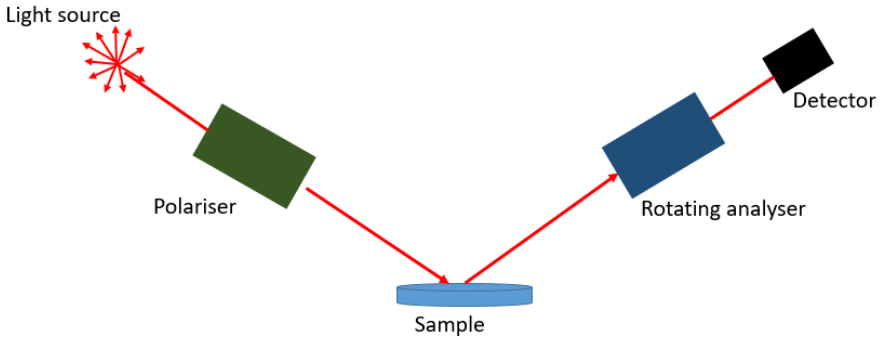

Figure 3.16 diagrammatic illustration of ellipsometer

Unpolarised light is produced by the light source, this light is then polarised by the help of the polariser (oriented to allow both the p and s components to be transmitted). The transmitted light incident on the sample and undergoes both reflection and refraction. The reflected light is collected by the analyser and detected by the detector for conversion into electrical signal. The measured signal (reflected) is then compared to the original signal (incident) and the change in polarisation extracted as defined in equation 3.7. This change in polarisation (ρ) is measured and plotted in terms of two parameters over a range of wavelength; polarisation amplitude (Ψ) and phase change (Δ).

$$\rho = \tan(\Psi)e^{i\Delta} \qquad (3.7)$$

In order to obtain the properties of interest, a model describing the sample needs to be built and simulated to produce the expected response using Fresnel's equations [20], this is done using known or estimated values. The resulting response is compared with the experimental response to achieve the best fit possible, variation of the unknown material's properties followed by subsequent simulations are usually done. The Mean Square Error (MSE) value quantifies the responses differences where the smaller its value, the closer the fit. Film thickness is measured thanks to the reflected and transmitted light interference therefore; the material needs to be transparent at the measured wavelengths. It should be noted that the thickness and optical constant measurements are not independent of each other and therefore must be measured simultaneously for best results

3.4 References

[1] S. A. Campbell, "The science and engineering of microelectronic fabrication," *Choice Rev. Online*, vol. 34, no. 04, pp. 34-2177-34–2177, 1996.

[2] J. J. Toriz-Garcia *et al.*, "Controlled-width track in through silicon via using 3D holographic photolithography with modified electrodepositable photoresist," *J. Micromechanics Microengineering*, vol. 20, no. 1, p. 015012, Nov. 2009.

[3] T. Ogi, L. B. Modesto-Lopez, F. Iskandar, and K. Okuyama, "Fabrication of a large area monolayer of silica particles on a sapphire substrate by a spin coating method," *Colloids Surfaces A Physicochem. Eng. Asp.*, vol. 297, no. 1–3, pp. 71–78, Apr. 2007.

[4] Y. Zhang, J. R. G. Evans, and S. Yang, "Corrected values for boiling points and enthalpies of vaporization of elements in handbooks," *J. Chem. Eng. Data*, vol. 56, no. 2, pp. 328–337, Feb. 2011.

[5] I. Adesida, C. Youtsey, A. T. Ping, F. Khan, L. T. Romano, and G. Bulman, "Dry and wet etching for group III - nitrides," *Mater. Res. Soc. Symp. - Proc.*, vol. 537, 1999.

[6] G. S. May and S. M. Sze, "Fundamentals of Semiconductor Fabrication." Wiley, 2004.

[7] J. S. Lewis and M. S. Weaver, "Thin-Film Permeation-Barrier Technology for Flexible Organic Light-Emitting Devices," *IEEE J. Sel. Top. Quantum Electron.*, vol. 10, no. 1, pp. 45–57, Jan.

2004.

[8] “Kiyon UK - Gloveboxe Purification Systems.” [Online]. Available https//kiyon.co.uk/products/gloveboxes/standard-range/3-port-double-sided/. [Accessed 25-Oct-2022].

[9] M. A. Meitl *et al.*, “Transfer printing by kinetic control of adhesion to an elastomeric stamp,” *Nat. Mater.*, vol. 5, no. 1, pp. 33–38, 2006.

[10] H. S. Kim *et al.*, “Unusual strategies for using Indium Gallium Nitride grown on Silicon (111) for solid-state lighting,” *Proc. Natl. Acad. Sci. U. S. A.*, vol. 108, no. 25, pp. 10072–10077, Jun. 2011.

[11] B. Corbett, R. Loi, W. Zhou, D. Liu, and Z. Ma, “Transfer print techniques for heterogeneous integration of photonic components,” *Prog. Quantum Electron.*, vol. 52, pp. 1–17, Mar. 2017.

[12] S. Perkowitz, “Optical Characterization of Semiconductors Infrared, Raman, and Photoluminescence Spectroscopy,” in *Techniques of Physics*, Academic Press, 1993, pp. 201–205.

[13] “Olympus FluoView Resource Center Introduction to Confocal Microscopy.” [Online]. Available http//www.olympusconfocal.com/theory/confocalintro.html. [Accessed 25-Oct-2022].

[14] E. V. Peán, S. Dimitrov, C. S. De Castro, and M. L. Davies, “Interpreting time-resolved photoluminescence of perovskite materials,” *Phys. Chem. Chem. Phys.*, vol. 22, no. 48, pp. 28345–28358, Dec. 2020.

[15] W.-R. Zhao *et al.*, “Temperature Dependence of Emission Properties of Self-Assembled InGaN Quantum Dots,” *Chinese Phys. Lett.*, vol. 31, no. 11, p. 114205, Nov. 2014.

[16] K. C. A. Smith and C. W. Oatley, “The scanning electron microscope and its fields of application,” *Br. J. Appl. Phys.*, vol. 6, no. 11, p. 391, Nov. 1955.

[17] E. Suzuki, “High-resolution scanning electron microscopy of immunogold-labelled cells by the use of thin plasma coating of osmium,” *J. Microsc.*, vol. 208, no. 3, pp. 153–157, Dec. 2002.

[18] R. F. Egerton, “Physical principles of electron microscopy An introduction to TEM, SEM, and AEM, second edition,” *Phys. Princ. Electron Microsc. An Introd. to TEM, SEM, AEM, Second Ed.*, pp. 1–196, Jan. 2016.

[19] K. J. Stout and L. Blunt, *Three-dimensional surface topography*. Penton Press, 2000.

[20] H. G. Tompkins and J. N. Hilfiker, *Spectroscopic ellipsometry practical application to thin film characterization*, 1st ed. Momentum Press, 2016.

4) Chapter 4 - Development of heterogeneous fabrication approaches for the fabrication of microcavity devices by transfer printing

One of the factors limiting the development of optical microcavity based devices is the limitation offered by the current conventional fabrication that is direct epitaxy and laser liftoff. Despite their numerous advantages, they also have some limitations such as costly process, extreme deposition conditions harmful to some active materials, limited compatible DBR materials within the GaN material series and small reflectivity bandwidth for the available compatible DBR configuration AlGaN/GaN DBRs due to the low refractive index contrast [1], limiting the types of active materials possible. We present a new platform for the heterogeneous integration of active materials of different forms and shape into optical microcavity via deterministic transfer printing. The platform involves the release of grown dielectric DBRs from their original substrate Si by KOH wet etch, followed by their transfer printing as stacks to form optical microcavities. Transfer printed dielectric DBR coupon showing high reflectivity of 99% and large bandwidth of 95nm were demonstrated. Passive microcavity with spacer layer PMMA was also fabricated. The platform showed a DBR coupon yield of almost 100% when optimised. Theoretical COMSOL simulations are also included to support the obtained results. All fabrication and characterisations steps including challenges encountered with their resolutions are presented below.

4.1 Introduction

Light-matter interaction is at the basis of most optoelectronic phenomena like the cavity quantum electrodynamics (QED) phenomena [2] and devices applications such as Resonant Cavity LEDs (RCLEDs) [3][4][5][6][7] and Lasers [8][9][10]. The effective control of such interactions is usually desired and this is achievable thanks to quantum micro-cavity structures [11] [2] [12][13]. These are planar Fabry-Perot based optical cavities having optical lengths comparable to processed light wavelength ($\frac{m\lambda}{2}$) [2][14]. These structures usually employ Distributed Bragg Reflectors (DBRs) as reflectors thanks to their spectrum band selective high reflectivity properties [15]. One of the determining factors affecting the light-matter interaction in microcavities is the cavity's quality factor (Q). The cavity's quality factor is highly dependent on the DBRs and cavity layers scattering, absorption and reflectivity losses [16]. High cavity quality factor is desired for optimal light-matter interaction. Effective integration of active material medium in such cavity in a non-destructive way without adding defects is

usually the limiting factor during their fabrication. Therefore, the mainstream fabrication of such micro-cavities generally involves monolithic integration that is, direct epitaxial growth techniques such as MOCVD and MBE of lattice matched DBRs and the inorganic quantum well active medium. This is because of the benefits they offer such as in situ fabrication and higher DBR conductivity compared to other DBR types. This allows for direct electrical current injection through the DBRs and the minimisation of the Joule's heating effect thanks to effective heat dissipation [17] [18]. However, they also present some drawbacks. First, the epitaxy growth processes are costly and complex with extreme deposition conditions of high temperatures and low pressure, which can be destructive to some classes of active layers emitters such as polymers. Secondly, slight lattice mismatch between DBR and active material will lead to defect propagation hence lowering the cavity's quality factor. Only a few lattice matched DBRs-active layers exist, especially in the GaN series, AlGaN/GaN DBRs and air based DBRs [1]. Finally, the small refractive index contrast existing between the latticed matched DBR configuration (in the exception of air based DBRs) leads to small reflectivity linewidth. This limits the amount of materials that can be incorporated in such cavities as emitter emission and cavity mode overlap is a requirement for resonance. The encountered challenges discussed above when monolithically integrating different active and passive components to form microcavity devices has been one of the major factors limiting their widespread on the market hence, the need for new heterogeneous integration technologies.

Recently developed transfer printing technique provide an effective method for the heterogeneous integration of various optoelectronics systems with potential of high yield and throughput [19] [20] [21] [22]. Various ink releasing techniques from their original substrate has been reported such as laser lift off and epitaxial lift off but they are less controlled processes. Anchor undercutting is another releasing technique, which involves the effective undercutting of the epilayer, leaving a suspended ink attached to the anchoring system; this offers a more controlled release and hence transfer printing [19] [23] [24]. We here by demonstrate a platform for the simple assembly of optical material systems (standard dielectric SiN_x/SiO_2 DBR and emitter) in order to form microcavity devices demonstrating microcavity effects. This platform involves the release of the DBR from their original Si substrate by anchor undercutting and transfer printing as stacks sandwiching the emitting layer. It is important to note that this platform is applicable to various material series and configurations requiring heterogenous integration.

Standard SiN_x/SiO_2 dielectric DBRs were chosen as they mitigate some of the issues mentioned above as they offer a wide range of available compatible material configuration, larger refractive index contrast and less costly growth processes such as sputtering and chemical vapour deposition processes. In addition, their extreme growth conditions will not have any impact on the active material as they are heterogeneously integrated. It should also be mentioned that dielectric DBRs have low conducting and heat dissipation properties due to their dielectric nature, hence additional device processing is required to ensure electrical injection (for example (intra-cavity current spreading layers [1]) and heat sinking (for example cavity lengthening, 3D CMOS heat sinks [25][17]).

4.2 Platform development

DBR mirrors are key components of resonant micro-cavity structures as they offer the required optical confinement. The micro-cavity fabrication platform can be separated into multiple steps PECVD growth of DBR, anchor undercutting of the grown DBR, Transfer printing fabrication of the empty micro-cavity. Below is a detailed description of these steps.

4.2.1 PECVD growth of DBR

As far as the DBR is concerned, micro-cavity design conditions required for strong optical confinement and hence optimal resonance are high reflectivity (close to 100%) and reflectivity band overlap with the emitter emission as discussed in Chapter 2. The peak reflectivity and bandwidth of a DBR is given in section 2.3.2**.** The refractive index contrast and the number of layer pairs are critical for the DBR reflectivity peak and line width.

SiN_x/SiO_2 DBR was used having SiN_x and SiO_2 as high and low refractive index materials respectively. SiN_x and SiO_2 were grown by PECVD and their growth rate and refractive indices needed to be calibrated. This was done by separately PECVD growing them on Si using PECVD (Plasma therm 790 series) followed by ellipsometry measurement of their thicknesses and refractive indices. Gasses used were SiH_4 (160sccm), N_2O (900sccm) and N_2(240sccm) for SiO_2 and SiH_4(160sccm), NH_3(5sccm) and N_2 (900sccm) for SiN_x. The growth conditions were; stage temperature of 300°C, pressure of 900mTorr and RF power of 25W. Five samples of each materials with thicknesses approximately 200nm were used for the calibration. The growth calibration experiments revealed SiN_x and SiO_2 growth rates of ≈ 10nm/mins and 40nm/mins respectively on average. The best-measured ellipsometry refractive index plots of the layers are shown in Figure 4.1.

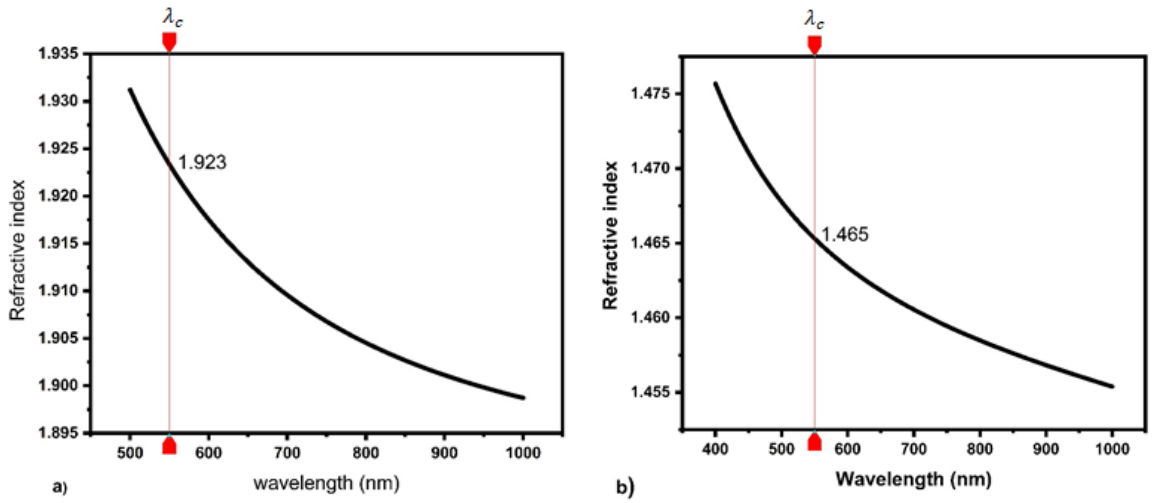

Figure 4.1 Ellipsometry measured refractive index dispersion of dielectrics a) SiN_x b) SiO_2

For a λ_c of 560nm, the SiN_x and SiO_2 refractive index at this wavelength are 1.923 and 1.465 respectively from figure 4.1. $\Delta\lambda$ can be calculated to be ≈ 97.9nm, with N = 12.5 (n_a is air and n_b silicon); a high reflectivity of approximately than 99% can be calculated. Hence, ensuring high reflectivity peak and wide linewidth

$$n_H T_H + n_L T_L = \frac{\lambda_c}{2} \qquad (4.1)$$

Where T_H and T_L are the geometrical thicknesses of high and low refractive index materials respectively

Equation 4.1 depicts the DBR layers thickness condition in order to ensure constructive interference between the multiple layers Fresnel reflections. The sum of alternating pairs optical thickness must be equal to half the Bragg wavelength [26]. As it can be seen, the optical thickness of the grown dielectric layers is critical in determining λ_c (and hence the position of the reflectivity band). DBR layer thicknesses of SiN_x/SiO_2 54/120nm were chosen which satisfy equation 4.1 for λ_c of 560nm. Theoretical simulations were also carried out using the software COMSOL multiphysics wave optics module. A 1D simulation was done; schematic representation of the structure was drawn with stacked materials having constant value thicknesses and refractive indices (fixed value that is refractive index at λ_c of 560nm) from the ellipsometry calibration done above (hence step index structures). Plane wave electrical field power excitation was done at right angles. Figure 4.2 presents the simulated DBR reflectivity spectrum and the measured as grown DBR (fabrication described in section 4.2.2) reflectivity spectrum.

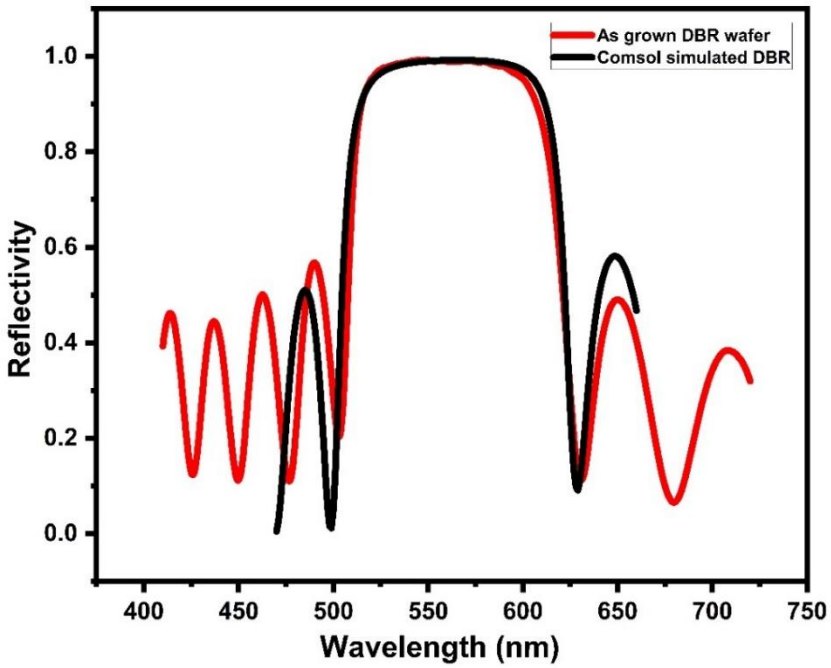

Figure 4.2 Reflectivity spectrum plot of the grown DBR and COMSOL simulation

Peak reflectivity of ≈ 99.9% (reference to standard calibration mirror STAN-SSH-NIST specular reflectance standard from Ocean Sight) can be seen from both curves, which corresponds to the calculated value of 99.9% above. The reflectivity bandwidth of the simulated reflectivity matches perfectly with measured bandwidth of ≈ 98nm (97.9nm calculated above), that of the as grown is also very close with a measured bandwidth of ≈ 95nm. This agrees well with the experimental results validating the calibrations and DBR growth process. The slight difference could be because of non-uniformity in deposited layers characteristics (thickness and refractive index) over the full DBR stack.

4.2.2 Anchor undercutting of the grown DBR

Anchor undercutting involves undercutting the material from its substrate while it remains attached to the wafer via tethers and anchors. This fabrication step can be divided into multiple different stages

- <110> crystallographic orientation direction marks definition on Si (111) wafer
- PECVD growth of the DBR
- DBR patterning as coupons attached to anchors by tethers by metallic masking followed by RIE etch (with anchors aligned parallel to <110> orientation lines)

- DBR coupons undercut by KOH wet etch
- Metallic mask stripping by HCl wet etch

Due to the anisotropic crystallographic KOH wet etch of Si; anchor undercutting can be achieved on materials grown on Si (111). KOH Si etch rate along the <110> direction is more than 100 times greater than along the orthogonal direction [27] [28]. Therefore, proper alignment of the coupons to the <110> direction is important.

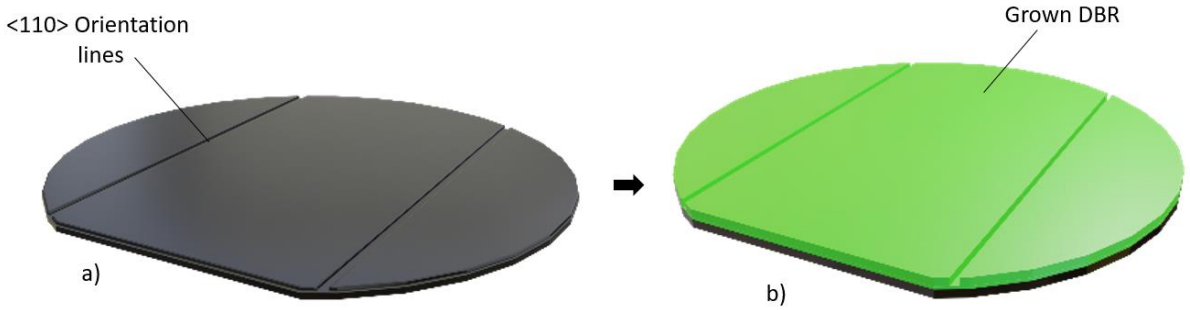

Figure 4.3 a) <110> orientation lines definition by RIE etch b) DBR grown by PECVD

First, the <110> orientation lines had to be created on the Si wafer, this was done via photolithography; three solvent cleaning of the wafer in n-butyl acetate, acetone and isopropyl alcohol. This was followed by dehydration baking of the wafer at 100^{o}C for 1 minute on the hot plate (electronic microsystems). Then, spin coating of positive resist SPR 350 at 4000 rpms for 30s using the spinner, soft baking at 100^{o}C for 1 minute. This was followed by exposure on the Karl Suss MJB3 UV400 mask aligner ($\approx$ 2.51 mW/cm^{-2} power density) for 4s, development in MF26A developer for 60s and finally oxygen plasma ashing (O_2/250sccm 150W 45s) using the asher (PVA Tepla). This yielded a 1.5um thick patterned resist mask. Post photolithography, the patterned masked Si (111) wafer were then submitted to dry RIE etch (CHF_3/O_2 35/5 sccm, RF power of 150W) for 6 minutes, this achieved 15um wide, approximately 150nm deep orientation lines with 8um separation as illustrated in figure 4.3 a). This pattern corresponded to the photo mask used during exposure.

The DBR with required reflectivity peak (99%) and stopband width (97nm) as derived from section 4.2.1 could then be grown. This was done using the PECVD where 12.5 pairs of SiN_x/SiO_2 54/120nm thicknesses were grown with single layer times of 324s and 180s respectively. The resulting grown DBR on patterned Si (111) substrate is shown in figure 4.3 b). SEM cross section image of the grown DBR is shown in figure 4.4 showing the 12.5 alternating dielectric pairs.

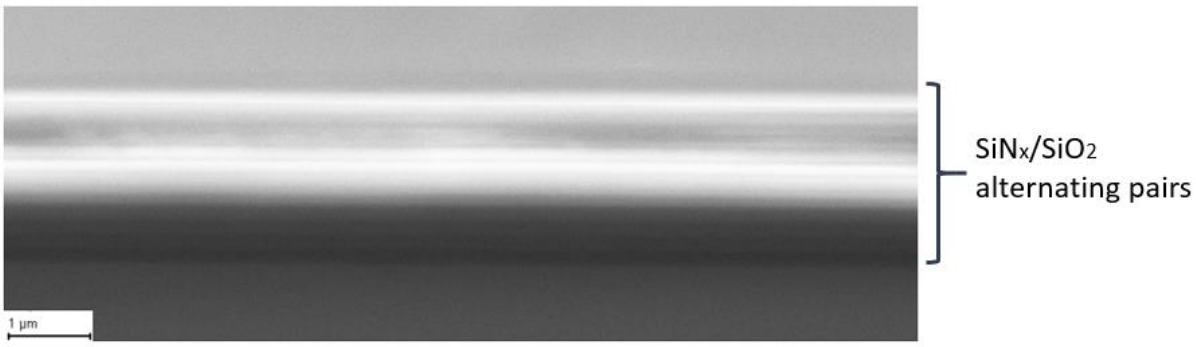

Figure 4.4 Cross-section image of 12.5 pairs SiN_x/SiO_2 dielectric DBR

Photolithography mask required for the patterning of the grown DBR on Si as arrays of coupons attached to anchors by tethers were then designed and fabricated. Different sets of masks were designed with various DBR coupons geometries, sizes and tethers geometries, sizes, numbers and positions. This was done using K-layout software and fabricated by Compugraphics, a mask fabrication company. Figure 4.5 shows an illustration of the main mask patterns used for 100x100um coupon sizes.

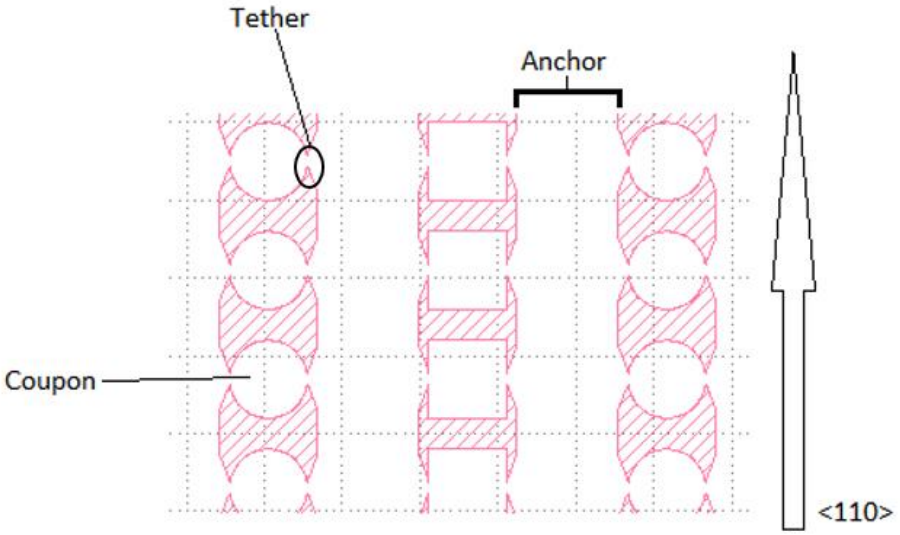

Figure 4.5 Illustration of designed and fabricated mask patterns for 100x100um coupon sizes; shaded areas are etch windows to form DBR coupons of various designs

As it can be seen, the devices coupons are attached to the anchors by tethers and are arranged to allow parallel anchors alignment to the <110> direction (that is , anchors should be aligned parallel to the orientation marks lines made above). This is important in preventing undercutting of the anchors during the undercut of device coupons by immersing in KOH

solution (described later). Using the photolithography mask, the grown DBR could then be patterned into coupons attached to anchors by tethers using a form of masking followed by RIE dry etching.

The first attempt involved the use of PMGI (Polydimethylglutarimide) plus thick resist SPR220 (total thickness of ≈ 4.3um) to serve as dry etch mask for the RIE etching. This was attempted due to convenience of faster processing with fewer steps required. Therefore, in this case, the shaded areas in Figure 4.5 were the exposed surface during photolithography. Photolithography was performed but this time using thick SPR220 resist, care was taken to make sure the anchors are parallel oriented to the <110> orientation line previously made. This yielded an SPR220 mask of thickness ≈ 4.2 um. RIE etching (CHF_3/O_2 35/5 sccm, RF power 150W) calibrations were done to obtain the etch rates of SiN_x/SiO_2 and Si, ≈ 105nm/min and 25nm/min respectively were calculated. The sample was RIE etched for 40 mins; this allowed etching through the full DBR dielectric stack and into the Si substrate to a depth of ≈ 500nm. This was followed by stripping of the any remaining SPR 220 resit by agitating the sample in resist stripper (posistrip EKC830) for 60s followed by oxygen plasma ashing. The final step involved anchor undercutting the grown DBR by submerging the wafers in hot aqueous solution of KOH (25%wt concentration) at 70^{o}C for 50 minutes for 100/100um coupons (so undercut etch rate of ≈ 2um/min). Microscopic images of the resulting sample are shown in Figure 4.6 taken using the optical microscope (Olympus).

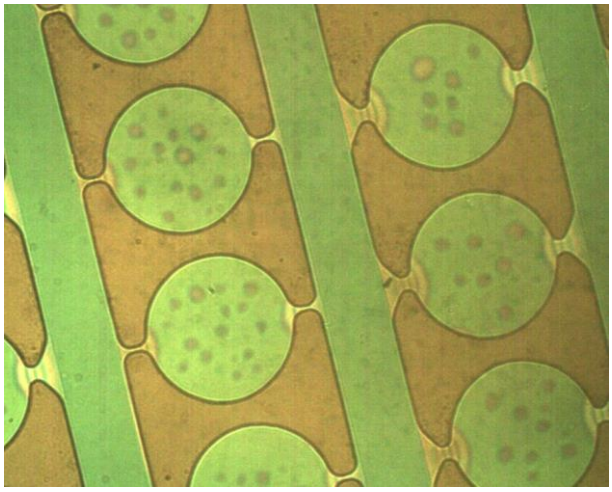

Figure 4.6 Optical microscope image of undercut DBR coupons – sample with PMGI + SPR220 mask, showing damage to the DBR coupon surfaces

Damaged DBR surfaces can be seen from the microscopic images with clear pinholes. This result pointed to the fact that the PMGI+SPR220 masking was not successful at protecting the

underlying DBR from reactive ion bombardment RF generated plasma RIE dry etching process and the KOH wet etch attack on the DBR layers. Therefore, better masking was required

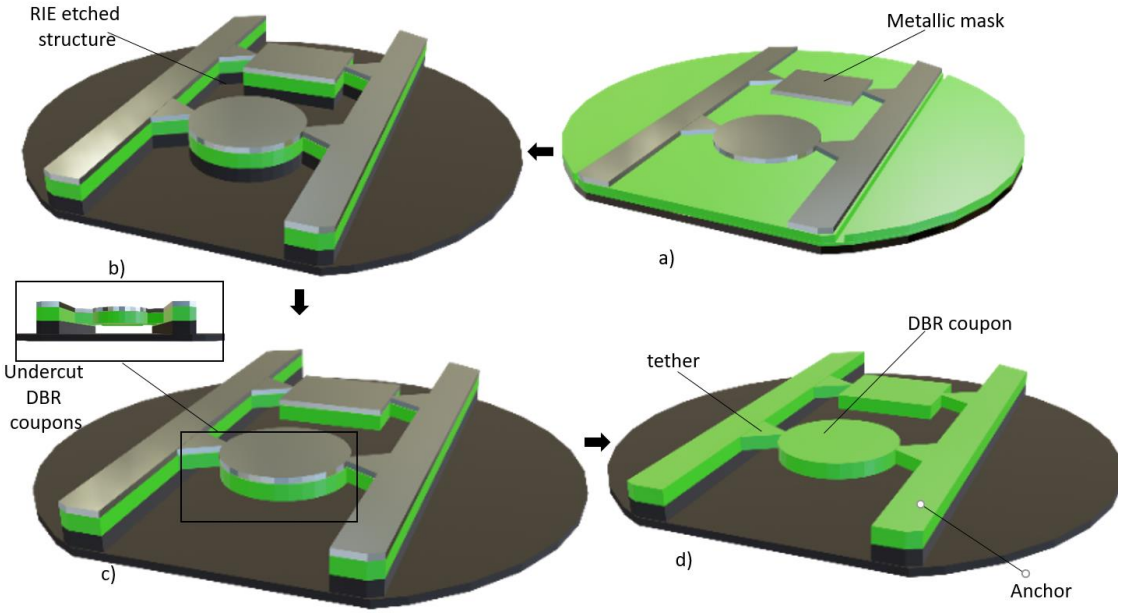

Figure 4.7 DBR anchor undercutting process a) Ti/Ni metallic masking by thermal evaporation b) RIE etch of DBR into coupons patterns c) DBR coupon undercut by KOW wet etch d) metallic mask stripping by HCl wet etch

Metallic masking was the obvious choice. This involved lithography patterning as described above but this time using polydimethylglutarimide (PMGI) resist spun at 4000 rpms for 30s followed by soft baking at 180^{o}C for 7 minutes. The PMGI acts as a lift off release layer and undercuts during the resist development. SPR350 resist was then deposited as described above. In addition, it should be noted that the mask polarity in figure 4.5 was then reversed, that is the non-shaded area was now the exposed area (resist area to be removed post development). After exposure, development and ashing, deposition of the metallic mask could then be performed. Thermal evaporation of metals Ti/Ni with thicknesses 50/200nm respectively was done followed with lift off by submerging and agitating the sample in resist stripper (posistrip EKC830) for 60s and ashing for 2 mins. This revealed metallic mask pattern covering the coupons, tethers and anchors areas of the DBR as shown in Figure 4.7 a). Ti serves as adhesion layer to Ni and both served as hard mask for the next steps RIE etching and KOH undercut etch. RIE etching (CHF3/O2 35/5sccm 150W) the sample for 40 mins allowed etching through the full DBR dielectric stack and into the Si substrate to a depth of ≈ 500nm as above. Figure 4.7 b) shows a representation of this stage of the process. Anchor undercutting was then performed as above, illustrated in figure 4.7 c). Finally, the metallic mask needed to be removed

and this was done by submerging the sample in hot aqueous solution of HCl (7% volume concentration) for ≈ 20 minutes at 70ºC, shown in figure 4.7 d). The resulting sample shown in figure 4.8 a) (made with different mask showing the different tether designs) shows better quality DBR proving the high resistant masking abilities of the Ti/Ni metallic mask compared to SPR220 resist

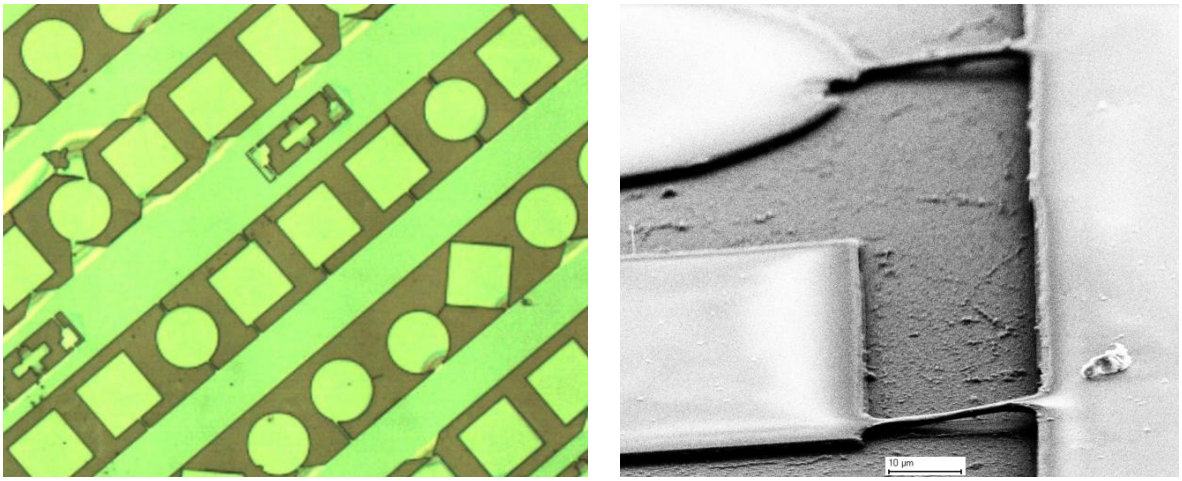

a) b)

Figure 4.8 Microscopic image of undercut coupon – sample with Ti/Ni metallic mask, showing non-damaged DBR but DBR coupon collapse a) optical microscope image b) SEM

It can also be seen from figure 4.8 b) that the undercut coupons are not suspended but rather collapsed and bonded to the underlying Si substrate surface. This bonding is mainly due to the Van der Waals forces that could exist between the two flat surfaces, DBR bottom surface and Si surface underneath. This was revealed a major issue for the transfer printing stage as the coupons though undercut could not be picked up even when using retraction speeds greater than 20mm/s. This was potentially due to the van der Waals forces been too strong, meaning the coupon collapsed and got stuck to the surface. Therefore, to solve this problem, Van der Waals bonding had to be avoided completely and this was done by increasing the Si etch depth by RIE from 500nm to ≈ 2um. Therefore, the process was repeated but this time with RIE etch time of ≈ 140 minutes to achieve ≈ 2um Si etch depth. Microscopic image of resulting sample is shown in figure 4.9.

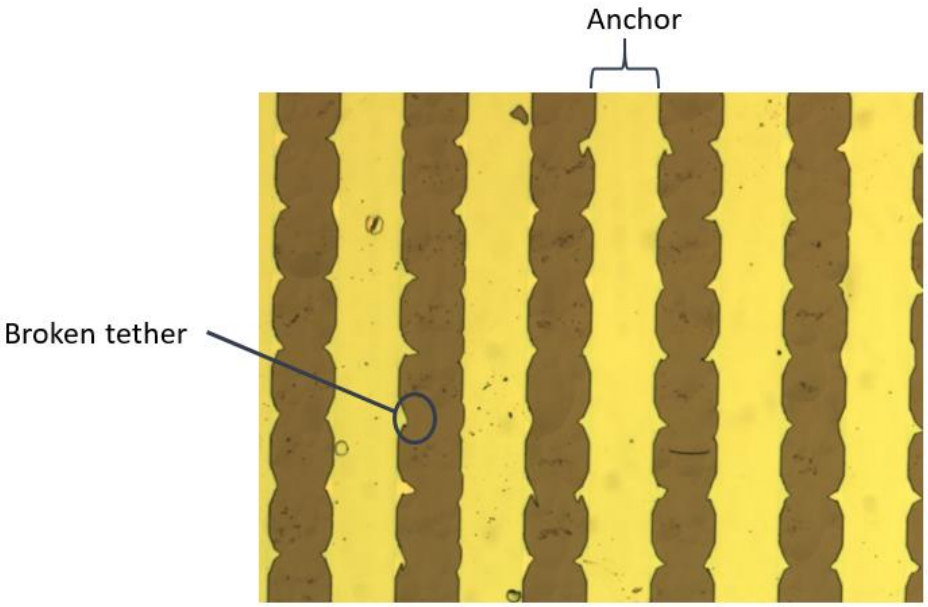

Figure 4.9 optical microscope image of poor yield DBR coupon due to non-optimised tether strength – coupon lost before transfer printing attempt

As it can be seen, the coupons did not remain after the etching, as they were washed away from the sample due to the breakage of their tether prior to transfer printing therefore, low DBR coupon yield. This was an indication of weak tethers not able to sustain the coupon weight. Therefore, the tethers needed to be strong enough to carry the coupons weight in order to maintain their suspension. As our tether thickness was already fixed by the DBR thickness itself of 2.1um, the tether width, length, shape (rectangular and trapeziodal), number and positioning was used for optimising the tether strength for coupon suspension (this is shown in figure 4.9). For coupon size of ≈ 100x100um square or 100um diameter circle with thickness ≈ 2.1um, triangular shaped tether with dimension height and bases 13.5um, 13um and 83um respectively as shown in figure 4.10

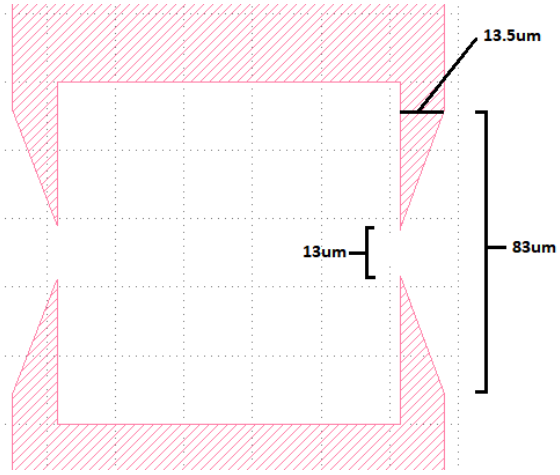

Figure 4.10 Optimised tether dimensions for 2.1um thick, 100x100um size coupon

A new mask were then designed and fabricated with tether dimensions above. Microscopic image showing the half undercut and full undercut respectively of the DBRs using the new mask with optimised tether sizes after the full anchor undercut process are shown in figure 4.11.

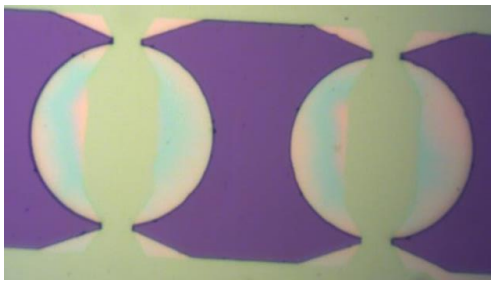

Figure 4.11 Optical microscope image of optimised masking and undercut for 2.1um thick, 100um diameter DBR coupon after 27mins immersion in KOH solution showing partial coupon undercut

As it can be seen, good quality DBR coupons were obtained with yield close to 100%. An SEM an array of suspended coupons is shown in figure 4.12

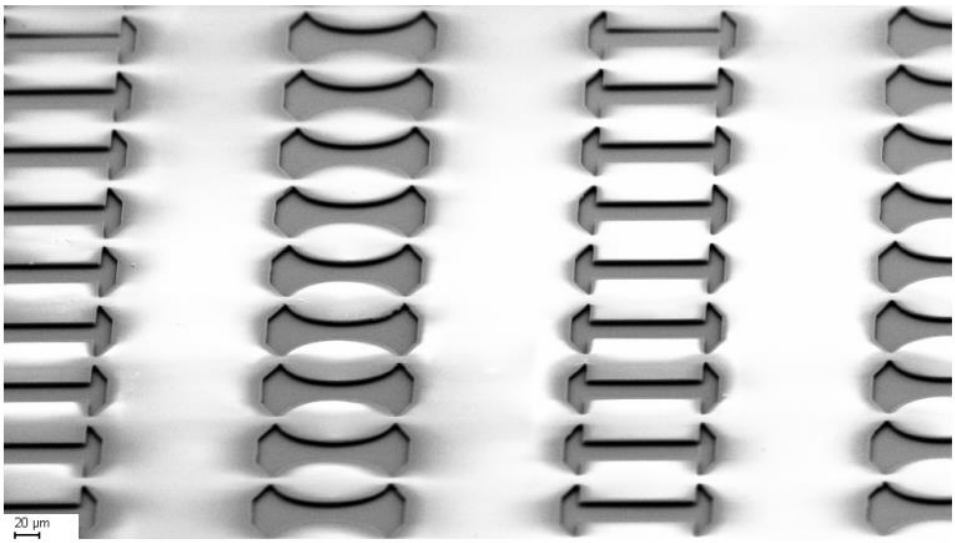

Figure 4.12 SEM image of undercut DBR coupons showing coupon suspension and very high yield.

As discussed, various parameters of effective masking for the RIE etch, Si RIE etch depth and tether dimensions and shape needed to be optimised to achieve high quality, suspended and high yield DBR coupons respectively. The sample is now ready for transfer printing

4.2.3 Transfer printing fabrication of the F8BT microcavity

Deterministic transfer printing was used for the assembly and fabrication of the F8BT resonant micro-cavity. Pedestalled stamps with elastomeric properties are essential for this process, polydimethylsiloxane (PDMS) based stamps were chosen thanks to their viscoelastic properties making their adhesion velocity dependent. The fabrication of such stamps and the microcavity deterministic transfer printing are described below

4.2.3.1 PDMS stamp fabrication

Double casting PDMS stamp process was performed. This involves the use of a master mould made out of patterned (pedestal pattern) photoresist on a solid substrate such as glass or silicon. This master mould is then used for the casting and curing of a PDMS sub master mould, having inverted pattern compared to the wanted pedestalled stamp. This PDMS sub-master mould finally serves in the casting of the pedestalled PDMS stamp. Double casting reduce the amount of casting on the master mould as the PDMS sub master mould is mainly used hence, longer master mould lifetime. Detailed fabrication procedure of all structures are given below

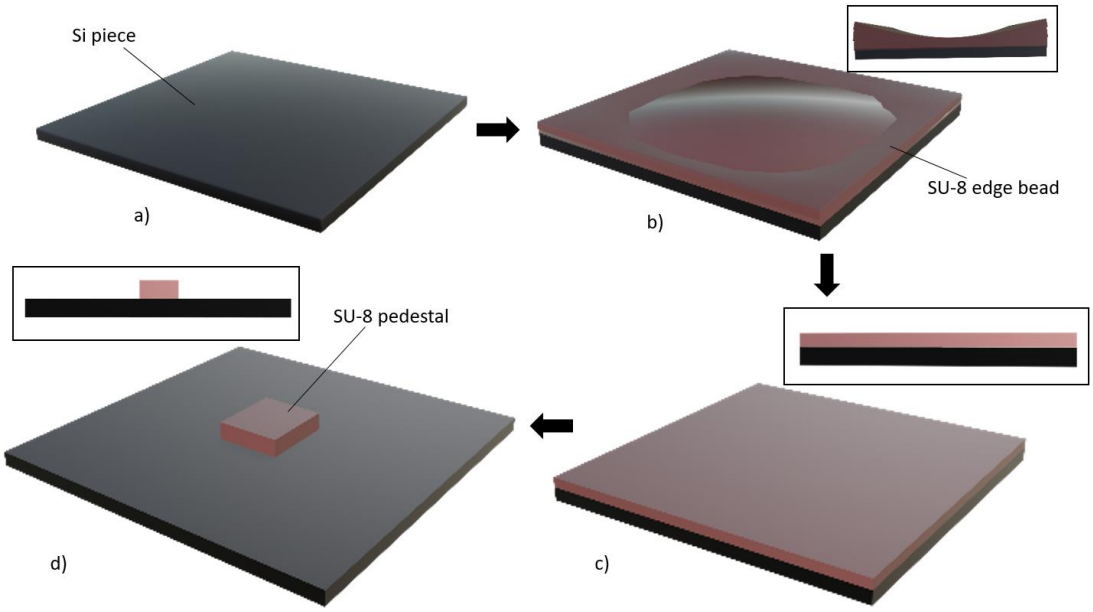

Figure 4.13 SU-8 resist master mould fabrication a) cleaved and cleaned Si piece to serve as substrate b) Spin coated SU-8 resist. Considerable edge bead c) Flatter SU-8 layer after edge bead treatment d) SU-8 master mould consisting of pedestalled SU-8 after photolithography

SU-8 2050 thick negative resist (from MicroChem) was selected for the fabrication of the master mould by photolithography. Figure 4.13 shows the SU-8 master mould fabrication. A silicon (100) wafer was cleaved to small substrate with dimensions ≈ 1.5x1.5cm, then it was solvent cleaned using solvents n-butyl acetate, acetone and isopropyl alcohol (all (from Fisher Chemical) to remove any dirt or contaminants on the surface. Then, following the dehydration bake (100 ^{o}C for 1min); The SU-8 resist was spun during two cycles; 500rpm for 15s with an acceleration of 100 rpm/s and 1700rpm for 30s with an acceleration of 300rpm/s. Significant amount of edge bead could be observed on the sample, meaning a non-flat SU-8. This non-flatness will be replicated on the final pedestal stamp, which can be detrimental during the transfer printing stage as unwanted contact could be made with the ink substrate. The edge bead was minimised by spraying some edge bead remover EBR PG (from MicroChem) on the coated surface. The sample was placed on a levelled surface and covered with a plastic cover with a small hole on top of ≈ 1mm diameter to allow the edge bead remover to evaporate. The sample was then left for 24 hrs to allow the coated surface to flatten, and any bubbles in the coating to be removed via the action of the edge bead remover. If the rested SU-8 layer still appeared non-flat after 24 hours, the edge bead remover spraying and resting was repeated for another 24 hours. After 24 hrs, the sample was then soft baked in 2 cycles, 65 ^{o}C for 5mins and 95 ^{o}C for 16mins. Next, the sample was exposed for 48s using UV 400 mask aligner. This was followed by two-post exposure bakes at 65 ^{o}C for 4mins and 95 ^{o}C for 9mins. Development

was carried out by submerging the sample in SU-8 developer solvent and ultra-sonicated using the UT8031/EUK ultrasonic cleaner for six mins under delicate mode. Visual checks were carried out on the developing sample using the microscope every two mins after rinsing in DI water and the process was stopped when the sample looked developed. Once development completed, the sample was then rinsed in DI water and blow-dried with nitrogen gas. Minor cracks on undeveloped SU-8 could be seen, this was reduced by baking the sample at 180 ^{o}C for 30s, which cause some SU-8 reflow and crack 'healing'. Finally, the coated SU-8 was subjected to another UV 400 exposure for 2mins, this helps in enhancing the resist bonding to the silicon substrate, which can increase the master mould lifetime. The result was a 100x100um size (dimensions matching the ink coupon size), 100um thick SU-8 master mould as shown in figure 4.14.

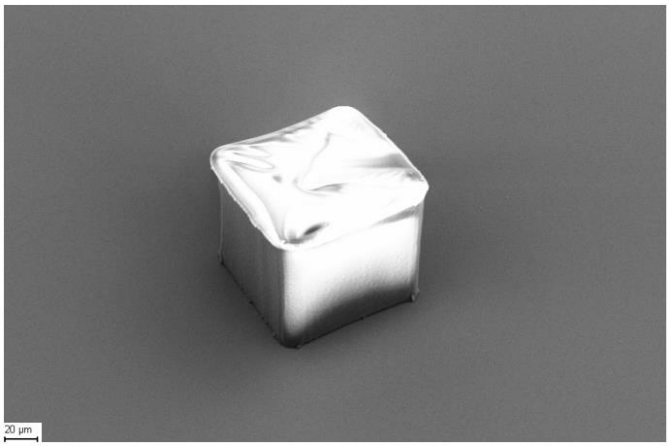

Figure 4.14 SEM of the completed SU-8 master mould

Multiple PDMS silicones exist such as Sylgard 184, Silgard 182, Silgard 170 and Silgard 105 with different physical properties. Silgard 184 was the silicone used for PDMS manufacturing, as it was reported to have stronger velocity dependent adhesion properties that is, a 4 fold increase in adhesion for velocity changes of 10um/s to 750 um/s [19]. Both the base and curing agent was used.

a) b)

Figure 4.15 PDMS mixture (Silgard 184 base and curing agent 101) a) before and b) after vacuum desiccator

Thorough mixing of the Sylgard 184 base and curing agent was done at a ratio 101 weight respectively in an aluminium tray using a plastic spoon. Numerous bubbles were generated that had to be removed before curing. This was done by placing the sample in a vacuum desiccator for 10mins and then back to atmospheric pressure. This vacuum pumping leads to outgas and hence bubble bursting, the desiccator process was repeated two times until the mixture became bubble free. Figure 4.15 shows images of the PDMS mixture before and after the desiccator used.

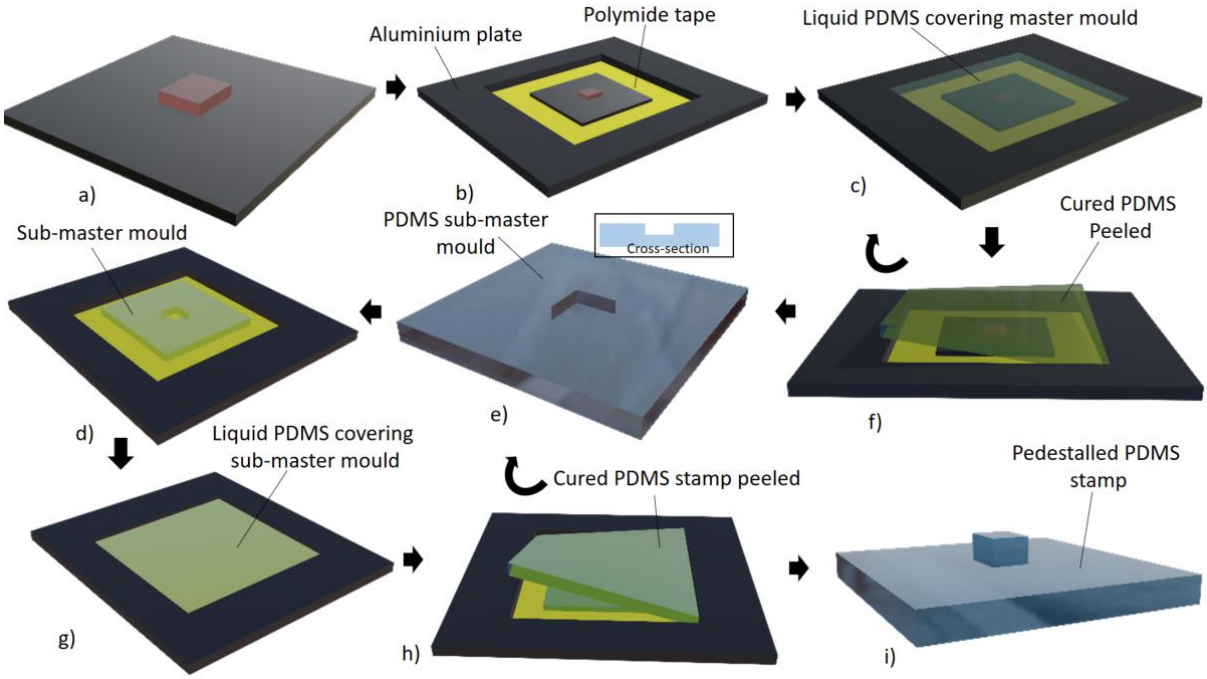

Figure 4.16 PDMS stamp casting fabrication steps a) SU-8 master mould b) master mould attached to the casting container made from polymide taped on aluminium plate c) casting liquid PDMS over master mould d) Cured PDMS sub-master mould peeled off the casting container e) PDMS sub-master mould reversed f) sub-master mould attached to the casting container g) casting liquid PDMS over sub-master mould h) Cured PDMS stamp mould peeled off the casting container i) Pedestalled PDMS stamp

The sub master PDMS mould could then be made by casting the PDMS liquid onto the SU-8 master mould. Figure 4.16 shows the casting process for the PDMS sub master mould and stamp fabrication. A 1cm thick 8x8cm area aluminium plate with a 4x4cm drilled hole was used as container. One surface was covered with polyimide tape onto which the master mould was attached as shown in figure 4.16 b. Polyimide tape was chosen as the back adhesive as it is resistant to the high curing temperature of ≈ 100^{o}C (having temperature stability of 260^{o}C [29]) and its silicone adhesive doesn't affect the PDMS curing process.

The PDMS was then poured over the master mould mounted structure making sure the aluminium plate hole is fully covered as shown in figure 4.16 c). Any extra-generated bubbles were burst by lightly blowing nitrogen gas on top of the liquid using a nitrogen gun. Quick curing was achieved by oven baking the whole setup at a temperature of 100 ^{o}C for 35mins. The curing process is a chemical reaction where the base and curing agent react with the help of a platinum catalyst H_2PtCl_6 (in the curing agent) to cause cross linkage of the siloxane chains

in the base leading to a solid elastomer PDMS [30]. This process is temperature dependent with the rate proportional to the temperature hence, 100 ^{o}C used. Figure 4.17 shows the reaction

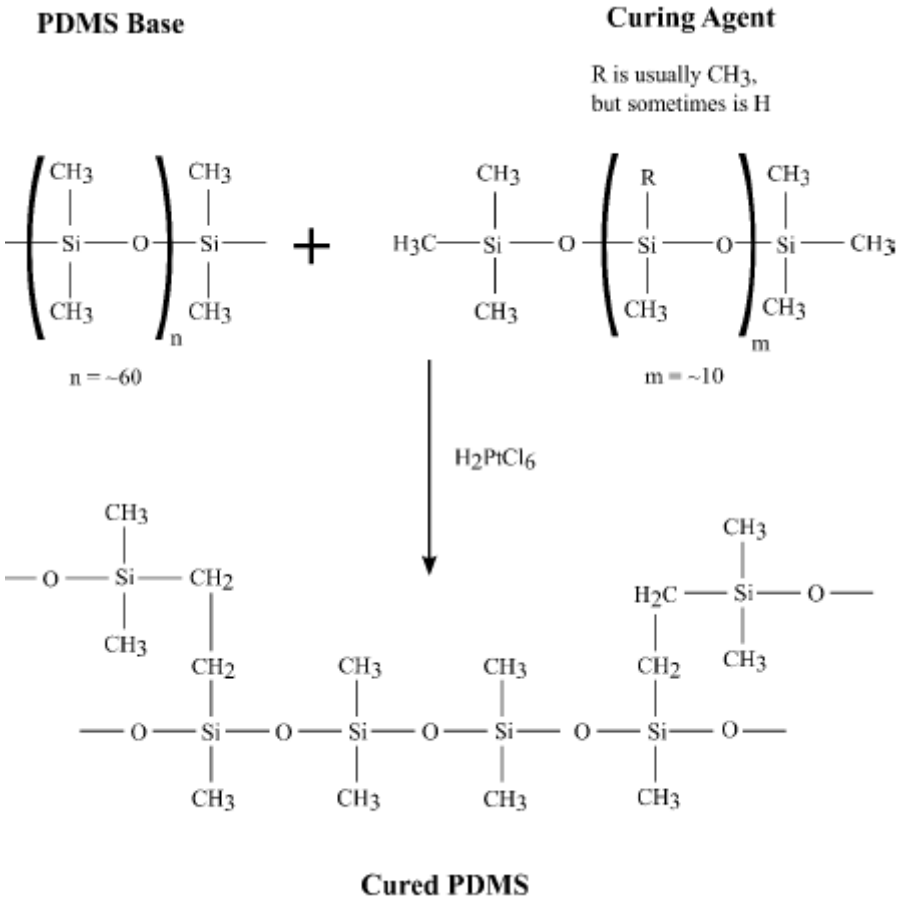

Figure 4.17 PDMS curing reaction [30]

Peeling the casted cured PDMS revealed the sub-master mould as shown in figure 4.13 d). Its surface needed to be treated and hardened before serving as a mould. The treatment process is required to change the PDMS sub master mould surface chemistry in order to prevent permanent bonding with the casted PDMS. Different PDMS treatment methods were reported; surfactants Brij52 and D-3005 treatment [37], thermal aging [38], oxygen plasma treatment [39] and UV/ozone treatment [40]. UV/ozone treatment was used. The sub-master mould surface was subjected to ultraviolet/ozone treatment using the UV/ozone cleaner for 30 mins, the ozone cleaner uses synthetic quartz UV grid lamp emitting at wavelengths 186nm and 254nm. The 186nm emission convert O_2 to O_3 and the 254nm emission reacts with the methyl group in the PDMS in the presence of O_3 to form oxygen compounds such as a SiO_x, SiOH, COH and COOH [31], the SiO_x forms a crust on the surface changing it to from soft to brittle that is less adhesive hydrophilic one.

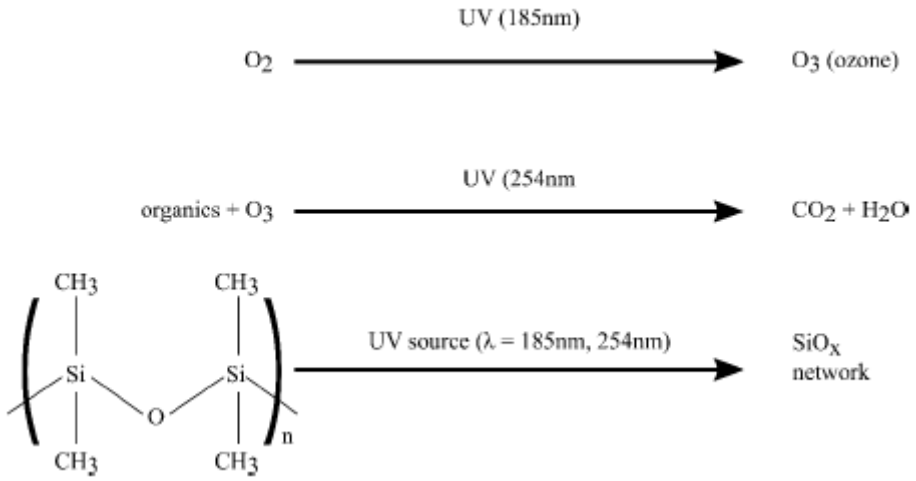

Figure 4.18 UV/ozone treatment of PDMS surface to form SiO_x crust [32]

The PDMS sub master mould was then left to rest for 24 hrs, this waiting time is necessary to allow any free siloxane to migrate out the crust and cure. This free siloxane could still favour PDMS-PDMS bonding and hence hindering its peeling from the mould. After 24 hrs, any dust, contaminants and remaining siloxanes were then removed by submerging the PDMS mould in iso-propyl alcohol solvent for 60s and nitrogen drying. Microscopic and SEM images of the achieved PDMS sub master mould are shown in figure 4.19

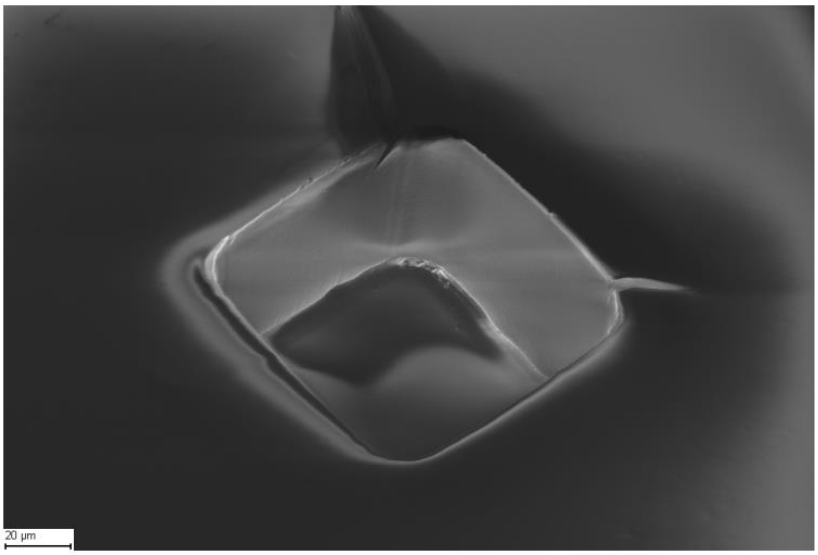

Figure 4.19 SEM image of the PDMS sub-master mould

The same casting used above for the PDMS sub master mould manufacture was repeated to achieve the pedestal stamp but in this case using the PDMS sub master mould instead of the

SU-8 master mould. This is shown in figures 4.16 f) g) h). The PDMS pedestalled stamp could then be used for transfer printing. Optical microscopic and SEM images of the achieved pedestalled PDMS stamp is shown in figure 4.20

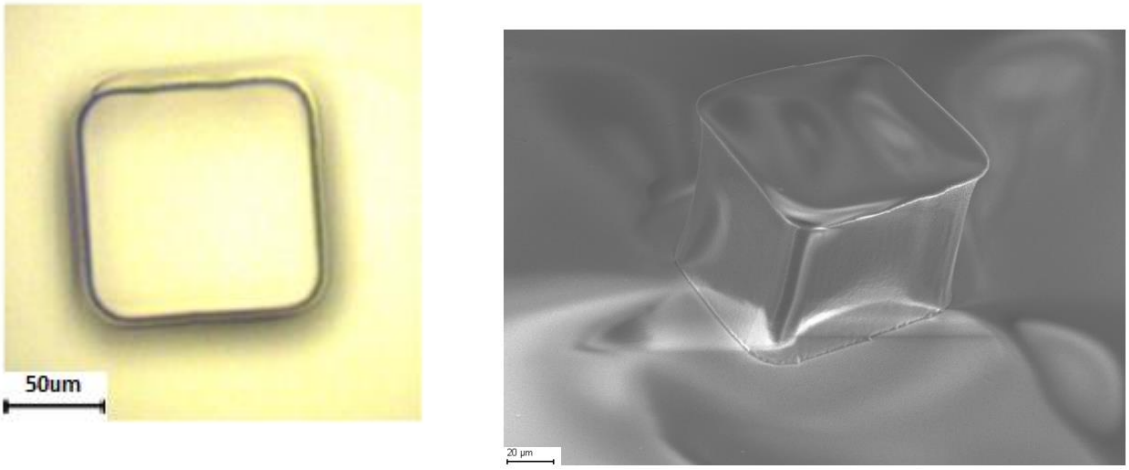

a) b)

Figure 4.20 Optical microscopic images of the pedestalled PDMS stamp a) microscopic top view b) SEM image

4.2.3.2 PMMA resonant micro-cavity fabrication by deterministic transfer printing

Before attempting to transfer print a resonant micro-cavity, transfer printing of the suspended DBR coupon on new substrate glass was first tried. This was necessary to understand the retraction speed parameter values required for the ink coupon picking and printing during the transfer print. This was also necessary in order to measure the effect if any of the processing and transfer printing could have had on the DBR coupon reflectivity peak and stop band. Below is a detailed description of the transfer printing process for the DBR and PMMA resonant micro-cavity

4.2.3.2.1 DBR coupon transfer printing on new glass substrate

The receiving surface flatness and cleanliness are critical parameters to ensure the efficient transfer printing [19]. For this reason, the glass substrate to be used as the receiving substrate first needed to be cleaned to remove any contaminant on the surface. This was done by performing a three solvent cleaning process using n-butyl acetate, acetone and Iso-propyl alcohol solvents as described in Chapter 3. The cleaned glass substrate was then oxygen plasma ashed using (O_2/250sccm 150W for 45s) to remove any organic material on the surface. PMMA was used as an adhesion promoter layer thanks to its adhesive properties. A thin layer of PMMA was deposited on the cleaned glass substrate by spin coating PMMA in toluene solution

of concentration 10mg/ml at speed 6000 rpms for 30s. This resulted in a 30nm thick PMMA layer with refractive index 1.5 measured using the ellipsometer (J.A. Woollam V- Vase), this is shown in figure 4.21 c).

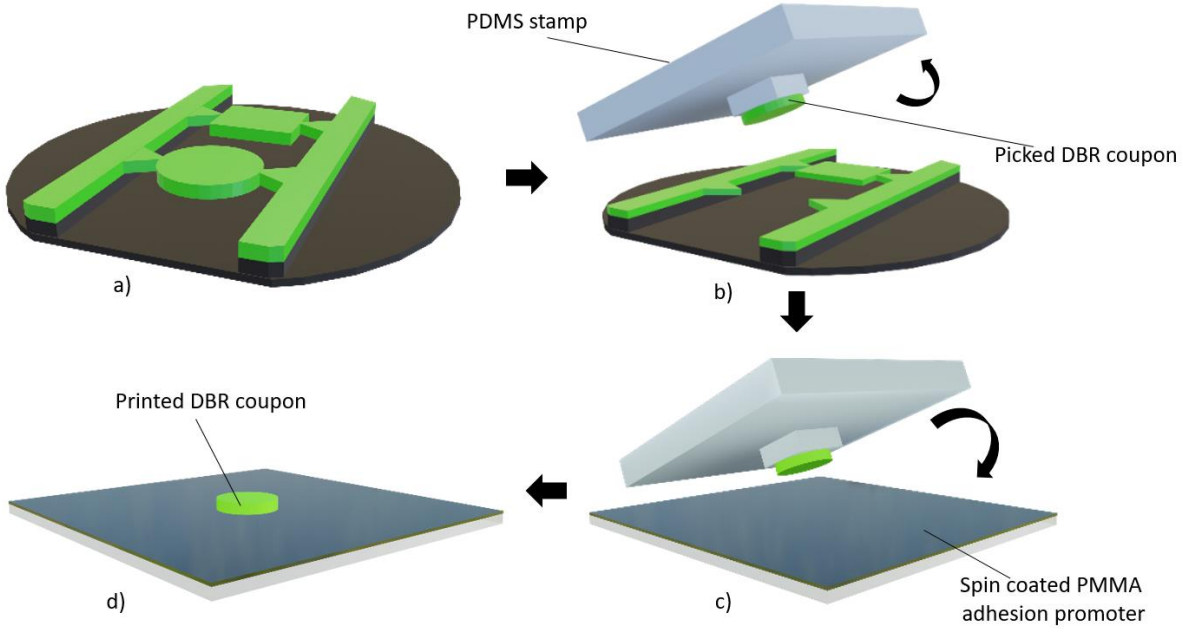

Figure 4.21 Transfer printing procedure of DBR coupon on glass substrate a) undercut DBR coupon sample b) DBR coupon picked by PDMS stamp c) DBR coupon printing d) DBR coupon transfer printed on new glass substrate

Transfer printing of the DBR on the new glass substrate were done as shown in figure 4.21. For pick up, the undercut DBR sample with suspended DBR coupons was positioned on the transfer printing sample stage held fixed by the vacuum. PDMS stamp pedestal surface was then brought in contact with a DBR coupon by lowering the stamp stage using the Ensemble Motion Composer software, retracting the stamp at high velocity of 15mm/s results in tether breaking and picking of the DBR coupon, a diagrammatic representation is shown in figure 4.21 b). Optical microscopic images of the pick-up process is shown in figure 4.22, here a 200um diameter circular coupon is picked using a 100x100um pedestal area stamp.

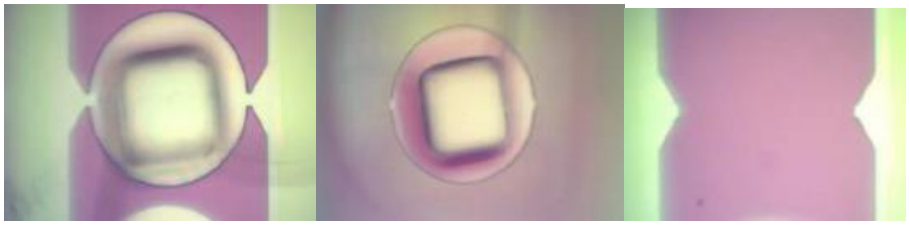

a) b) c)

Figure 4.22 DBR coupon (200um diameter) picking procedure using 100x100um pedestalled stamp a) stamp's pedestal-coupon contact b) coupon picked c) broken tethers

Optical microscopic and SEM images of a 100x100um square and 100um diameter circular picked DBR coupons respectively on the stamp pedestal are shown in figure 4.23

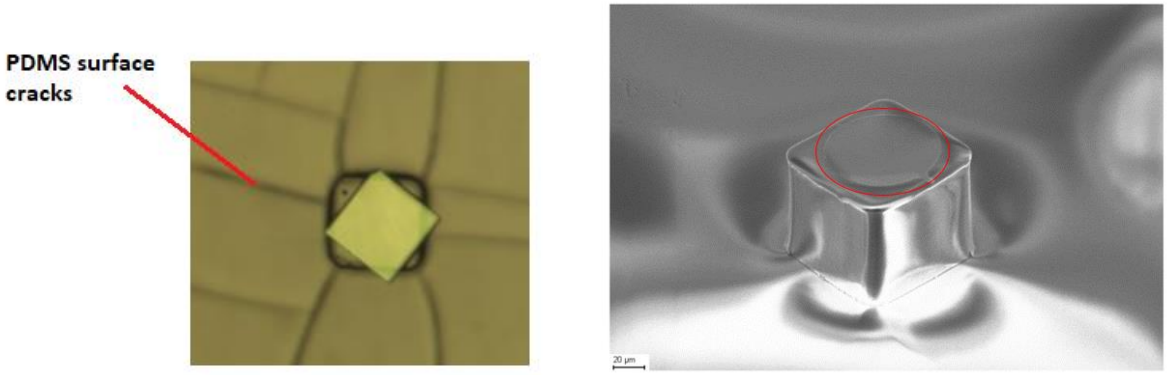

a) b)

Figure 4.23 Images of picked DBR coupons a) optical microscopic image of picked 100x100um square b) SEM image of picked 100um diameter circular DBR coupon (highlighted) on top of the PDMS stamp

For the printing, the undercut DBR sample on the sample stage was first replaced with the receiving PMMA coated glass receiving substrate, also held in place by the vacuum chuck. The DBR coupon on the PDMS pedestal was then brought in contact with the PMMA layer on the glass surface and by performing a slow retraction at velocity of 0.8um/s, the DBR coupon were printed on the receiving glass substrate, this is represented in figure 4.21 c). Therefore, 0.8um/s is below the critical velocity for printing DBR coupons. Optical microscopic and SEM images of the transfer printed DBR on glass as shown in figure 4.24

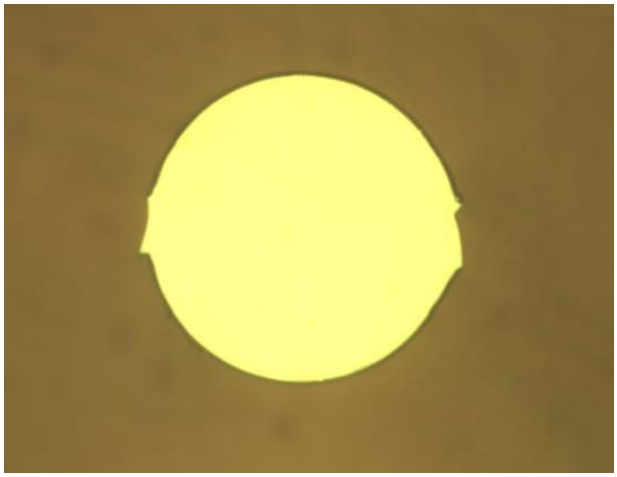

Figure 4.24 optical microscope image of DBR coupon (100um diameter) transfer printed on glass substrate

4.2.3.2 PMMA resonant micro-cavity fabrication by transfer printing

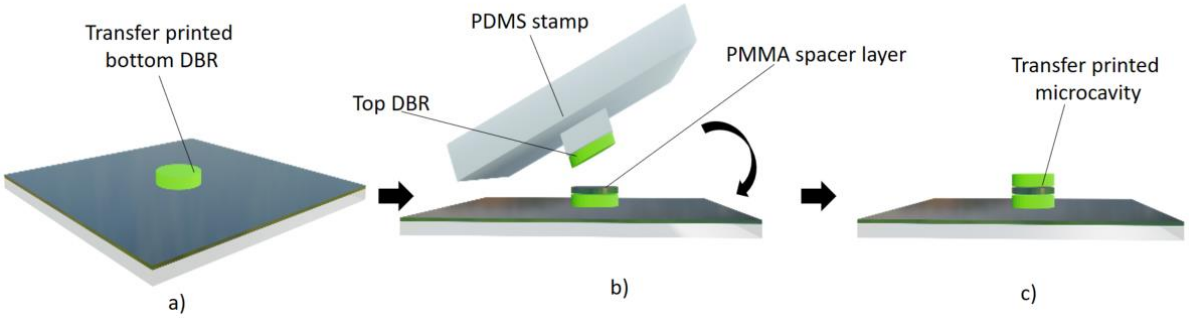

Figure 4.25 Transfer printing of PMMA micro-cavity a) transfer printed bottom DBR b) Transfer printing of top DBR on PMMA coated bottom DBR c) Transfer printed microcavity

In the non-emissive PMMA microcavity, the PMMA served as both spacer layer and adhesion promoter layer for the transfer printing. In order to sustain cavity modes within the microcavity, equation 2.38 in section 2.4 need to be obeyed. That is the cavity optical length must be an integer multiple of half the wanted cavity centre wavelength, usually chosen to overlap the emitter emission wavelength.

Calibration of the PMMA spacer layer thickness and refractive index from spin coating was required. The calibration involved spinning different concentrations of PMMA in toluene at different speeds for 30s followed by ellipsometry characterisation. The calibrations revealed PMMA with concentration 22mg/ml spun at speed 5000rpm for 30s yield a thickness of ≈ 178nm. Refractive index plot of the PMMA from ellipsometry is shown in figure 4.26 showing a PMMA refractive index of ≈ 1.518 at wavelength 550nm.

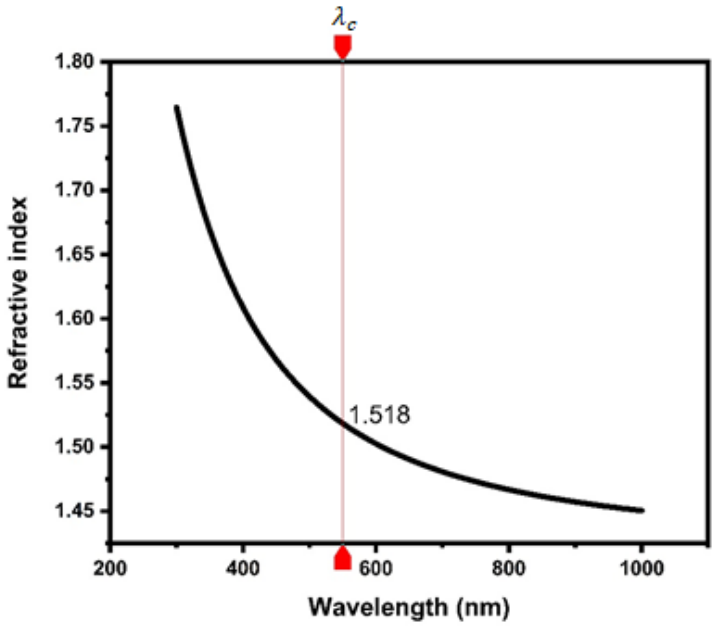

Figure 4.26 ellipsometry measurement of PMMA layer showing refractive index dispersion

Calculated λ_c of 538nm were obtained. A piece of DBR grown on silicon substrate of ≈ 1x1cm was obtained from cleaving the original DBR grown on Si (111). This is to serve as the cavity bottom DBR. The bottom DBR sample was three solvent cleaned and oxygen plasma ashed like the glass substrate above. 177nm thick PMMA spacer layer was then deposited on the cleaned bottom DBR as described above. The top DBR coupon could then be transfer printed on the PMMA layer; this was done using similar parameters as in section 4.2.3.2.1. The full process is shown in figure 4.25. SEM image of the printed cavity is shown in figure 4.27

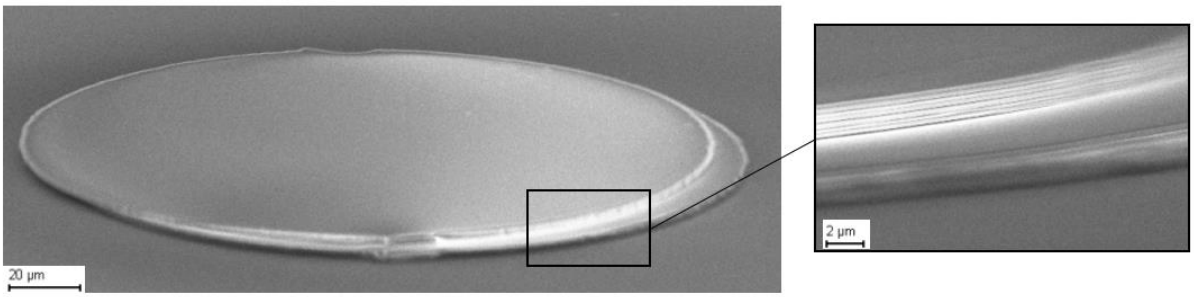

Figure 4.27 SEM of transfer printed PMMA microcavity

4.3 DBR reflectivity plots

The integrity of the newly transfer printed DBR needed to be checked and compared to the original grown DBR. This was done to measure any impact the undercut and transfer printing processing could have had on the DBR and the overall success of the newly developed undercut and transfer printing process. Dielectric DBRs being reflectors have major parameters

reflectivity peak and reflectivity bandwidth, which can both be obtained from the reflectivity spectrum measurements. Reflectivity spectrum measurements of PECVD grown DBR on Si (before any processing) as described in section 4.2.1 and of the undercut and transfer printed DBR coupon on glass as described in sections 4.2.3.1 and 4.1.2.3 were done using the electroluminescence and reflectivity measurement setup described in Chapter 3. The sample to be measured were placed on the Standa motorised stage, brought in position and focused (with the help of a 50x magnification 0.42 NA objective lens) to the XIMEA xiQ digital camera for visualisation. A halogen broadband light set to maximum intensity was used as the incident light source; the light was directed to the sample via a beam splitter the objective lens. Reflected light from the sample is collected and directed to a fibre collimator using the same objective lens and beam splitter. The light is then coupled in a multi-mode fibre, which directs it into a monochromator and CCD for spectrum detection.

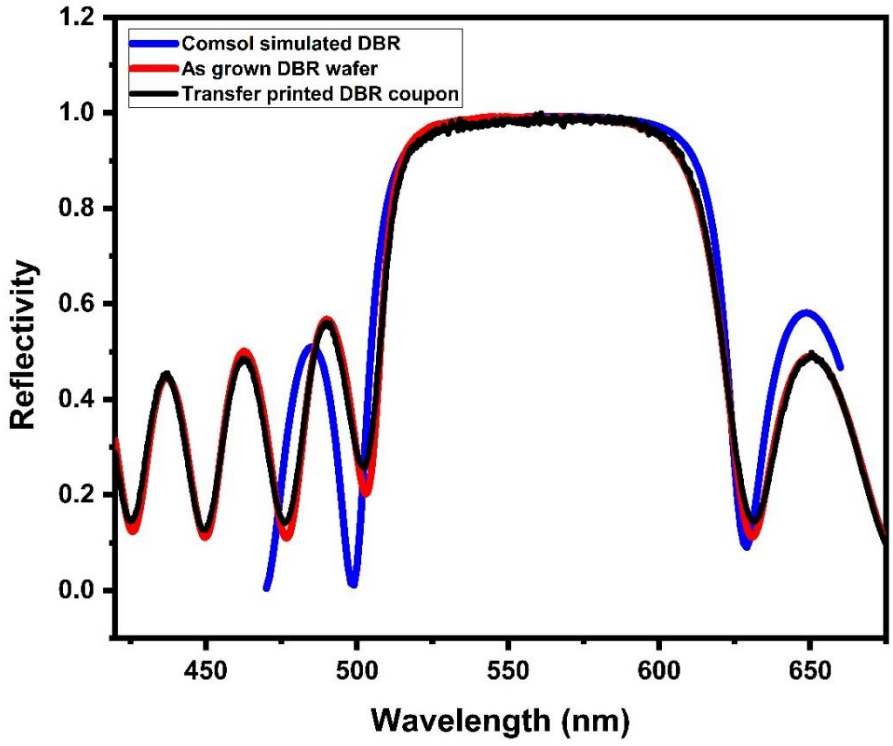

Figure 4.28 Reflectivity spectrum plot of DBR at different fabrication stages; showing as grown, transfer printed DBR coupon and simulated reflectivity

Figure 4.28 shows the measured reflectivity spectra of the as grown DBR, transfer printed DBR coupon and COMSOL simulated DBR. Peak reflectivity of ≈ 99% and linewidth of ≈ 95nm were obtained for the as transfer printed DBR coupon, and trace matching very closely the as

grown DBR reflectivity plot. This result shows that the anchor undercutting process and DBR coupon transfer printing had little to no effect on the DBR reflective nature

4.4 PMMA cavity reflectivity plot

Reflectivity measurements of the transfer printed PMMA microcavity described in section 4.2.3.2 were also done to investigate the resonant cavity effects. This was done in a similar way described in section 4.3. The resulting reflectivity plot together with the COMSOL simulated cavity reflectivity is shown in figure 4.29. Clear reflectivity dip can be seen on the simulated cavity reflectivity plot at the expected λ_c of 539nm. This reflectivity dip is an indication of microcavity effects as they represent optical cavity modes created within the cavity. A small decrease in reflectivity can be seen in the PMMA cavity reflectivity plot at wavelength region between 530nm to 540nm, this region corresponds to the expected λ_c indicating a possible reflectivity dip. The characterisation setup limitation could be the reason for the not well-pronounced reflectivity dip of the measured cavity reflectivity.

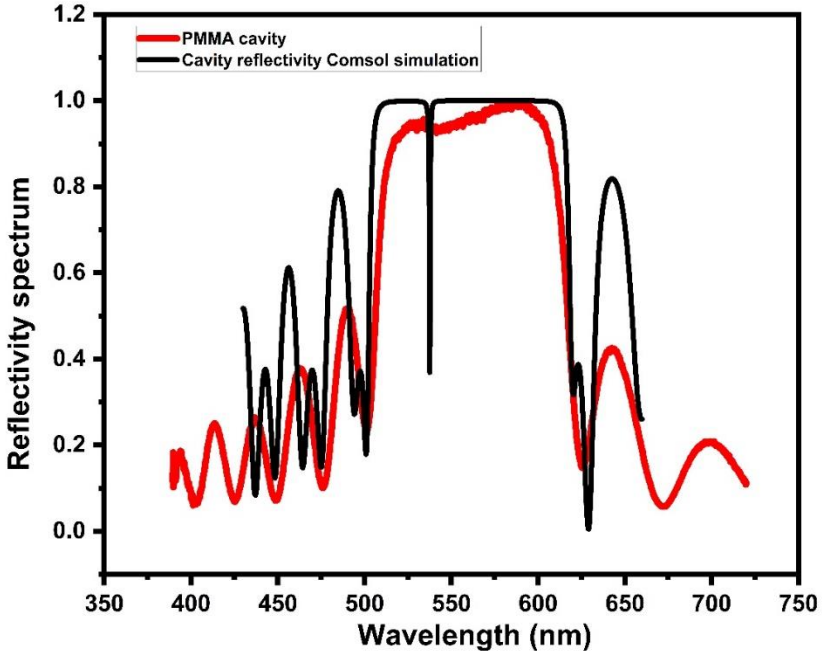

Figure 4.29 Measured and COMSOL simulated reflectivity spectrum plot of PMMA microcavity

The exposed area from the incident halogen light source onto the sample and collection area from the sample was more than 100um in diameter. This is not an issue for full wafer sample measurements but appears to be critical for samples 100um and less in size, as in the case for 100um diameter cavity printed on glass. A considerable amount of photons are not incident on

the 100um size coupon hence are lost away. In addition, surrounding reflections and scattering not from the DBR coupon are collected too. Therefore, a narrow reflectivity dip may get lost in the integrated intensity. The use of a higher magnification objective lens to focus the incident beam to a smaller spot together with the installation of a pinhole along the collection path to filter spatially the collected light and finally introducing angular resolution using an iris (collection of emissions only at the normal to the surface) could mitigate these measurement limitations.

4.5 Conclusion

To conclude, we demonstrated a new platform for the fabrication of optical microcavity devices with the aim of mitigating some limitations and challenges offered by monolithic direct epitaxy optical microcavity fabrication, specifically increasing the variety of emitters and materials that can be incorporated in various different configurations in a microcavity. The platform involves the use of standard dielectric SiN_x/SiO_2 DBRs grown by PECVD on Si (111). The grown DBRs are then released from their substrate via anchor undercutting by exploiting the KOH crystallographic selective wet etch of Si. Followed by transfer printing onto new substrates as stacks to form optical microcavities. Various process optimisations were done in order to ensure the protection and suspension of the DBR coupons after processing such as hard metallic masking for the RIE dry etch and tether/anchor strength optimisation. A DBR coupon yield of almost 100% was achieved. This was a necessity to achieve high quality transfer printed DBR coupons. Reflectivity measurement of the grown DBR, transfer printed DBR coupon (100um diameter) and DBR COMSOL simulations were carried out and plotted together showing close matching with high peak reflectivity and wide bandwidth of approximately 99% and 95nm respectively demonstrating the effectiveness of our platform. Cavity reflectivity measurements did not show clear cavity mode effects due to the limitations of our measurement set up. This platform also offer advantages of versatility, scalability and potential high throughput as array of coupons can be transfer printed in parallel.

4.6 References

[1] C. Zhang, R. Afandy, and J. Han, "Distributed Bragg reflectors for GaN-based vertical-cavity surface-emitting lasers," *Applied Sciences (Switzerland)*, vol. 9, no. 8. Multidisciplinary Digital Publishing Institute, p. 1593, 17-Apr-2019.

[2] M. S. Skolnick, T. A. Fisher, and D. M. Whittaker, "Strong coupling phenomena in quantum microcavity structures," *Semiconductor Science and Technology*, vol. 13, no. 7. pp. 645–669, 1998.

[3] E. F. Schubert, N. E. J. Hunt, R. J. Malik, M. Micovic, and D. L. Miller, "Temperature and modulation characteristics of resonant-cavity light-emitting diodes," *J. Light. Technol.*, vol. 14,

no. 7, pp. 1721–1728, 1996.

[4] S. Yang *et al.*, "GaN-based green resonant-cavity light-emitting diodes with Al mirror and copper plate," *Opt. Lett. Vol. 47, Issue 11, pp. 2858-2861,* vol. 47, no. 11, pp. 2858–2861, Jun. 2022.

[5] D. Delbeke, R. Bockstaele, P. Bienstman, R. Baets, and H. Benisty, "High-efficiency semiconductor resonant-cavity light-emitting diodes A review," *IEEE J. Sel. Top. Quantum Electron.*, vol. 8, no. 2, pp. 189–206, Mar. 2002.

[6] H. Wu, H. Li, S. Y. Kuo, B. Y. Chen, T. C. Lu, and H. Huang, "High Output Power GaN-Based Green Resonant-Cavity Light-Emitting Diodes with Trapezoidal Quantum Wells," *IEEE Trans. Electron Devices*, vol. 67, no. 9, pp. 3650–3654, Sep. 2020.

[7] F. A. Al-Saymari, A. P. Craig, Q. Lu, A. R. J. Marshall, P. J. Carrington, and A. Krier, "Mid-infrared resonant cavity light emitting diodes operating at 4.5 μm," *Opt. Express*, vol. 28, no. 16, p. 23338, Aug. 2020.

[8] C. Zhang, R. Afandy, and J. Han, "Distributed Bragg reflectors for GaN-based vertical-cavity surface-emitting lasers," *Applied Sciences (Switzerland)*, vol. 9, no. 8. MDPI AG, Apr-2019.

[9] O. Svelto, *Principles of lasers*, 5th ed. Springer, 2010.

[10] B. Saleh, "The laser," *Opt. Our Time*, pp. 71–85, Jan. 2016.

[11] V. Savona, L. C. Andreani, P. Schwendimann, and A. Quattropani, "Quantum well excitons in semiconductor microcavities Unified treatment of weak and strong coupling regimes," *Solid State Commun.*, vol. 93, no. 9, pp. 733–739, Mar. 1995.

[12] R. P. Stanley, R. Houdré, U. Oesterle, M. Gailhanou, and M. Ilegems, "Ultrahigh finesse microcavity with distributed Bragg reflectors," *Appl. Phys. Lett.*, vol. 65, no. 15, pp. 1883–1885, Oct. 1994.

[13] A. H. W. Choi, *Handbook of optical microcavities*, 1st ed. Jenny Stanford Publishing, 2014.

[14] E. F. Schubert, Y. H. Wang, A. Y. Cho, L. W. Tu, and G. J. Zydzik, "Resonant cavity light-emitting diode," *Appl. Phys. Lett.*, vol. 60, no. 8, p. 921, Jun. 1998.

[15] E. F. Schubert, "Reflectors," in *Light-Emitting Diodes*, Cambridge University Press, 2006, pp. 163–190.

[16] E. Y. Paik *et al.*, "High Quality Factor Microcavity for Van der Waals Semiconductor Polaritons Using a Transferrable Mirror," *Adv. Opt. Mater.*, vol. 11, no. 1, p. 2201440, Jan. 2023.

[17] S. G. Lee *et al.*, "Continuous-wave operation of nonpolar GaN-based vertical-cavity surface-emitting lasers," in *Gallium Nitride Materials and Devices XIII*, 2018, vol. 10532, no. 23, pp. 94–104.

[18] J. Piprek, T. Tröger, B. Schröter, J. Kolodzey, and C. S. Ih, "Thermal conductivity reduction in GaAs-AlAs distributed Bragg reflectors," *IEEE Photonics Technol. Lett.*, vol. 10, no. 1, pp. 81–83, Jan. 1998.

[19] A. Carlson *et al.*, "Transfer Printing Techniques for Materials Assembly and Micro/Nanodevice Fabrication," *Adv. Mater.*, vol. 24, no. 39, pp. 5284–5318, Oct. 2012.

[20] Y. Xia and G. M. Whitesides, "Soft Lithography," *Angew. Chemie Int. Ed.*, vol. 37, no. 5, pp. 550–575, 1998.

[21] H. Ahn, K. J. Lee, A. Shim, J. A. Rogers, and R. G. Nuzzo, "Additive soft-lithographic patterning of submicrometer- and nanometer-scale large-area resists on electronic materials," *Nano Lett.*, vol. 5, no. 12, pp. 2533–2537, Dec. 2005.

[22] E. Menard *et al.*, "Micro- and nanopatterning techniques for organic electronic and optoelectronic systems," *Chem. Rev.*, vol. 107, no. 4, pp. 1117–1160, Apr. 2007.

[23] B. Corbett, R. Loi, W. Zhou, D. Liu, and Z. Ma, "Transfer print techniques for heterogeneous integration of photonic components," *Prog. Quantum Electron.*, vol. 52, pp. 1–17, Mar. 2017.

[24] J. Yoon, S. M. Lee, D. Kang, M. A. Meitl, C. A. Bower, and J. A. Rogers, "Heterogeneously Integrated Optoelectronic Devices Enabled by Micro-Transfer Printing," *Adv. Opt. Mater.*, vol. 3, no. 10, pp. 1313–1335, Oct. 2015.

[25] S. Mishkat-Ul-Masabih, J. Leonard, D. Cohen, S. Nakamura, and D. Feezell, "Techniques to reduce thermal resistance in flip-chip GaN-based VCSELs," *Phys. status solidi*, vol. 214, no. 8, p. 1600819, Aug. 2017.

[26] R. Kumar, K. Thakor, S. Gupta, R. Maripeddi, and D. Nag, "Design and Optimization of Dielectric DBR for VCSEL , Targeting Emission Range of 520-550 nm," Bombay, 2019.

[27] H. S. Kim *et al.*, "Unusual strategies for using Indium Gallium Nitride grown on Silicon (111) for solid-state lighting," *Proc. Natl. Acad. Sci. U. S. A.*, vol. 108, no. 25, pp. 10072–10077, Jun. 2011.

[28] K. E. Bean, "Anisotropic etching of silicon," *IEEE Trans. Electron Devices*, vol. 25, no. 10, pp. 1185–1193, 1978.

[29] 3M, *3M™ Polyimide Film Tape 5413*. 2021.

[30] M. W. Lee, S. S. Yoon, and A. L. Yarin, "Release of Self-Healing Agents in a Material What Happens Next?," *ACS Appl. Mater. Interfaces*, vol. 9, no. 20, pp. 17449–17455, May 2017.

[31] K. Zhou, X. G. Zhu, Y. Li, and J. Liu, "Fabrication of PDMS micro through-holes using micromolding in open capillaries," *RSC Adv.*, vol. 4, no. 60, pp. 31988–31993, 2014.

[32] Y. Kwak, Y. Kang, W. Park, E. Jo, and J. Kim, "Fabrication of fine-pored polydimethylsiloxane using an isopropyl alcohol and water mixture for adjustable mechanical, optical, and thermal properties," *RSC Adv.*, vol. 11, no. 29, pp. 18061–18067, May 2021.

5) Chapter 5 - Fabrication of GaN based RCLED via a Modified Transfer Printing Technique

Resonant Cavity LEDs are important optoelectronic device thanks to their interesting properties of enhanced, purer, more directional emission compared to conventional LEDs [1][2][3] hence, their use in applications such as infrared wireless communication and Plastic Optical Fibre (POF), high brightness lighting applications [4][5], display technology and more. Traditional RCLEDs are mainly fabricated via direct epitaxy, which offers some challenges especially in the GaN material series such as high cost process, lattice mismatching issues, scarcity of compatible DBR materials configuration and small reflectivity bandwidth from available compatible DBRs. We present a novel approach involving the use of LED and dielectric DBRs separately grown, integrated heterogeneously together as stacks of optical microcavities via deterministic transfer printing. This approach involves the anchor undercutting of each material system from their original substrates into coupons and then their transfer printing as stacks with configuration DBR/LED/DBR forming an RCLED. The achieved electrically injected RCLED showed increased device series resistance and multiple mode emission spectrum (because of resonance cavity effect) compared to transfer printed open LED devices. With some process optimisation, this approach has the potential of achieving good performing RCLED with linewidth narrowing from 21nm to 3nm.

5.1 Introduction

When it comes to solid state lighting within the shorter wavelength emission section of the visible spectrum (ultraviolet, blue and green) and white light, the GaN family of materials series are the dominant choices. This is thanks to the key features of direct band gap tuneability across the complete visible spectrum via alloying [6]. This has revolutionised the LED industry as it led to the possibility of realisation of white light by solid-state lighting using various methods [7]. The advent of resonant micro-cavities have led to the development of various innovative hybrid practical optoelectronic devices and configurations, among all the Resonant Cavity Light Emitting Diode (RCLED) stand out thanks to the work of Schubert et al [8]. Properties exclusively reserved to lasers such as high efficiency, high spectral purity, high radiance, and modulation possibilities are now achievable with RCLEDs, distinguishing them from conventional LEDs [1][2][3][9]. The emitted light intensity (along the cavity emission axis) from the RCLED is enhanced compared to a conventional LED; this is thanks to the resulting enhanced spontaneous emission. In resonant cavities, the main factor determining

emission linewidth is the cavity quality factor, for this reason, RCLEDs offers purer emission as a notable reduction in emission linewidth is common in the RCLED. The RCLED also offers better thermal stability compared to its conventional counterpart and better beam directionality along the cavity axis [1][2][3], therefore, reducing total internal reflection suffered by conventional LEDs leading enhanced external quantum efficiency. In addition, as they are vertical cavity devices, they offer the convenience of ease of manufacture and high reliability [10].

Thanks to the above numerous benefits plus the conventional LED advantages (ease and low cost fabrication, low temperature sensitivity and higher reliability), RCLEDs made its way from the laboratory to commercial applications, in particular data communication applications such as infrared wireless communication and Plastic Optical Fibre (POF). RCLEDs also serve in lighting applications requiring high brightness [4][5], display technology and medical esthetics [11].

The realisation of such GaN based RCLED despite the major developments is still a topic of research due to the challenge of effectively integrating the active layer in between high quality DBRs while developing routes allowing electrical current injection into the device [12] [13]. Compatibility issues of lattice mismatch between certain material configurations (lattice mismatch of approximately 2.4% in AlN/GaN DBR configuration) leading to cracks and other defects, which hinders the device performance [14]. Also, there exist a small refractive index contrast between the available lattice matched DBR material configurations (approximately 0.34 for AlInN/GaN DBR) meaning a small reflectivity bandgap and large number of pairs are required to achieve high reflectivity [15] [16]. This narrows the choices of materials that can be included in the cavity. Scarcity of compatible DBR GaN based material configurations is another challenge [12]. Also, p-type GaN based DBRs tend to have high absorption losses and poor electrical conductivity [17]. Air based DBRs (air gap and nanoporous DBRs [12]) are a new class of DBR providing a notable upgrade in refractive index contrast as the ultimate low refractive index material (air) is used. Their fabrication usually involves a two-step process, growth followed by some form of selective etching of a layer by various etching methods. This include photo-electrochemically etching the InGaN in GaN/InGaN stacks [18][19], electrochemical etching of highly doped n^+ GaN in GaN/ n^+ GaN stacks [20], hot nitric acid etching of AlInN in GaN/AlInN stacks [21][22] and thermal desorption of GaN in AlGaN/GaN stacks to form AlGaN/airgap DBR [23]. Air based DBRs still suffer from low heat dissipation and requiring epitaxial growth, which is a costly process with extreme conditions of high

temperature and low pressure, which are detrimental to some classes of emitters such as polymers. For these reasons, GaN based optical micro-cavity generally employ dielectric DBRs or are hybrid in nature with n-type epitaxial DBR and dielectric DBR [12].

Two routes are generally used for GaN based RCLEDs fabrication. Wafer bonding followed by laser lift off lithography in order to expose the backside of the grown epilayer for further device processing of contacts and dual dielectric DBR deposition [24] or hybrid cavity consisting of bottom GaN based DBR epitaxially grown and top reflector being a dielectric DBR or metallic [25][26]. Both methods present challenges; the earlier requires complex flip chip structure processing hindering their mass production and the later suffers from epitaxial grown GaN based DBR issues of lattice mismatch, small reflectivity band width and poor hole injection [27][28][29].

We here by propose a new route involving the separate fabrication of all the RCLED components (LED device and DBRs). This is followed by their separation from their native substrate using conventional low cost fabrication techniques (lithography, metallisation, dry and wet etch) anchor undercutting procedure and their heterogeneous integration as stacks layers in an RCLED configuration on a new substrate by the process of transfer printing.

5.2 LED Epitaxial structure confocal Photoluminescence

As discussed in chapter 2, GaN based LEDs are conventionally grown on sapphire substrate as they offer good lattice matching with a buffer layer. However, for us to exploit the anchor undercutting technique and transfer printing platform developed in Chapter 4, LED epilayer grown on Si (111) substrate were needed. These LEDs were commercial purchased from Xiamen Powerway Wafer Co. Ltd. These were 4 inches GaN on Si LED wafers with layer structure, composition, doping and thicknesses depicted in table 5.1

Layer	Composition	Doping	Thickness
p-layer	(AlIn)GaN	Mg greater than $1x10^{19}$	80 ± 25nm
Active layer	InGaN/GaN MQW	/	200 ± 40nm
n-layer	GaN	Si approximately $5x10^{18}$	1500 ± 100nm
Buffer	Al(Ga)N	/	1650 ± 100nm
Substrate	Si	/	800um

Table 5.1 Commercial GaN on Si LED layer structure

The purchased LED epilayer was characterised by confocal photoluminescence (CPL) as it offered quick and non-destructive characterisation in order to obtain the emission spectrum,

FWHM and peak wavelength parameters necessary for effective cavity tuning. Excitation was done using a continuous wave laser at wavelength 375nm at power of 1mW. The obtained CPL plot is shown in figure 5.1. Clear emission in the blue spectral region can be seen with emission peak at 466nm. It can also be seen that the emission is affected by Fabry-Perot interference oscillations because of the large refractive index contrast at the Si substrate-GaN and GaN-air interfaces [30] hence the apparent multiple peaks. A Gaussian fitting was done using software Origin; this allowed extraction of the FWHM of approximately 19nm. The lower energy emission seen is as a result of the Quantum Confined Stark Effect (QCSE) band bending as a result of the GaN spontaneous polarisation [31] [32] [33].

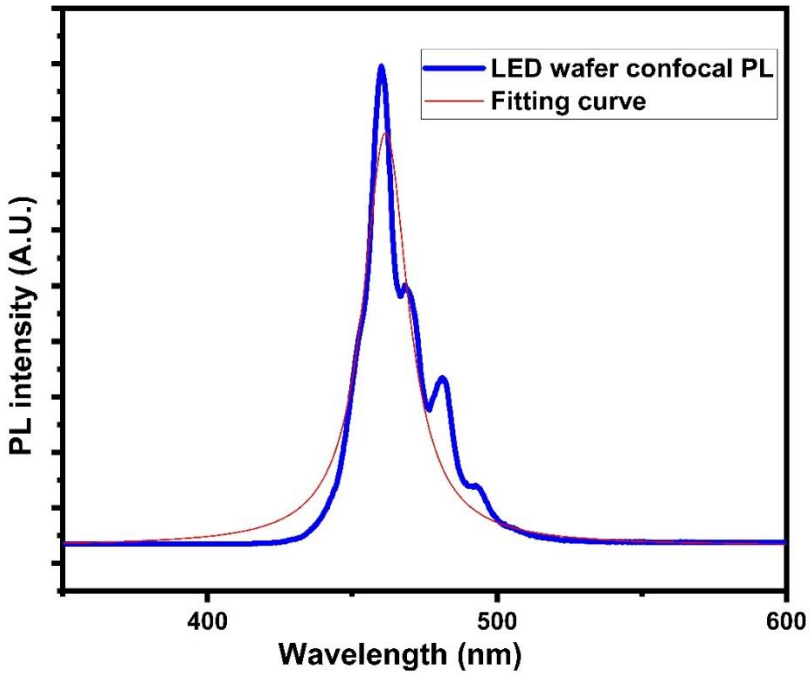

Figure 5.1 commercial GaN on Si LED confocal PL spectrum

5.3 LED device fabrication, characterisation and discussion

The fabrication of the RCLED by transfer printing involved the printing of the LED epilayer and DBR in a configuration allowing sandwiching of the LED between the DBR reflectors. This involved many different fabrication steps such as planar LED fabrication from the commercial LED wafer, anchor undercutting to achieve free suspended LED coupons, transfer printing of the LED and DBR as stacks to form RCLED. Various characterisation methods were used such as current-voltage measurements, electroluminescence, photoluminescence,

SEM, ellipsometry and more. Below is a detailed description of all the steps with relevant images for demonstration and illustration with discussion.

5.3.1 Planar Conventional rectangular (CR) LED

5.3.1.1 LED device processing of Conventional rectangular (CR) LED

As explained in Chapter 4, selective crystallographic wet etch of Si can be achieved thanks to the difference in KOH etch rates along the <110> direction compared to the direction orthogonal to it (100 times greater) [34][35]. For this reason, the first fabrication step was the patterning of the LED wafer with orientation lines parallel to the <110> direction. These orientation lines are important in alignment of the device coupons for effective undercut (as explained in Chapter 4). This was done by photolithography positive resist SPR350 patterning process followed with ICP-RIE ($SiCl_4/Cl_2/Ar_2$ 1.5/15/4sccm, 4mTorr, 20^oC, RF/ICP power 150/450W) etching for 3 minutes of the wafer achieving 15um wide, 360nm deep orientation lines with 8um separation, the result is illustrated in figure 5.2 a).

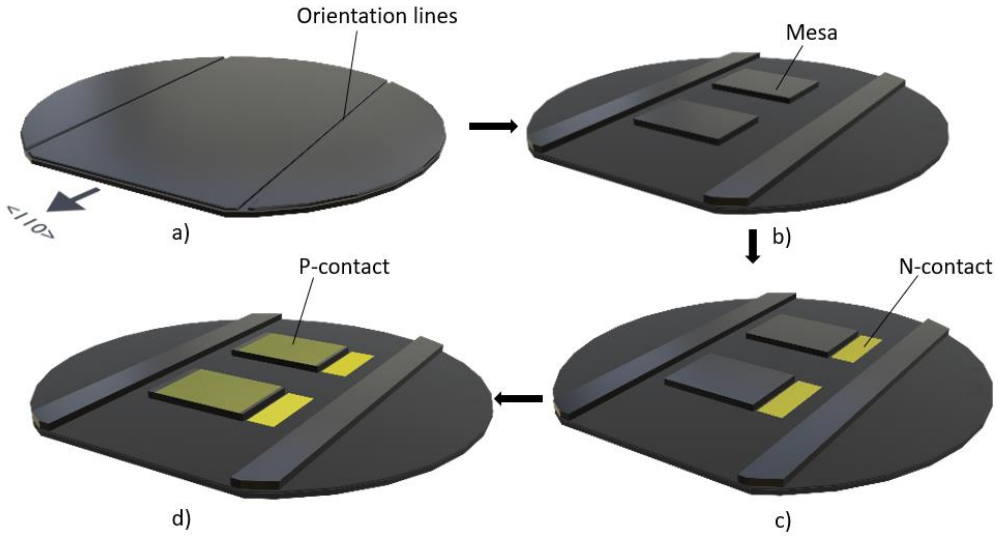

Figure 5.2 Conventional rectangular (CR) LED fabrication steps a) Orientation lines formed by RIE etch b) Mesa formation by ICP-RIE c) n-contact deposition and d) p-contact deposition by thermal evaporation

Next, the planar LED device was fabricated. Photolithography masks were newly designed for the fabrication of the LEDs as arrays of LED coupons attached to anchors by tethers, to be transfer printed. Figure 5.3 shows an illustration of the superimposed layers showing the different fabrication steps for a single device coupon. These are the mesa etch, n-contact, p-contact, bond pad and coupon etch. The devices coupons are attached to the anchors by tethers and are arranged to allow anchor alignment in parallel to the <110> direction (should be aligned

to the orientation marks lines made above). This is important in preventing undercutting of the anchors during the undercut of device coupons by immersing in KOH solution.

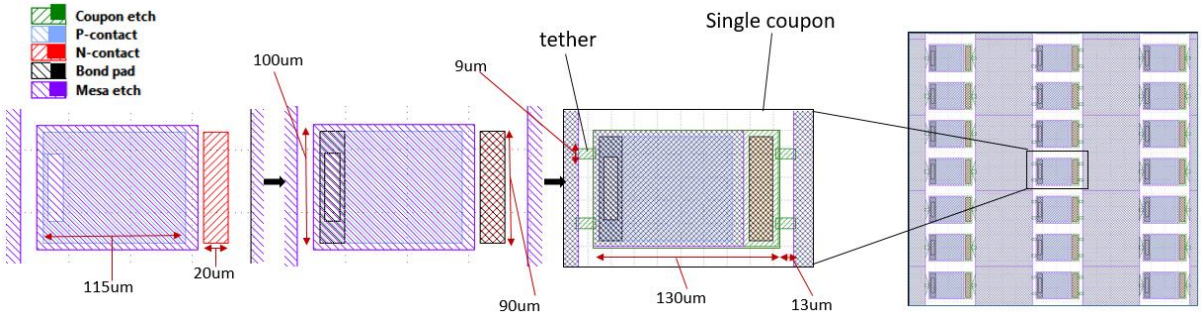

Figure 5.3 Photolithography mask design for Conventional Rectangular (CR) LED fabrication

The next fabrication step-involved mesa etching the wafer, this involves selective etching part of the wafer up to the n-GaN. Design mask shown in figure 5.3 was used to pattern the wafer using resist masking by photolithography, followed by ICP RIE ($SiCl_4/Cl_2/Ar_2$ 1.5/15/4sccm, 4mTorr, 20^{o}C, RF/ICP power 150/450W) for six minutes. Mesa etch with etch depth of approximately 750nm into the wafer (this etched region is represented by the shaded mesa etch region in figure 5.3) was done. Stripping the remaining resist using resist stripper (posistrip EKC830) and oxygen ashing yielded mesa etched patterned wafer as illustrated in figure 5.2 b).

Next, contacts (n-contact, p-contact and bond pads) needed to be deposited; this involved photolithography patterning, followed with metallisation and then lift off. In this case, a PMGI (polydimethylglutarimide polymer) is pre-deposited before the SPR350 positive resist. SPR350 upon development has a positive slope, which can be covered by the deposited metallic layer hence making the lift off challenging. The PMGI mitigates this problem by allowing a window opening for resist remover to penetrate and ease lift off. PMGI deposition was done by spin coating at 4000 rpms for 30s followed by baking at 180^{o}C for 7 minutes. n-contact consisted of metals Ti/Al/Ti/Au at thicknesses 20/100/20/60nm meanwhile the p-contact consisted of Ni/Au at thicknesses 5/5nm. These are illustrated in figures 5.2 c) and d) respectively. The wafer was then thermally annealed at temperature 520^{o}C in nitrogen (1600 sccm) and oxygen (400 sccm) rich environment for 1 minute. This enables the partial diffusion of the metal into the material (leading to almost transparent p-contact) and the formation of NiO_2 complex for efficient conduction (Ohmic contact); the result is illustrated in figure 5.4 a). This was followed

by bond pad deposition. Metals Ti/Au with thicknesses 20/200nm are used for the bond pad, figure 5.4 b) illustrates the result.

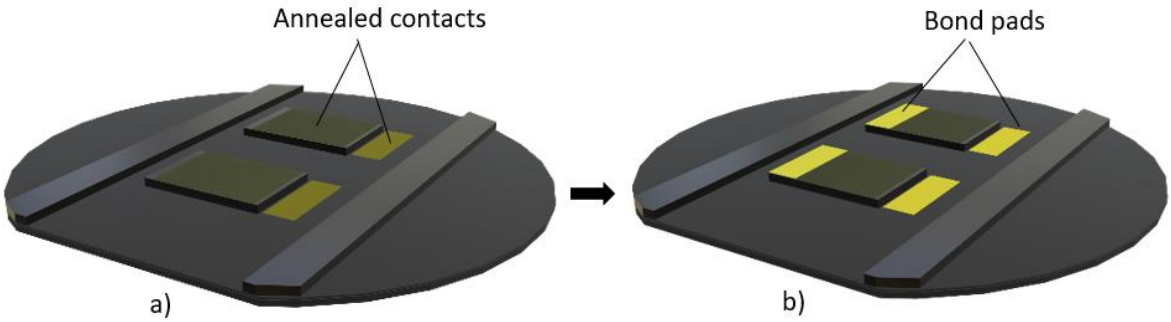

Figure 5.4 Conventional rectangular (CR) LED fabrication steps a) contacts annealing b) Bond pads deposition by thermal evaporation

This resulted to "Processed LED" array whose microscopic image is presented in figure 5.5

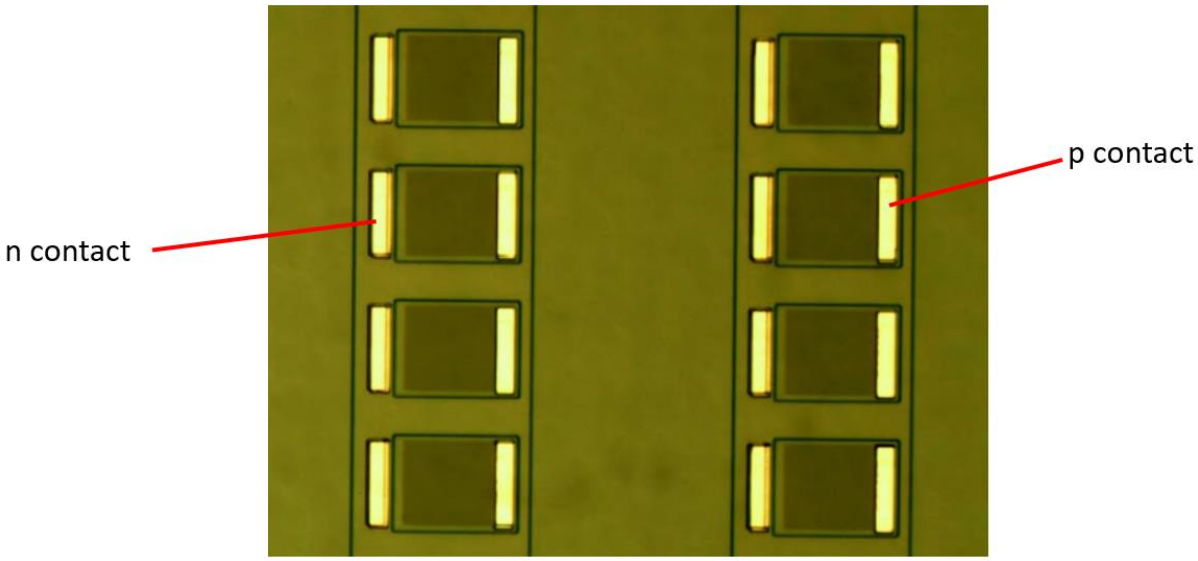

Figure 5.5 optical microscope image of Processed LED arrays

5.3.1.2 Anchor undercutting to achieve free suspended LED coupons for Conventional rectangular (CR) LED

5.3.1.2.1 STRESS COMPENSATION OPTIMISATION CONVENTIONAL RECTANGULAR (CR) LED

GaN LED epitaxially grown on Si substrate involves the use of a buffer layer Al(Ga)N to compensate the lattice and thermal expansion mismatches that exist between GaN and Si. This is engineered to ensure wafer flatness and minimise defects such as cracks within the grown epilayer hence achieving better quality grown materials. These grown materials have built-in residual stress, which may cause the epilayer to deform when released from its grown substrate [36][37][38] with the deformation more pronounced with increasing device sizes. The

deformation is a constraint to transfer printing as stamp-coupon contact is reduced and constraints further device processing after the printing. Hence, the need for compensating the residual stress.

Si based dielectric layers such as SiN_x and SiO_2 are commonly used in device fabrication to serve roles of hard mask for dry etching and diffusion, passivation layer and device encapsulation [39][40] . They offer the advantage of ease of deposition as high quality layers can be deposited at relatively low temperatures approximately 300^{o}C using Plasma Enhanced Chemical Vapour Deposition (PECVD). The mechanical stress of the dielectric also affects the underlying device properties and performance [41][42] hence, need to be considered. Shaban et al proposed a stress compensation mechanism for the LED release from Si substrate involving the deposition of 1um thick compressive SiN_x layer on top of the LED epilayer with compressive stress of 200 MPa [36]. This helps in compensating the built-in 70 MPa compressive stress on the LED epilayer [36] and in achieving a flat release coupon. The stress magnitude and stress profile can be controlled by the PECVD deposition parameters pressure, RF frequency of source, temperature, power density and gas stoichiometry [43].

To compensate the residual compressive epilayer stress from the released LED device, a dielectric material with compressive stress profile was required as discussed above. Dielectric film composition also determines its stress profile. This is dependent on the N_2O/SiH_4 (900/160) and NH_3/SiH_4 (5/100) gas flow ratios in the PECVD chamber during deposition for the SiO_2 and SiN_x layers respectively. This yield a SiO_2 and SiN_x layers primarily compressive and tensile respectively [43]. SiN_x was also required to serve as passivation etch barrier layer to the KOH undercut process to protect the underlining contacts and device. Four different compensation dielectric thicknesses were investigated; SiN_x/SiO_2 54/500nm, 54/1000nm, 54/1700nm and 54/2000nm. These were deposited by PECVD on the LED wafer prior to processing at temperatures 300^{o}C, pressure 900 mTorr and power 25W. The wafers were then patterned into device coupons sizes 100x100um using photolithography patterning (where the coupons attached to the anchors by tethers were left non-covered by the resist, followed by Ti/Ni (50/150nm) metallisation to serve as RIE etch mask. RIE etch (CHF3/O2 35/5 sccm, RF power 150W) for 60 mins through the full unmasked dielectric was then done, followed by stripping the metallic mask via submerging the samples in hot aqueous solution of HCl (7% volume concentration) for 20 minutes at 70^{o}C. Etching through the full LED stack and into the Si (1um) was done by ICP-RIE ($SiCl_4/Cl_2/Ar_2$ 1.5/15/4sccm, 4mTorr, 20^{o}C, RF/ICP power 150/450W) for 23 mins, this etched 800nm from the SiO_2 compensation layer (from SiO_2 etch

calibration using the same ICPRIE process above) and approximately 1.7um into the Si substrate. Therefore, the dielectric also serve as hard etch mask for the ICP-RIE, the final dielectric compensation layer (also serving KOH etch mask function) is actually SiNx/SiO_2 54nm/900nm. It should be noted that the first RIE etch steps were necessary as metal etching in our available ICP-RIE etch machine is forbidden, so metallic masking ICP-RIE etch could not be performed. Finally, anchor undercutting was done by submerging the wafers in hot aqueous solution of KOH (25%wt concentration) at 70^{o}C for 50 minutes. This yielded freely suspended LED coupons as shown in figure 5.6.

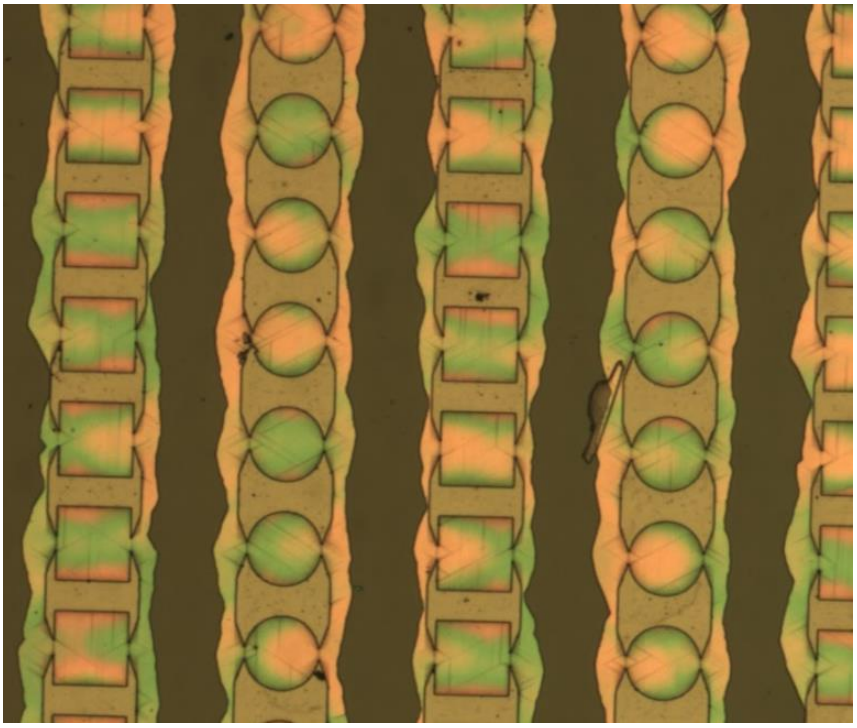

Figure 5.6 Optical microscope image of undercut suspended LED coupons

The stress compensation could be determined via deformation measurement using the Dektak Veeco 150 profiler. Figure 5.7 shows the obtained average step height (ASH) profiles for the four test configurations. Best stress compensation and almost flat coupon were achieved using dielectric layer thicknesses SiN_x/SiO_2 54/1700nm for 100x100um coupon sizes. These dielectric thicknesses configurations were used to stress compensate the released LED epilayer as described below

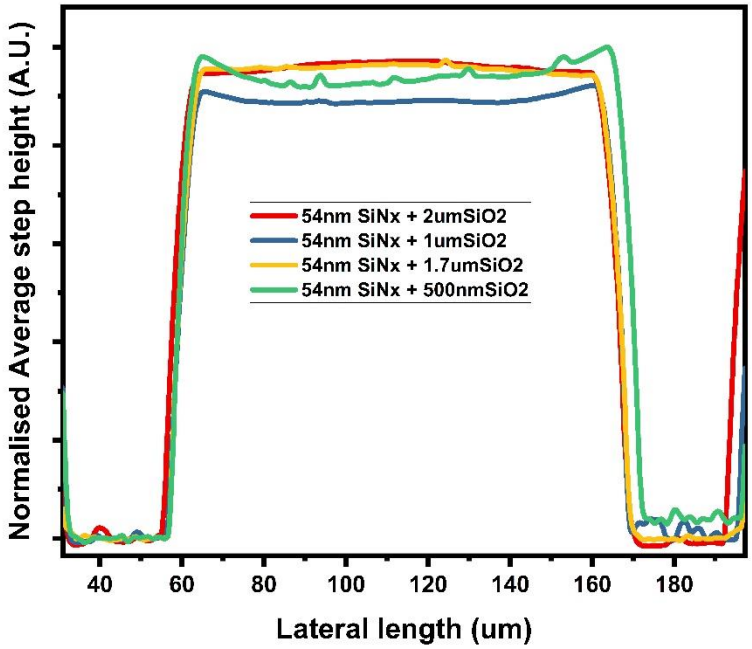

Figure 5.7 Profilometry step height measurement of undercut LED coupons showing level strain induced of deformation

5.3.1.2.1 STRESS COMPENSATION AND ANCHOR UNDERCUTTING OF LED COUPONS CONVENTIONAL RECTANGULAR (CR) LED

After the bond pads deposition as shown in figure 5.2 b), the built-in compressive stress needed to be compensated. This was done as described in section 5.3.1.2.1 with the exception of using a metallic Ti/Ni dry RIE etch mask to etch through the dielectric. This is because the Ti/Ni stripping required sample submerging in hot aqueous solution of HCl, which is a metal etchant hence not ideal. Therefore, a thick SPR220 photoresist mask was used instead. First, the SiN_x/SiO_2 54/1700nm layers were deposited by PECVD shown in figure 5.8 a). Next, the wafers were then patterned into device coupons sizes by photolithography patterning using photomask coupon etch shown in figure 5.3 (shaded area corresponds to resist masking). Effective alignment during the photolithography patterning leads to effective device masking by SPR220 resist. RIE etch (CHF_3/O_2 35/5 SCCM RF power 100W) for 35 mins through the unmasked (exposed) dielectric was then done. SPR220 re-masking followed by 35 mins RIE etch was repeated two more times in order to etch fully through the un-masked dielectric (total thickness of approximately 1700nm), shown in figure 5.8 b). This was followed by ICP-RIE using ($SiCl_4/Cl_2/Ar_2$ 1.5/15/4 sccm, 4mTorr, 20^oC, RF/ICP power 150/450W) for 23 minutes through the full LED stack and into the Si (approximately 1.7um), resulting wafer is illustrated

in figures 5.8 c). For device operation, electrical connection with the device contacts were required therefore, windows need to be open through the strain compensating dielectric on the n and p contact areas for making electrical connection to the bond pads. This was done by photolithography thick SPR220 resist masking as above (contact windows un-masked), followed by RIE etching (CHF3/O2 35/5 sccm 100W) for 35 mins. SPR220 re-masking followed by 35 mins RIE etch was repeated two more times in order to etch fully through the un-masked dielectric. Non-optimised dielectric RIE etch means some of the contacts would be etched too, causing some contacts damage. The resulting structure is illustrated in figure 5.8 d) and microscopic image shown in figure 5.8 e)

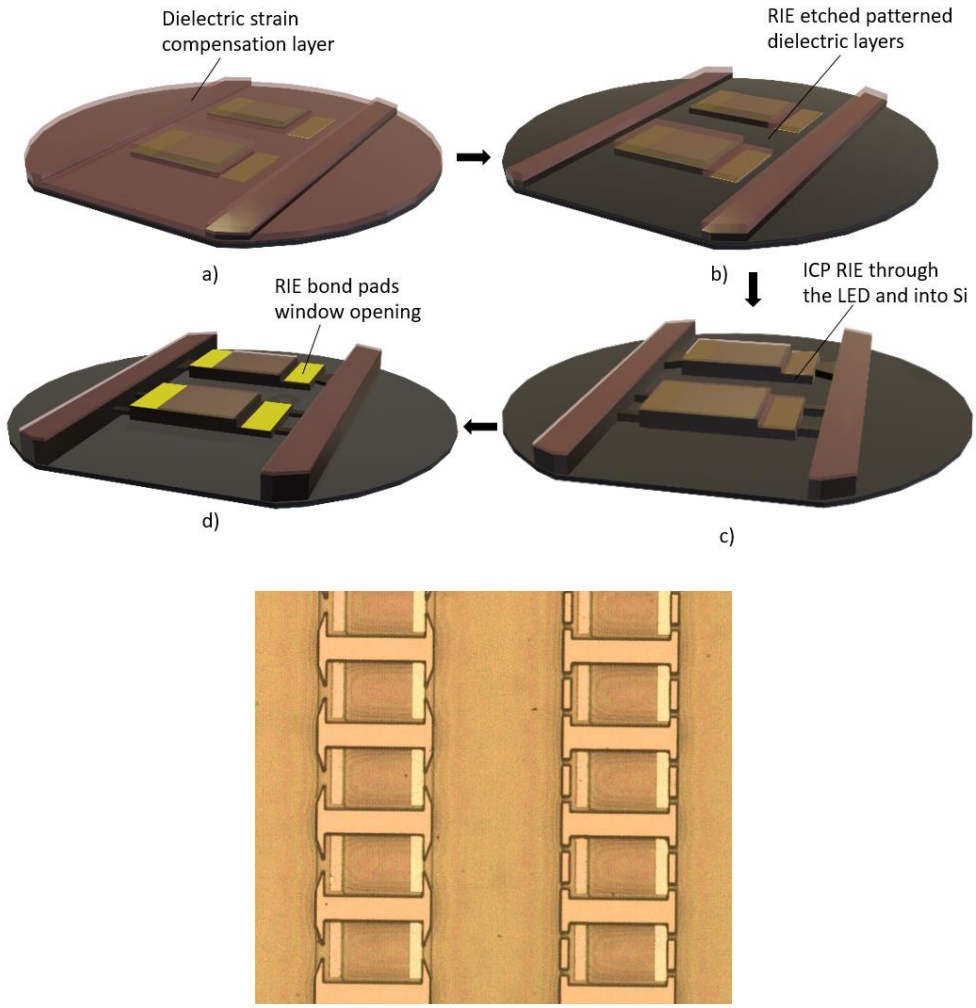

e)

Figure 5.8 Conventional rectangular (CR) LED fabrication steps a) Dielectric strain compensation layer deposition by PECVD b) Dielectric layer selective etch by RIE c) LED coupon patterning by ICP-RIE d) contacts window opening by RIE e) Optical microscope image of LED formed LED array

Anchor undercutting was done by submerging the wafers in hot aqueous solution of KOH (25%wt concentration) at 70^{o}C for 50 minutes (100x100um coupon size device) resulting to freely suspended LED coupons ready for transfer printing as shown in figure 5.9. The suspended LED devices where then ready for transfer printing

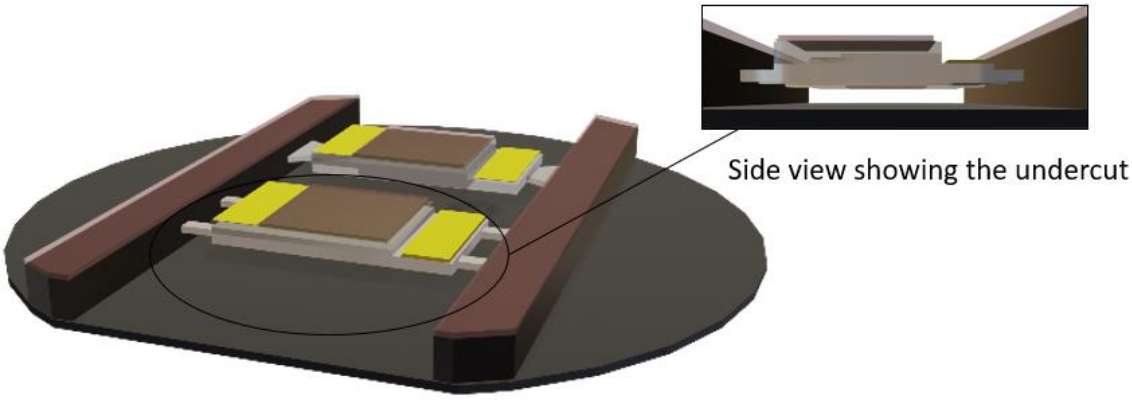

Figure 5.9 Illustration of KOH wet etch undercut LED coupon

Very high yield close to 100% where achieved confirming the suitability of our design. SEM images of the undercut LEDs coupon array were also taken as shown in figure 5.10. Empty space left from transfer printed (TP) LED coupon are also shown.

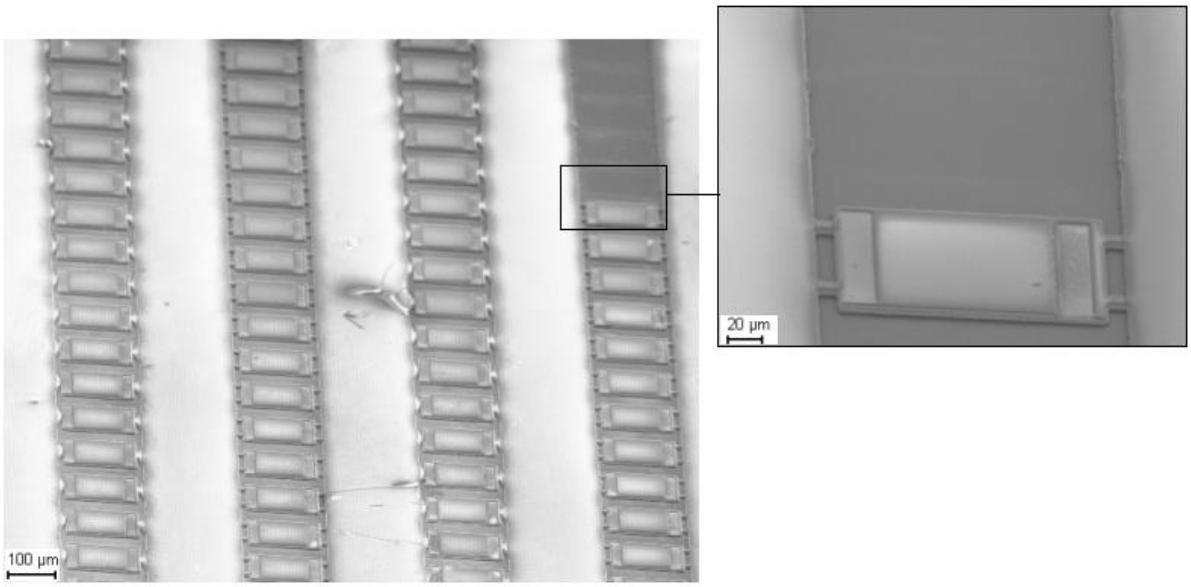

Figure 5.10 SEM of undercut array of Conventional Rectangular (CR) LED (inset showing a single device coupon)

5.3.1.3 Transfer printing of the LED and DBR as stacks to form RCLED for Conventional Rectangular (CR) LED

The full LED coupon transfer printing is illustrated in figure 5.11

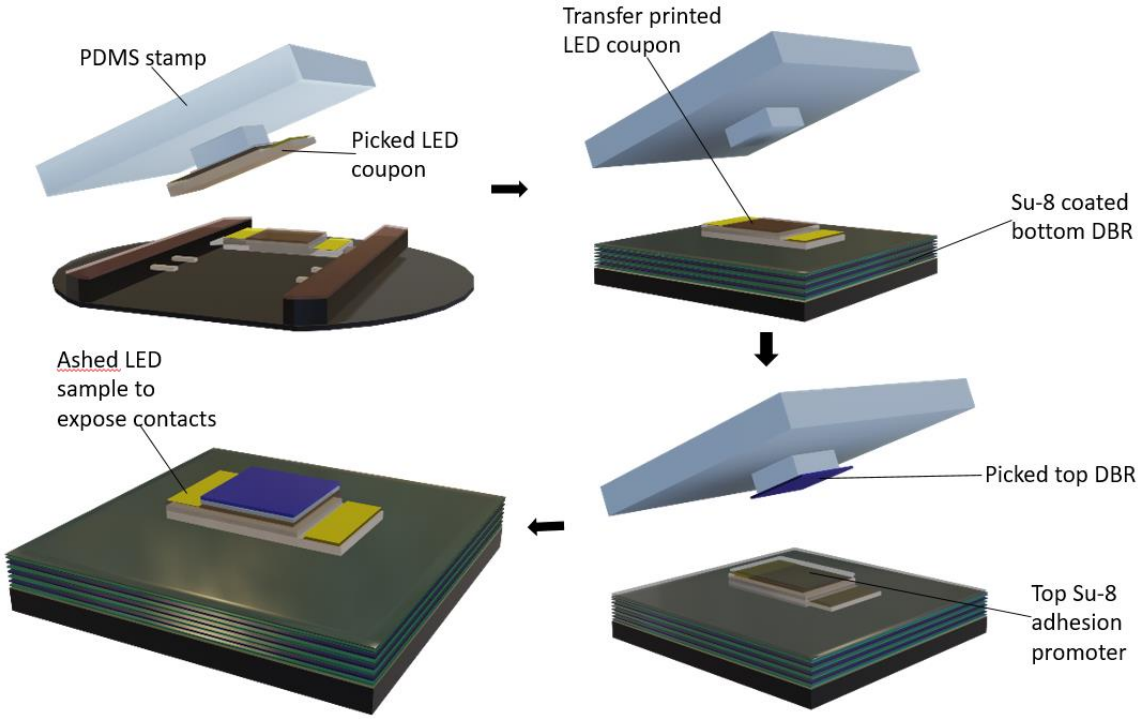

Figure 5.11 Transfer printing of LED coupon on bottom DBR

PDMS stamp with pedestal size (100x100um) were made as described in Chapter 4. Prior to transfer printing, SiN_x/SiO_2 dielectric DBR with thicknesses 54nm/78nm tuned for centre wavelength corresponding to the LED emission peak of approximately 460nm were grown on Si (111) substrate. Two different sets were grown, 12.5 pairs and 5.5 pairs with calculated peak reflectivity 99% and 60% to serve as the bottom and top reflectors respectively of the RCLED. Figure 5.12 shows their measured reflectivity spectra, showing reflectivity peak matching the theory.

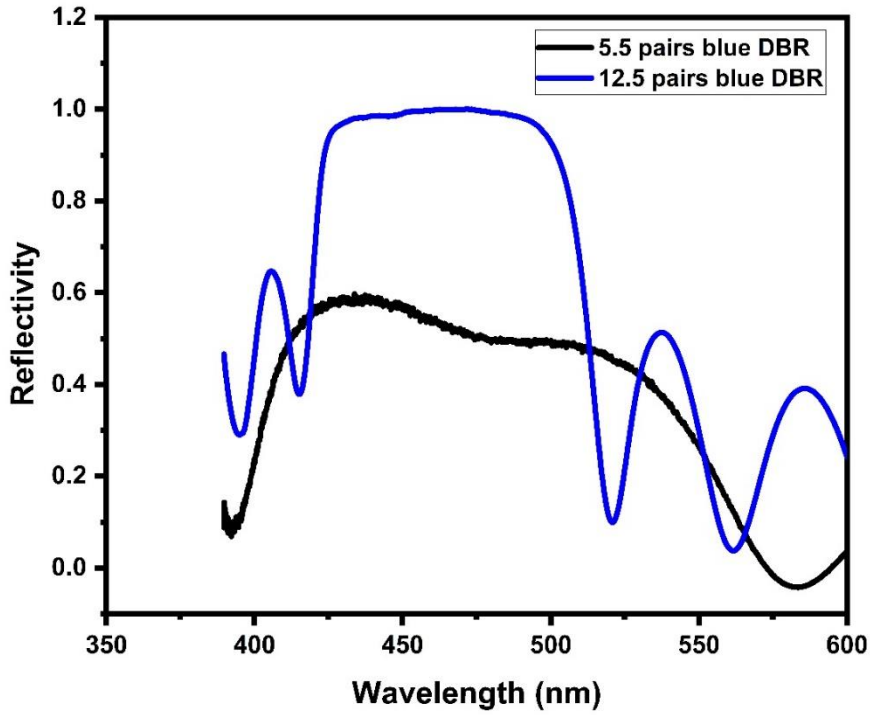

Figure 5.12 measured reflectivity spectrum plot of 12.5 pairs (bottom DBR) and 5.5 pairs (top DBR)

Freely suspended DBRs were achieved by anchor undercutting as described in chapter 4. SU-8 3000 photoresist was used as adhesion promoter for the transfer printing thanks to its high tackiness. An SU-8 layer of thickness approximately 1.5um was deposited on the bottom DBR by spin coating at a speed of approximately 12000rpm for 30s. The suspended LED coupon was then transfer printed on the SU-8 coated bottom DBR using the pedestalled stamp, similar retraction speed values of 15mm/s was enough to break the tethers and perform the LED coupon pick-up. The LED coupon could then be printed on the SU-8 coated blue DBR sample (bottom DBR); for this, slower retraction speed of 0.003mm/s was used. Microscopic images of the picking process and resulted transfer printed LED device on a blue DBR are shown in figure 5.13. This represents the “Transfer Printed LED” device

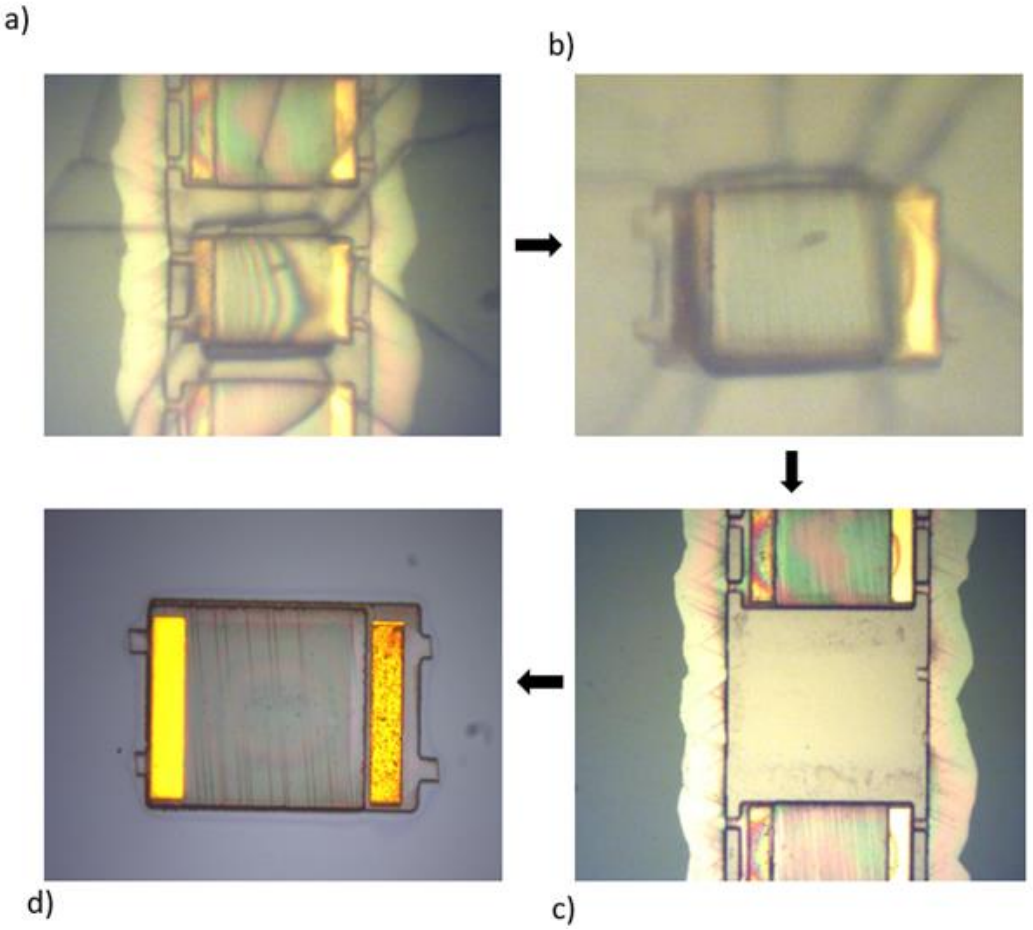

Figure 5.13 Optical microscope images of LED coupon transfer printing a) PDMS stamp pedestal brought in contact with LED coupon (view from top through the transparent PDMS) b) LED coupon picked by stamp c) image of broken tethers from picked LED coupon d) printed LED coupon on bottom DBR

Taking a closer look at figure 5.13 d), some Newton interference rings can be seen. These occurs as a result of existing air gaps between the LED coupon bottom surface and the substrate, this shows the transfer printed LED coupon is not perfectly flat as expected. In order to check the level of flatness, profilometry measurement of the transfer printed LED coupon were carried out along the lateral direction as shown in figure 5.14. Minimal deformation can be seen from the printed LED coupon, this shows the importance of the SiN_x/SiO_2 strain compensation layers.

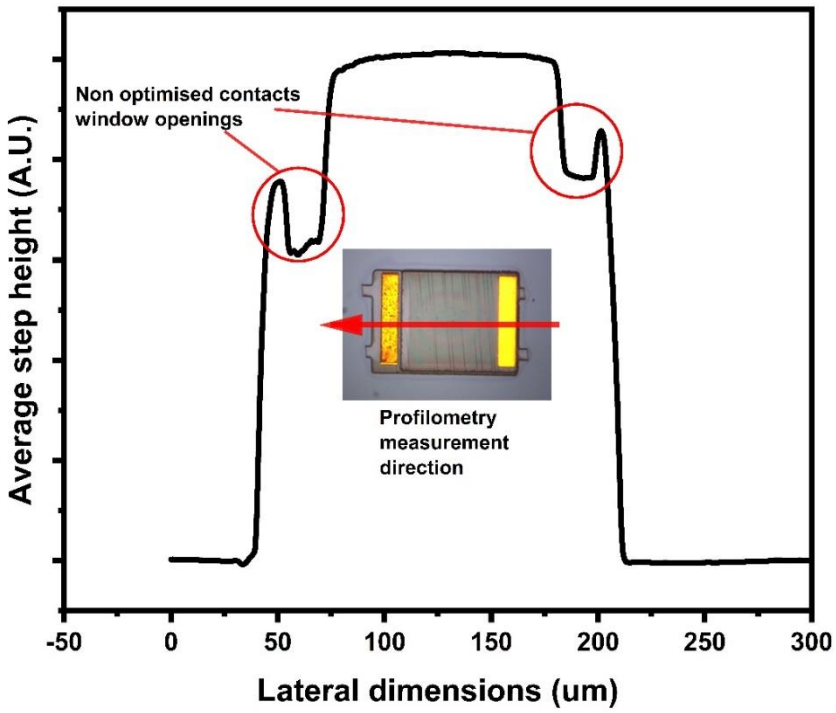

Figure 5.14 profilometry measurement of average step height of transfer printed LED coupon

A thicker top 1.7um thick SU-8 adhesion layer was deposited. Then the top DBR was transfer printed on the LED emission area. For effective contact probing, the SU-8 spin coated on the contacts needed to be removed; this was done by ashing (O_2 250sccm 150W for 60s) the sample for 6 cycles. Hence a cavity LED was formed, illustrated in figure 5.15

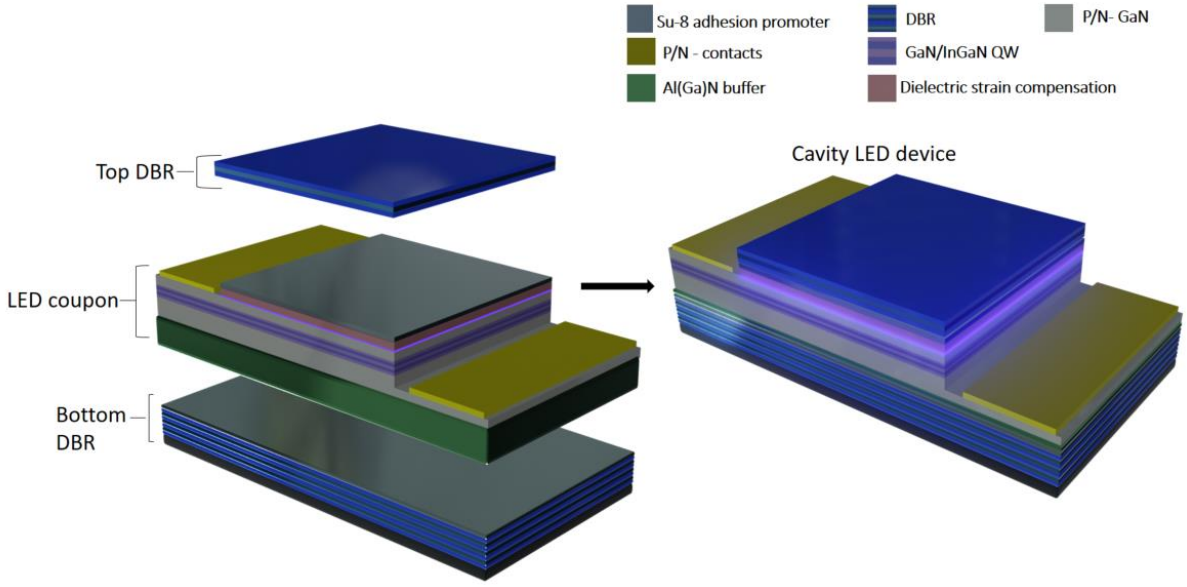

Figure 5.15 Assembled conventional rectangular cavity LED illustration

Optical microscope and SEM images of the final "cavity LED" device is shown in figure 5.16. As it can be seen, ashing leads to twisting and wrinkling of the bottom SU-8. This has important implications as discussed in later sections

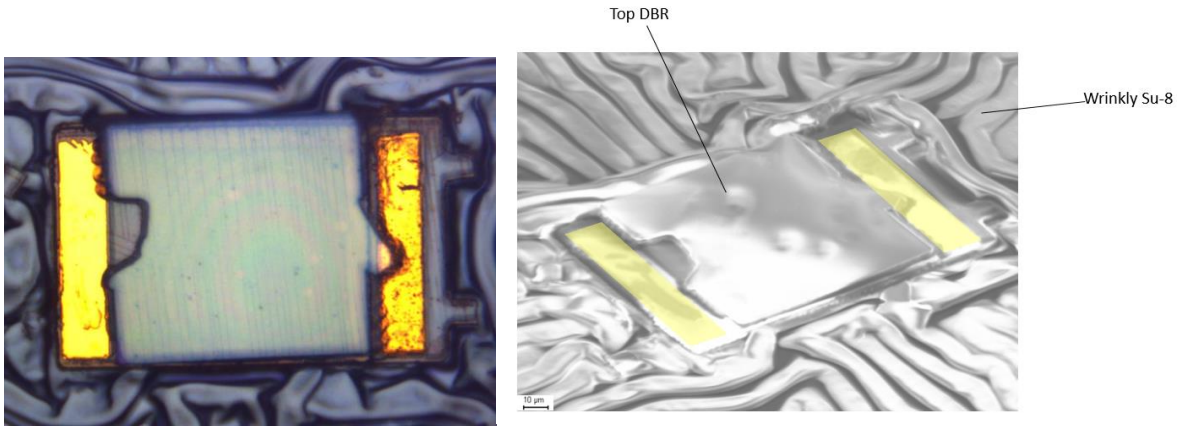

Figure 5.16 Optical microscope (left) and SEM images of the transfer printed conventional rectangular cavity LED device

5.3.1.4 Electrical and optical characterisation of Conventional rectangular (CR) LED

The fabricated cavity LED device could then be characterised, this was done both electrically and optically by carrying out IV (current-voltage) plots and electroluminescence measurements. These measurements were carried out at three different stages of the fabrication process; Processed LED, Transfer Printed LED (TP LED) and LED cavity. The processed LED characterisation stage represents the stage after the bond pads deposition that is before the

dielectric layers strain compensation step. The TP LED stage represents that after transfer printing the LED coupon device onto the bottom DBR pre-coated with SU-8 resist adhesion layer. The LED cavity stage represents the final stage that is after the transfer printing of the top DBR and adhesion layer (SU-8) ashing to expose the contacts. Figure 5.17 shows the obtained IV curves

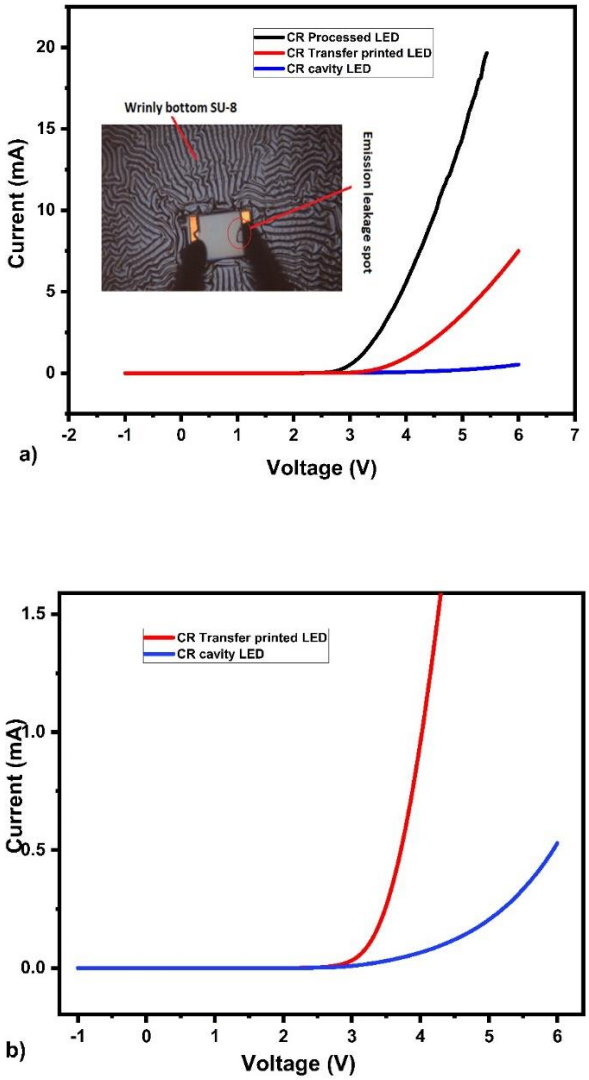

Figure 5.17 Current-Voltage plots of CR LED devices a)processed, transfer printed and cavity (probed image shown in inset) b) transfer printed and cavity

An optical microscopic image of the probed turned OFF cavity LED is also shown in the inset of figure 5.17 a). Turn-on voltage of approximately 2.7V can be seen with processed device IV behaving similar to literature [36]. Considerable reduction in device voltage for similar current values as the device processing goes from processed to transfer printed and finally cavity can

be seen. This is an indication of an increase in device series resistance. The increase in series resistance from the processed device to the transfer printed and cavity could be explained by the potential damage of the p and n contacts during their window opening via RIE etching through the strain compensation SiN_x/SiO_2 dielectric layers as explained in section 5.3.1.2.1. These window openings were necessary for probing. In addition to that, the samples were next submerged in hot aqueous solution KOH for coupon undercut. Hot aqueous solutions of KOH have been shown to attack and chemically wet etch some of the metals used as our device contacts and bond pads Ti and Al [44] [45]. Therefore, the combined efforts of the dry RIE contacts window opening and KOH wet etch potentially caused some damage to the contacts hence the increase in device series resistance. Transfer printing of the top DBR required spin coating of another layer of SU-8 layer to serve as adhesion promoter layer as described in section 5.3.1.3. In order to remove the SU-8 covering the contacts (for effective probing), the sample was subjected to long ashing which removed the top SU-8 layer. However, some SU-8 residue could have remained on the contact. This could explain the increase in series resistance of the cavity LED compared to the transfer printed LED as the SU-8 residue acts as a barrier to carrier injection.

Injected current dependent electroluminescence measurement of the Processed LED, Transfer Printed LED and cavity LED are shown in figure 5.18. Fabry-Perot interference oscillations as in the case of CPL measurements above can be seen for the processed LED EL. Overall increase in EL peak intensity as injected current is increased can be seen, this is because of an increase in injected carriers into the device quantum wells. This leads to an increase in the recombination rate hence more photons released via spontaneous emission. In addition, Fabry-Perot interference oscillations were reduced in the transfer printed and cavity LED thanks to the reduction in total internal reflection due to the strain compensation layers. Emission peak wavelength position for all 3 device configurations were also plotted as a function of injected current as shown in figure 5.18 d). An overall blue shift in emission peak can also be seen with increase in injection current, this can be explained by the Quantum Confined Stark Effect (QCSE) screening due to the band filling effect from the injected carriers [46] [47].

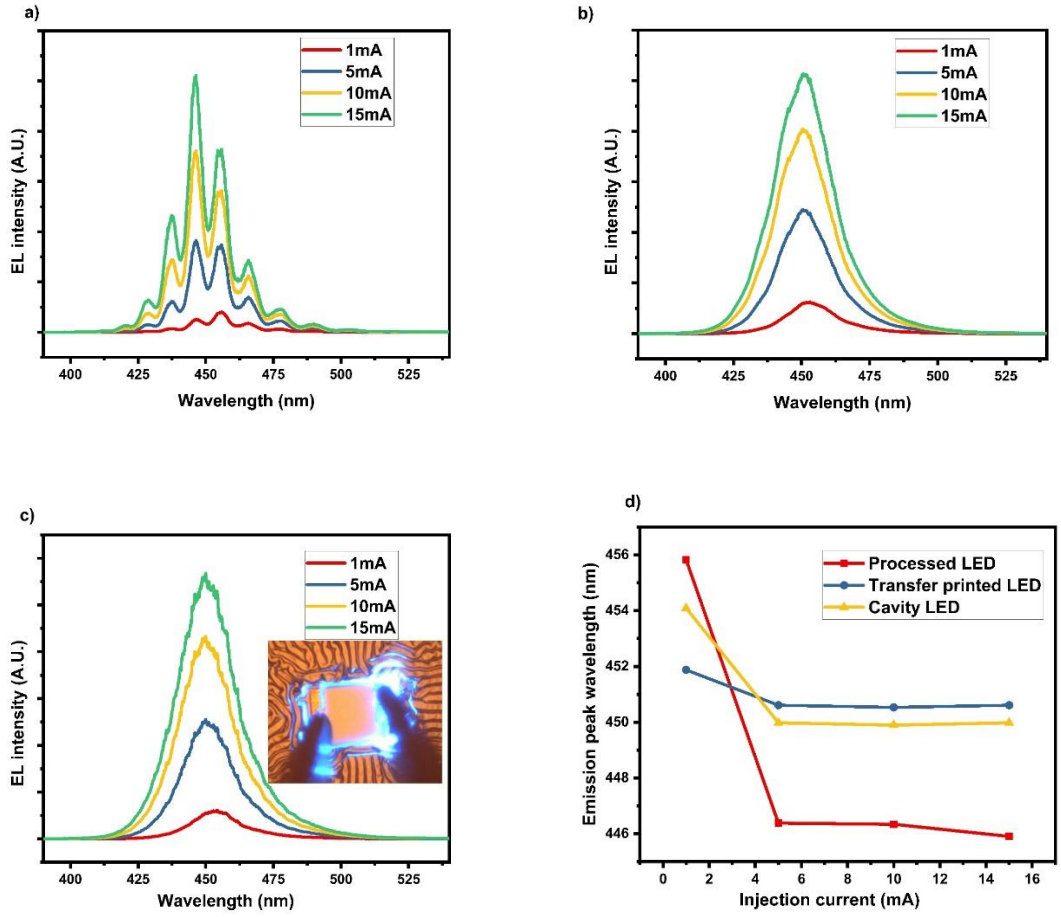

Figure 5.18 Optical characterisation of conventional rectangular LED; Injection current dependent EL of a) Processed b) transfer printed and c) cavity LED d) emission peak position against injection current

Comparing the EL peak wavelength position at injection current of 1mA for all three devices, values of 455.8nm, 451.8nm, and 454.1nm for processed, transfer printed and cavity LED respectively can be seen. Transfer printing the device from its original semiconducting Si substrate to the new insulating SU-8 polymer coated dielectric DBR substrate greatly reduces the device's heat dissipation capabilities. For this reason, the self-heating effect is higher in the transfer printed LED than in the original LED. In addition, the deposited strain compensation dielectric increases the self-heating. One of the well-known effect of self-heating in GaN based LED is bandgap shrinkage. Increase of carriers into the QW causes a blue shift in emission thanks to QCSE screening. This effect is seen in all LED devices but clearly less in the transfer printed and cavity LEDs. The increased heating effect on both the Transfer Printed LED and Cavity LED could explain their reduced emission blue shift as injection current increases compared to the Processed LED.

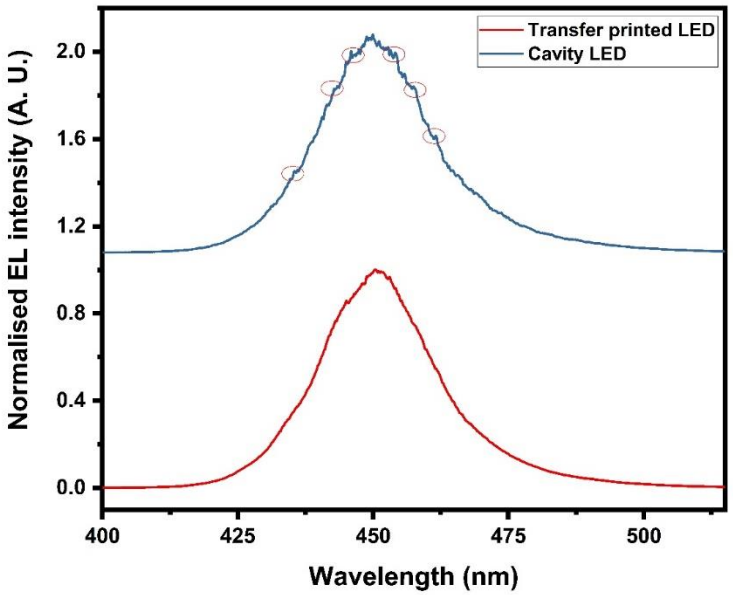

Figure 5.19 Normalised EL plot of transfer printed and cavity LED at 10mA injection current; small peaks can be seen on the cavity LED plot (annotated using red circles)

Figure 5.19 shows a plot of the normalised EL of the transfer printed (TP) LED (non-cavity) and the cavity LED at similar injection current of 10mA. Both curves have FWHM approximately 21.5nm. Reduction in the emission FWHM that is a typical characteristic of RCLEDs could not be achieved. However, what appears to be some resonant micro-cavity effects, small peaks can be seen on the cavity LED plot (annotated using red circles), which could potentially be an indication of cavity mode effects from the resonant cavity as they are evenly spaced. Nonetheless, those peaks are weak and almost unnoticeable. Confocal PL (CPL) measurements of a cavity LED sample of the same configuration but different cavity length (different spacer layer) were taken and shown in figure 5.20. The CPL shows more dominant multiple peaks for the incavity measurements adding more credibility to the cavity mode hypothesis. CPL small spatial resolution allow for light collection only at the spatial plane and spot size (pinhole) of 10um. Therefore, mostly cavity coupled light is detected.

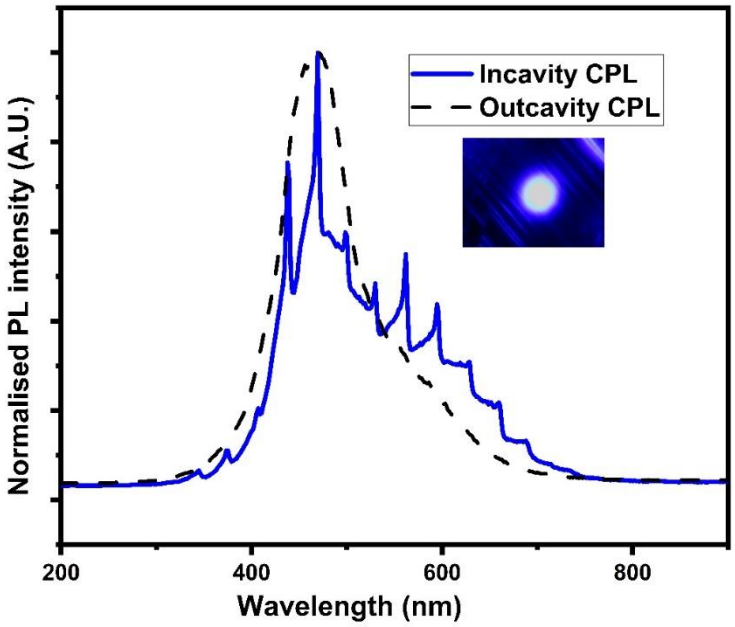

Figure 5.20 Confocal PL measurements of conventional rectangular LED for both transfer printed device (outcavity CPL) and cavity device (incavity CPL)

Assuming these peaks appear because of cavity mode coupling, their low intensity seen on the EL is an indication of a low cavity coupling strength. The low cavity coupling strength could be an indication of major emission leakage from the cavity, which are collected by the EL system objective and coupled to the system's monochromator and CCD. This is supported by the image of the probed turned off device shown in figure 5.21 showing an emission leakage spot from broken top DBR. Image of the turned on cavity LED (figure 5.21) also shows considerable p-bond pad region emission side device emission plane scattered by the wrinkly SU-8, which are not coupled to the cavity.

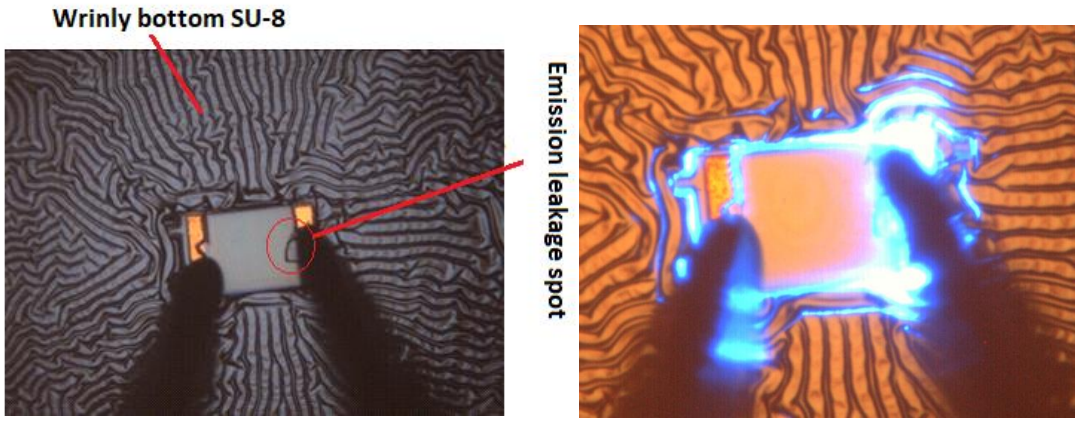

Figure 5.21 conventional rectangular cavity design flaws allowing emission leakage from the cavity

Therefore, the structure of our transfer printed cavity LED needed to be modified to ensure minimal LED emission leakage out of the cavity. Making the LED emission area considerable smaller than the top DBR area appeared to be a possible solution. New strategies were developed in order to implement emission area reduction for the LED device; these are discussed in the following section.

5.3.2 Reduced emission area LED (RD LED)

5.3.2.1 Design and fabrication of reduced area LED

Various methods have been reported for GaN based LED emission area reduction that is, restricting the LED emission to an area less than the mesa. Notable methods include selective Si diffusion into the p-GaN [48] and selective dielectric masking of the mesa [49][50]. p-GaN deactivation via CHF_3 plasma treatment were reported [51], the full deactivation mechanism remains without full scientific explanation but potential causes are p-GaN Mg acceptors deactivation by hydrogen in CHF_3 leading to lower hole concentration and hence lower p-GaN conductivity. In addition, the F from CHF_3 could implant on the p-GaN leading to increased metal-semiconductor Schottky barrier height [52] [51]. p-GaN deactivation by RIE CHF_3 treatment was chosen as it offers more effective emission area reduction.

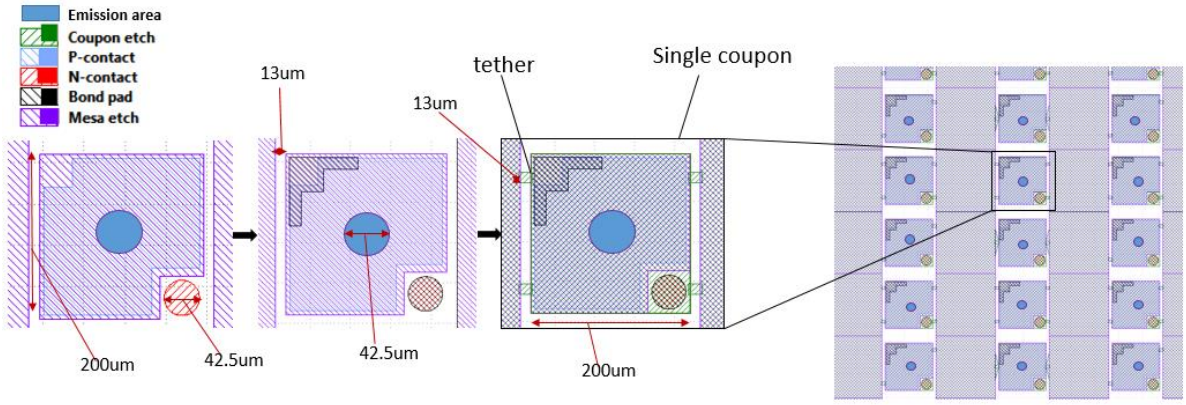

Figure 5.22 Photolithography mask design for Emission reduced area (ER) LED fabrication

A more standard LED structure of size 200x200um was used. Figure 5.22 shows a representation of the mask superimposed layers showing the different fabrication steps for a single device. Apart from the size difference compared to the Conventional Rectangle (CR) LED above, there is also the inclusion of the emission-reduction area step. This step will allow deactivation of the full mesa except centred small circle of diameter 42.5um, which is considerably smaller than the DBR (100x100um) as wanted. The selective p-GaN deactivation was done at the start of the device fabrication. This is the only fabrication difference when compared to the conventional rectangle (CR) LED fabrication described in section 5.3.1. Figure 5.23 illustrates these steps.

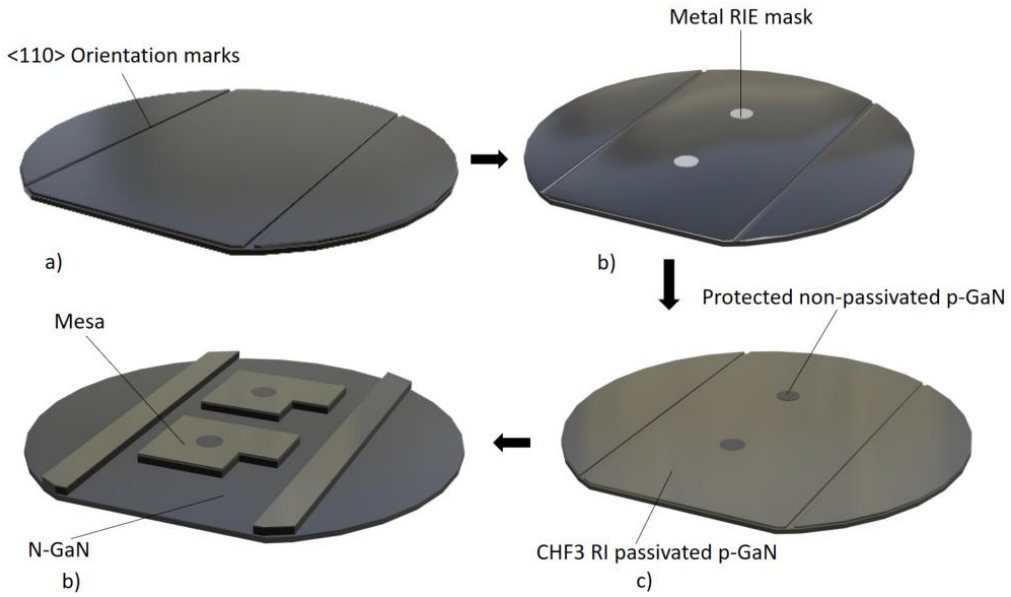

Figure 5.23 Emission reduced area (ER) LED fabrication steps a) orientation marks produced by ICP-RIE b) emission area metallic masking via thermal evaporation c) non-emission area p-GaN passivation by CHF_3 RIE treatment d) mesa formation by ICP-RIE

Selective RIE CHF_3 treatment of the LED wafer required adequate masking, metallic masking was chosen for this purpose. First the LED wafer was patterned to define the <110> orientation directions as described in section 5.3.1.1. Next, selective masking of the wafer regions corresponding to the emission areas were done via lithography followed by metallisation Ti/Ni 20/100nm to serve as mask. The wafer could then be RIE etched under conditions RF power 150W, gasses CHF_3/O_2 at concentrations 35/5 sccm for 2.5mins for deactivation of the unmasked p-GaN. Removal of the metallic mask were then done by submerging the wafer in a hot aqueous solution of (35% HCl diluted as 25% volume in water) at 70^{o}C for 20 mins. From this step the LED fabrication was exactly the same as described in section 5.3.1; mesa etch, n-contact deposition, p-contact deposition, contacts annealing, bond pads deposition. This yielded the ER processed LED. Dielectric strain compensation layer deposition was also done followed by dry etch through the dielectric-LED structure and into the Si substrate, contacts window opening by RIE etch and LED coupon undercut using KOH solution (longer etch time of 100mins as the coupons are larger in size). SEM image of the achieved undercut LED coupon array is shown in figure 5.24

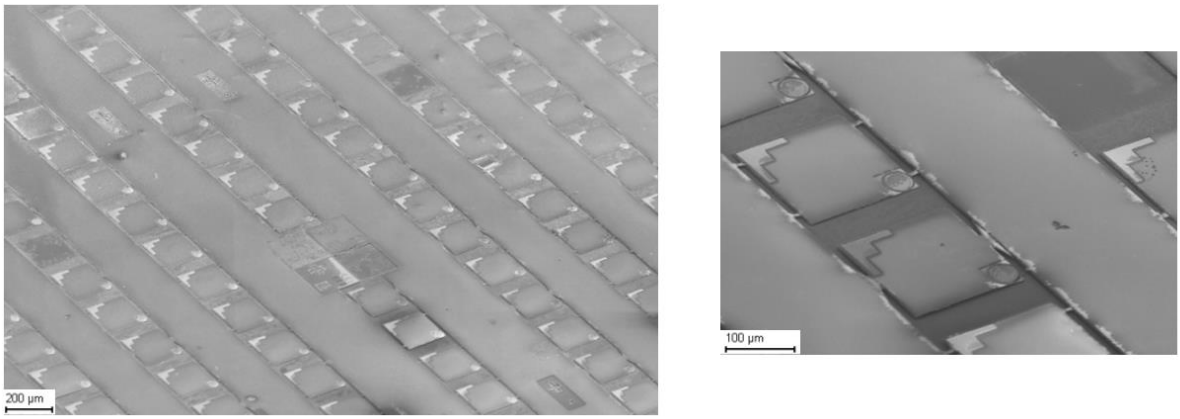

Figure 5.24 SEM of undercut array of emission reduced (ER) LED

Transfer printing of an LED coupon was done on bottom DBR substrate as in the case of CR transfer printed LED above, this yielded the ER transfer printed LED. Figure 5.25 presents transfer printed LED SEM.

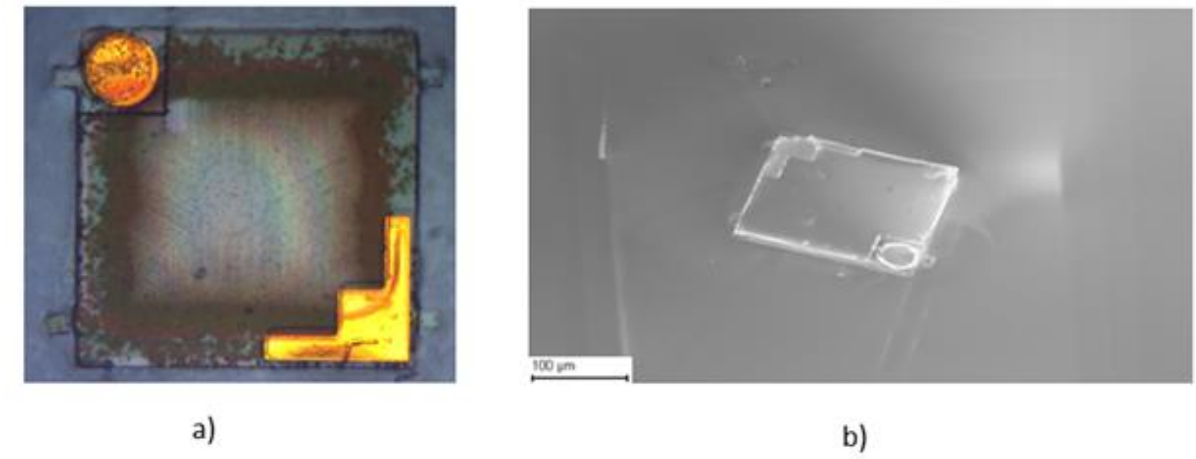

Figure 5.25 images of transfer printed emission reduced (ER) LED on bottom DBR a) optical microscope b) SEM

Finally, the ER cavity device was fabricated by transfer printing a top DBR, figure 5.26 illustrates the final new LED cavity structure with reduced emission areas. Optical microscope and SEM of the cavity LED are also shown. Edges of the device appear to have been attacked by the KOH, this is because a longer KOH etch time was required to fully undercut the 200x200um coupons. Therefore, KOH etch mask greater than SiNx/SiO_2 54nm/900nm is required for 200x200um devices. In addition, the bottom SU-8 adhesion layer is also wrinkly so the heating effects discussed above should also exist in these devices

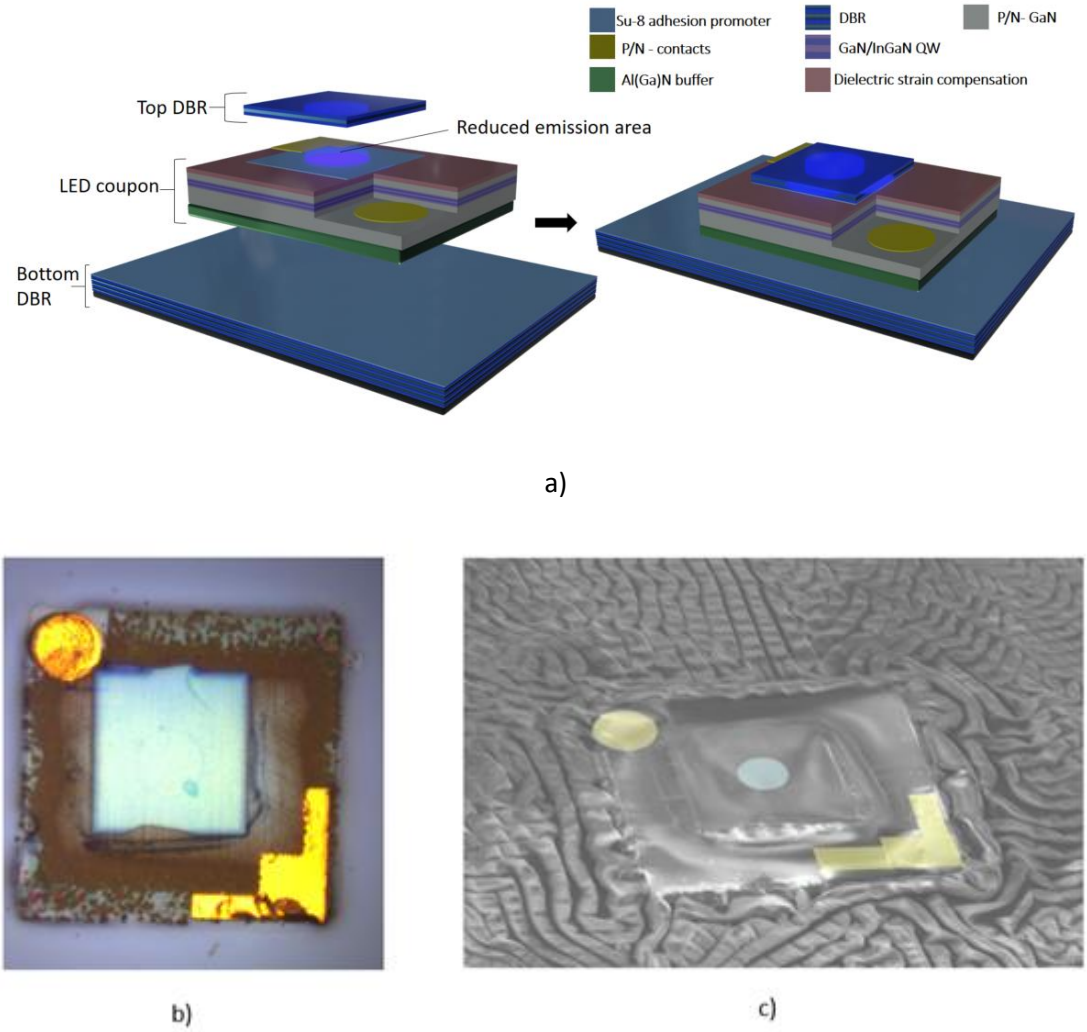

Figure 5.26 Transfer printed emission reduced (ER) LED cavity device a) assembly illustration b) SEM c) optical microscope images

5.3.2.2 Electrical and Optical characterisation of reduced emission area LED

Similar characterisation as in section 5.3.1.4 were done. Figure 5.27 shows the IV curve of the LED device at the 3 stages of process, transfer printed LED and cavity LED. Similar behaviour as in the case of CR LED structure above can be seen, that is, the device series resistance increases from processed to transfer printed LED and finally cavity LED. The explanations given in section 5.3.1.4 still holds as the fabrication procedures and steps were the same. Nonetheless, the slope decrease appears to be lower for the ER devices, therefore the series resistance increase is lower for these new device. This is because smaller emission area devices tend to have better p layer spreading [34] hence better p conduction compared to larger 100x100um emission area from the conventional rectangle LED above.

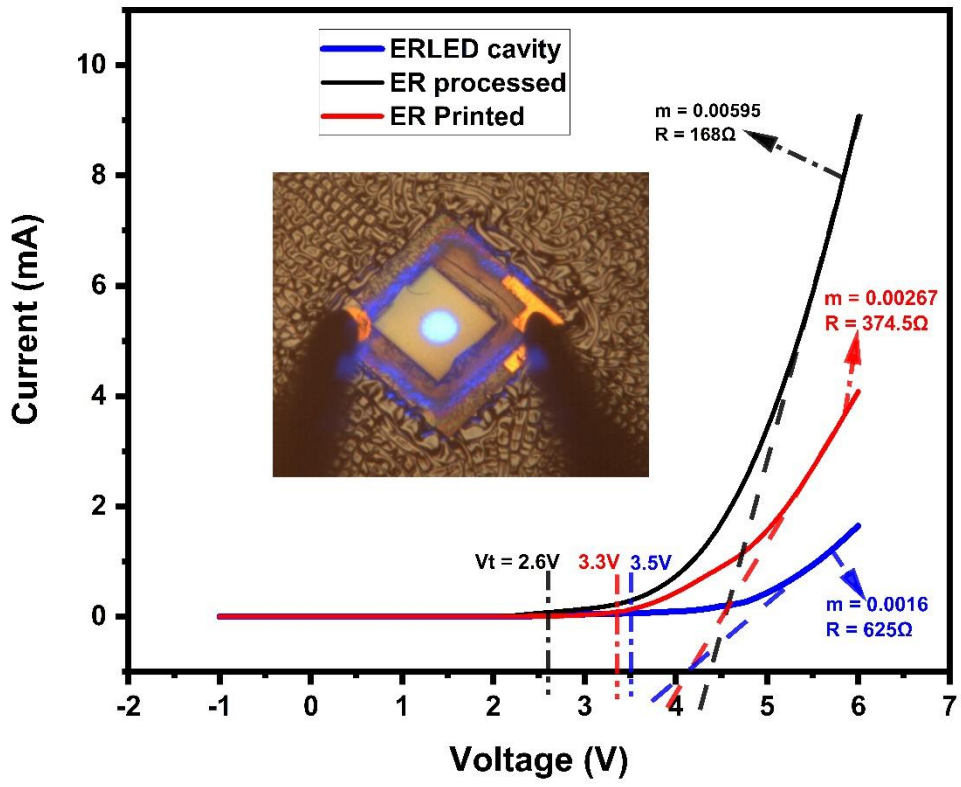

Figure 5.27 current-voltage plot of emission reduced (ER) processed, transfer printed and cavity LED devices

The probed turned on cavity LED device is also shown in the inset of figure 5.27, the LED emission leakage can be seen to have been considerably reduced as most of the light can be seen coupled to the cavity thanks to the reduced emission area compared to the top DBR. EL measurements of the device at different injection currents were also carried out as shown in figure 5.28. Fabry-Perot interference effects can also be seen in the processed LED, which are eliminated during the next stages just like in case of the rectangular LED above. Emission intensity increases with injection current increase and emission blue shift can be seen in the processed LED, which become almost unnoticeable for the transfer printed LED and cavity LED for similar reasons as discussed in section above for the case of CR LED.

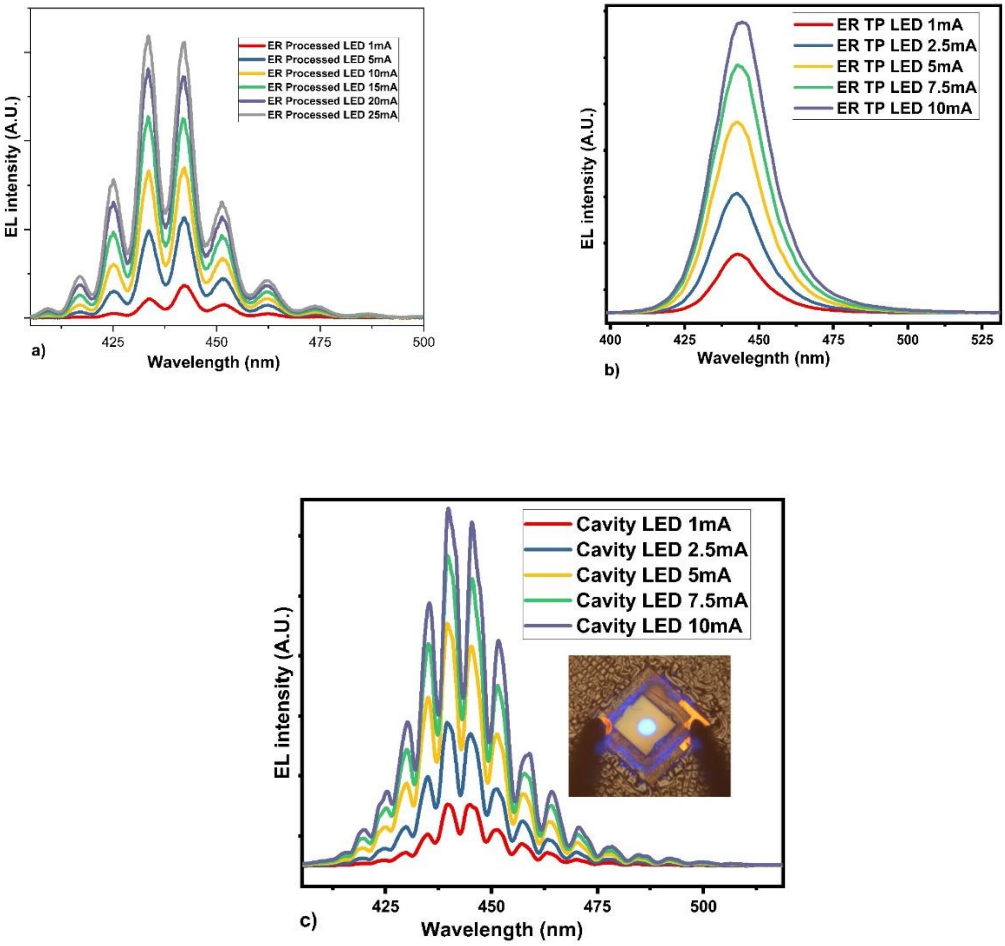

Figure 5.28 Injection current dependent EL measurements of a) processed b) transfer printed and c) cavity LED

Plotting of the transfer printed (TP) LED (non-cavity) and the cavity LED's normalised ELs at similar current injection value of 10mA is shown in figure 5.29.

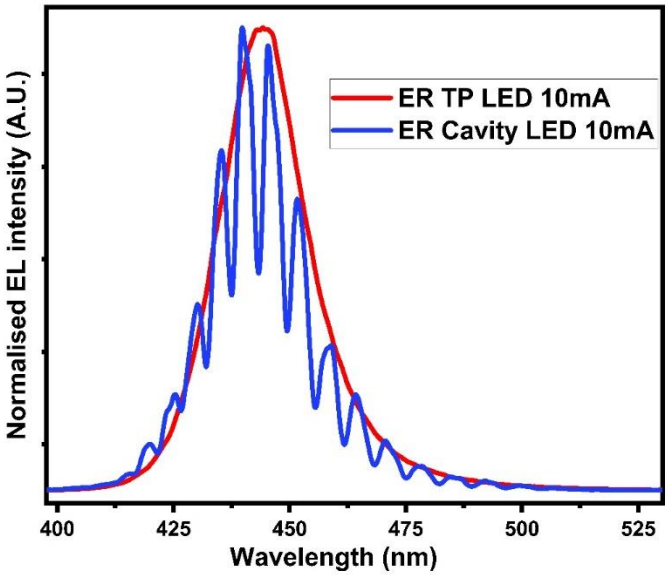

Figure 5.29 Normalised EL of transfer printed and cavity LED at 10mA injection current

Unlike the CR LED device above, clear resonant cavity effects can be seen on the cavity LED plot. Numerous well-defined peaks can be seen which are evenly spaced with spacing of 6nm. These peaks appear to be cavity modes because of the coupling effect of the LED emission to the cavity modes. ER cavity LED EL peak appears to be at a lower wavelength (440nm) than that of the transfer printed LED (444nm), this could be because of heating effects or cavity mode effects as microcavity modes are independent of injection current [53] but solely on the cavity length. It could also be because of potential LED wafer non-uniformity. Therefore, a theoretical evaluation of our micro-cavity was required.

5.3.2.3 Cavity LED (ER) theoretical evaluation using COMSOL multi-physics

Looking at the RCLED design criterion discussed in the introduction above and in details in chapter 2, certain criteria could not be fulfilled due to the structural nature of our cavity LED, these are the smallest cavity length criterion of $\frac{\lambda_c}{2}$ and positioning the emitter at the created standing wave's antinode. Traditional RCLEDs in particular GaN based ones are fully fabricated via epitaxy allow accurate control over the cavity length and QW cavity position [48] [50]. They often have a $\frac{\lambda_c}{2}$ cavity length; this is allow only a single cavity mode to which the QW emission can couple to if adequately tuned. The coupling to a single cavity mode maximises resonating strength and hence emission intensity. Shortest cavity length also ease the effective positioning of the emitter at the standing wave's antinode (cavity centre) hence

maximising the emission rate enhancement factor [3]. Our transfer printed cavity LEDs involves the transfer of the full LED structure including the buffer layer Al(Ga)N. In addition to that, SU-8 adhesion layer were used. This leads to a wide cavity with minimum length of approximately 5430nm. The thick cavity could explain the multiple modes seen in the emission. Free spectral range FSR (mode spacing) investigations provide a legitimate comparison route for evaluating our cavity LED device to theory. FSR can be calculated from equation 5.1

$$\Delta\lambda = \frac{(\lambda_c)^2}{2nd} \qquad (5.1)$$

Where n, d and λ_c are the cavities refractive index, length and centre wavelength

Effective calculation of the FSR using equation 5.1 is challenging for our cavity LED due to the different refractive index materials present within the cavity. Nonetheless, Finite Element analysis software are often use to perform such computations. COMSOL multiphysics wave optics module was used to theoretically determine our cavity LED's reflectivity spectrum and electric field distribution along the structure. A 2D simulation was done; schematic representation of the structure was drawn with stacked materials with their thicknesses and theoretical refractive indices. Plane wave electrical field power excitation was done at right angles to the structure. Figure 5.30 illustrate the simulated structure together with the electric field distribution within the cavity at peak wavelength of 440nm.

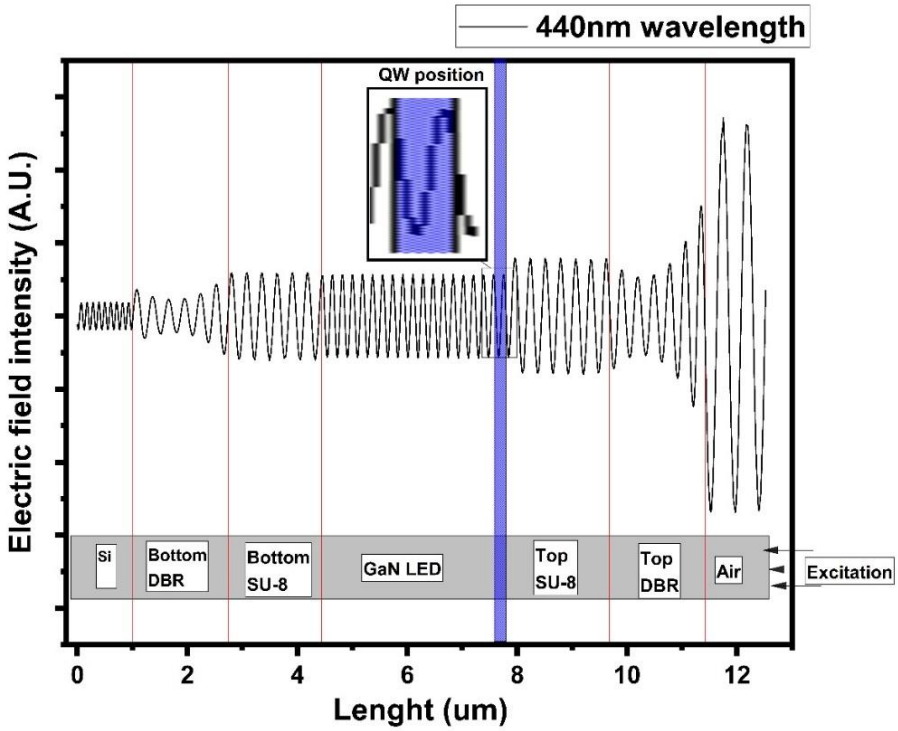

Figure 5.30 COMSOL simulation of cavity LED electric field distribution showing approximated quantum well position

As expected, multiple λ_c periods can be seen in the cavity (29.5 periods can be counted). It can be seen that the QW position (estimated from LED layers in table 5.1) span over two standing wave node and antinode therefore, according to RCLED design criterion discussed in section 2.8.4, the antinode enhancement factor should be close to unity. Reflectivity spectrum simulation results of the cavity is presented in figure 5.31 plotted together with the ER cavity LED's EL at 10mA injection current

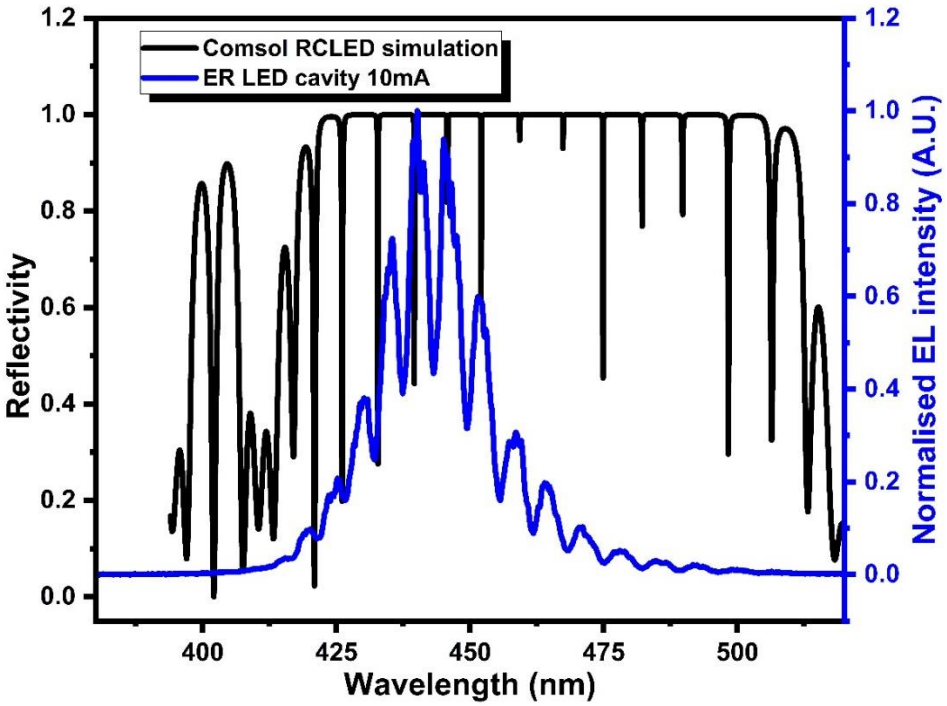

Figure 5.31 COMSOL simulation of cavity LED reflectivity spectrum with added emission reduced (ER) cavity LED's EL at 10mA injection current

Cavity simulation reveals numerous optical cavity modes due to the long cavity length, FSR close to 6nm can be seen from the reflectivity plot with reflectivity's mode position closely matching EL peaks. The slight differences seen can be as a result the LED, SU-8 adhesion and DBR optical thickness uncertainties. This confirms that the occurring EL peaks are indeed emission due to the resonant micro-cavity effects therefore Resonant Cavity Light emitting Diode (RCLED). The peak mode has FWHM of approximately 3nm, which corresponds to a linewidth narrowing of approximately 18.5nm. Therefore, reducing the cavity length has the potential of yielding a single mode with emission narrowing of up to 18.5nm.

5.4 Conclusion

In summary, electrically injected resonant cavity LED using a new approach that is heterogeneously integrating the LED in an optical microcavity via deterministic transfer printing has been demonstrated. The LED architecture consisted of standard LED epilayer commercially purchased with a modified structure having a reduced emission area (via p-GaN deactivation by CHF_3 treatment). Emission area reduction was done to make sure most of the emitted light was coupled to the cavity. The LED was anchor undercut into individual coupons

and transfer printed into a stacked optical microcavity (transfer printed DBRs). Device characterisation showed turn on voltage of approximately 2.7V increase in series resistance over the course of the processing potentially because of the electrical contacts damage and SU-8 adhesion layer residue left on the contacts. These negative effects can be mitigated by optimisation of the contact window opening (with minimal contact damage) via HF wet etch of the dielectric and using thinner adhesion layer to minimise the residue on the contact. EL measurements showed resonant cavity effects with multiple modes on the cavity LED emission closely matching the cavity optical modes (from COMSOL simulation) with free spectral range of approximately 6nm. The non-enhancement of the emission in the cavity LED was attributed to the fact that the emitter (QW) covers multiple standing wave periods as demonstrated by the COMSOL electric field distribution simulation and the multiple modes attributed to the long cavity with optical thickness of at least SU-8/GaN/SU-8 1.5um/3.43um/1.7um ($> 17\lambda_c$). The cavity length can be reduced by using thinner adhesion layers and reducing the LED coupon thickness by selective etching of the LED buffer layer using TMAH solution and/or electrochemical etch undercutting of the LED around the n-GaN region (for modified n^+GaN structures), this will considerably reduce the n-GaN thickness. To conclude, despite the low performance of the transfer printed RCLED due to the non-optimised processing, we were able to demonstrate a clear new approach for the fabrication of RCLED with potential FWHM reduction up to 3nm

5.5 References

[1] E. F. Schubert, "Spontaneous emission from resonant cavities," in *Light-Emitting Diodes*, Cambridge University Press, 2010, pp. 239–254.

[2] S. Yang *et al.*, "GaN-based green resonant-cavity light-emitting diodes with Al mirror and copper plate," *Opt. Lett.*, vol. 47, no. 11, p. 2858, Jun. 2022.

[3] E. F. Schubert, N. E. J. Hunt, R. J. Malik, M. Micovic, and D. L. Miller, "Temperature and modulation characteristics of resonant-cavity light-emitting diodes," *J. Light. Technol.*, vol. 14, no. 7, pp. 1721–1728, 1996.

[4] K. Streubel, U. Helin, V. Oskarsson, E. Bäcklin, and Å. Johansson, "High brightness visible (660 nm) resonant-cavity light-emitting diode," *IEEE Photonics Technol. Lett.*, vol. 10, no. 12, pp. 1685–1687, Dec. 1998.

[5] R. Wirth, C. Karnutsch, S. Kugler, and K. Streubel, "High-efficiency resonant-cavity LEDs emitting at 650 nm," *IEEE Photonics Technol. Lett.*, vol. 13, no. 5, pp. 421–423, May 2001.

[6] D. Zhu and C. J. Humphreys, "Solid-state lighting based on light emitting diode technology," *Opt. Our Time*, pp. 87–118, Jan. 2016.

[7] J. Bruckbauer *et al.*, "Colour tuning in white hybrid inorganic/organic light-emitting diodes," *J. Phys. D. Appl. Phys.*, vol. 49, no. 40, p. 405103, Sep. 2016.

[8] E. F. Schubert, Y.-H. Wang, A. Y. Cho, L.-W. Tu, and G. J. Zydzik, "Resonant cavity light-

emitting diode," *Appl. Phys. Lett*, vol. 60, no. 8, 1992.

[9] D. Delbeke, R. Bockstaele, P. Bienstman, R. Baets, and H. Benisty, "High-efficiency semiconductor resonant-cavity light-emitting diodes A review," *IEEE J. Sel. Top. Quantum Electron.*, vol. 8, no. 2, pp. 189–206, Mar. 2002.

[10] S. Y. Huang, R. H. Horng, W. K. Wang, and D. S. Wuu, "GaN-based green resonant cavity light-emitting diodes," *Japanese J. Appl. Physics, Part 1 Regul. Pap. Short Notes Rev. Pap.*, vol. 45, no. 4 B, pp. 3433–3435, 2006.

[11] P. S. Yeh *et al.*, "Blue resonant-cavity light-emitting diode with half milliwatt output power," in *Light-Emitting Diodes Materials, Devices, and Applications for Solid State Lighting*, 2016, vol. 9768, p. 97680P.

[12] C. Zhang, R. Afandy, and J. Han, "Distributed Bragg reflectors for GaN-based vertical-cavity surface-emitting lasers," *Applied Sciences (Switzerland)*, vol. 9, no. 8. Multidisciplinary Digital Publishing Institute, p. 1593, 17-Apr-2019.

[13] C. Zhang, K. Xiong, G. Yuan, and J. Han, "A resonant-cavity blue–violet light-emitting diode with conductive nanoporous distributed Bragg reflector," *Phys. Status Solidi Appl. Mater. Sci.*, vol. 214, no. 8, 2017.

[14] M. Gherasimova *et al.*, "Heteroepitaxial evolution of AlN on GaN Grown by metal-organic chemical vapor deposition," *J. Appl. Phys.*, vol. 95, no. 5, p. 2921, Feb. 2004.

[15] J. Pastrňák and L. Roskovcová, "Refraction Index Measurements on AlN Single Crystals," *Phys. status solidi*, vol. 14, no. 1, pp. K5–K8, Jan. 1966.

[16] A. S. Barker and M. Ilegems, "Infrared Lattice Vibrations and Free-Electron Dispersion in GaN," *Phys. Rev. B*, vol. 7, no. 2, p. 743, Jan. 1973.

[17] N. A. A. Manaf, M. S. Alias, S. M. Mithani, M. F. Maulud, M. R. Yahya, and A. F. A. Mat, "Design and optimization of distributed bragg reflector for 1310nm vertical cavity surface emitting lasers," *IEEE Int. Conf. Semicond. Electron. Proceedings, ICSE*, no. November, pp. 254–258, 2008.

[18] F. Kuhn-Kuhnenfeld and ; Lu, "Photoelectrochemical wet etching of group III nitrides," *Mater. Sci. Eng.*, vol. 108, no. 8, pp. 1118–1119, Apr. 1996.

[19] R. Sharma, E. D. Haberer, C. Meier, E. L. Hu, and S. Nakamura, "Vertically oriented GaN-based air-gap distributed Bragg reflector structure fabricated using band-gap-selective photoelectrochemical etching," *Appl. Phys. Lett.*, vol. 87, no. 5, p. 051107, Jul. 2005.

[20] D. Chen and J. Han, "High reflectance membrane-based distributed Bragg reflectors for GaN photonics," *Appl. Phys. Lett.*, vol. 101, no. 22, p. 221104, Nov. 2012.

[21] M. Bellanger, V. Bousquet, G. Christmann, J. Baumberg, and M. Kauer, "Highly reflective GaN-based air-gap distributed Bragg reflectors fabricated using AlinN wet etching," *Appl. Phys. Express*, vol. 2, no. 12, p. 121003, Dec. 2009.

[22] C. Xiong *et al.*, "High-reflectivity GaN/air vertical distributed Bragg reflectors fabricated by wet etching of sacrificial AlInN layers," *Semicond. Sci. Technol.*, vol. 25, no. 3, p. 032001, Feb. 2010.

[23] R. Tao, M. Arita, S. Kako, and Y. Arakawa, "Fabrication and optical properties of non-polar III-nitride air-gap distributed Bragg reflector microcavities," *Appl. Phys. Lett.*, vol. 103, no. 20, p. 201118, Nov. 2013.

[24] Y. K. Song, M. Diagne, H. Zhou, A. V. Nurmikko, R. P. Schneider, and T. Takeuchi, "Resonant-cavity InGaN quantum-well blue light-emitting diodes," *Appl. Phys. Lett.*, vol. 77, no. 12, p. 1744, Sep. 2000.

[25] J. Dorsaz, J. F. Carlin, C. M. Zellweger, S. Gradecak, and M. Ilegems, "InGaN/GaN resonant-cavity LED including an AlInN/GaN bragg mirror," *Phys. Status Solidi a-Applied Res.*, vol. 201, no. 12, pp. 2675–2678, Sep. 2004.

[26] T. C. Lu *et al.*, "GaN-based high-Q vertical-cavity light-emitting diodes," *IEEE Electron Device Lett.*, vol. 28, no. 10, pp. 884–886, Oct. 2007.

[27] J. M. Redwing, D. A. S. Loeber, N. G. Anderson, M. A. Tischler, and J. S. Flynn, "An optically pumped GaN–AlGaN vertical cavity surface emitting laser," *Appl. Phys. Lett.*, vol. 69, no. 1, p. 1, Aug. 1998.

[28] G. Cosendey, A. Castiglia, G. Rossbach, J. F. Carlin, and N. Grandjean, "Blue monolithic AlInN-based vertical cavity surface emitting laser diode on free-standing GaN substrate," *Appl. Phys. Lett.*, vol. 101, no. 15, p. 151113, Oct. 2012.

[29] T. Czyszanowski, M. Wasiak, R. P. Sarzała, and W. Nakwaski, "Exactness of simplified scalar optical approaches in modelling a threshold operation of possible nitride vertical-cavity surface-emitting diode lasers," *Phys. status solidi*, vol. 204, no. 10, pp. 3562–3573, Oct. 2007.

[30] D. Zhu *et al.*, "Efficiency measurement of GaN-based quantum well and light-emitting diode structures grown on silicon substrates," *J. Appl. Phys.*, vol. 109, no. 1, Jan. 2011.

[31] M. E. Aumer, S. F. LeBoeuf, S. M. Bedair, M. Smith, J. Y. Lin, and H. X. Jiang, "Effects of tensile and compressive strain on the luminescence properties of AllnGaN/lnGaN quantum well structures," *Appl. Phys. Lett.*, vol. 77, no. 6, pp. 821–823, Aug. 2000.

[32] M. E. Aumer, S. F. LeBoeuf, B. F. Moody, and S. M. Bedair, "Strain-induced piezoelectric field effects on light emission energy and intensity from AlInGaN/InGaN quantum wells," *Appl. Phys. Lett.*, vol. 79, no. 23, p. 3803, Nov. 2001.

[33] C. McAleese *et al.*, "Electric fields in AlGaN/GaN quantum well structures," *Phys. status solidi*, vol. 243, no. 7, pp. 1551–1559, Jun. 2006.

[34] H. S. Kim *et al.*, "Unusual strategies for using Indium Gallium Nitride grown on Silicon (111) for solid-state lighting," *Proc. Natl. Acad. Sci. U. S. A.*, vol. 108, no. 25, pp. 10072–10077, Jun. 2011.

[35] K. E. Bean, "Anisotropic etching of silicon," *IEEE Trans. Electron Devices*, vol. 25, no. 10, pp. 1185–1193, 1978.

[36] Z. Shaban, Z. Li, B. Roycroft, M. Saei, T. Mondal, and B. Corbett, "Transfer Printing of Roughened GaN-Based Light-Emitting Diodes into Reflective Trenches for Visible Light Communication," *Adv. Photonics Res.*, vol. 3, no. 8, p. 2100312, Aug. 2022.

[37] A. J. Trindade *et al.*, "Heterogeneous integration of gallium nitride light-emitting diodes on diamond and silica by transfer printing," *Opt. Express, Vol. 23, Issue 7, pp. 9329-9338*, vol. 23, no. 7, pp. 9329–9338, Apr. 2015.

[38] B. F. Spiridon *et al.*, "Method for inferring the mechanical strain of GaN-on-Si epitaxial layers using optical profilometry and finite element analysis," *Opt. Mater. Express, Vol. 11, Issue 6, pp. 1643-1655*, vol. 11, no. 6, pp. 1643–1655, Jun. 2021.

[39] X. Zhang, K. S. Chen, and S. M. Spearing, "Thermo-mechanical behavior of thick PECVD oxide films for power MEMS applications," *Sensors Actuators A Phys.*, vol. 103, no. 1–2, pp. 263–270, Jan. 2003.

[40] Y. T. Kim, S. M. Cho, Y. G. Seo, H. D. Yoon, Y. M. Im, and D. H. Yoon, "Influence of hydrogen on SiO2 thick film deposited by PECVD and FHD for silica optical waveguide," *Cryst. Res. Technol.*, vol. 37, no. 12, pp. 1257–1263, Dec. 2002.

[41] E. Y. Chang, G. T. Cibuzar, and K. P. Pande, "Passivation of GaAs FET's with PECVD Silicon

Nitride Films of Different Stress States," *IEEE Trans. Electron Devices*, vol. 35, no. 9, pp. 1412–1418, 1988.

[42] J. Yota, H. Shen, and R. Ramanathan, "Characterization of atomic layer deposition HfO2, Al2O3, and plasma-enhanced chemical vapor deposition Si3N4 as metal–insulator–metal capacitor dielectric for GaAs HBT technology," *J. Vac. Sci. Technol. A Vacuum, Surfaces, Film.*, vol. 31, no. 1, p. 01A134, Dec. 2012.

[43] K. D. Mackenzie, D. J. Johnson, M. W. DeVre, R. J. Westerman, and B. H. Reelfs, "Stress control of Si-based PECVD dielectrics," in *Proceedings - Electrochemical Society*, 2005, vol. PV 2005-01, pp. 148–159.

[44] K. Biswas and S. Kal, "Etch characteristics of KOH, TMAH and dual doped TMAH for bulk micromachining of silicon," *Microelectronics J.*, vol. 37, no. 6, pp. 519–525, Jun. 2006.

[45] O. J. Powell, D. Sweatman, H. B. Harrison, O. J. Powell, D. Sweatman, and H. B. Harrison, "The use of titanium and titanium dioxide as masks for deep silicon etching," *SPIE*, vol. 5276, pp. 26–35, Apr. 2004.

[46] A. Chitnis *et al.*, "Visible light-emitting diodes using a-plane GaN–InGaN multiple quantum wells over r-plane sapphire," *Appl. Phys. Lett.*, vol. 84, no. 18, p. 3663, Apr. 2004.

[47] W. Yao *et al.*, "Stress engineering for reducing the injection current induced blue shift in InGaN-based red light-emitting diodes," *CrystEngComm*, vol. 23, no. 12, pp. 2360–2366, Mar. 2021.

[48] P. S. Yeh *et al.*, "Blue resonant-cavity light-emitting diode with half milliwatt output power," in *Light-Emitting Diodes Materials, Devices, and Applications for Solid State Lighting XX*, 2016, vol. 9768, p. 97680P.

[49] S. Y. Huang, R. H. Horng, W. K. Wang, and D. S. Wuu, "GaN-based green resonant cavity light-emitting diodes," *Japanese J. Appl. Physics, Part 1 Regul. Pap. Short Notes Rev. Pap.*, vol. 45, no. 4 B, pp. 3433–3435, Jan. 2006.

[50] C. Zhang, K. Xiong, G. Yuan, and J. Han, "A resonant-cavity blue–violet light-emitting diode with conductive nanoporous distributed Bragg reflector," *Phys. Status Solidi Appl. Mater. Sci.*, vol. 214, no. 8, p. 1600866, Aug. 2017.

[51] D. Massoubre *et al.*, "Fabrication of planar GaN-based micro-pixel light emitting diode arrays," *Conf. Proc. - Lasers Electro-Optics Soc. Annu. Meet.*, pp. 84–85, 2009.

[52] Y. Cai, Y. Zhou, K. M. Lau, and K. J. Chen, "Control of threshold voltage of AlGaN/GaN HEMTs by fluoride-based plasma treatment From depletion mode to enhancement mode," *IEEE Trans. Electron Devices*, vol. 53, no. 9, pp. 2207–2214, 2006.

[53] G. Martinez De Arriba, P. Feng, C. Xu, C. Zhu, J. Bai, and T. Wang, "Simple Approach to Mitigate the Emission Wavelength Instability of III-Nitride μlED Arrays," *ACS Photonics*, vol. 9, no. 6, pp. 2073–2078, Jun. 2022.

6) Chapter 6 - Transfer printed optical microcavities with active materials

Optical microcavities are ubiquitous in the field of optoelectronics. They help in light confinement and have been at the origin of numerous phenomena including coupling. Fine-tuning is often required for optimal device performance. These include; maximum cavities quality factor, minimum cavity's length, antinode positioning of emitter and cavity mode and emitter emission overlap [1] [2] [3]. Device configuration sometimes makes it challenging to fulfil some of these parameters for example minimal cavity length as seen in chapter 5. We here by investigate the microcavity effects on different classes of emitters; light emitting polymer (F8BT) and nanocrystal colloidal QDs ($CsPbBr_3$) which are solution based and offer advantage of low cost simple processing and deposition by spin coating, which provides some control over the active layer thickness. Purcell effect in the F8BT microcavity was demonstrated with emission band narrowing of 80.5nm to 8.3nm from emission outside to inside the cavity and TRPL measurement of comparable resonant microcavity and non-resonant microcavity showed carrier lifetime decrease of 0.553ns (68%). QD microcavity with high quality factor of 1305 was demonstrated with power dependent measurements showing an increase in integrated intensity, non-significant change in emission linewidth with power and no definitive threshold.

6.1 Introduction

Quantum confinement has led to the advent of numerous applications stemming from various phenomena occurring thanks to the microcavity. Optimisation of cavity's mode volume and cavity strength are key in maximising the cavity's coupling strength [4][5]. The advent of new classes of materials such as nanostructures and light emitting polymers favoured the integration of active materials in such small cavities therefore, allowing novel material visible wavelength lasers (organic material and QD). They also serve as down conversion materials [6][7][8][9]for LED/MicroLED applications such as display technology.

Using Fabry-Perot cavities, mode decay and non-resonant emitter's exciton decay losses can never be reduced to zero, as the mirrors reflectivity can never reach 100% and non-radiative recombination and absorption centres are always present due to defects and materials present. Nonetheless, the cavity mode decay can be minimised by using top and bottom mirrors close to 100% hence, maximising the cavity's quality factor. In addition, the cavity's length is

proportional to the cavity mode volume, ensuring the emitter's emission energy overlap with a minimal amount of cavity mode is essential in maximising the integrated intensity for resonance [10]. For this reason, the cavity length needs to be minimised and therefore $\frac{\lambda_c}{2}$ cavity lengths are usually preferred. In Chapter 5, an RCLED was fabricated by transfer printing a full LED stack between two DBRs. Some of the factors required to maximise light-matter interaction could not be met due to the nature of the device stack, these include; maximum light confinement, minimum compatible cavity length and ensuring the emitter is positioned at the cavity's standing wave antinode. However, there exist other classes of emitters, which are solution based therefore offering advantages of low cost processing and thin film deposition using techniques such as ink jet printing, drop casting and spin coating. This provides the potential for improved controllability of the cavity length and emitter positioning for our transfer printed quantum microcavities. Optically pumped Poly(9,9-dioctylfluorene-*alt*-benzothiadiazole) light emitting polymer and $CsPbBr_3$ perovskite quantum dots microcavities were fabricated and studied.

Poly(9,9-dioctylfluorene-*alt*-benzothiadiazole) commonly known as F8BT light emitting polymer in the yellow and green region of the visible spectrum was used as light emitting material. F8BT refers to a copolymer consisting of 9,9-dioctylfluorene (F8) and benzothiadiazole (BT) group as shown in figure 6.1 [11][12]. It is an organic light emitting polymer from the polyfluorene family [13], the conjugation effect causes the delocalisation of π-electrons across several carbon atoms along the chain while keeping structural stability [14] [15] [16]. This leads to the formation of molecular orbital the HOMO (Highest energy Occupied Molecular Orbital) and the LUMO (Lowest energy Unoccupied Molecular Orbital) separated by the band gap [14] [15] and this accounts for their semiconducting abilities. F8BT has properties of high quantum efficiency of approximately 60% to 80% and high electron affinity of approximately 3.3 eV [17]. Electron and hole mobilities of 6.3×10^{-4} cm^2/Vs and 2.2×10^{-3} cm^2/Vs respectively were reported [18]. In addition to their appealing semiconducting properties, F8BT and light emitting polymers in general offer advantages of colour tuning via structure modification, relatively low cost and solution based hence can simply be processed and deposited using techniques such as drop casting and spin coating [17] [19]. It also has a wide absorption (with peaks at 320 and 455nm) and a wide emission spectrum spanning from 500nm to 650nm therefore, its choice as potential functional material. However, F8BT like other light emitting polymers is not immune to degradation due to excitation in oxygen and moisture presence (photo-oxidation and photo-bleaching) [20]. For this reason,

preferably no exposure to air or moisture during the material processing is required. F8BT has served already as functional material of various optoelectronic devices such as OLEDs [21], lasers [22] and solar cells [23].

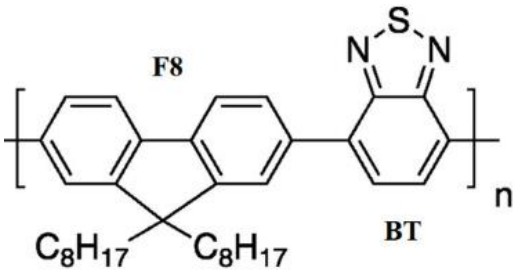

Figure 6.1 chemical structure of Poly(9,9-dioctylfluorene-*alt*-benzothiadiazole) F8BT polymer

$CsPbBr_3$ perovskite quantum dots belong to a class of QDs known as lead halide perovskite. As QDs, they have specific characteristic of optical and electronic properties tune-ability via material compositional and dimensional changes [24][25][26][27]. When reduced to 0 dimension material (3D confinement), that is nanocrystal of size approximately 10 – 20nm, they show strong quantum confinement in all directions [28][29][30]. This leads to the formation of discrete quantized carrier density of states in all directions (unlike bulk material with continuous carrier density of states). This modifies the band edge and therefore the emission wavelength can be tuned by varying the confinement energy (which is inversely proportional to the nanocrystal radius) as given in equation 2.29.

Compared to other available quantum dots, $CsPbBr_3$ and halide perovskite in general offer better resistance to structural defects and degradation [31][32][33]. This is because the generated trap sites upon photo-oxidation are outside the bandgap and their structure are covered with functional ligands reducing the amount of available free dangling bonds resulting in better photo and thermal stability [34] [35]. They also show better quantum yield, up to 95-100% [26][36] and very narrow emission with bandwidth of approximately 10 – 40nm with emission peak between 520 – 530nm. Thanks to their above exceptional properties halide perovskite ($CsPbBr_3$) have found application in LEDs [37][38], solar cells [39], amplified spontaneous emission and lasing [40] [41].

6.2 Microcavities fabrication

6.2.1 F8BT resonant micro-cavity fabrication by transfer printing

The active layer of this resonant cavity was the light emitting polymer F8BT that can be easily deposited by spin coating. One of the main conditions required to sustain optical modes within

the micro-cavity is that, the optical cavity length must be an integer multiple of half the centre wavelength as depicted in equation 2.18

The use of a spacer layer allows effective positioning of the emitter only at the cavity's centre while achieving a cavity length of $\frac{\lambda_c}{2}$ (m = 1). PMMA was used as the spacer layer material. DBR with linewidth overlapping the F8BT wide emission were required. F8BT thin film emission spectrum needed to be determined. An F8BT in toluene solution with concentration 10mg/ml was spun at 6000 rpm on silicon substrate followed by baking on a hot plate at a temperature of 100℃ for 5 minutes to ensure solvent evaporation (this was done inside the glove box nitrogen atmosphere with solvent purification). Ellipsometry and Micro PL measurement of the F8BT thin film were carried out and results shown in figure 6.2 a). F8BT thickness of approximately 40nm were obtained, emission peak can be seen at wavelength 538nm with a refractive index of approximately 2.098 at that wavelength.

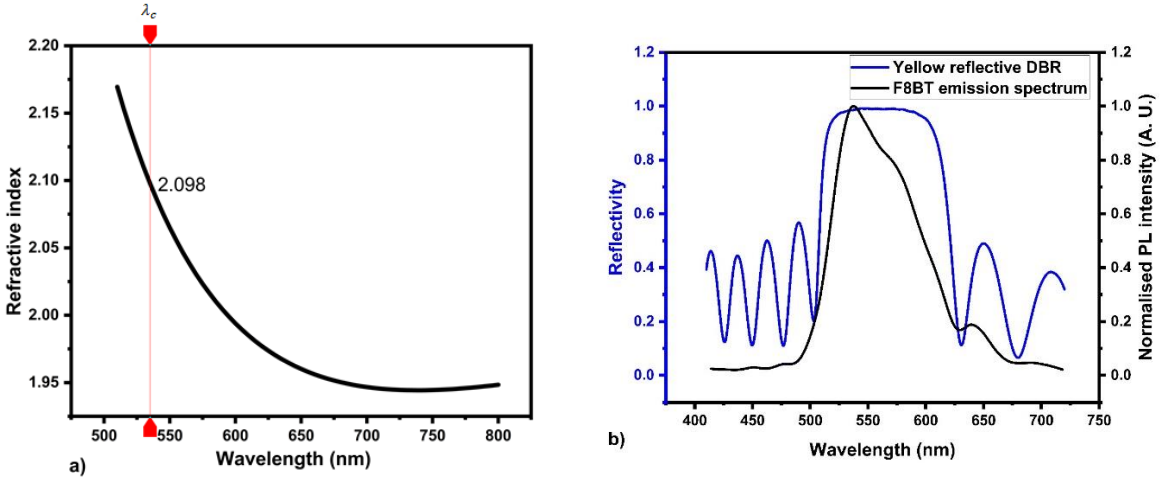

Figure 6.2 a) Ellipsometry measurement of F8BT showing refractive index plot b) Yellow DBR reflectivity and F8BT PL plots showing overlap between bands

A DBR showing good overlap with the F8BT emission was required. The yellow DBR grown in chapter 4 appeared to be a good candidate. It had large reflectivity stopband width of 93nm, which overlapped with the F8BT emission spectrum (Figure 6.2 (b)) therefore, was chosen. DBR grown on Si wafer substrate was cleaved into a small piece with 1x1cm dimensions. This was to serve as the bottom DBR. This was done for convenience as the bottom DBR transfer printing step could be avoided. In addition, this ensured much uniform spacer layer thickness deposited by spin coating (this is highly important as the cavity thickness determines the cavity mode position). The DBR piece was first cleaned by three solvent cleaning and oxygen plasma ashed using PVA Tepla asher. Next, adequate PMMA spacer layer needed to be determined.

For cavity mode around 538nm, PMMA spacer with total thickness of approximately 177nm was required. For microcavity with centred functional material structure as shown in figure 6.4, spin coating of PMMA layer with thickness $\frac{177nm}{2}$ that is 88.5nm was required to serve as spacer layers. PMMA of concentration 22mg/ml in toluene was then spun on the bottom DBR at speed of 5000 rpm for 30s followed by 10 mins bake on a hot plate at 100°C, ellipsometry measurements revealed a thickness of 89nm and refractive index of approximately 1.526 at 538nm as shown in figure 6.3.

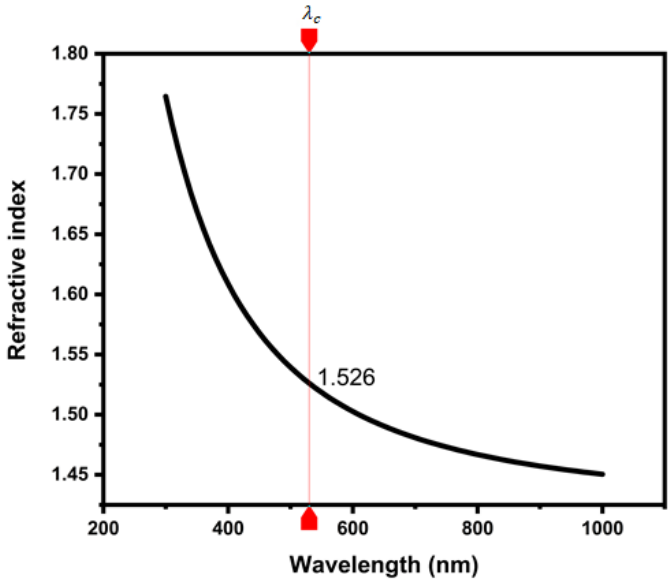

Figure 6.3 Ellipsometry measurement PMMA refractive index plot

The first 89nm PMMA layer was deposited, followed by 40nm F8BT and then the final 89nm PMMA spacer layer (in glove box nitrogen atmosphere). Transfer printing of the top DBR could then be executed. The DBR anchor undercutting and transfer printing were done as described in chapter 4. This yielded an F8BT microcavity device with configuration DBR/PMMA/F8BT/PMMA/DBR as shown in figure 6.4. It should be noted that, performing the transfer printing required the sample to be taken out of the glove box and illuminated with a halogen broadband light source for alignment. The illumination was done from the top via the microscope objective across the transparent PDMS stamp. The stamp was partially opaque to certain wavelengths of light at its pedestal thanks to the presence of the top DBR to be transfer printed. This means the F8BT was to some degree photo-oxidised and is an important consideration to bear in mind for characterisation of the cavities.

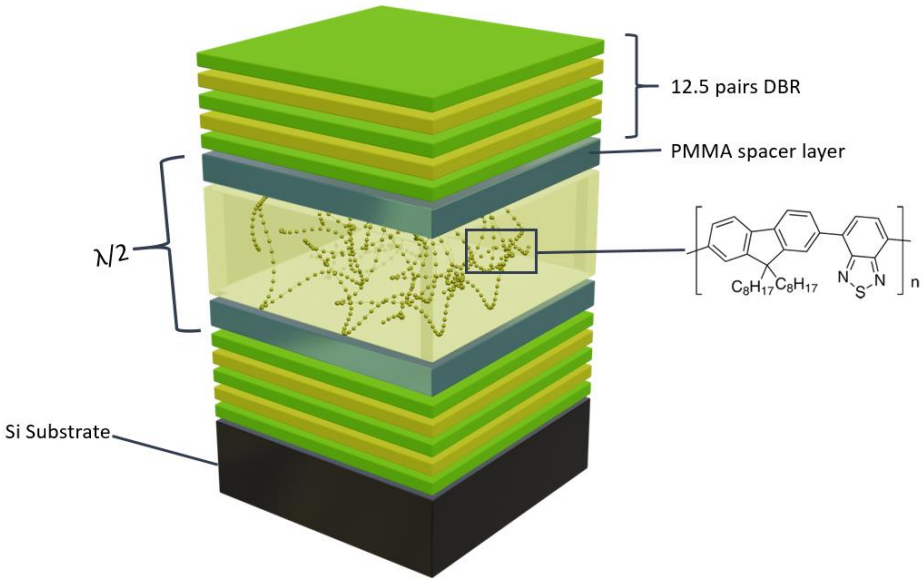

Figure 6.4 Schematic illustration (not to scale) of the fabricated F8BT microcavity

6.2.2 $CsPbBr_3$ perovskite quantum dot micro-cavity fabrication by transfer printing

New sets of high reflectivity DBRs with stop-bands matching the QD emission band were required. Similar DBR types to above were used, that is PECVD grown 12.5 pairs SiN_x/SiO_2 DBRs. The new growth conditions were; growth time of 5 mins 24s and 2mins 36s for SiN_x and SiO_2 to yield thicknesses of 54nm and 105nm respectively. For SiN_x and SiO_2 with refractive index of approximately 1.92 and 1.46 respectively, this ensured a λ_c around 514nm. Reflectivity spectra plot of the grown and COMSOL simulated DBR are shown in figure 6.5. As can be seen, the spectrum has high peak reflectivity of approximately 99% and wide bandwidth approximately 86nm and there are no major differences between the plots proving the correctness of the PECVD growth conditions.

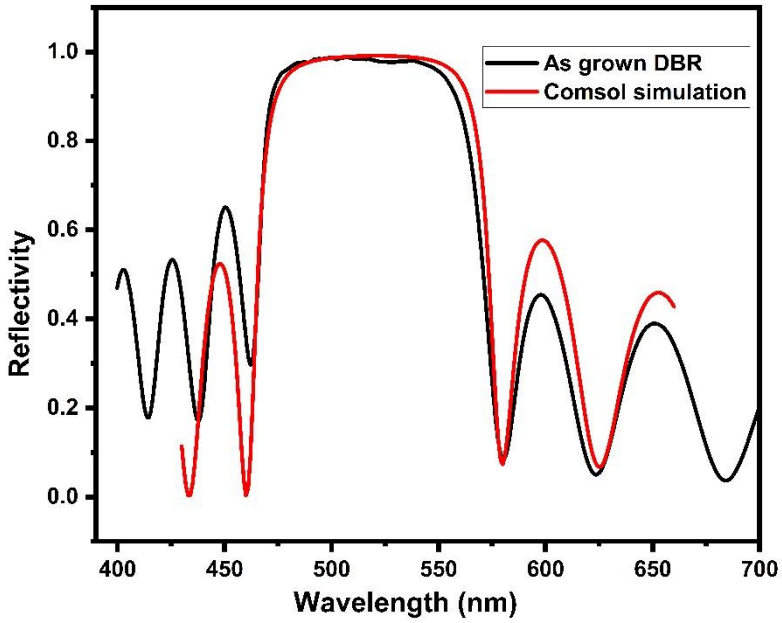

Figure 6.5 Comparison of COMSOL simulated DBR reflectivity with as grown green DBR reflectivity

Next, the cavity needed to be fabricated. Similar procedures described in Chapter 4 were used to fabricate the microcavity. Just like in the case of the F8BT micro-cavity above, a piece of DBR 1x1cm size was cut from the DBR on Si wafer. The bottom DBR pieces were then cleaned by three solvent cleaning and oxygen plasma ashing using the asher. $CsPbBr_3$ perovskite colloidal QD with concentration 10mg/ml in toluene were purchased from Ossila. The QD solution supernatant was spin coated on the cleaned DBR piece at a speed of 1800 rpm for 30s. The spin speed was kept low in order to minimise the dots losses during spinning. This yielded an uneven coated DBR surface consisting of agglomerated quantum dots

A spacer layer (QD host material) with specific optical thickness was required to ensure adequate cavity mode positioning (overlap with the QD emission). PMMA polymer just like above was used. The PMMA also served as adhesion promoter for the transfer printing of the top DBR. From equation 2.18, a thickness of approximately 169nm is required to ensure a λ_c around 520nm for PMMA cavity with refractive index of 1.53 at 520nm. PMMA with molecular weight 120000 dissolved in solvent toluene with concentration 30.9mg/ml was found to produce thickness of approximately 165nm when spin coated at a speed of 1800 rpm for 30s followed by 10mins baking on a hot plate at 100°C (determined via ellipsometry calibration measurements). Therefore, a 165nm PMMA layer was deposited on the sample by

spin coating. The DBR was anchor undercut into suspended 100um sized coupons. Transfer printing was carried out as described in Chapter 4 with the PMMA also serving as adhesion promoter hence, a QD microcavity. An overview of the process is illustrated in figure 6.6.

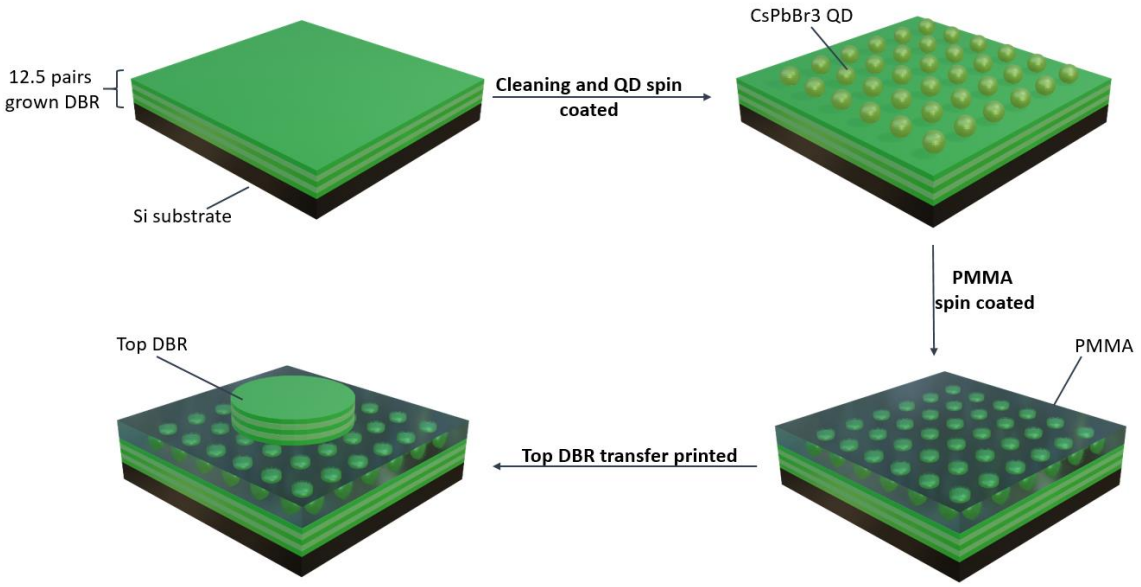

Figure 6.6 Quantum dot microcavity fabrication

6.3 Microcavities characterisations and discussion

6.3.1 F8BT microcavity characterisation

Optical characterisation techniques of microPL (uPL) and Time Resolved PL (TRPL) were used to characterise the F8BT micro-cavities as they offer quick characterisation without the need of electrical connections. Room temperature uPL measurements were done with the sample under vacuum by putting the sample in an optical cryostat kept at pressure 10^{-6} mBar. Laser with pulse width 83ps, excitation at wavelength 375nm and average power of 0.1mW was made incident on the cavity (area of the sample covered with the top DBR) and on F8BT outside the cavity but on the bottom DBR (area of the sample not covered with the top DBR). The obtained results are shown in figure 6.7; bandwidth narrowing can be seen as the bandwidth reduces from 80.5nm, to 8.3nm from outside to inside the cavity respectively. The micro-cavity reflectivity spectrum was also simulated in COMSOL using the materials parameters (refractive indices and thicknesses) above. This plot is superimposed in figure 6.7. Cavity mode can be seen at wavelength 537nm; this should correspond to the designed cavity mode position. The designed cavity mode position is not far from the micro-cavity peak emission wavelength of 534nm. These confirms the occurrence of micro-cavity effects by coupling between the emitter and cavity modes due to the presence of the cavity. Reflectivity

side lobes effects from the bottom DBR can also be seen on both the F8BT outside and inside cavity measurements.

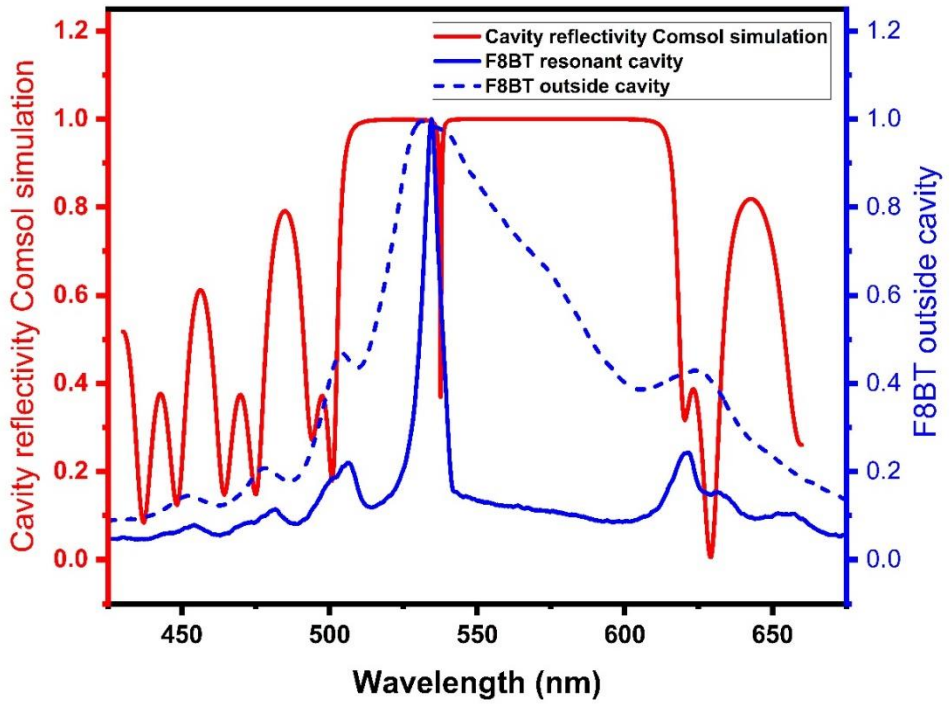

Figure 6.7 Plot of the F8BT resonant micro-cavity and non-cavity photoluminescence together with the cavity's Comsol simulated reflectivity; showing emission linewidth narrowing at the micro-cavity mode

In addition to emission linewidth narrowing, the decay carrier dynamics measurements through time resolved PL is a common method often used for measuring and comparing the carrier's spontaneous emission rate [42][43] [44] , hence for Purcell effect investigation. Therefore, this needed to be performed for further investigating coupling effects. TRPL was carried out at the respective peak wavelengths (530nm outside cavity and 534nm inside the cavity from figure 6.7). Here, the same-pulsed laser was used as in the case of uPL with repetition rate of 10MHz. The system employs the Time Correlated Single Photon Counting (TCSPC) technique as explained in Chapter 3. The obtained decay dynamics were then deconvolved from the IRF to obtain the actual decay plot using an iterative deconvolution process using the software Fluofit. The plot could then be fitted using a bi-exponential exponential function as shown in equation 6.1. The bi-exponential fitting can be explained from the conjugated polymer physical model consisting of intra-molecular excitons (represented by primary exponential, usually having

shorter decay times) and interchain states (represented by secondary exponential, usually having longer decay times) [45] [46]

$$I(t) = A_1 e^{-\frac{t}{\tau_1}} + A_2 e^{-\frac{t}{\tau_2}} \qquad (6.1)$$

Where A_1 and A_2 are the fast and slow decays respectively, τ_1 and τ_2 are the fast and slow time constants respectively, $I(t)$ is the instantaneous intensity

Optical excitation was performed at the same laser average power of 0.1mW for both cavity and non-cavity measurements but the received power by the F8BT in the cavity should be lower than that outside the cavity due to some attenuation from the top DBR reflective nature.

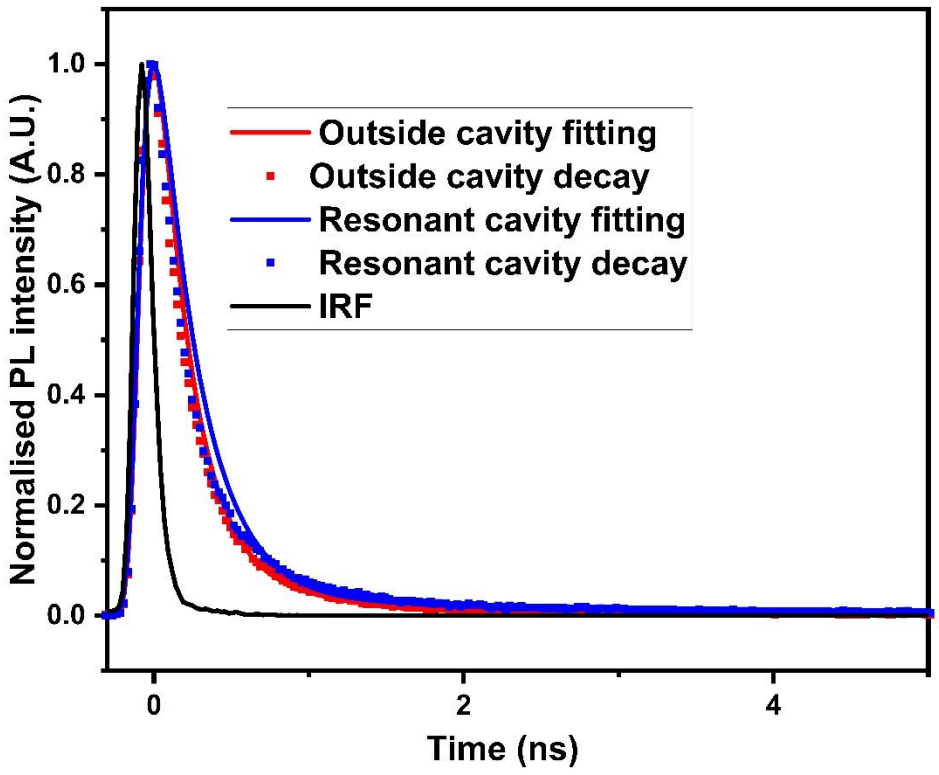

Figure 6.8 Plot of the F8BT resonant micro-cavity and non-cavity Time Resolved PL; showing decay dynamics of the carriers

Figure 6.8 shows the plotted TRPL decays together with the IRF function. Measured decay time constants of F8BT in cavity and F8BT outside the cavity are shown in table 6.1.

Samples	**τ_1/ns**
F8BT resonant cavity	0.253
F8BT outside cavity	0.199

Table 6.1 Extracted time constants for F8BT resonant cavity and photo-oxidised F8BT

As seen from Figure 6.8 and Table 6.1, the carrier decay plots appear very similar with a very small decrease from F8BT in resonant cavity to F8BT outside the cavity of 0.054ns (21% decrease). According to literature, micro-cavity effects even in the weak coupling regime should increase the recombination rate; that is, carrier lifetime should decreased because of the Purcell effect [32] [47], [48] which is the opposite here.

The difference in actual excitation power as a result of the top DBR attenuation effect discussed above appeared to be the most noticeable difference and hence, was considered to be a potential reason for the higher seen recombination rate (smaller carrier lifetime) outside the cavity. Therefore, power dependent TRPL measurements were carried out for the F8BT outside the cavity to check the extent of its importance. An attenuator with two sets of six optical filters (attenuation ND values of 1, 0.6, 0.5, 0.4, 0.3 and 0.2) were used, combining any two filters were possible therefore allowing a wide range of optical power density attenuation. Four outside the cavity TRPL measurements were carried out at power attenuations of approximately 73.6%, 66%, 46%, 42% and 0%. Figure 6.9 shows the obtained plots. It should be noted that unlike the TRPL plots in figure 6.8, these power varying TRPL was not carried out under vacuum but ambient air (that is the sample was removed from the vacuumed optical cryostat).

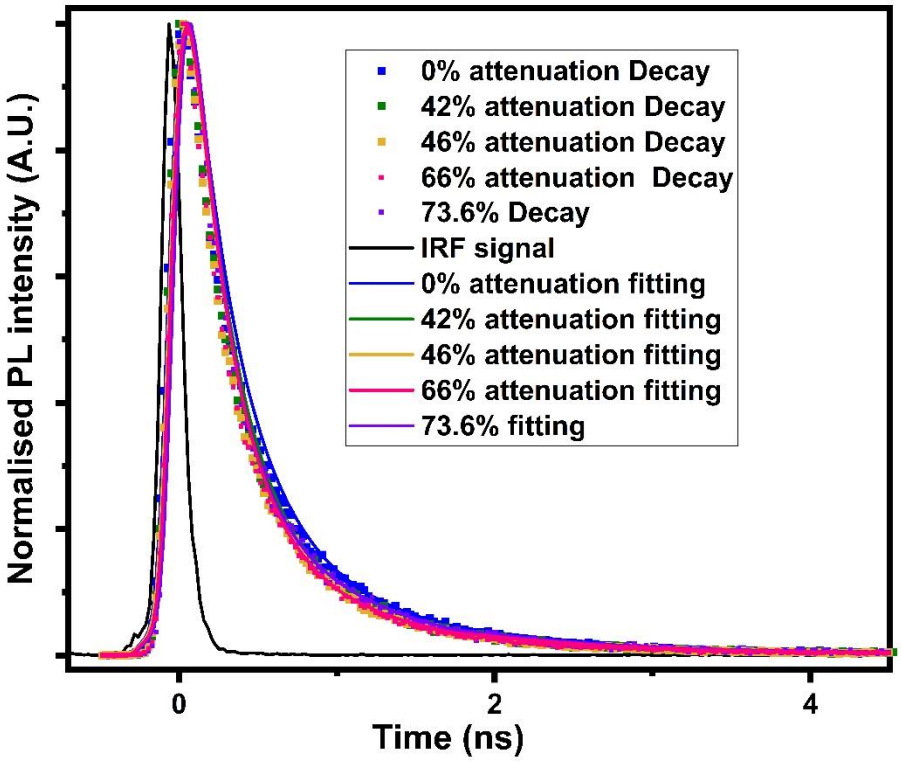

Figure 6.9 Plots of time resolved PL of F8BT outside the cavity at different excitation power intensities; showing slight increase in carrier life time

Table 6.2 shows the measured time constants for all excitation power plots

Power attenuation percentage	**τ_1/ns**
73.6%	0.203
66%	0.244
46%	0.246
42%	0.263
0%	0.289

Table 6.2 Extracted time constants for photo-oxidised F8BT at different excitation powers

As it can be seen in Figure 6.9 and Table 6.2, decrease in excitation power (increasing the power attenuation percentage) has the effect of slightly decreasing the average lifetime, by 0.086ns (30%) even for up to 73.6% power attenuation. Therefore, the excitation power attenuation for the cavity measurements due to the top DBR is not enough to explain the observed low outside cavity F8BT lifetime shown in figure 6.8. Apart from the micro cavity

coupling effect, another difference between the microcavity F8BT and non-microcavity F8BT is the level of photo-oxidation during the transfer printing process as explained in section 6.3.1. The top DBR does not only provide optical confinement for the microcavity effects but also serves as a light filter (attenuator) during the transfer printing process and covers the F8BT surface post transfer printing therefore, providing some level of protection to photo-oxidation induced degradation, this is illustrated in figure 6.10

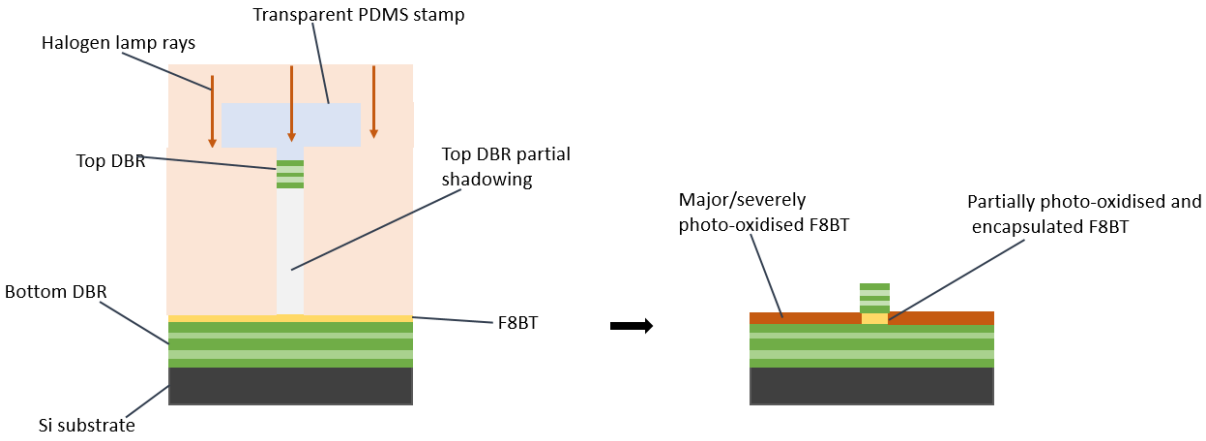

Figure 6.10 diagrammatic illustration of protection offered by top DBR during transfer printing

Photo-oxidation induced degradation on conjugated polymers and F8BT polymer in particular have been shown to have many effects such as degradation in conductivity, absorbance and PL efficiency [49][50][51]. A decrease in PL lifetime as a result of photo-oxidation was also noticed in conjugated polymers, this was demonstrated by Salvador et al in their work involving the suppression of photo-oxidation in various π – conjugated polymers and their blends using nickel chelate nickel (III) dibutyldithiocarbamate $Ni(dtc)_2$ antioxidants [52]. Using PL lifetime (TRPL) measurement as a robust degradation mechanism determination technique, they were able to demonstrate an unchanged PL lifetime for polymer PTB7 with 10%wt $Ni(dtc)_2$ after 30mins photo-oxidation meanwhile, the pure PTB7 showed noticeable decrease in PL lifetime after 30 mins photo-oxidation [52]. For this reason, the difference of level of photo-oxidation degradation of the inside cavity and outside cavity F8BT were considered as a potential reason for the higher recombination rate outside the cavity compared to inside. To check this hypothesis, a new outside cavity F8BT sample were fabricated under the same conditions as in section 6.3.1 (with configuration DBR on silicon/PMMA/F8BT/PMMA, in the glove box), no top DBR was transfer printed and the sample was transferred immediately into the uPL vacuum cryostat under no illumination (in a black box). This was to ensure little to no photo-oxidation. Figure 6.11 shows the uPL and TRPL of this non-photo-oxidised outside cavity (at emission

peak wavelengths that is 537nm and 531nm for outside and inside the cavity respectively) compared to the photo-oxidised outside cavity F8BT thin film measured previously.

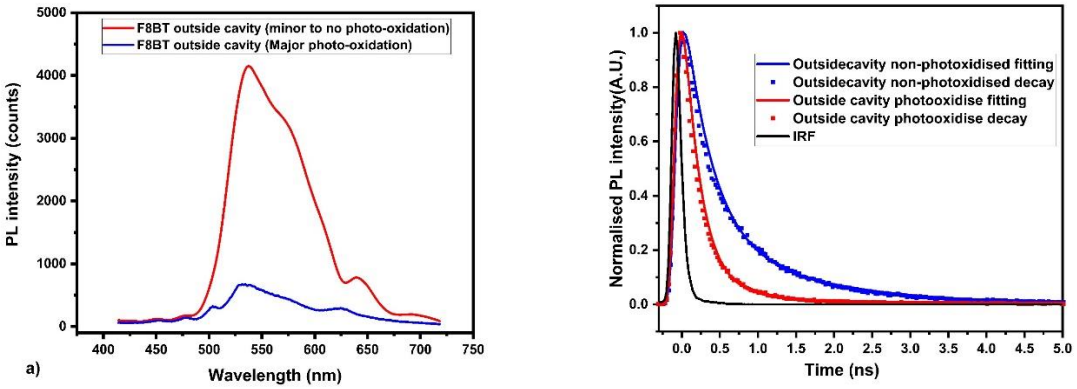

Figure 6.12 Optical plots comparison between severely photo-oxidised and non/minor photo-oxidised F8BT a)PL plot b) time resolved PL plot

The photo-oxidation degradation can clearly be seen to cause a considerable approximate 6x decrease in PL intensity and average PL lifetime decrease of 0.301ns (60% decrease, which is more significant lifetime change than in the case of power dependent TRPL above) from the minor photo-oxidised and major photo-oxidised F8BT. Table 6.3 shows the time constants for both F8BT samples.

F8BT sample	**τ_1/ns**
Major photo-oxidised	0.199
Minor photo-oxidised	0.500

Table 6.3 Extracted time constants for photo-oxidised and non/minor photo-oxidised F8BT

This confirms our hypothesis above and therefore the more pronounced photo-induced degradation effects in the outside cavity F8BT film explains the seen higher recombination rate outside the cavity compared to inside shown in figure 6.10. The non-radiative recombination component accounts for this increase and therefore, the photo-oxidised outside cavity F8BT TRPL measurements are not comparable to the F8BT micro-cavity.

However a non-resonant F8BT micro-cavity that is, one where the cavity mode does not overlap with the F8BT emission presents a more similar configuration to the resonant cavity as it also involves the transfer printing of a top DBR helping in light filtering (attenuation) during the transfer printing process and F8BT encapsulation as in the case of the resonant cavity. Therefore, can be compared to the resonant F8BT micro-cavity. A non-resonant F8BT micro-

cavity was fabricated by transfer printing using the same parameters and conditions described in section 6.2.1 but this time using DBRs having reflectivity band (and therefore cavity mode) not overlapping with the F8BT emitter emission. Blue reflective DBR (from Chapter 5) with λ_c of 455nm was used as it could serve this purpose. Figure 6.11 shows the blue DBR COMSOL simulated reflectivity spectrum and F8BT emission showing the non-overlap between the reflectivity band (and hence cavity mode) with the F8BT emission.

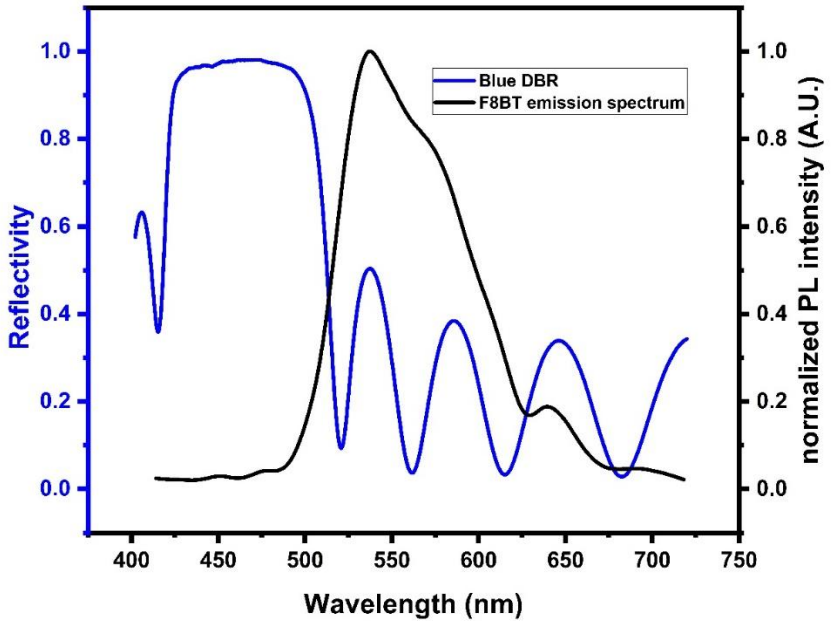

Figure 6.11 Plot showing reflectivity spectrum of blue DBR together with F8Bt emission showing non-overlap between their bands

uPL and TRPL of the non-resonant cavity was carried out at emission peak wavelength of 515nm. Figure 6.12 shows the non-resonant cavity uPL emission together with the cavity's DBR reflectivity. The TRPL comparison between F8BT inside resonant cavity and inside the non-resonant cavity is also shown.

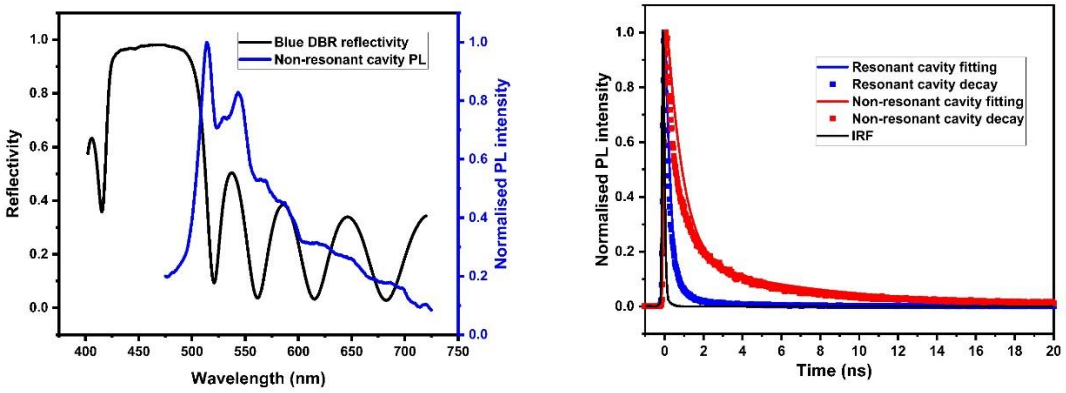

a) b)

Figure 6.12 a) non-resonant cavity uPL emission together with the cavity's DBR reflectivity b) time resolved PL plot of F8BT in resonant cavity and non-resonant cavity

Table 6.4 shows the extracted time constants

F8BT sample	**τ_1/ns**
Resonant cavity	0.253
Non-resonant cavity	0.806

Table 6.4 Extracted time constants for F8BT resonant cavity non-resonant cavity and outside cavity (non photo-oxidised)

A clear decrease in average carrier lifetime of 0.553ns (68% decrease) can be seen from F8BT in the resonant cavity to that in the non-resonant cavity. This can only be because of the resonant micro-cavity effect existing in the case of the resonant microcavity F8BT sample. This carrier lifetime decrease with the emission linewidth narrowing of approximately 72nm are clear indications of increase in recombination rate as a result the micro-cavity effect hence micro cavity Purcell effect. The cavity's quality factor can be calculated using equation 2.24

Inserting the values for the resonant F8BT micro-cavity from figure 6.7 gives a quality factor of approximately 64. The cavities quality factor defines how good the cavity is at confining light that is, avoiding its leakage outside the cavity. However, absorption losses of the F8BT material and lateral emission could be potential reason for the low quality factor. In addition, the F8BT low quantum yield, film roughness caused by mixing caused at the interlayer boundaries (PMMA-F8BT) may lead to scattering losses hence reduction in cavity's quality factor.

6.3.2 QD microcavity characterisation

The QD microcavity was also characterised using optical techniques; the confocal PL (CPL) system described in Chapter 3. Confocal PL measurements of the QD cavity (measured with excitation from the top transfer printed DBR) and QD outside cavity (measured from regions without top DBR) were done using continuous laser excitation at 375nm at power 1mW. Figure 6.13 a) shows the normalised emission spectra with CPL scan image of some of the cavity area with their respective emission plots in the inset. QD outside the cavity shows emission spectrum with bandwidth of 100nm while cavity measurements shows smaller emission linewidth of minimum value of 0.4nm. That is a considerable bandwidth narrowing of up to 99.6nm due to the micro-cavity effects.

COMSOL simulations of the cavity was also carried out, this is also shown in figure 6.13 a), a cavity mode can be seen at wavelength of approximately 520nm, which is close to the QD micro-cavity emission peak wavelength of 522nm. The slight difference could be as a result slight differences between the wanted DBR layers and cavity thickness to the actual deposited ones. The enormous linewidth narrowing confirms micro-cavity coupling effects between the QDs excitonic mode and cavity mode leading to the band narrowing. The CPL scan shows uneven distribution of the QDs as emission can only be seen at certain spots of the scanned area, showing the limitation of spin coating as a deposition technique for colloidal QD (even at a slow spinning speed of 1800rpm). Similar bandwidth narrowing can be seen at all emission spots with small emission linewidth of approximately 0.4, 0.6 and 0.7nm for points A, B and C respectively, confirming the micro-cavity effects. Such emission linewidth narrowing is a commonly observed lasing behaviour, for this reason, power dependent measurements had to be done for investigation of potential lasing from the QD micro-cavity as described below.

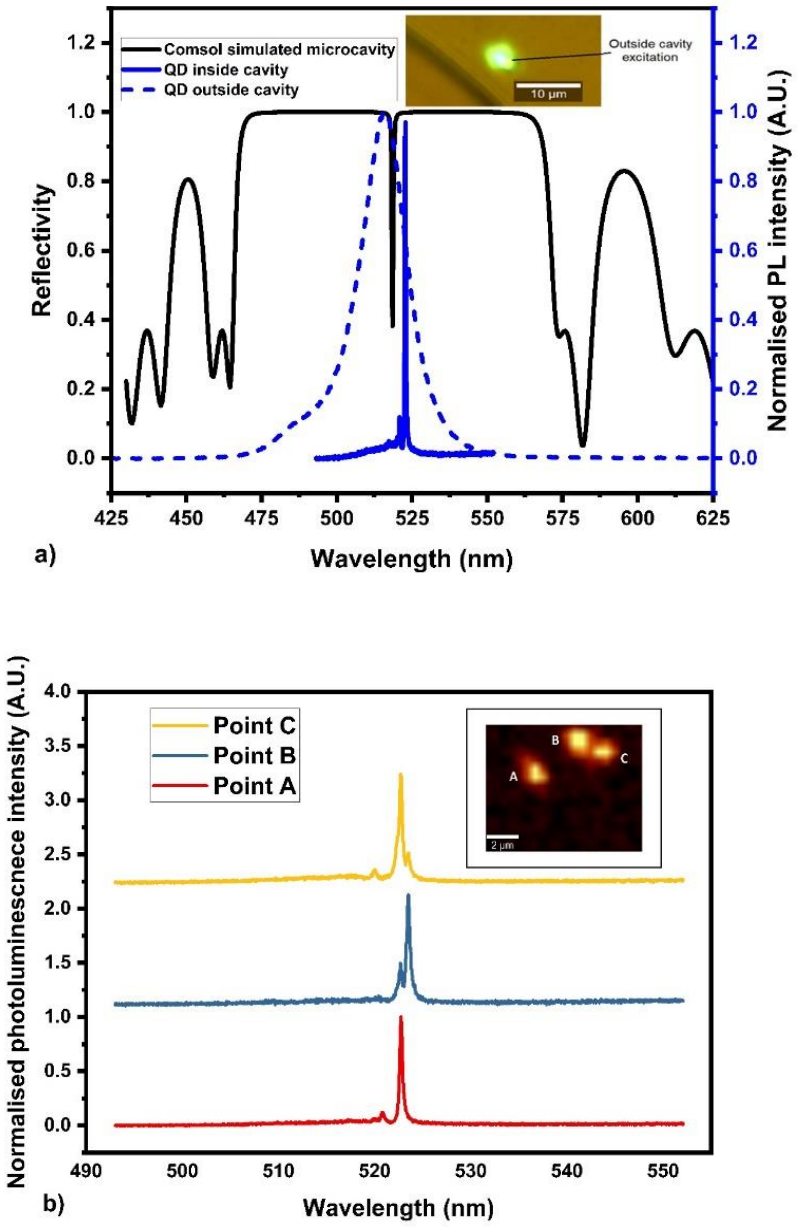

Figure 6.13 a) Plot of the QD emission outside and inside the cavity with superimposed Comsol simulated Cavity reflectivity spectrum (inset showing outside cavity excitation optical microscope image) b) Plot showing QD emission inside cavity at different spots showing repeatable linewidth narrowing (inset showing different spot excitation scan inside cavity)

Using equation 2.24, a high cavity quality factor of approximately 1305 were calculated, this shows a high degree of confinement and hence a good microcavity quality. Next, power dependent CPL were performed in order to investigate lasing characteristics. The CPL of the microcavity was measured at various excitation powers from range 10.25µW to 233.9µW. The emission plots are shown in figure 14 a)

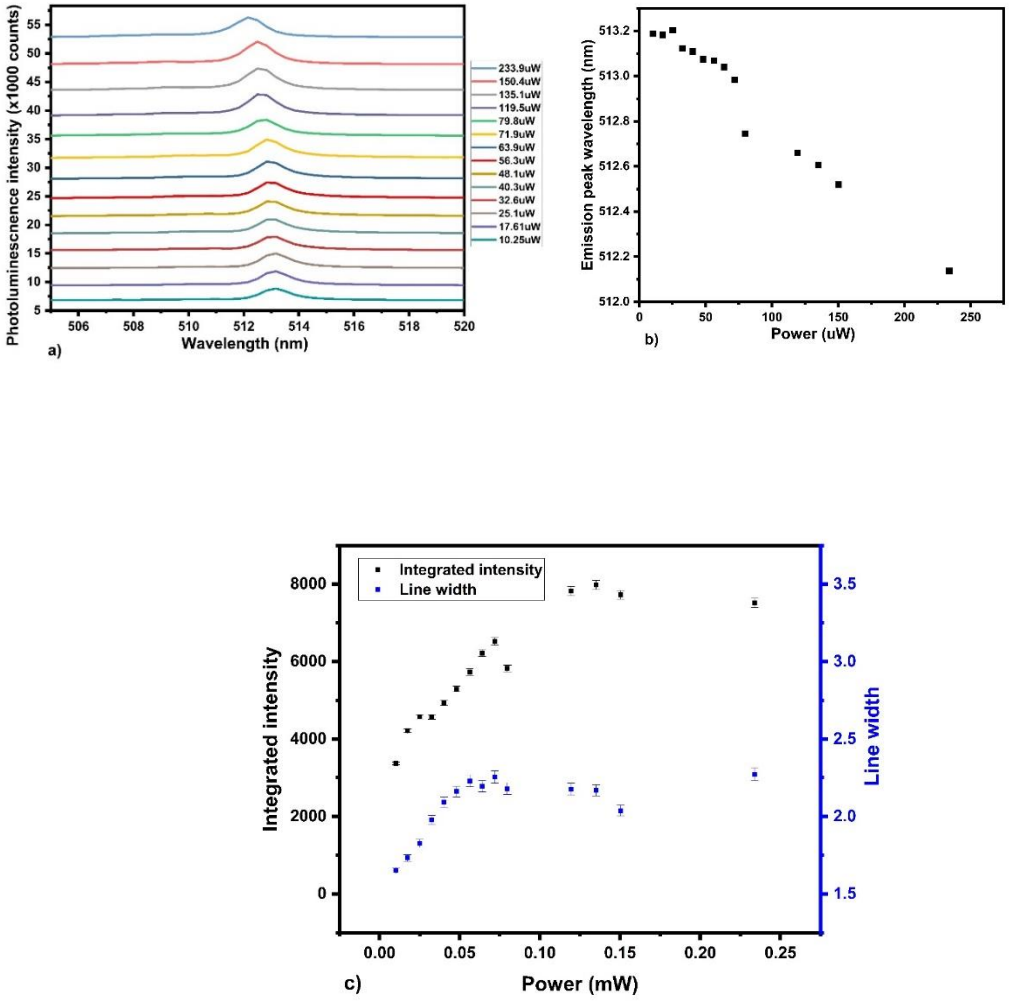

Figure 6.14 a) QD cavity emission spectrum plots at different excitation powers b) emission peak wavelength against power c) Power dependent plot of emission intensity area and linewidth from confocal PL

As it can be seen, increasing the power led to a noticeable increase in the emission peak as more carriers are injected leading to increased recombination and hence increase in emission peak. In addition, a blue shift in the emission can be seen as shown in figure 6.14. This could be an indication of photo-oxidation induced degradation because of surface state formation due to oxygen and water vapour molecules adsorption to the surface [53][54][55] as discussed in Chapter 2.

It should be noted that, the CPL system's was set up for the use of a power meter (Thorlabs cal 2015-1124) connected to one of the objectives ports on the microscope for determining actual incident power therefore, continuous swapping of objectives were required in between the measurements to measure the emission plot and the set excitation power. This was necessary

for measurements below 1mW. These subsequent objectives swapping caused slight displacements on the sample and/or pin hole, which led to different spot measurements, making the measurement non-repeatable because of the uneven distribution of the QDs, adding uncertainty. This was a limitation of the measurement set up which, potentially affected the obtained results.

Integrated area and linewidth of all the plots were measured by fitting a Gaussian function to the plots, this was then plotted on against power as shown in figure 6.14 c) to investigate the power dependent non-linearity effect. The results show an overall increase and saturation in intensity and linewidth with power but does not show clear evidence of threshold behaviour characterising lasing action. This could be because of the noticeable decrease in the QDs quantum yield upon excitation caused by photo-oxidation excitation hence, no gain. The low QD density seen as result of the inefficiency of their deposition technique (spin coating) could also be a reason for no gain. The cavity planar configuration also means there exist lateral leakage of photon (loss) therefore not enough confinement for lasing and finally this could be because of the measurement limitation.

In order to mitigate the CPL measurement limitations discussed above and explore a wider range of excitation powers, the uPL system described in Chapter 3 were used. Here an attenuator with two sets of six optical filters (attenuations ND values of 1, 0.6, 0.5, 0.4, 0.3 and 0.2) were positioned on the excitation laser path and used. Power variations could easily be done by matching any combination of two filters allowing a wide range of optical power density attenuation. In addition, all set excitation powers could be measured before excitation experiments, therefore no objective swapping hence, single spot measurement for all measurements unlike the CPL above.

Measurements were carried out for excitation power of from 2.3uw to 4.47mW (but with all data still above 10uA except 2.3uW). Using uPL, the very narrow linewidth of approximately 0.4nm seen in the CPL could not be replicated with minimum obtained linewidth of approximately 2.1nm. This could be because of the degradation of the deposited QDs as the sample was previously excited by CPL under ambient air hence photo-oxidisation induced degradation. This could also have been because adequate focusing of the objective onto the QD cavity were not possible as the motor required for fine adjusting the vertical sample stage via software was faulty, therefore, only manual focusing was done. Finally, the uPL system used did not offer any spatial resolution therefore all neighboring emission and scattered light was

also collected. Figure 6.15 shows the plotted power dependent integrated area and linewidth of the QD emission via uPL excitation. The results are very similar to the CPL in figure 6.14 c, noticeable increase then flattening of the intensity can be seen with power increase and very little changes in linewidth can be observed except at power 2.3μW. This could mean the threshold is below 2.3μW power excitation and excitation at lower powers could reveal it. This shows further optimisation is required in ensuring a higher concentration of QDs with even spreading in the transfer printed cavity, reduction in cavity optical leakage and better power dependent measurement set up without the limitation discussed above.

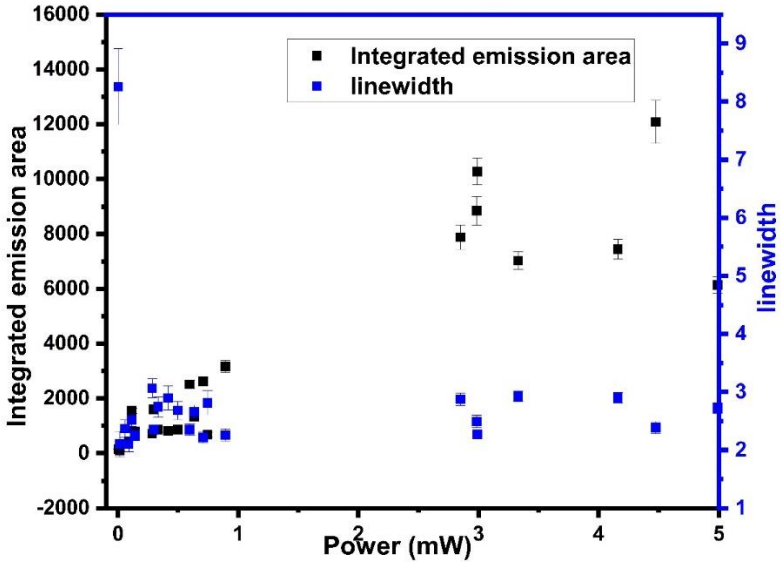

Figure 6.15 Power dependent plot of emission intensity area and linewidth from uPL

6.4 Conclusion

We demonstrated the fabrication of two types of low cavity length active material resonant microcavity devices; F8BT and QD ($CsPbBr_3$ CQD) by transfer printing. Active layer deposition was done by simple low cost spin coating and cavity built by deterministic transfer printing. F8BT cavity PL measurements showed a considerable emission band narrowing of 80.5nm to 8.3nm from emission outside to inside the cavity and TRPL measurement of comparable resonant microcavity and non-resonant microcavity showed carrier lifetime decrease of 0.553ns (68%). This was attributed to microcavity Purcell effect because of the microcavity. Photo-oxidation were also seen to have significant impact on carrier emission and carrier lifetimes as emission intensity drop and carrier lifetime decrease were seen as a result of increase in non-radiative processes due to the photo-oxidation induced degradation. F8BT

quality factor of approximately 64 was calculated from the emission band narrowing, the photo-oxidation, high absorption coefficient, low quantum yield and optical roughness of the layers were suggested as possible reasons for the seen quality factor. QD cavity showed a higher quality factor of 1305 with emission band narrowing from 100nm to 0.4nm from outside the cavity to inside the cavity. This is thanks to their higher quantum yield and spatially resolved measurement (confocal PL). Repeatability of the results were shown with measurements at different spots. Power dependent measurements were non-conclusive as no threshold behaviour was seen for the emission linewidth. Potential reasons for this are QDs photo-oxidation degradation, QD low density, and emission lateral leakage and measurement technique limitations hence the need for better optimisations.

6.5 References

[1] H. Megahd *et al.*, "All-Polymer Microcavities for the Fluorescence Radiative Rate Modification of a Diketopyrrolopyrrole Derivative," *ACS Omega*, vol. 16, p. 25, 2022.

[2] A. M. Vredenberg, N. E. J. Hunt, E. F. Schubert, D. C. Jacobson, J. M. Poate, and G. J. Zydzik, "Controlled atomic spontaneous emission from Er3+ in a transparent Si/SiO2 microcavity," *Phys. Rev. Lett.*, vol. 71, no. 4, pp. 517–520, 1993.

[3] D. Goldberg and V. M. Menon, "Enhanced amplified spontaneous emission from colloidal quantum dots in all-dielectric monolithic microcavities," *Appl. Phys. Lett.*, vol. 102, no. 8, Feb. 2013.

[4] Y. F. Xiao and Q. Gong, "Optical microcavity from fundamental physics to functional photonics devices," *Sci. Bull.*, vol. 61, no. 3, pp. 185–186, Feb. 2016.

[5] K. J. Vahala, "Optical microcavities," *Nat. 2003 4246950*, vol. 424, no. 6950, pp. 839–846, 2003.

[6] J. McKittrick and L. E. Shea-Rohwer, "Review Down conversion materials for solid-state lighting," *J. Am. Ceram. Soc.*, vol. 97, no. 5, pp. 1327–1352, 2014.

[7] S. Coe-Sullivan, W. Liu, P. Allen, and J. S. Steckel, "Quantum Dots for LED Downconversion in Display Applications," *ECS J. Solid State Sci. Technol.*, vol. 2, no. 2, pp. R3026–R3030, Nov. 2013.

[8] J. Kundu, Y. Ghosh, A. M. Dennis, H. Htoon, and J. A. Hollingsworth, "Giant nanocrystal quantum dots stable down-conversion phosphors that exploit a large stokes shift and efficient shell-to-core energy relaxation," *ACS Publ.*, vol. 12, no. 6, pp. 3031–3037, Jun. 2012.

[9] J. H. Burroughes *et al.*, "Light-emitting diodes based on conjugated polymers," *Nat. 1990 3476293*, vol. 347, no. 6293, pp. 539–541, Oct. 1990.

[10] E. F. Schubert, Y. H. Wang, A. Y. Cho, L. W. Tu, and G. J. Zydzik, "Resonant cavity light-emitting diode," *Appl. Phys. Lett.*, vol. 60, no. 8, p. 921, Jun. 1998.

[11] C. Wang, H. Dong, W. Hu, Y. Liu, and D. Zhu, "Semiconducting π-conjugated systems in field-effect transistors A material odyssey of organic electronics," *Chem. Rev.*, vol. 112, no. 4, pp. 2208–2267, Apr. 2012.

[12] S. Günes, H. Neugebauer, and N. S. Sariciftci, "Conjugated polymer-based organic solar cells," *Chem. Rev.*, vol. 107, no. 4, pp. 1324–1338, Apr. 2007.

[13] D. Neher, "Polyfluorene homopolymers Conjugated liquid-crystalline polymers for bright blue

emission and polarized electroluminescence," *Macromolecular Rapid Communications*, vol. 22, no. 17. pp. 1365–1385, 2001.

[14] J. H. Robertson, "Electrical transport in solids, with particular reference to organic semiconductors by K. C. Kao and W. Hwang," *Acta Crystallogr. Sect. B Struct. Crystallogr. Cryst. Chem.*, vol. 38, no. 1, pp. 350–350, Jan. 1982.

[15] Martin Pope and C. E. Swenberg, "Electronic Processes in Organic Crystals and Polymers - 2nd edition, ISBN 9780195129632," *Oxford Univ. Press USA 2nd Ed.*, p. 1360, 1999.

[16] M. Jaiswal and R. Menon, "Polymer electronic materials a review of charge transport," *Polym. Int.*, vol. 55, no. 12, pp. 1371–1384, Dec. 2006.

[17] B. Ghasemi *et al.*, "Thickness Dependence of Electronic Structure and Optical Properties of F8BT Thin Films," *Polymers (Basel).*, vol. 14, no. 3, p. 641, Feb. 2022.

[18] M. J. Bird, J. Bakalis, S. Asaoka, H. Sirringhaus, and J. R. Miller, "Fast Holes, Slow Electrons, and Medium Control of Polaron Size and Mobility in the da Polymer F8BT," *J. Phys. Chem. C*, vol. 121, no. 29, pp. 15597–15609, Jul. 2017.

[19] M. Mamada, R. Komatsu, and C. Adachi, "F8BT Oligomers for Organic Solid-State Lasers," *ACS Appl. Mater. Interfaces*, vol. 12, no. 25, pp. 28383–28391, Jun. 2020.

[20] S. Linde and R. Shikler, "Comprehensive study of the influence of different environments on degradation processes in F8BT Correlating optoelectronic properties with Raman measurements," *J. Appl. Phys.*, vol. 114, no. 16, p. 164506, Oct. 2013.

[21] B. R. Lee *et al.*, "Highly efficient inverted polymer light-emitting diodes using surface modifications of ZnO layer," *Nat. Commun. 2014 51*, vol. 5, no. 1, pp. 1–8, Sep. 2014.

[22] M. Mamada, R. Komatsu, and C. Adachi, "F8BT Oligomers for Organic Solid-State Lasers," *ACS Appl. Mater. Interfaces*, vol. 12, no. 25, pp. 28383–28391, Jun. 2020.

[23] S. Nam, M. Shin, S. Park, S. Lee, H. Kim, and Y. Kim, "All-polymer solar cells with bulk heterojunction nanolayers of chemically doped electron-donating and electron-accepting polymers," *Phys. Chem. Chem. Phys.*, vol. 14, no. 43, pp. 15046–15053, Oct. 2012.

[24] G. E. Eperon, S. D. Stranks, C. Menelaou, M. B. Johnston, L. M. Herz, and H. J. Snaith, "Formamidinium lead trihalide A broadly tunable perovskite for efficient planar heterojunction solar cells," *Energy Environ. Sci.*, vol. 7, no. 3, pp. 982–988, 2014.

[25] F. Zhang *et al.*, "Brightly luminescent and color-tunable colloidal CH3NH3PbX3 (X = Br, I, Cl) quantum dots Potential alternatives for display technology," *ACS Nano*, vol. 9, no. 4, pp. 4533–4542, Apr. 2015.

[26] L. Protesescu *et al.*, "Nanocrystals of Cesium Lead Halide Perovskites (CsPbX3, X = Cl, Br, and I) Novel Optoelectronic Materials Showing Bright Emission with Wide Color Gamut," *Nano Lett.*, vol. 15, no. 6, pp. 3692–3696, Jun. 2015.

[27] J. A. Sichert *et al.*, "Quantum Size Effect in Organometal Halide Perovskite Nanoplatelets," *Nano Lett.*, vol. 15, no. 10, pp. 6521–6527, Oct. 2015.

[28] H. Huang, L. Polavarapu, J. A. Sichert, A. S. Susha, A. S. Urban, and A. L. Rogach, "Colloidal lead halide perovskite nanocrystals synthesis, optical properties and applications," *NPG Asia Mater. 2016 811*, vol. 8, no. 11, pp. e328–e328, Nov. 2016.

[29] Y. Wang, G. Ding, J. Y. Mao, Y. Zhou, and S. T. Han, "Recent advances in synthesis and application of perovskite quantum dot based composites for photonics, electronics and sensors," *Sci. Technol. Adv. Mater.*, vol. 21, no. 1, p. 278, Jan. 2020.

[30] H. Moon *et al.*, "Stability of Quantum Dots, Quantum Dot Films, and Quantum Dot Light-

Emitting Diodes for Display Applications," *Adv. Mater.*, vol. 31, no. 34, p. 1804294, Aug. 2019.

[31] H. Huang, M. I. Bodnarchuk, S. V. Kershaw, M. V. Kovalenko, and A. L. Rogach, "Lead Halide Perovskite Nanocrystals in the Research Spotlight Stability and Defect Tolerance," *ACS Energy Lett.*, vol. 2, no. 9, pp. 2071–2083, Sep. 2017.

[32] Q. Van Le, K. Hong, H. W. Jang, and S. Y. Kim, "Halide Perovskite Quantum Dots for Light-Emitting Diodes Properties, Synthesis, Applications, and Outlooks," *Adv. Electron. Mater.*, vol. 4, no. 12, p. 1800335, Dec. 2018.

[33] H. Huang, M. I. Bodnarchuk, S. V. Kershaw, M. V. Kovalenko, and A. L. Rogach, "Lead Halide Perovskite Nanocrystals in the Research Spotlight Stability and Defect Tolerance," *ACS Energy Lett.*, vol. 2, no. 9, pp. 2071–2083, Sep. 2017.

[34] J. Pan *et al.*, "Highly Efficient Perovskite-Quantum-Dot Light-Emitting Diodes by Surface Engineering," *Adv. Mater.*, vol. 28, no. 39, pp. 8718–8725, Oct. 2016.

[35] H. Y. Yang *et al.*, "Multifunctional polymer ligand interface CdZnSeS/ZnS quantum dot/Cy3-labeled protein pairs as sensitive FRET sensors," *ACS Publ.*, vol. 8, no. 51, p. 10, Dec. 2016.

[36] L. Protesescu *et al.*, "Dismantling the 'red Wall' of Colloidal Perovskites Highly Luminescent Formamidinium and Formamidinium-Cesium Lead Iodide Nanocrystals," *ACS Nano*, vol. 11, no. 3, pp. 3119–3134, Mar. 2017.

[37] X. Zhang *et al.*, "Enhancing the Brightness of Cesium Lead Halide Perovskite Nanocrystal Based Green Light-Emitting Devices through the Interface Engineering with Perfluorinated Ionomer," *Nano Lett.*, vol. 16, no. 2, pp. 1415–1420, Feb. 2016.

[38] F. Palazon, F. Di Stasio, Q. A. Akkerman, R. Krahne, M. Prato, and L. Manna, "Polymer-Free Films of Inorganic Halide Perovskite Nanocrystals as UV-to-White Color-Conversion Layers in LEDs," *Chem. Mater.*, vol. 28, no. 9, pp. 2902–2906, May 2016.

[39] R. J. Sutton *et al.*, "Bandgap-Tunable Cesium Lead Halide Perovskites with High Thermal Stability for Efficient Solar Cells," *Adv. Energy Mater.*, vol. 6, no. 8, p. 1502458, Apr. 2016.

[40] S. Yakunin *et al.*, "Low-threshold amplified spontaneous emission and lasing from colloidal nanocrystals of caesium lead halide perovskites," *Nat. Commun.*, vol. 6, 2015.

[41] Y. Wang, X. Li, X. Zhao, L. Xiao, H. Zeng, and H. Sun, "Nonlinear Absorption and Low-Threshold Multiphoton Pumped Stimulated Emission from All-Inorganic Perovskite Nanocrystals," *Nano Lett.*, vol. 16, no. 1, pp. 448–453, Jan. 2016.

[42] H. Li *et al.*, "Polymer spacer tunable Purcell-enhanced spontaneous emission in perovskite quantum dots coupled to plasmonic nanowire networks," *Phys. Chem. Chem. Phys.*, vol. 21, no. 41, pp. 22831–22838, Oct. 2019.

[43] A. V. Kavokin, J. J. Baumberg, G. Malpuech, and F. P. Laussy, "Weak-coupling microcavities," *Microcavities*, pp. 243–276, Aug. 2017.

[44] Q. Gu and Y. Fainman, "Purcell Effect and the Evaluation of Purcell and Spontaneous Emission Factors," *Semicond. Nanolasers*, pp. 65–90, Mar. 2017.

[45] V. Robbiano *et al.*, "C-Si hybrid photonic structures by full infiltration of conjugated polymers into porous silicon rugate filters," *Nanomater. Nanotechnol.*, vol. 8, Aug. 2018.

[46] J. Brédas, J. Cornil, A. H.-A. Materials, and undefined 1996, "The exciton binding energy in luminescent conjugated polymers," *Wiley Online Libr.*, vol. 8, no. 5, pp. 447–452, 1996.

[47] S. Noda, M. Fujita, and T. Asano, "Spontaneous-emission control by photonic crystals and nanocavities," *Nature Photonics*, vol. 1, no. 8. Nature Publishing Group, pp. 449–458, Aug-2007.

[48] M. Höijer and G. Björk, “Modification of spontaneous emission rate in planar dielectric microcavities - Seen as superradiance and subradiance,” *Opt. Commun.*, vol. 150, no. 1–6, pp. 319–330, May 1998.

[49] H. Hintz, H. J. Egelhaaf, L. Lüer, J. Hauch, H. Peisert, and T. Chassé, “Photodegradation of P3HT - A systematic study of environmental factors,” *Chem. Mater.*, vol. 23, no. 2, pp. 145–154, Jan. 2011.

[50] A. Distler *et al.*, “Effect of PCBM on the photodegradation kinetics of polymers for organic photovoltaics,” *Chem. Mater.*, vol. 24, no. 22, pp. 4397–4405, Nov. 2012.

[51] E. Yousif and R. Haddad, “Photodegradation and photostabilization of polymers, especially polystyrene review,” *Springerplus*, vol. 2, no. 1, 2013.

[52] M. Salvador *et al.*, “Suppressing photooxidation of conjugated polymers and their blends with fullerenes through nickel chelates,” *Energy Environ. Sci.*, vol. 10, no. 9, pp. 2005–2016, Sep. 2017.

[53] S. R. Cordero, P. J. Carson, R. A. Estabrook, G. F. Strouse, and S. K. Buratto, “Photo-activated luminescence of CdSe quantum dot monolayers,” *J. Phys. Chem. B*, vol. 104, no. 51, pp. 12137–12142, Dec. 2000.

[54] S. Dembski *et al.*, “Photoactivation of CdSe/ZnS quantum dots embedded in silica colloids,” *Wiley Online Libr.*, vol. 4, no. 9, pp. 1516–1526, 2008.

[55] C. Carrillo-Carrión, B. M. Simonet, and M. Valcárcel, “Colistin-functionalised CdSe/ZnS quantum dots as fluorescent probe for the rapid detection of Escherichia coli,” *Biosens. Bioelectron.*, vol. 26, no. 11, pp. 4368–4374, Jul. 2011.

7) Chapter 7 - Conclusion

In this Chapter, an overview of all research undertaken is presented together with the main findings. In addition, future research suggestions are device performance improvement.

7.1 Overview

The developed fabrication approach involved the fabrication of DBR Fabry-Perot planar microcavitty, this was chosen due to the ease of fabrication and characterisation. It is important to note that the developed platform serves as a proof of concept with the potential of better performance after process parameter optimisation. Nonetheless, important microcavity effects described in literature could be observed. These are summarised below

7.1.1 Development of heterogeneous fabrication approaches for the fabrication of microcavity devices by transfer printing

Reflectors in general and DBRs in particular for our chosen type of cavity are essential components as they are the elements in charge of light confinement. In this chapter, the platform allowing the anchor undercutting and transfer printing of DBRs was described. This involved the PECVD growth of the DBRs on Si (111) substrate, patterning of the grown DBR into coupons attached to anchors by tethers while making sure the anchors are parallel align to the <110> direction and two of the coupon sides normal to the <110> direction. This was to ensure adequate undercut of the coupon and their tethers only (not anchors) thanks to the high KOH Si etch rate along the <110> direction compared to the orthogonal direction. Transfer printing of individual DBR coupons on new substrate and transfer printing of passive microcavities as stacked DBRs separated with a spacer layer was performed. Some processing optimisation of effective DBR pattern masking using Ti/Al metals and tether strength optimisation by sizing was necessary to achieve a high coupon yield of approximately 100%. Reflectivity measurements showed strong similarity between the grown, transfer printed and COMSOL simulated DBR with peak reflectivity of 99% and wide linewidth of 95nm. Therefore, our platform was successful at the transfer printing of high quality DBRs. Microcavity reflectivity measurements didn’t show a clear cavity mode as expected due to the measurement setup limitations of no spatial and angular resolution which are critical for our small size coupons (100um) reflectivity measurments. It is also important to note that our platform provides advantages of scalability, versatility and potential of high through put fabrication

7.1.2 Fabrication of GaN based RCLED via a Modified Transfer Printing Technique

In this chapter, an important GaN based functional device, the RCLED was fabricated using our platform. The RCLED serves in many applications such as infrared wireless communication and Plastic Optical fibre (POF) [1], high brightness lighting applications [2][3] and display technology thanks to their attractive properties of enhanced emission intensity, purer emission, and more directional emission with relatively low cost of fabrication. Using our platform, a wide cavity length RCLED was demonstrated. Strain compensation was done using SiO_2 dielectric to make sure the LED coupon is as flat as possible. Anchor undercutting of both LEDs and DBR into coupons attached to anchors by the tethers was done. The DBRs used was grown to have stopband corresponding to LED emission. The LED and DBR were transfer printed in a configuration where the LED is sandwiched by two DBRs. Device structure was modified to have a reduced emission area, this limit the non-coupled emission hence maximising resonance. Electrical characterisation showed the device processing need some optimisation as series resistance were seen to increase due to the damage caused on the device contact during their window opening. Some considerable self-heating because of the strain compensation dielectric and adhesion layer SU-8 were also seen causing the emission band blue shift. Despite all the non-optimised steps, the device worked with turn-on voltage of about 2.7V with EL measurements showing cavity mode emission with FSR of approximately 6nm and peak emission mode with FWHM of approximately 3nm. COMSOL simulation were carried out and this matched the seen emission with some slight differences due to the layers thicknesses uncertainties. Therefore, we demonstrated a proof of concept new approach of RCLED fabrication by transfer printing with potential of single mode narrow emission of 3nm when fully optimised.

7.1.3 Transfer printed optical microcavities with active materials

One of the main limiting factor for our fabricated RCLED in chapter 5 was the wide cavity length. Thankfully there exist other classes of emitters which are solution based and therefore can be deposited as thin film active layers using simple and low cost techniques such as spin coating and drop casting. In this Chapter, light emitting polymer F8BT and CQD $CsPbBr_3$ optical microcavity were fabricated and characterised. This involved their spinning on bottom DBR with spacer layers PMMA to ensure accurate cavity length tuning. This was then followed by the transfer printing of the top DBR to form the active optical microcavity. PL measurement showed considerable emission band narrowing due to the microcavity 80.6nm to 8.3nm for F8BT and 100nm to 0.4nm for QD cavity measured by microPL and confocalPL respectively.

Due to photo-oxidation effects leading to an increase in non-radiative processes, carrier decay measurements (TRPL) of the resonant cavity F8BT could not be compared to outside cavity F8BT as it was considerably degraded due to photo-oxidation. However, comparison was made between the resonant and non-resonant F8BT microcavity, which went through similar processing, and hence similar levels of photoxidation. Carrier lifetime was seen to decrease by 0.553ns (68% decrease) from non-resonant to resonant cavity hence, Purcell effect demonstration. Despite the large line width narrowing, cavity quality factor measurement of the F8BT cavity was only 64, this can be attributed to the active material high absorption coefficient at the cavity emission, low quantum yield and potential rough optical interfacing with the spacer PMMA layer. Lasing investigations were carried out for the QD microcavity by measuring the Power dependent PL. Non-linearity behaviour was not clear as the integrated intensity were seen to increase with power but the emission FWHM was relatively constant.

The above results demonstrate the successful fabrication and characterisation of various active material optical microcavity devices using our develop platform. Despite the low performance of the devices, the concept was demonstrated and this provide a novel approach for optical microcavity devices fabrication by transfer printing offering advantages of scalability, versatility and potential of high through put fabrication. Various processing and characterisation optimisations are needed for better device performance as seen. Below is an overview of all with the next step of the research.

7.2 Future works

In terms of the LED self-heating issue, alternative optically passive adhesion layers could be used, which are thinner and as sticky. The use of InterVia was demonstrated by Shaban et al [4] where they were able to transfer print LED coupons into trenches. Their transfer printed LED showed I-V plot not very different from their processed LED, there was a slight decrease in resistance due to the band gap shrinking effect of self-heating. Effective SiO_2 etching for exposing the contacts is needed for better device electrical properties. This may be done by effectively calibrating the dry etch rates RIE and/or ICPRIE. Alternative etch methods such as HF wet etch could also be used and it is effective at etching SiO_2 and not the contact metals used in our LED. Strategies could also be implemented for the reduction of the LED coupon thickness such as selective etching of the LED buffer layer using TMAH solution [4] and/or electrochemical etch undercutting of the LED around the n-GaN region (for modified n^+GaN structures).

QD microcavity showed some optimistic results with high quality factor greater 1000. Challenges encountered include; low density and uneven QD distribution as most are washed away due to the spinning deposition. This could be solved via other deposition methods such as drop casting, but drop casting adds uncertainty on the cavity length (another critical cavity parameter to ensure coupling). As the solvent plays an important role in the dismissal of the dots from the surface to be coated, solvent free transfer printing of the QD provides another alternative for QD deposition, this was demonstrated by Kim et al for display technology [5].

The obvious next step of the research will be the heterogeneous integration of more than one active material in the cavity; that is an LED and a down conversion material. Here, the high-energy photons from the GaN based blue emitting LED will be absorbed by the down conversion material and reemitted at lower energy hence down conversion. This is a highly popular method utilised for colour tuning and conversion for example in white light generation using blue LEDs. Various polymers and QD having characteristics; low light scattering, high quantum yield, high photo, chemical and thermal stability and long lifetime [6] could serve as down conversion materials. In addition, non-radiative energy transfer between spatially separated but quantum entangled molecules in optical microcavities were demonstrated [7]. This could serve as pathway to resolution of the green gap problem resolution

7.3 References

[1] R. G. Baets, D. Delbeke, R. Bockstaele, and P. Bienstman, "Resonant-Cavity Light-Emitting Diodes a review," 2003.

[2] K. Streubel, U. Helin, V. Oskarsson, E. Bäcklin, and Å. Johansson, "High brightness visible (660 nm) resonant-cavity light-emitting diode," *IEEE Photonics Technol. Lett.*, vol. 10, no. 12, pp. 1685–1687, Dec. 1998.

[3] R. Wirth, C. Karnutsch, S. Kugler, and K. Streubel, "High-efficiency resonant-cavity LEDs emitting at 650 nm," *IEEE Photonics Technol. Lett.*, vol. 13, no. 5, pp. 421–423, May 2001.

[4] Z. Shaban, Z. Li, B. Roycroft, M. Saei, T. Mondal, and B. Corbett, "Transfer Printing of Roughened GaN-Based Light-Emitting Diodes into Reflective Trenches for Visible Light Communication," *Adv. Photonics Res.*, vol. 3, no. 8, p. 2100312, Aug. 2022.

[5] T. H. Kim *et al.*, "Full-colour quantum dot displays fabricated by transfer printing," *Nat. Photonics*, vol. 5, no. 3, pp. 176–182, Mar. 2011.

[6] J. McKittrick and L. E. Shea-Rohwer, "Review Down conversion materials for solid-state lighting," *J. Am. Ceram. Soc.*, vol. 97, no. 5, pp. 1327–1352, 2014.

[7] X. Zhong *et al.*, "Energy Transfer between Spatially Separated Entangled Molecules," *Angew. Chemie*, vol. 129, no. 31, pp. 9162–9166, Jul. 2017.

[1] R. G. Baets, D. Delbeke, R. Bockstaele, and P. Bienstman, “Resonant-Cavity Light-Emitting Diodes a review,” 2003.

[2] K. Streubel, U. Helin, V. Oskarsson, E. Bäcklin, and Å. Johansson, “High brightness visible (660 nm) resonant-cavity light-emitting diode,” *IEEE Photonics Technol. Lett.*, vol. 10, no. 12, pp. 1685–1687, Dec. 1998.

[3] R. Wirth, C. Karnutsch, S. Kugler, and K. Streubel, “High-efficiency resonant-cavity LEDs emitting at 650 nm,” *IEEE Photonics Technol. Lett.*, vol. 13, no. 5, pp. 421–423, May 2001.

[4] Z. Shaban, Z. Li, B. Roycroft, M. Saei, T. Mondal, and B. Corbett, “Transfer Printing of Roughened GaN-Based Light-Emitting Diodes into Reflective Trenches for Visible Light Communication,” *Adv. Photonics Res.*, vol. 3, no. 8, p. 2100312, Aug. 2022.

[5] T. H. Kim *et al.*, “Full-colour quantum dot displays fabricated by transfer printing,” *Nat. Photonics*, vol. 5, no. 3, pp. 176–182, Mar. 2011.

[6] J. McKittrick and L. E. Shea-Rohwer, “Review Down conversion materials for solid-state lighting,” *J. Am. Ceram. Soc.*, vol. 97, no. 5, pp. 1327–1352, 2014.

[7] X. Zhong *et al.*, “Energy Transfer between Spatially Separated Entangled Molecules,” *Angew. Chemie*, vol. 129, no. 31, pp. 9162–9166, Jul. 2017.